Effect of Cascade Size and Damage Rate on α' Precipitate Stability on Fe-15Cr

by

Katey Nicole Thomas

A dissertation submitted in partial fulfillment
of the requirements for the degree of
Doctor of Philosophy
(Nuclear Engineering and Radiological Sciences)
in The University of Michigan
2022

Doctoral Committee:

Professor Gary S. Was, Chair
Professor Fei Gao
Research Scientist, Zhijie Jiao
Professor Emmanuelle Marquis

Katey Nicole Thomas

knthomas@umich.edu

ORCID iD: 0000-0001-9485-6253

Dedication

To my friends and family

Acknowledgements

I would first like to thank my advisor, Dr. Gary Was. His insight, suggestions, and input have been instrumental throughout my doctoral program. I would also like to thank my committee members, Dr. Zhijie Jiao, Dr. Fei Gao, and Dr. Emmanuelle Marquis for their input, which improved this thesis.

I am grateful to all members of the Was research group, past and present, including Dr. Zhijie Jiao, Dr. Peng Wang, Dr. Miao Song, Dr. Mi Wang, Dr. Calvin Lear, Dr. Anthony Monterosa, Dr. Justin Hesterberg, Dr. Gerrit VanVoevering, Dr. Drew Johnson, Dr. Stephen Taller, Dr. David Woodley, Robert Wahlen, Samara Lavine, Rajan Bhambroo, Valentin Pauly, and Logan Clowers. Their mentorship, friendship, and support has played a tremendous role in my graduate studies and getting me to this point.

Thank you to the past and present staff members at the Michigan Ion Beam Laboratory, Dr. Ovidiu Toader, Dr. Fabian Naab, Dr. Kai Sun, Dr. Ethan Uberseder, Thomas Kubley, Robert Hensley, and Dr. Prashant Niraula. Without their experience, and hard work, these experiments would not have been possible. I want to thank the staff at the Michigan Center for Materials Characterization for help with FIB liftouts, APT, TEM, and SEM and care of the associated instruments. Thank you to the DOE NE program DE-NE0000639 and Nanotechnology Platform Japan (NTPJ) sponsored by MEXT through A-21-KU-0391 for providing funding.

To my family, my parents, Dr. Keith and Dr. Angela Thomas, and my sister, Jodi Thomas, thank you for you love and support. Without you, this would not have been possible.

To my friends, my life-long friends and those I've made during my time here, thank you for your friendship, support, and making the time here in Michigan far better.

To my dog, Phoebe, thank you for the unconditional love and joy a dog provides. The many late nights were made better with you at my feet.

Lastly, to Tobias Burger thank for you for your constant support, encouragement, and love. Thank you for all the late nights, proof-reading, and discussions at any time I needed. A PhD is difficult task, but I am thankful we did this together.

Table of Contents

List of Figures

List of Tables

List of Appendices

Abstract

High Cr ferritic-martensitic (F-M) steels are candidates for nuclear reactor structural components due to their high resistance to swelling and adequate corrosion resistance. However, these steels are susceptible to the formation of Cr-rich α' precipitates at low to intermediate temperatures (below ~500°C) in both thermal and irradiation environments leading to hardening and embrittlement, commonly known as "475°C embrittlement". α' precipitates are not consistently observed under heavy ion irradiation and have dissimilar properties (radius, number density, concentration, volume fraction) than those formed under neutron, proton, or electron irradiation or by thermal aging. The dissimilar properties are a result of ballistic dissolution of the α' precipitate, which is dependent on both damage rate and cascade size.

The objective of this thesis is to understand the roles of damage rate and cascade size on the stability of α' precipitates in Fe-15Cr under irradiation. A systemic study using heavy ion, proton, and electron irradiation was conducted with variations in damage rate at 400°C to doses of 1 and 10 dpa to examine the stability of α' precipitates under irradiation. A steady state α' precipitate distribution was first established in Fe-15Cr samples using 2 MeV proton irradiation at a damage rate of $1x10^{-5}$ dpa/s to 1 dpa at 400°C. These samples were then subjected to irradiation with Fe ions, proton, or electrons also at 400°C, to 1 and 10 dpa, over a range of damage rates. The α' precipitate microstructure evolution was characterized for each irradiation experiment using atom probe tomography (APT).

Under heavy ion irradiation, the α' precipitates were observed to decrease to a steady state size and Cr concentration or completely dissolve. At doses of 1 dpa, the α' precipitate was the same size and was shown to be independent of damage rate. For higher doses of 10 dpa, the α' radius is stable for low damage rates but the precipitate dissolves completely at higher damage rates. However, under electron and proton irradiation, the α' precipitates increased in size and Cr concentration. The ballistic dissolution parameter (BDP), a constant describing the atom flux ballistically ejected from a precipitate surface per dpa, was calculated for both proton and heavy ion irradiation using two methods to describe the effects of cascade size and damage rate on

ballistic dissolution of α’ precipitates. A critical temperature analysis was further used to explain the balance in the roles of ballistic dissolution and radiation enhanced diffusion between heavy ion, proton, and electron irradiation.

This work provided substantial insight into the roles of cascade size and damage rate on α’ precipitate stability under irradiation.

Chapter 1: Introduction

Advanced nuclear power plants, called Generation IV reactors, offer many advantages over the current nuclear reactor fleet with decreased radioactive waste, reduced carbon footprint, and more efficient fuel use through higher burnup. However, to meet the higher burnup, the structural materials within the reactor will experience more extreme radiation and temperature conditions.

Historically, austenitic stainless steels have been used for structural materials in light water reactors. However, it was discovered that their susceptibility to irradiation creep and swelling made them unsuitable for fast reactor applications. After showing potential in initial testing at the Fast Flux Test Facility (FFTF), ferritic-martensitic steels became the leading candidates for high temperature-high dpa applications. Ferritic-martensitic (F-M) steels are body-centered cubic (BCC), iron-based alloys, with typically 7-15% Cr. Minor solute elements, such as Mo, Ni, Nb, Mn, Si, V, Cu, Ta, Ti, and W, are common additions to add strength, ductility or reduce activation of the alloys. Unlike austenitic stainless steels, ferritic-martensitic steels have a complex microstructure, composed of small grains, sub-grains, precipitates, laths, and a high dislocation density. The complex microstructure delivers a high sink strength for point defect annihilation, contributing to the radiation tolerance of the material.

The development of radiation-tolerant materials for current or future nuclear power plants requires extensive research and development. Typically, radiation effects studies are conducted using materials test reactors followed by extensive and time-consuming post-irradiation examination, primarily as a result of the neutron induced radioactivity. Neutron irradiations are typically at damage rates on the order of 10^{-8} dpa/s to 10^{-6} dpa/s, in fast reactors. Meanwhile, heavy ions can span damage rates on the order of 10^{-5} dpa/s to 10^{-3} dpa/s, proton irradiations are typically ~10^{-5} dpa/s, and electron irradiation typically can span 10^{-5} dpa/s to 10^{-3} dpa/s. Ion and electron irradiation are more cost effective and can be a fast alternative to emulate neutron irradiation up to higher damage levels. However, there are still critical gaps in the literature in the stability of α' phase under ion irradiation.

Under neutron irradiation, the α' phase can form, leading to embrittlement and degradation of the alloy. And α' has not always been observed using ion irradiation, and when it has been observed, the microstructural properties are dissimilar to that under thermal or neutron irradiation conditions. This is thought to be because of ballistic dissolution as a result of the higher damage rates of heavy ion irradiation. One such gap in the field is the understanding of α' precipitate stability under irradiation. A systemic study of the effect of damage rate and cascade size is necessary to understand the effects of ballistic dissolution on α' precipitate stability. Many previous studies have only observed effects on nucleation and growth of α' precipitates or have been at low doses and temperatures.

The objective of this thesis is to understand the roles of damage rate and cascade size on the stability of α' precipitates in Fe-15Cr under irradiation. A combination of ion irradiation experiments, with careful post-irradiation characterization techniques coupled with computational models were used to achieve this objective. Chapter 2 provides a background on Fe-Cr alloys and the effects of neutron, ion, and electron irradiation on the microstructure. Chapter 3 summarizes the objective of the thesis and the approach taken to achieve the objective. Chapter 4 describes the experimental procedures and techniques used for ion and electron irradiation experiments and post-irradiation characterization. Chapter 5 summarizes the results gathered from the experiments. Chapter 6 offers an interpretation and discussion of the experimental results and address the objective. Chapter 7 provides the conclusions drawn from the thesis and suggests future work.

Chapter 2: Background

This chapter will provide the background necessary to understand the results of this work and place them in context of existing literature. A general overview of FM steels and Fe-Cr alloys will be provided followed by a comprehensive review of the existing experimental and theoretical work regarding α' precipitate evolution under irradiation. Various factors affecting α' precipitate evolution under irradiation will also be considered.

2.1 Metallurgy and microstructure of ferritic-martensitic steels/Fe-Cr alloys

Iron-chromium alloys are the model system for ferritic and ferritic-martensitic steels that will be used in advanced nuclear reactors. The Fe-Cr model alloys in literature typically have Cr concentrations up to ~18% Cr. Fe-Cr alloys are typically produced by heating the metal to an austenitizing temperature (between 850-1200°C). Then the material is rapidly cooled by air cooling or quenching to transform the austenite to martensite. The metal is subsequently tempered to develop a good combination of strength, ductility, and toughness.

2.1.1 α' phase

The high chromium F-M steels are susceptible to α' precipitate formation primarily at lower temperatures, resulting in hardening and embrittlement, known as "475 embrittlement". In the Fe-Cr system, the α' phase results from the α-α' phase separation, where α' phase is a chromium rich phase and the α phase is an iron rich phase. The α' phase separation can occur under thermal conditions but has also been formed under irradiation. Figure 2.1 shows the phase diagram. From the diagram, the nominal α' chromium concentration at 400°C, the temperatures used for experiments in this thesis, is ~94at% with a matrix concentration of ~10.5at%. Additionally, as the α' is coherent with matrix and the matrix is still a concentration alloy, making characterization using transmission electron microscopy (TEM) difficult, so atom probe

tomography (APT) or small-angle neutron scattering (SANS) is more appropriate [1,2]. Under thermal aging conditions, chromium diffusion in bcc iron is very slow [3–5].

The α' phase separates coherently and homogeneously. Both the α and α' phases are BCC, with little difference in the lattice parameters (~1.5%). There is conflict in the literature as to whether or not the α' precipitates form by classical or non-classical nucleation [6–9]. The main observable differences between classical and non-classical nucleation are the precipitate concentration. Classical nucleation defines the precipitate concentration as uniform throughout the entirety of the precipitate and non-classical nucleation displays a non-uniform concentration with the highest-solute concentration in the core and a diffuse matrix-precipitate interface. Additionally, with non-classical nucleation, the core chromium concentration increases with increasing precipitate size [7].

Bonny, et al [10] conducted simulation studies of the phase decomposition of Fe-(12, 15, 18)Cr under thermal aging between 327-527°C (600-800K). The study focused on the evolution of α' number density, mean size, shape, and composition with time. The study showed a clear identification of the three stages of precipitation process (nucleation, growth, and coarsening). Additionally, the expected concentration dependent trends were observed such as the increase in number density with chromium concentration and decrease in number density with increase in temperature.

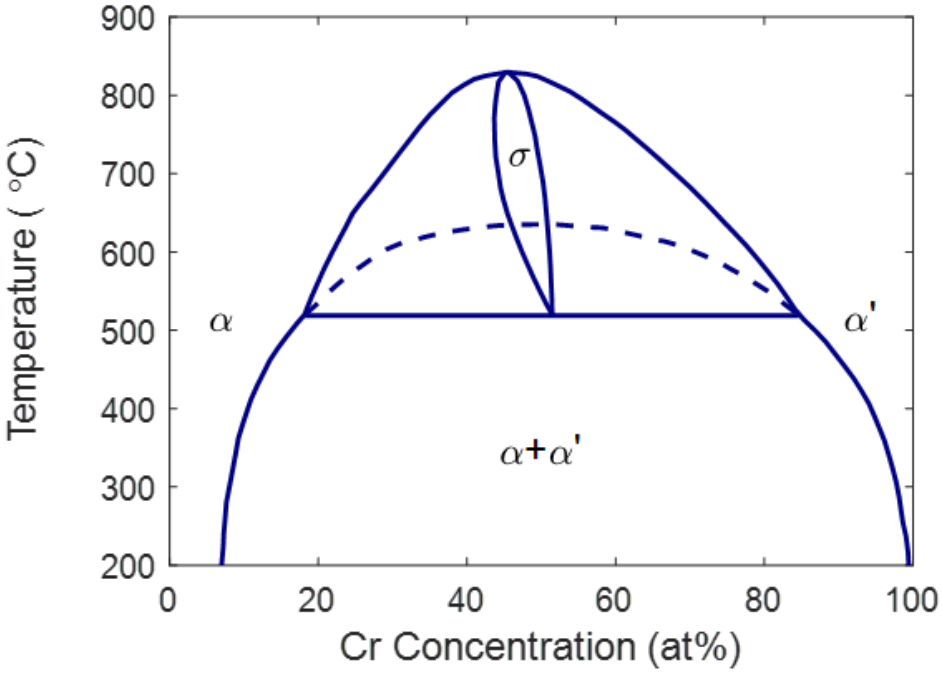

Figure 2.1 Phase diagram for Fe-Cr, from Ref [11].

2.2 α’ precipitation under irradiation in Fe-Cr alloys

Under irradiation, a neutron, or ion, causes atomic displacements when it strikes an atom in the crystal lattice. A portion of the energy from the neutron or ion is transferred to the lattice atom and displaces it from its site. This is called a primary knock-on atom (PKA). This displaced atom continues throughout the lattice, colliding with other lattice atoms and forming other displaced atoms, which continuing this process until the energy of the particles drops below the threshold energy for displacement. The displaced atoms are interstitials, the empty lattice sites are vacancies, and the collection of damage created from the PKA is the damage cascade. The damage on the lattice is measured as displacement per atom, or dpa. The accumulation and migration of the point defects can lead to dislocation loops or cavities. And under irradiation, the concentration of vacancy and interstitial defects exceeds those driven by thermodynamics, enabling an enhanced diffusion, or radiation-enhanced diffusion (RED). This radiation-enhanced diffusion allows for increased mobility of defects to migrate more quickly, thus influencing the microstructure. α’ is one such phase that is formed through radiation enhanced diffusion under irradiation.

Under irradiation, α’ phase has been observed to have different microstructural properties, dependent on the type of irradiation, damage rate, and other irradiation conditions. Most changes in the α’ phase is observed as changes in the precipitate size or number density, volume fraction, or Cr concentration. The α’ precipitates are modified under irradiation as a result of ballistic dissolution primarily under neutron and heavy ion irradiation. The modified α’ precipitates are generally smaller, denser, and possess lower solute concentration in comparison to thermally aged α’ precipitates. The modification of the α’ precipitates affect the stability, meaning the composition and the long-term presence of the α’ precipitates. The instability of the α’ precipitates under irradiation is caused by the ballistic dissolution, and the observed effects on the precipitates are variable between the various types of irradiations.

2.2.1 Neutron irradiation

The α’ precipitates have been observed under neutron irradiation at low temperatures ranging from ~290 to 500°C and doses ranging from less than 1 dpa to more than 200 dpa in Fe-Cr model alloys, Fe-Cr-Al, and commercial Fe-Cr-based F/M steels. The α’ precipitates formed

under neutron irradiation are typically at or near maximum solute concentration (as determined from the phase diagram). Neutron irradiation results in the ballistic dissolution effects of the α' precipitates and are observed at low temperatures, less than 300°C, as evidenced by the modified α' precipitates (lower radius, higher number density, and lower solute concentration) [6,12,13].

Gelles [14] studied the swelling effects in Fe-Cr commercial and model alloys subjected to neutron irradiation in FFTF/MOTA at 420°C up to ~200 dpa. The purpose of these studies was to observe the effects of chromium concentration on the swelling to high doses. And α' precipitates were noted to be observed in the alloys with a higher chromium concentration and followed the solubility limit estimated by the phase diagram. No chemical composition nor size or density was provided for the observed α' precipitates, but it was concluded that the reduced swelling occurred in the alloys with higher chromium concentrations as a result of the increased precipitate density.

Bachhav, et al. [13,15,16] studied model Fe-Cr (3, 6, 9, 12, 15, and 18% Cr) neutron irradiated in ATR at 290°C to 1.82 dpa for the purpose of observing the α' precipitate properties. This study established that the solubility limits at 290°C for neutron irradiated samples were in good agreement with the phase diagram and that the α' precipitates formed through radiation-enhanced precipitation as opposed to radiation-induced precipitation. Additionally, radiation-induced segregation of chromium to dislocation loops was observed to occur with a chromium concentration below the solubility limit.

W. Y. Chen, et al. [6] studied model Fe-Cr alloys neutron irradiated at either 300°C and 450°C to 0.01, 0.1, and 1 dpa in ATR. This study found that by 1 dpa, the volume fraction of α' phase matched that predicted by the phase diagram, but the α' precipitates were below the chromium concentration predicted by the phase diagram. Chen, et al. also observed that with increasing temperature, the volume fraction, number density, and radius of the α' precipitates decreased, which is as expected based on the phase diagram with the exception of the precipitate radius. Chen, et al. noted that this may be a result of another mechanism controlling the growth but did not investigate further.

Konobeev, et al. [17] studied the microstructure of annealed and heavily cold worked pure Fe and various Fe-Cr (2, 6, 12, and 18at% Cr) model alloys that were neutron irradiated to 25.8 dpa at $4x10^{-7}$ dpa/s at 400°C in the BR-10 fast reactor. The primary objectives for this study were to observe the effects of chromium concentration on the swelling in annealed and cold worked samples under neutron irradiation. The study looked at all aspects of the microstructure including

voids, dislocations, and precipitates. The α' precipitates were observed using TEM and ranged from 5-7 nm radius between the annealed samples and the heavily cold-worked samples. M_7C_3 carbides were also observed in the grain boundaries and the matrix in the supersaturated Fe-Cr alloys.

Kuksenko, et al. [12] studied the microstructure of a low purity Fe-Cr (2.5, 5, 9, 12% Cr) model alloys neutron irradiated at 300°C to 0.6 dpa in MTR reactor. The objective of this study was to observe the effects of the impurities on the microstructural evolution under irradiation. This study found that two types of clusters were observed: α' precipitates and NiSiPCr clusters. The α' precipitates were chromium-rich and precipitated homogeneously. The NiSiPCr clusters were found to precipitate heterogeneously, nucleating on dislocation loops. Hernández-Mayoral, et al. [18] studied these samples further, focusing on the chromium concentration effect on the dislocation microstructure under neutron irradiation. Bergner, et al. [19] also studied the low purity Fe-Cr model alloys. This study investigated the solubility limit of Cr in Fe at 300°C under neutron irradiation and showed that the solubility limit matches that estimated by the phase diagram for thermal phase separation.

Mathon, et al. [1] studied commercial steels and reduced activation steels (7-12% Cr) neutron irradiated to 0.7-2.9 dpa between 250-400°C irradiated in OSIRIS reactor or the HFR reactor. This study observed α' precipitation in the steels with a supersaturation of chromium. The α' precipitates had a similar radius of ~1-1.5 nm and number density that ranged from ~0.5-34x10^{23} m^{-3}.

Reese, et al. [20] studied Fe-Cr (9-18% Cr) model alloys that were neutron irradiated to doses up to 17 dpa and temperatures between 320-455C. This study was primarily focusing on the post-irradiation annealing effects on the α' precipitates but did characterize the α' precipitates prior to annealing. The α' precipitates were larger in size with average radii ranged from 1.2 to 3.9 nm and number densities ranged from 0.34 to 160x10^{24} m^{-3}, where the samples at higher temperatures were larger and less dense, as expected based on the phase diagram. The α' precipitate size was not dependent on the dose (7 dpa versus 17 dpa), but rather more closely related to temperature. The α' precipitates reached a higher fraction of the maximum chromium concentration with increasing temperature. The matrix (α phase) follows the phase diagram, increasing with temperature. The Fe-18Cr samples were then annealed to at 500 or 600°C for 300 or 7200 hours.

The α' precipitates dissolved 600°C, as expected based on the phase diagram. At 500°C, the precipitates grew in size, reduced in number density, and grew richer in chromium concentration.

2.2.2 Proton irradiation

α' precipitation has been noted to form though proton irradiation, though not commonly reported as the experiments on F-M steels are typically outside of the α-α' miscibility gap. Jiao, et al. [21] observed α' precipitates in the commercial steels HT-9 and HCM12A at 400°C at a damage rate of ~$1x10^{-5}$ dpa/s. These clusters had an average size and number density similar to that of neutron irradiated samples and also had a chromium concentration less than the maximum expected concentration, based on the phase diagram.

Haley, et al. [22] investigated 1.2 MeV proton irradiated Fe-9Cr at 300°C at a damage rate of $1x10^{-5}$ dpa/s to 1.9 dpa. This work also compared heavy ion irradiation and neutron irradiation at similar damage rates and doses to observe the differences in the α' precipitate evolution (and other microstructural features). α' precipitates were found to nucleate and grow under proton irradiation under these conditions. Using a TEM, in place of the typical APT, for microscopy, the α' was found to have a reasonable size with an average diameter of 4.4±1.0 nm and composition of ~68at% Cr. Cavities were also observed in the microstructure, and the larger cavities were faceted.

2.2.3 Electron irradiation

Under electron irradiation, there is no damage cascade produced from the electrons, only Frenkel pairs (vacancy-interstitial pair). There is only one known experimental study for Fe-Cr alloys that resulted in α' precipitation, conducted by Tissot, et al. [23]. The electron irradiation clearly showed the radiation-enhanced diffusion by the accelerated precipitation of the α' phase and no indication of ballistic dissolution. Under electron irradiation, the α' precipitates also reached the maximum solute concentration (96±2at% Cr) and the matrix reached the predicted solubility limit for chromium in iron at 300°C (8.7±0.5at% Cr) by 0.7 dpa. This work illustrated primarily the effect of the cascade, as there is no cascade present in electron irradiation and there are cascades present in all other forms of irradiation. This showed that in the absence of the

cascades, the precipitates were capable of coarsening by less than 1 dpa. This is in contrast to neutron and heavy ion irradiation data, where the α' precipitates are typically smaller, denser, and do not reach the maximum solute concentration at damage levels greater than 1 dpa.

An additional study was conducted on the damage rate effects under electron irradiation using simulation by Ke, et al. [24]. This work was targeted at separating the effects of damage rate and cascade mixing effects. The electron irradiation simulations were conducted considering cascade mixing and without considering cascade mixing at damage rates ranging from 10^{-8} dpa/s to 10^{-3} dpa/s at 300°C to 10 dpa in Fe-15Cr. The simulation results showed minimal differences between cascade mixing and without cascade mixing, and also showed reduced precipitate stability at higher damage rates, though the α' was still larger and higher chromium concentration than under heavy ion irradiation at the same temperature and damage rates. Reduced precipitate stability with increased damage rate under electron irradiation was attributed to the increasing role of recombination.

2.2.4 Heavy ion irradiation

There has been very little success in the precipitation of α' under heavy ion irradiation, with the only published successes within the past few years by Tissot, et al. [25], Reese, et al. [8], and Zhao, et al [26]. Under heavy ion irradiation, α' is only observed to reach ~50-60% of the maximum concentration predicted by the phase diagram at 300°C [8,25,26]. Under thermal aging and other forms of irradiation, the α' precipitates were observed to reach or approach the maximum solute concentration, even at low doses [13,23]. The low chromium α' precipitate concentration in heavy ion irradiated samples may be an effect of the ballistic dissolution preventing the α' phase from becoming larger and reaching a higher solute concentration. Zhao, et al. described this lower chromium concentration, in combination with non-equilibrium radius and number density, as radiation modified precipitation. This phenomena displays steady state precipitate parameters that are modified by the damage rate, temperature, and type of irradiation.

Hernández-Mayoral, et al. [18] studied Fe-Cr model alloys (5-12% Cr) irradiated at 300°C to ~0.5 dpa at ~$1x10^{-4}$ dpa/s in a multi-step heavy ion irradiation at 0.5, 2, and 5 MeV to create a semi-constant damage profile. This study was investigating the chromium concentration effects on the microstructure after heavy ion irradiation. This study did not observe any α' precipitation at

any condition. The low purity model Fe-9Cr and Fe-12Cr were also studied by Pareige, et al. [27] at 100°C, 300°C, and 420°C with Fe^{+} ions at ~$1x10^{-4}$ dpa/s in the same multi-step irradiation as Hernández-Mayoral, et al. [18] at 0.5, 2, 5 MeV. The purpose of this study was to observe the phase transformation and solute segregation in the Fe-Cr alloys under self-ion irradiation. In this study, no α' precipitates were observed under any conditions. But homogeneously distributed Cr, P, Si, and Ni clusters were observed at 300°C and 420°C. These same alloys were neutron irradiated by Kuksenko, et al. [12] where α' precipitates were observed. So, the lack of α' precipitates under heavy ion irradiation may be a combined result of the increased damage rate resulting in increased ballistic dissolution.

Hardie, et al. [28] studied pure iron and model Fe-Cr alloys (5-14% Cr) irradiated with 2 MeV Fe^{2+} to 0.6 dpa at either $6x10^{-4}$ dpa/s or $3x10^{-5}$ dpa/s at 300°C, 400°C, and 500°C. This study was investigating the effects of temperature and damage rate on mechanical properties of pure Fe and Fe-Cr alloys. The alloys showed a larger change in the hardness at the lower temperatures and lower damage rate. APT was also used and identified Cr-clustering, where in low chromium alloys the chromium segregated to dislocations, and in high chromium alloys the Cr-clusters where also rich in impurities (such as nitrogen). The chromium concentration of these clusters was low (<25%). It was concluded that the increase in hardness was a result of the combination of precipitation and other irradiation defects. At the lowest temperature of 300°C, there was no observed damage rate effect on hardening but there was an observed effect at 400°C in Fe-14Cr, which was attributed to the increased defect mobility with temperature.

Korchuganova, et al. [29] sought to show ballistic dissolution in Fe-22Cr model alloys under heavy ion irradiation by using pre-existing α' precipitates. The experiments were conducted at room temperature to <1 dpa. The results are mostly inconclusive, as the irradiation effects on the α' precipitates seemed to be dependent on the initial precipitate properties of the α' precipitates, where a very small growth was possibly observed in one set of pre-existing α' precipitates and a very small dissolution was possibly observed in the other set of pre-existing α' precipitates. The inconclusive results are likely due to the properties of the pre-existing α' precipitates, where the α' precipitates were at very similar conditions to those observed after irradiation and would be expected based on other heavy ion irradiations of Fe-Cr alloys.

Zhao, et al [26] investigated both the nucleation and stability of α' precipitates in Fe-18Cr at a range of temperatures and damage rates to either 0.37 or 3.7 dpa. The samples irradiated

included as received and aged samples in order to investigate the influence of the initial α' precipitate microstructure. The as received samples were irradiated at 10^{-5}, 10^{-4}, and 10^{-3} dpa/s at combinations of 300°C, 350°C, and 450°C to 0.37 dpa. Samples irradiated at 10^{-4} dpa/s were irradiated additionally to 3.7 dpa. The APT results did show α' precipitate microstructure may be dependent on the damage rate, where comparing the results from the as received 18Cr irradiated at various damage rates at 450°C, the average α' precipitate radius, number density, and α' concentration decreased with increasing damage rate and matrix concentration increased with increasing damage rate. This dependence on damage rate suggests that the ballistic dissolution is increasing with damage rate, leading to a higher solute concentration in the matrix, lower solute in the α' precipitate and smaller, dissolving α' radius. But, when comparing at similar irradiation conditions at lower experiment temperatures of 300°C and 350°C, the dependence of the α' precipitate microstructure on damage rate is no longer prominent with no strong conclusions about damage rate effects possible. Aged samples were also irradiated at 300°C, 350°C, and 450°C at 10^{-3} dpa/s to a dose of 0.37 dpa. The α' was completely dissolved at 300°C and was reduced in size and chromium concentration at 350 and 450°C. The α' microstructure (radius, number density, precipitate concentration, and matrix concentration) from the irradiated aged sample matched the corresponding irradiated as received sample at the same dose and damage rate at 350°C at 0.37 dpa. Yet the sample at 450°C did not match the corresponding as received irradiated sample at 450°C to 0.37 dpa. This indicates that the temperature plays a role in dictating the dose at which steady state is achieved. These experiments also revealed the initial microstructure played little influence on the steady state α' precipitate microstructure.

The heavy ion irradiations of Fe-Cr alloys have shown that the α' precipitates are sensitive to other factors involved in heavy ion irradiation: damage rate and injected interstitials. Tissot, et al. [25] demonstrated that the injected interstitials potentially have an effect on the α' precipitate stability leading to smaller size, lower density, and lower solute concentration. However, this effect was not observed from Reese, et al. [8]. Reese, et al. showed that with increasing damage rate, there was a corresponding decrease in a' precipitate radius, increase in number density, and decrease in solute concentration. Under heavy ion irradiation, the α' precipitates reached a steady-state non-equilibrium with low chromium concentration. And compared to neutron irradiation, the Fe-Cr decomposition was lower, reflecting the effects of ballistic dissolution at increasing damage rates.

2.2.5 Damage rate effects

Heavy ions have a similar cascade size and weight spectra to neutron irradiation with the added benefit of the higher damage rates achievable. However, as the damage rate increases, the α' phase stability is decreased as a result. This is observed in the change of the microstructural features including the radius, number density, volume fraction, solute concentration, and matrix concentration. The increasing damage rates leads to less time for diffusional recovery, eventually leading to a steady state between the mixing and unmixing processes at lower than thermodynamic equilibrium clusters chromium concentrations. As damage rate increases higher, there no steady state can become established and the chromium clusters are completely unstable, or at least become undetectable [8,24,25].

Recent work by Zhao, et al. [26] elucidated the possibility that damage rate may play a role on the precipitate microstructure through heavy ion irradiation of Fe-18Cr over a range of temperatures and damage rates. At the highest temperature of 450°C, the increasing damage rate led to a decrease in number density, precipitate size, chromium concentration, and an increase in matrix concentration, suggesting an increase in the role of ballistic dissolution over radiation enhanced diffusion. But experiments at lower temperatures of 350°C and 300°C did not necessarily observe these trends nor were a range of damage rates tested at lower temperatures.

A simulation study by Ke, et al. [24] demonstrated the damage rate effects under neutron/heavy ion irradiation and electron irradiation in Fe-15Cr at 300°C and 400°C up to 10 dpa As previously described in Section 2.2.3, α' was observed to precipitate under electron irradiation at damage rates ranging from 10^{-8} dpa/s to 10^{-3} dpa/s, although the slightly reduced chromium concentration at higher damage rates. Under heavy ion or neutron irradiation, the α' precipitation was significantly altered, even a strong mixing effect and reduction in chromium concentration at damage rates relevant to neutron irradiation. At 300°C, the α' precipitates were found to not form under damage rates $\geq 10^{-4}$ dpa/s. Additional simulations were conducted at 400°C at 10^{-5} dpa/s and 10^{-4} dpa/s demonstrating that the critical damage rate (above which α' is not stable) is only slightly above 10^{-4} dpa/s based on the concurrent re-precipitation and dissolution. The increased temperature from 300°C to 400°C increased the critical damage rate.

2.2.6 Cascade size effects

The cascade size is determined based on the PKA energy, and consequently heavy ion and neutron irradiation produce large damage cascades, proton irradiation produces smaller cascades, and electron irradiation produces Frenkel defects. A comparison the damage cascades at the same energy is shown in Figure 2.2. The figure shows that for electrons, as they are typically conducted at ~1 MeV, no large cascades can be produced, and only a Frenkel defect is formed. Under proton irradiation, the damage cascades are small and widely spaced with many isolated Frenkel pairs due to the Coulomb interaction. And neutron and heavy ion irradiation produce dense cascades.

A few recent experimental and simulation studies have investigated the effects of cascade size on the stability of α' precipitates under irradiation. One of the first studies, by Tissot, et al., conducted electron irradiations at similar conditions to that of heavy ion irradiations with Fe-15Cr model alloys. As previously discussed in Section 2.2.3, the results showed a strong dependence on cascade size. Harrison, et al. [30] investigated the effects of cascade size and damage rate on α' precipitation in Fe-14Cr using 100 keV He, 350 keV Ne, and 1 MeV Kr at 300°C to 2.5 dpa. This work showed that increasing ion mass and PKA energy resulted in decreased precipitate number density most likely due to the increasing ballistic mixing from the high energy cascades leading to spatial and temporal cascade overlap. Haley, et al. [22] also investigated the cascade size effect on α' precipitate stability in Fe-9Cr comparing between neutron, proton, and heavy ion irradiation at ~300°C. In this study, the Fe-9Cr was irradiated with neutron irradiation at ~$9x10^{-8}$ dpa/s to 2 dpa; the ion irradiations were conducted at similar damage rates of ~$1x10^{-5}$ dpa/s to ~2 dpa at the peak with 1.2 MeV protons and 2 MeV Fe. α' precipitates were observed after neutron and proton irradiation, but not after heavy ion irradiation. And again, this result was concluded to be because of the ballistic mixing, where the large cascades under heavy ion irradiation did not allow for a stable α' precipitate, for the much smaller, sparse, proton cascades allowed the α' to grow and enrich in chromium.

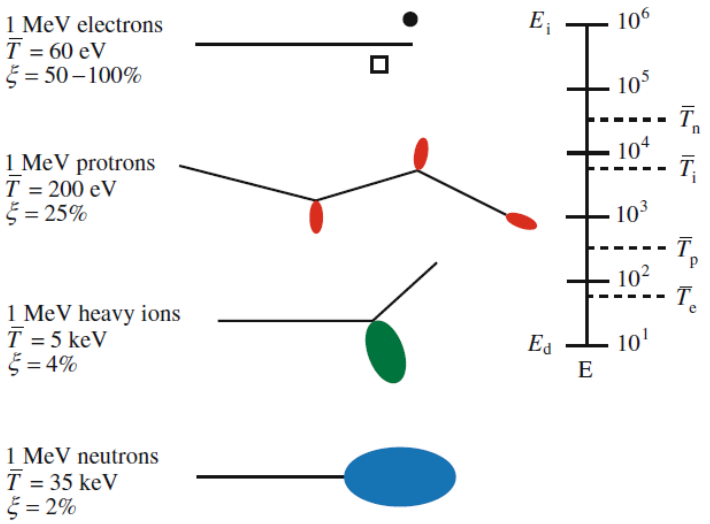

Figure 2.2. Comparison of cascade size, average recoil energy ($\bar{T}$), and displacement efficiency (ξ) for 1 MeV particles of different types incident on nickel.

2.3 Factors effecting α' precipitation under irradiation

Ballistic dissolution of precipitates under irradiation can be sensitive to many factors leading to the lack of formation or decreased stability of the α' precipitates. These factors include alloy composition, temperature, dose, damage rate, and cascade size. Some of these factors have been studied in the Fe-Cr alloys, while other have not been studied very extensively at all.

The composition of the alloy, both solute concentration and impurity concentration, determines the stability of the α' precipitates. The solute concentration, and temperature, determine whether the α' phase will form based on the phase diagram (shown in Figure 2.1). Typical ranges for reported experiments on Fe-Cr alloys range from ~9-18% and temperatures up to ~300-500°C. The alloy composition also dictates the precipitate behavior, where higher chromium concentration will lead to higher thermodynamic driving force resulting in higher number density and smaller precipitate size. Additionally, the presence of impurities may lead to the instability of α', particularly under heavy ion irradiation. A series of irradiation experiments by Pareige, et al. [27] demonstrated the effect of P, Si, and Ni impurities on the formation of α' under heavy ion irradiation at 2.2×10^{-4} dpa/s to 0.5 dpa in Fe-9Cr and Fe-12Cr at temperatures ranging from 100-420°C. Two classes of clusters were observed: Cr-P-Si clusters and Ni-α' particles, but no α' particles. Whereas under neutron irradiation at 300°C, α' was observed. The differences suggest that the impurities play a role in the stability of the α' particles or that the damage rate is too high for α' to be stable.

Temperature, in combination with alloy composition, determines if the α' precipitates will be able to form, based on the phase diagram. The temperature also relates to the thermodynamic driving force for nucleating and growing the α' precipitates. At a lower temperature, the driving force is high, and the kinetics are slower, leading to a high density of smaller precipitates. But at higher temperatures, the driving force is lower, and kinetics are faster, leading to a low density of larger precipitates.

The temperature dependence of the ballistic dissolution can be observed through compilation of literature data, shown Figure 2.6. A large portion of literature studies were conducted at ~290-300°C, with remaining studies conducted at higher temperatures typically ~400-500°C. Also, at the lower temperatures, the ballistic dissolution plays a stronger role in the α' precipitate formation and evolution under both neutron and heavy ion irradiation. This is shown

in the data compilation in Figure 2.6 where at ~300°C, the α' precipitates have not fully reached the maximum solute concentration under both neutron irradiation (at ~80-90% of maximum solute concentration) nor heavy ion irradiation (at ~50-60%). At higher temperatures, the ballistic dissolution does not play as strong a role in the dissolution of the α' precipitates so they are typically larger, less dense, and a higher solute concentration. This is shown again in Figure 2.6, where at >400°C, the α' precipitates formed through neutron have or nearly have reached the maximum solute concentration (at >95%) and those α' precipitates formed through heavy ion irradiation have also increased the fraction of the maximum solute concentration rather significantly (to ~75%). The α' precipitates at higher temperatures are also increasing in the chromium concentration, though to a lesser degree than for neutron irradiation.

Dose is important to consider, as the effects of the irradiation and ballistic dissolution can be dependent on the dose. At higher damage rates, a higher dose may be required to reach the maximum α' precipitate size and solute concentration. This was demonstrated by Nelson, et al [31] in the NHM model, in Figure 2.3. In the figure, there are two sets of lines, representing the two different damage rates. In each set, there are another two lines, representing the precipitate sizes under irradiation where the large precipitates are shrinking, and the small precipitates are growing until the lines converge at the equilibrium precipitates size. The dose at which the equilibrium precipitate size is reached is dependent on the damage rate.

Experiments from Zhao, et al. [26] showed that α' precipitates were sensitive to the dose, with temperature playing a strong role determining the dose at which α' reaches steady state. Heavy ion irradiation of both as received and aged samples at two temperatures (350°C and 450°C) at 10^{-3} dpa/s to 0.37 dpa showed that the α' had reached steady state at 350°C but not at 450°C. This is due to a lessening of the role of ballistic dissolution at a higher temperature leading to a higher dose for the α' to reach the steady state.

Reese, et al. [8] also looked at the dose, though not specifically, but primarily the damage rate effects on α' precipitates in Fe-18Cr model alloys. In the published data from the study, APT images illustrate α' precipitate evolution with increasing dose over a range from 0.2-6 dpa.

Under electron irradiation, the α' precipitates showed a dependence on the dose as the precipitates grew and underwent coarsening at less than 1 dpa [23]. For heavy ion irradiations, there is not a lot of data collected to observe a dose dependence on the α' precipitates. But from the precipitate radius and number density data for heavy ion irradiations at 1 and 3 dpa in Figure

2.4, they are very similar at different doses. This may mean that the irradiation effects have already taken full effect by ~1 dpa in heavy ion irradiation at ~10^{-5} dpa/s.

The damage rate is known to affect the precipitate stability and properties in many alloy systems. Ballistic dissolution is known to play a large role in precipitate stability at higher damage rates and lower temperatures. The effects of the damage rate on α' precipitate stability has recently been investigated in neutron and heavy ion irradiated Fe-18Cr model alloys. Reese, et al. [8] showed that increasing from a damage rate ~10^{-6}-10^{-3} dpa/s, the degree of ballistic mixing is increased, as evidenced by the increase in number density and decrease in radius. The study does not provide numerical data, but it also appears from the APT images the solute concentration is also decreasing with increasing damage rate. Zhao, et al. [26] also showed that the role of ballistic dissolution increases with damage rate, from 10^{-5}-10^{-3} dpa/s. The ballistic dissolution was evidenced again by the decreasing chromium concentration and radius.

Figure 2.5 shows the effects of the cascade size on the maximum solute concentration observed in the α' precipitates. In the neutron and heavy ion data, where there are sizable cascades, the increasing damage rate lowers the maximum solute concentration observed in the α' precipitates. But in the electron irradiation at a similar damage rate to the heavy ion irradiations but with no cascade, the precipitates are able to reach the maximum solute concentration in the α' precipitates.

Soisson, et al. [9] and Morgan, et al. [32] also showed that the effects of damage rate through modeling. Soisson, et al. showed that heavy ion irradiations at higher damage rates showed less propensity for α' precipitation. It was concluded that this is likely due to the increased sink density reducing the point defect mobilities. Morgan, et al. [32] also showed that the higher damage rates lead to higher precipitate densities, lower precipitate radii, as well as lower chromium concentration. And it was concluded this is likely due to the ballistic dissolution. This study also showed that this effect was observed under neutron irradiation too, contradictory to the conclusion for Soisson, et al. [9].

A simulation work by Ke, et al. [24] investigated the damage rate effects on Fe-15Cr under heavy ion irradiation at 300°C up to 10 dpa at damage rates ranging from 10^{-8} dpa/s to 10^{-3} dpa/s. This work showed a clear ballistic mixing effect strongly dependent on the damage rate as the precipitate stability decreased with increasing damage rate. The model predicted lower solute concentration in the α', decreasing volume fraction, and decreasing radius present at damage rates

$\geq 10^{-4}$ dpa/s. Additional simulations conducted at 400°C at 10^{-5} dpa/s and 10^{-4} dpa/s indicated α' precipitates were stable under both conditions.

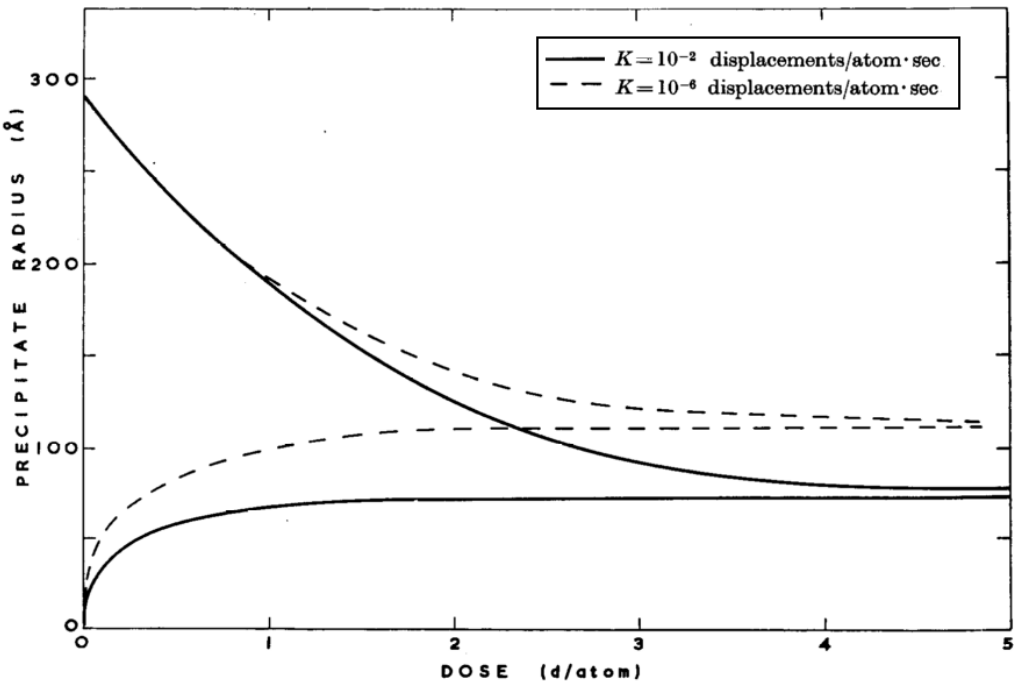

Figure 2.3 Dose dependence of the equilibrium precipitate size under irradiation, as predicted by NHM model. The solid lines ($K_0=10^{-2}$ dpa/s) converge to the equilibrium precipitate size at a higher dose than the dashed lines ($K_0=10^{-6}$ dpa/s).

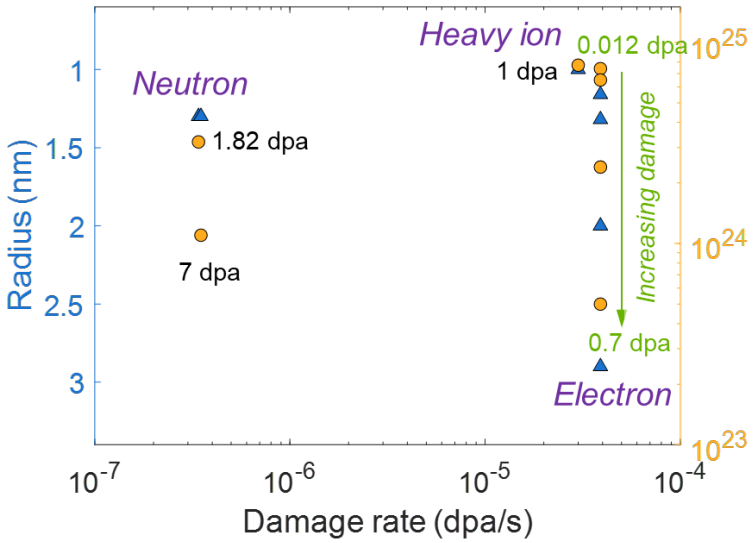

Number density
Radius

Neutron

Fe-15Cr, ATR, 290°C, 3.4×10^{-7} dpa/s, 1.82 dpa [13]

Fe-15Cr, ATR, 320°C, ~3.5×10^{-7} dpa/s, 7 dpa [20]

Heavy ion

Fe-15Cr, JANNuS-Saclay facility, 300°C, 3.5-6.1$\times 10^{-5}$ dpa/s, 0.5-1 dpa [25]

Electron

Fe-15Cr, HVEM-Saclay facility, 300°C, 3.5×10^{-5} dpa/s, 0.012-0.7 dpa [23]

Figure 2.4 Compilation of literature data for Fe-15Cr model alloys to demonstrate cascade size effects on α' precipitate density and radius. Under neutron and heavy ion irradiation, α' precipitates have higher precipitate densities and smaller precipitate radii. Whereas under electron irradiation, α' undergoes coarsening and the average radii increases, and number density decreases with increasing dose.

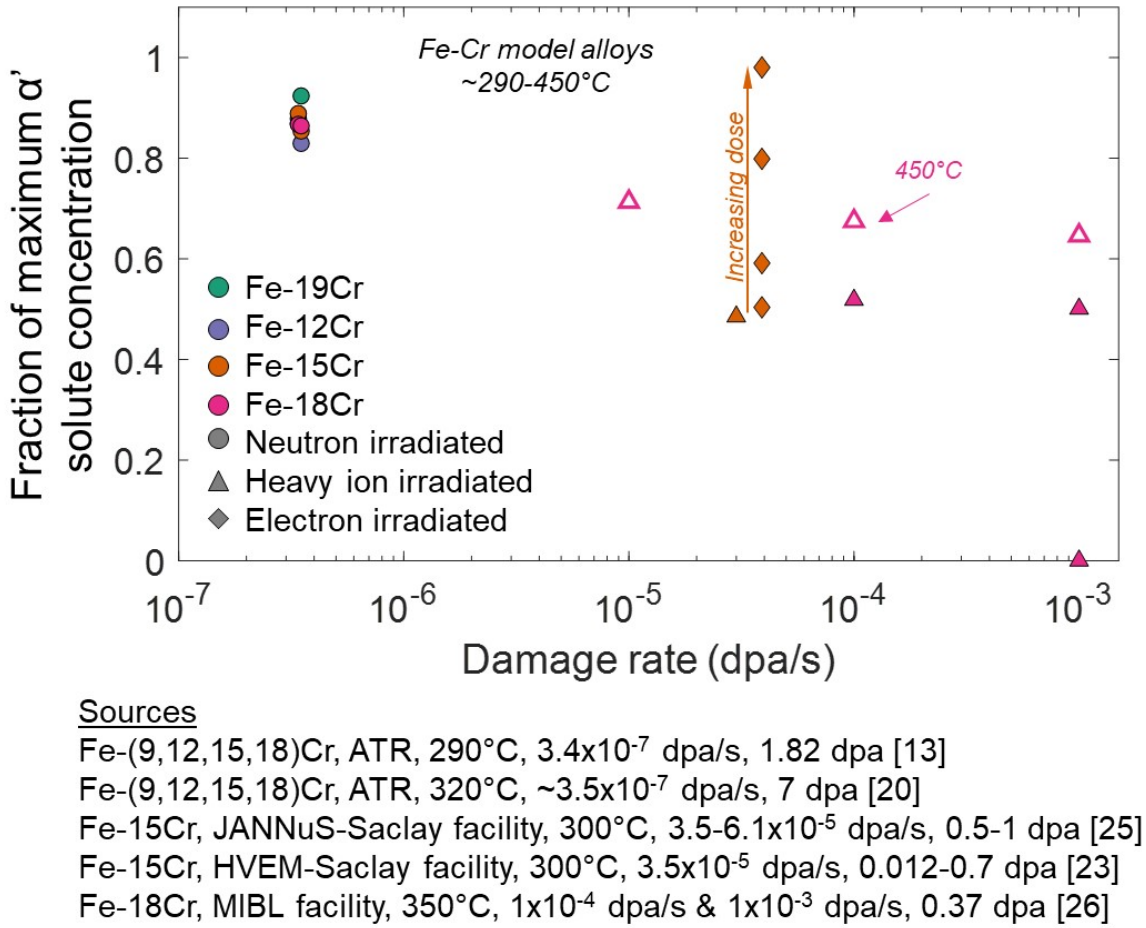

Sources

Fe-(9,12,15,18)Cr, ATR, 290°C, 3.4×10^{-7} dpa/s, 1.82 dpa [13]

Fe-(9,12,15,18)Cr, ATR, 320°C, ~3.5×10^{-7} dpa/s, 7 dpa [20]

Fe-15Cr, JANNuS-Saclay facility, 300°C, 3.5-6.1$\times 10^{-5}$ dpa/s, 0.5-1 dpa [25]

Fe-15Cr, HVEM-Saclay facility, 300°C, 3.5×10^{-5} dpa/s, 0.012-0.7 dpa [23]

Fe-18Cr, MIBL facility, 350°C, 1×10^{-4} dpa/s & 1×10^{-3} dpa/s, 0.37 dpa [26]

Figure 2.5 Comparison of literature data demonstrating the ballistic dissolution effects on α' precipitate concentration at temperatures at or around (with one data set at 450°C). The fraction of the nominal α' solute concentration is a ratio of the solute concentration observed experimentally to the nominal predicated α' solute concentration predicted by the phase diagram.

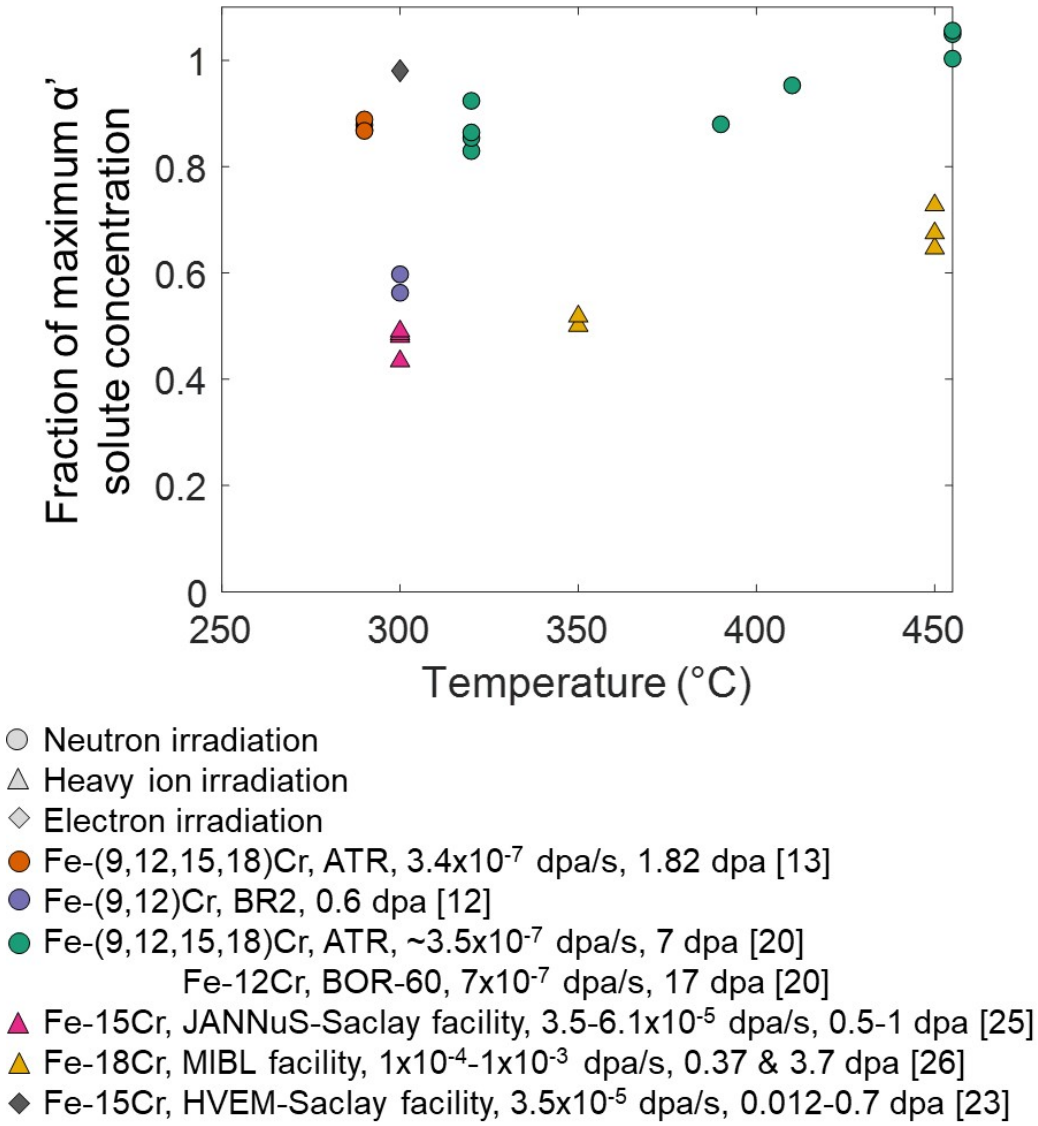

Figure 2.6 Compilation of literature data to show the effect of damage rate and temperature on the fraction of nominal α' solute concentration.

2.4 Models for precipitate stability

The stability of precipitates, particularly α', under irradiation is typically governed by competing effects of radiation enhanced diffusion and ballistic dissolution. One model that captures the balance between radiation enhanced diffusion and ballistic dissolution is the Nelson-Hudson-Mazey (NHM) model [31]. Descriptions of growth or dissolution in the NHM model have been modified multiple times [26,31,33–36]. Another method for describing the balance between these mechanisms involves determination of the critical temperature, or the temperature at which rates of radiation enhanced diffusion and ballistic dissolution are equal to one another. Each of these methods will be discussed further in the following sub-sections.

2.4.1 Nelson-Hudson-Mazey (NHM) model

The NHM model is a first-order differential equation describing the change in precipitate radius time. The NHM model treats precipitate stability as the balance between precipitate growth, through diffusion, and precipitate dissolution, through ballistic dissolution. Under irradiation, precipitates grow or dissolve, finding a balance between the enhanced growth and the ballistic dissolution at a steady state size dictated by the damage rate (as well as other irradiation conditions, such as temperature, etc.). The precipitate growth term is based on the theory of supersaturated solution [37,38]:

$$\frac{dV}{dt} = \frac{3D_{irr}Cr}{C_p} \tag{2.1}$$

where D_{irr} is the radiation enhanced diffusion coefficient, C is the concentration of the dynamic solute in solution (or the difference between the matrix concentration and the solubility limit), r is the precipitate radius, and C_p is the precipitate concentration. The total concentration of solute does not change, so a conservation condition for the total solute concentration can be applied such that:

$$C_b = \frac{4}{3}C_p\pi r^3 n + C \tag{2.2}$$

where C_b is the bulk concentration of the solute. The growth rate can be described radially, as:

(2.3)

$$\frac{dr}{dt} = \frac{3D_{irr}C}{4\pi C_p r} - D_{irr}r^2 n$$

Several efforts have been made recently to modify both the growth term and the dissolution term in the NHM model. One such work from Zhao, et al. [26] modified the growth term. The first change was a correction of the constant from 3 to 4π due to a mathematical error; the second was a clarification of the solute supersaturation term, C, which not clearly defined in Nelson, et al. [31]. The supersaturation term (or the dynamic solute term, as referred to by Nelson, et al.) was replaced by the definition, which is the difference in the matrix concentration (C_m) and the solubility limit (C_e). The modified NHM growth term appears as:

$$\frac{dr}{dt} = \frac{D_{irr}(C_m - C_e)}{rC_p} \tag{2.4}$$

where $C_b = \frac{4}{3}n\pi r^3 C_p + C_m\left(1 - \frac{4}{3}\pi r^3 n\right)$, which was the last modification made by Zhao, et al. [26] to better account for larger volume fractions of precipitates.

Chen, et al. [35] further modified the growth term of the NHM model to better describe the stability of nanoprecipitates. The authors took into consideration the Gibbs Thomson effect to account for the variability in the high curvature in nanoprecipitates. The new growth term was given as:

$$\frac{dr}{dt} = \frac{D_{irr}}{r} \cdot \frac{C_m - C_r}{C_p - C_r} \tag{2.5}$$

where C_m is the solute concentration in the matrix, C_p is the solute concentration in the dispersoid, and C_r is:

$$C_r = C_\infty \exp\left(\frac{2\gamma_i V_{at}}{kTr}\right) \tag{2.6}$$

C_∞ is the solubility limit at a flat interface of the two phases, γ_i is the interfacial energy at the precipitate-matrix interface, V_{at} is the average atomic volume of the precipitate, T is the temperature, and k is the Boltzmann constant.

The dissolution term describes the scattering of solute atoms from a precipitate by irradiation. The dissolution term is given by:

$$\frac{dV}{dt} = -4\pi r^2 \frac{\varphi K_0}{N_{at}} \tag{2.7}$$

where φ is the ballistic dissolution parameter (BDP) in units of atoms per m^2 per dpa, K_0 is the defect production rate, and N_{at} is the atomic density. The dissolution term can be described radially as:

$$\frac{dr}{dt} = -\frac{\varphi K_0}{N_{at}} \tag{2.8}$$

The ballistic dissolution parameter accounts for the flux of atoms ejected from the precipitate surface per dpa.

The combined NHM model, using the modified growth term from Zhao, et al. [26], is then described as:

$$\frac{dr}{dt} = \frac{D_{irr}(C_m - C_e)}{rC_p} - \frac{\varphi K_0}{N_{at}} \tag{2.9}$$

or described as:

$$\frac{dr}{dt} = \frac{D}{r} \cdot \frac{C_m - C_r}{C_p - C_r} - \frac{\varphi K_0}{N_{at}} \tag{2.10}$$

in which the modified growth term comes from Chen, et al. [35].

Swenson [34,36] and Adisa [33] modified the dissolution term to capture disorder dissolution by incorporating the work of Nelson, et al. [31]. This mechanism for dissolution is defined as the mixing of atoms within the precipitate. Both works described the disorder dissolution parameter as $\psi = l \cdot f$, where l is the effective cascade diameter and f is the disordering efficiency. The authors used the dissolution parameter to fit data to the NHM model as its values are the least established in literature. Both works accounted for disorder dissolution, which is a relevant mechanism for nanoprecipitates. However, in the case of α', atom probe cannot identify disorder within the precipitate. Additionally, both works used the set value for BDP defined by Nelson, et al [31] of 10^{18} atoms/m^2·dpa and used the recoil dissolution as a fitting parameter for the model. The recoil dissolution term was dependent on the cascade size and a fitting term, defined as relative efficiency.

Experimental BDP characterization in the literature has been limited. Values for the dissolution parameter are typically imprecise estimates or determined through fitting the NHM model to experimental data. Nelson, et al. [31,39] estimated the BDP to be ~10^{18} atoms/m^2·dpa based on the energy spectra within collision cascades and the number of atoms sputtered from solid surfaces during irradiation. Marwick [40] calculated the BDP by based on the principals of Fick's first law:

$$\frac{\varphi}{K} = D_{displ}\frac{C_p - C_0}{\delta}N_{at} \tag{2.11}$$

Here, $D_{displ} = \frac{1}{6}\Gamma R^2$, R is the minimum stable separation of an interstitial-vacancy pair from a displacement event, Γ is the frequency of such events, C_p is the precipitate concentration, C_0 is the solute concentration in the atom layers adjacent to the precipitate, and δ is the thickness of the interface. Marwick estimated the BDP value based on heavy ion irradiation precipitate dissolution studies at ~5x10^{19} atoms/m^2·dpa [41,42]. Rusbridge [42] estimated the BDP from heavy ion irradiation (100-200 keV Al^+) of Ge precipitates in Al-Ge binary alloy to be ~1.7x10^{19} atoms/m^2·dpa. Chang and Baron [43] reported a BDP of ~3x10^{19} atoms/m^2·dpa for heavy ion and neutron irradiation of γ' in PE16. The work from Zhao, et al. showed efforts to estimate the BDP through two different calculations. The first calculation estimated the BDP based on the number of recoils per dpa using SRIM and the replacements per displacement (rpa) ratio for 8 MeV Fe. This method estimated the BDP to be ~1.17x10^{21} atoms/m^2·dpa. The second estimate of the BDP considered ballistic mixing described by Marwick but defined the value for R as the ratio of atoms ejected beyond a critical distance to residual displacements following a displacement event calculated using SRIM, and Γ as the average distance traveled by an ejected atom. Using values for the Ni in Ag-Cu system, the BDP estimated by Zhao, et al. using this method was ~1.4x10^{20} atoms/m^2·dpa. The values for both BDPs from Zhao, et al. were found to be too high and too low, respectively, as use of these values in the NHM model yielded underestimated or overestimated a' precipitate size compared to experimental results, and so an intermediate BDP value was fit to the NHM model and experimental data in that work.

2.4.2 Wilkes model

The Wilkes model adapted the NHM model to create a cellular model and presented the solute concentration profile in the matrix. This model assumes an even distribution of equally sized precipitates. Under irradiation, the precipitate solute atoms are scattered uniformly into the matrix. This model assumes the precipitate interface is stationary under irradiation. The matrix solute concentration at steady state is described as:

$$C(r) = C_e + \frac{\varphi K_0 r_0^2}{2D_{irr}N_{at}(R^3 - r_0^3)}\left[\frac{2R^3(r - r_0)}{r\,r_0} - r^2 + r_0^2\right] \tag{2.12}$$

where R is the interparticle spacing and r_0 is the initial precipitate radius. The BDP can be calculated from the Wilkes model by calculating the average matrix concentration from the concentration profile and correlating this the APT value, as:

$$C_m^{avg} = \frac{1}{\frac{4}{3}\pi(R^3 - r_0^3)} \int_0^{2\pi} \int_0^{\pi} \int_{r_0}^{R} C(r)\, r^2 \sin(z)\, dr\, dz\, d\theta \tag{2.13}$$

This model assumes that the precipitate is at steady state and no longer undergoing any microstructural changes. The BDP may not be calculated correctly if applying this model to a system that has not achieved steady state.

2.4.3 Frost and Russell model

Frost and Russell proposed a more complex model, building on the Wilkes [44] and NHM model [31]. The Frost and Russell model [45,46] assumes an even distribution of equally sized precipitates to estimate the solute in the matrix at steady state. This model assumes that atoms are recoiled a constant distance into the matrix, while solute atoms that diffuse back to the precipitate are assumed to recombine at the interface. The precipitate interface is treated as stationary and assumes the matrix solute concentration and growth rate are small. Similar to the Wilkes model [44], the Frost and Russell model [45,46] provides the matrix concentration profile at steady state. The Frost and Russell model utilizes a source generation term, or the rate at which solute atoms enter the matrix. Additionally, this model can predict a regime at which inverse coarsening and steady state will occur.

2.4.4 Critical temperature

The dominant atom transport mechanism is dependent on the temperature range of irradiation. Ballistic mixing, or displacement mixing, is the dominant atom-mass transport mechanism at lower temperatures, at which vacancies are immobile. This process is considered athermal. The effective displacement-induced diffusion coefficient is approximated as:

$$D_{bal} \cong \frac{1}{6}\lambda^2 \eta K \tag{2.14}$$

where λ is jump length (or lattice parameter), K is the defect production rate, and η is the number of replacements per displacement (or rpa) [9]. At higher temperatures, radiation enhanced diffusion becomes dominant, with vacancy and interstitial concentrations exceeding the thermodynamic equilibrium concentrations by multiple orders of magnitude. At much higher temperatures, thermal diffusion becomes dominant. The contributions of ballistic mixing, radiation enhanced diffusion, and thermodynamic equilibrium to the diffusion process are shown in Figure 2.7, adapted from Lam [47]. In the lower temperature range for radiation enhanced diffusion, the diffusion exhibits an Arrhenius-type temperature dependence. This total diffusion coefficient can be written as:

$$D = D_{bal} + D_{irr} \exp\left({}^{-Q}/_{kT}\right) \tag{2.15}$$

where $Q = E_m^v/2$ and k is the Boltzmann constant. The temperature at which the athermal ballistic mixing is equal to the Arrhenius-type RED region is defined as the critical temperature:

$$T_C = \frac{Q}{k \ln\left({}^{D_{irr}}/_{D_{bal}}\right)} \tag{2.16}$$

At $T > T_C$, radiation enhanced diffusion is the dominant atom transport mechanism, and if $T < T_C$, ballistic mixing is the dominant atom transport mechanism.

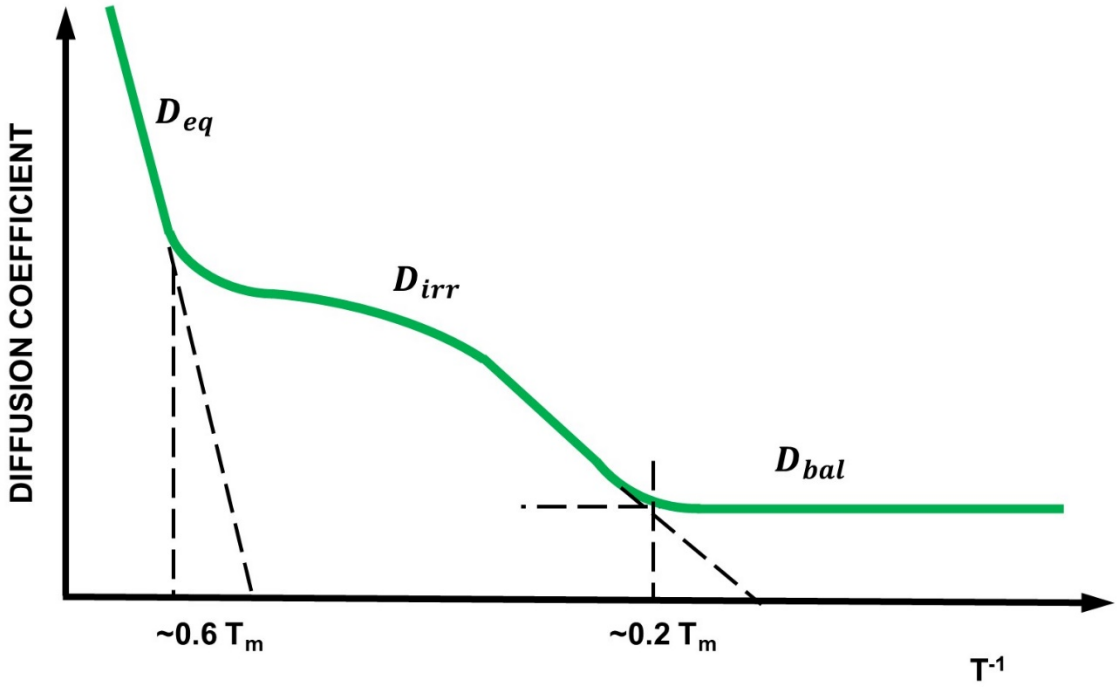

Figure 2.7 Schematic plot relating the temperature dependence of ballistic mixing (D_{bal}), radiation enhanced mixing (D_{irr}), and thermal diffusion (D_{eq}). Figure adapted from Lam [47]**.**

2.5 Summary

Past research has demonstrated the many factors effecting the α' precipitate nucleation and stability under irradiation, such as temperature, chromium concentration, damage rate, and cascade size. Under heavy ion and neutron irradiation, with a large cascade present, the stability of α' decreases with increasing damage rate due to ballistic dissolution. There is less time for recovery, leading to a steady state at a lower than thermodynamic equilibrium chromium concentration and limited sizes. Under electron irradiation, with no cascade, there is no ballistic dissolution affecting the α' precipitate stability. The majority of studies focus on the effect any factor has on precipitate nucleation under irradiation. Few studies have studied the effects of precipitate stability by utilizing an existing α' population subjected to irradiation. The combination of the works presented in this chapter have emphasized that ballistic dissolution results in the α' precipitate instabilities and that ballistic dissolution is dependent on both damage rate and cascade size.

2.6 References

[1] M.H. Mathon, Y. De Carlan, G. Geoffroy, X. Averty, A. Alamo, C.H. De Novion, A SANS investigation of the irradiation-enhanced a-a' phases separation in 7-12 Cr martensitic steels, J. Nucl. Mater. 312 (2003) 236–248. doi:10.1016/S0022-3115(02)01630-6.

[2] M.H. Mathon, Y. De Carlan, G. Geoffroy, X. Averty, C.H. De Novion, A. Alamo, Microstructural evolution of reduced activation and conventional martensitic steels after thermal aging and neutron irradiation, 2000. doi:10.1520/stp10564s.

[3] R. Braun, M. Feller-Kniepmeier, Diffusion of chromium in α-iron, Phys. Status Solidi. 90 (1985) 553–561. doi:10.1002/pssa.2210900219.

[4] A.W. Bowen, G.M. Leak, Self-diffusion in alpha and gamma iron, Metall. Trans. 1 (1970) 1695–1700. doi:10.1007/bf03398989.

[5] P.J. Alberry, C.W. Haworth, Interdiffusion of Cr, Mo, and W in Iron, Met. Sci. 8 (1974) 407–412. doi:10.1179/msc.1974.8.1.407.

[6] W.Y. Chen, Y. Miao, Y. Wu, C.A. Tomchik, K. Mo, J. Gan, M.A. Okuniewski, S.A. Maloy, J.F. Stubbins, Atom probe study of irradiation-enhanced α' precipitation in neutron-irradiated Fe-Cr model alloys, J. Nucl. Mater. 462 (2015) 242–249. doi:10.1016/j.jnucmat.2015.04.005.

[7] S. Novy, P. Pareige, C. Pareige, Atomic scale analysis and phase separation understanding in a thermally aged Fe-20 at.%Cr alloy, J. Nucl. Mater. 384 (2009) 96–102. doi:10.1016/j.jnucmat.2008.10.008.

[8] E.R. Reese, N. Almirall, T. Yamamoto, S. Tumey, G. Robert Odette, E.A. Marquis, Dose rate dependence of Cr precipitation in an ion-irradiated Fe18Cr alloy, Scr. Mater. 146 (2018) 213–217. doi:https://doi.org/10.1016/j.scriptamat.2017.11.040.

[9] F. Soisson, E. Meslin, O. Tissot, Atomistic modeling of a' precipitation in Fe-Cr alloys under charged particles and neutron irradiations: Effects of ballistic mixing and sink densities, J. Nucl. Mater. 508 (2018) 583–594.

[10] G. Bonny, D. Terentyev, L. Malerba, D. Van Neck, Early stages of a-a' phase separation in Fe-Cr alloys: An atomistic study, Phys. Rev. B - Condens. Matter Mater. Phys. 79 (2009) 1–9. doi:10.1103/PhysRevB.79.104207.

[11] G. Bonny, D. Terentyev, L. Malerba, New contribution to the thermodynamics of fe-cr alloys as base for ferritic steels, J. Phase Equilibria Diffus. 31 (2010) 439–444. doi:10.1007/s11669-010-9782-9.

[12] V. Kuksenko, C. Pareige, P. Pareige, Cr precipitation in neutron irradiated industrial purity Fe-Cr model alloys, J. Nucl. Mater. 432 (2013) 160–165. doi:10.1016/j.jnucmat.2012.07.021.

[13] M. Bachhav, G. Robert Odette, E.A. Marquis, α′ precipitation in neutron-irradiated Fe-Cr alloys, Scr. Mater. 74 (2014) 48–51. doi:10.1016/j.scriptamat.2013.10.001.

[14] D.S. Gelles, Void swelling in binary Fe-Cr alloys at 200 dpa, J. Nucl. Mater. 225 (1995) 163–174. doi:10.1016/0022-3115(95)00053-4.

[15] M. Bachhav, L. Yao, G. Robert Odette, E.A. Marquis, Microstructural changes in a neutron-irradiated Fe-6 at.%Cr alloy, J. Nucl. Mater. 453 (2014) 334–339. doi:10.1016/j.jnucmat.2014.06.050.

[16] M. Bachhav, G. Robert Odette, E.A. Marquis, Microstructural changes in a neutron-irradiated Fe-15 at.%Cr alloy, J. Nucl. Mater. 454 (2014) 381–386. doi:10.1016/j.jnucmat.2014.08.026.

[17] Y. V. Konobeev, A.M. Dvoriashin, S.I. Porollo, F.A. Garner, Swelling and microstructure of pure Fe and Fe-Cr alloys after neutron irradiation to ~26 dpa at 400°C, J. Nucl. Mater. 355 (2006) 124–130. doi:10.1016/j.jnucmat.2006.04.011.

[18] M. Hernández-Mayoral, C. Heintze, E. Oñorbe, Transmission electron microscopy investigation of the microstructure of Fe–Cr alloys induced by neutron and ion irradiation at 300 °C, J. Nucl. Mater. 474 (2016) 88–98. doi:10.1016/j.jnucmat.2016.03.002.

[19] F. Bergner, A. Ulbricht, C. Heintze, Estimation of the solubility limit of Cr in Fe at 300°C from small-angle neutron scattering in neutron-irradiated Fe-Cr alloys, Scr. Mater. 61 (2009) 1060–1063. doi:10.1016/j.scriptamat.2009.08.028.

[20] E.R. Reese, M. Bachhav, P. Wells, T. Yamamoto, G. Robert Odette, E.A. Marquis, On α′ precipitate composition in thermally annealed and neutron-irradiated Fe- 9-18Cr alloys, J. Nucl. Mater. 500 (2018) 192–198. doi:10.1016/j.jnucmat.2017.12.036.

[21] Z. Jiao, V. Shankar, G.S. Was, Phase stability in proton and heavy ion irradiated ferritic-martensitic alloys, J. Nucl. Mater. 419 (2011) 52–62. doi:10.1016/j.jnucmat.2011.08.020.

[22] J.C. Haley, S.D.M. Shubeita, P. Wady, A.J. London, G.R. Odette, S. Lozano-perez, S.G.

Roberts, Microstructural examination of neutron , proton and self-ion irradiation damage in a model Fe9Cr alloy, J. Nucl. Mater. 533 (2020) 152130. doi:10.1016/j.jnucmat.2020.152130.

[23] O. Tissot, C. Pareige, E. Meslin, B. Decamps, J. Henry, Kinetics of α′ precipitation in an electron-irradiated Fe15Cr alloy, Scr. Mater. 122 (2016) 31–35. doi:10.1016/j.scriptamat.2016.05.021.

[24] J.H. Ke, E.R. Reese, E.A. Marquis, G.R. Odette, D. Morgan, Flux effects in precipitation under irradiation – Simulation of Fe-Cr alloys, Acta Mater. 164 (2019) 586–601. doi:10.1016/j.actamat.2018.10.063.

[25] O. Tissot, C. Pareige, E. Meslin, B. Décamps, J. Henry, Influence of injected interstitials on α′ precipitation in Fe–Cr alloys under self-ion irradiation, Mater. Res. Lett. 3831 (2016) 1–7. doi:10.1080/21663831.2016.1230896.

[26] Y. Zhao, A. Bhattacharya, C. Pareige, C. Massey, P. Zhu, J.D. Poplawsky, J. Henry, S.J. Zinkle, Effect of heavy ion irradiation dose rate and temperature on α precipitation in high purity Fe-18 % Cr alloy R, Acta Mater. 231 (2022) 117888. doi:10.1016/j.actamat.2022.117888.

[27] C. Pareige, V. Kuksenko, P. Pareige, Behaviour of P, Si, Ni impurities and Cr in self ion irradiated Fe-Cr alloys - Comparison to neutron irradiation, J. Nucl. Mater. 456 (2015) 471–476. doi:10.1016/j.jnucmat.2014.10.024.

[28] C.D. Hardie, C.A. Williams, S. Xu, S.G. Roberts, Effects of irradiation temperature and dose rate on the mechanical properties of self-ion implanted Fe and Fe-Cr alloys, J. Nucl. Mater. 439 (2013) 33–40. doi:10.1016/j.jnucmat.2013.03.052.

[29] O.A. Korchuganova, M. Thuvander, A.A. Aleev, S. V. Rogozhkin, T. Boll, T. V. Kulevoy, Microstructural evolution of Fe-22%Cr model alloy under thermal ageing and ion irradiation conditions studied by atom probe tomography, J. Nucl. Mater. 477 (2016) 172–177. doi:10.1016/j.jnucmat.2016.05.007.

[30] R.W. Harrison, A.W. Carruthers, J.A. Hinks, M.G. Burke, S.E. Donnelly, Cascade size and dose rate effects on α′ precipitation in ion-irradiated Fe14Cr alloy, Scr. Mater. 172 (2019) 33–37. doi:10.1016/j.scriptamat.2019.06.034.

[31] R.S. Nelson, J.A. Hudson, D.J. Mazey, The stability of precipitates in an irradiation environment, J. Nucl. Mater. 44 (1972) 318–330. doi:10.1016/0022-3115(72)90043-8.

[32] G.S. Was, “Fe-Cr Model Alloys” from Quarterly Technical Progress Report: High Fidelity Ion Beam Simulation of High Dose Neutron Irradiation, 2017.

[33] S.B. Adisa, J. Hu, M.J. Swenson, APT characterization and modeling of irradiation-induced Nb-rich nanoclustering in Zr-1.0 % Nb alloys, Materialia. 16 (2021). doi:10.1016/j.mtla.2021.101040.

[34] M.J. Swenson, The mechanism of radiation-induced nanocluster evolution in oxide dispersion strengthened and ferritic-martensitic alloys, Boise State University, 2017.

[35] T. Chen, J.G. Gigax, L. Price, D. Chen, S. Ukai, E. Aydogan, S.A. Maloy, F.A. Garner, L. Shao, Temperature dependent dispersoid stability in ion-irradiated ferritic-martensitic dual-phase oxide-dispersion-strengthened alloy: Coherent interfaces vs. incoherent interfaces, Acta Mater. 116 (2016) 29–42. doi:10.1016/j.actamat.2016.05.042.

[36] M.J. Swenson, J.P. Wharry, Rate Theory Model of Irradiation-Induced Solute Clustering in b.c.c. Fe-Based Alloys, JOM. 72 (2020) 4017–4027. doi:10.1007/s11837-020-04365-4.

[37] C. Zener, Theory of growth of spherical precipitates from solid solution, J. Appl. Phys. 20 (1949) 950–953. doi:10.1063/1.1698258.

[38] F.S. Ham, Theory of diffusion-limited precipitation, J. Phys. Chem. Solids. 6 (1958) 335–351. doi:10.1016/0022-3697(58)90053-2.

[39] R.S. Nelson, The Physical State of Ion Implanted Solids, Proc. R. Soc. London A. 311 (1969) 53–61.

[40] A.D. Marwick, Solute segregation and precipitate stability in irradiated alloys, Nucl. Instruments Methods. 182–183 (1981) 827–843. doi:10.1016/0029-554X(81)90815-6.

[41] R.H. Jones, Thoria redistribution in a Ni/ThO2 alloy irradiated with 5 MeV Ni++, J. Nucl. Mater. 74 (1978) 163–166. doi:10.1016/0022-3115(78)90545-7.

[42] K.L. Rusbridge, Modification of near-surface precipitation in Al-Ge alloy by ion irradiation, J. Nucl. Instruments Methods Phys. Res. B. 182/183 (1981) 521–529.

[43] A.L. Chang, M. Baron, Particle redistribution and phase stability in ion and neutron irradiated gamma prime strengthened Fe-Cr-Ni based alloys, J. Nucl. Mater. 83 (1979) 214–222.

[44] P. Wilkes, Phase stability under irradiation - a review of theory and experiment, J. Nucl. Mater. 83 (1979) 166–175. doi:10.1016/0022-3115(79)90602-0.

[45] H.J. Frost, K.C. Russell, Recoil resolution and particle stabilty under irradiation, J. Nucl.

Mater. 104 (1981) 1427–1432.

[46] H.J. Frost, K.C. Russell, Particle stability with recoil resolution, Acta Metall. 30 (1982) 953–960. doi:10.1016/0001-6160(82)90202-4.

[47] N.Q. Lam, Ion bombardment effects on the near-surface composition during sputter profiling, Surf. Interface Anal. 12 (1988) 65–77. doi:10.1002/sia.740120202.

Chapter 3: Objective

The objective of this work is to understand the roles of damage rate and cascade size on the stability of α' precipitates in Fe-15Cr under irradiation. A hypothesis for the behavior of α' precipitates is as follows:

The degree of ballistic dissolution by a ballistic process is dependent on both the damage rate and cascade size.

When there is no cascade present in the irradiation (as in electron irradiation), existing α' precipitates are only affected by the radiation-enhanced diffusion and will continue to grow in size.

When the particle creates a damage cascade that can ballistically dissolve the precipitate (as in proton, heavy ion, and neutron irradiation), existing α' precipitates are additionally affected by ballistic dissolution, which recoil the precipitate atoms into the matrix. The recoiled atoms can then diffuse back to the precipitate, remain in the matrix, or reprecipitate. And the dominance between ballistic dissolution or radiation enhanced diffusion mechanisms then in turn predicts the stability of the α' precipitates.

To test the hypothesis, a combination of heavy ion, light ion and electron irradiation experiments with careful characterization of the α' microstructure was used.

To achieve the main objective, two sub-objectives were established. The first sub-objective was aimed at determining *the effects of damage rate and cascade size* on an established α' microstructure. To complete this sub-objective, a series of experiments were performed in the laboratory with varying conditions. This required the establishment of a controlled and consistent process of performing the experiments and analyzing and processing the experimental data. The development of the following methods was essential in acquiring the relevant experiment data:

- A method for consistent and controlled ion irradiation experiments
- A post-characterization process utilizing atom probe tomography (APT) to analyze the α' precipitate microstructure, including a method to develop APT needles from electron irradiated TEM liftouts

- A method for consistent quantification of the α' microstructure

Through these methods, the effects of damage rate and cascade size were determined. The evolving size and concentration distributions provided for each irradiation condition illustrated the effects of cascade size and/or damage rate for the same damage level.

The second sub-objective was aimed at understanding *why* a change in damage rate and cascade size resulted in the observed changes in the α' microstructure. A detailed analysis of the α' size and chromium concentration distributions accomplished this sub-objective. Existing precipitate stability models were applied to the data from this work to provide insight into the roles of damage rate and cascade size on the stability of α' precipitates.

Completion of these two sub-objectives demonstrated the role of damage rate and cascade size on α' precipitate microstructure in Fe-15Cr.

Chapter 4: Experimental Procedures

This chapter will describe the experimental procedures used in this work to prepare, irradiate, and characterize the Fe-15Cr samples.

4.1 Alloy and sample preparation

The Fe-15Cr model alloy used was manufactured from AMES laboratory specifically for this study. The ingots were formed by triple arc melting in an argon atmosphere. The ingots were heated in air in a preheated furnace at 871°C for 20 minutes then hot rolled 30% in a single pass. The rolled ingot was then austenitized in a furnace in air at 1049°C for 1 hour. The samples were then tempered placing them in a preheated furnace at 760°C for 1 hour, followed by air cooling. Metallography on the as-received Fe-15Cr alloy revealed grain size approximately 389±16 μm in size. Figure 4.1 shows the microstructure of the unirradiated, as-received Fe-15Cr alloy imaged using EBSD. Table 4.1 provides the alloy composition.

Prior to irradiation, the 15Cr ingot was cut into 1.5 x 1.5 x 20mm^3 bars using electrical discharge machining (EDM) and polished. The polishing process utilizes progressively finer grits of grinding papers proceeding to diamond polish and concluding with electropolishing. The samples were mounted on a flat aluminum disk with a thin layer of Crytalbond^{TM} adhesive resin. The sample bars for each irradiation were arranged in the center of the puck, side-by-side, in the desired order for the irradiation. Two additional bars were used on each side of the samples to be irradiated as guide bars. These guide bars provide extra stability with polishing to better ensure a flat surface and provide a weld spot for the thermocouple during the irradiation. A flat surface is important as it ensures good thermal contact between the samples and the stage during irradiation. After the resin is set, the samples were polishing by hand using SiC paper beginning with #400 grit and working up to #1200. The polishing direction was rotated 90° between each grit step so that it was easier to identify when the damage layer from the previous grit was fully removed. After polishing with the #1200 grit on the sample, the samples were flipped over, and the process

repeated on the opposite side. After reaching #1200 grit on the second sample surface, the samples were polished using successively finer diamond solutions starting with 3 μm suspension and ending with a 0.25 μm suspension to produce a mirror-like finish. The samples were then removed from the aluminum disk and residual Crytalbond^{TM} adhesive was removed by placing the samples in acetone. The samples were then cleaned in methanol and ethanol before allowing to air dry.

To remove any deformation layer induced by mechanical polishing, the samples were then electropolished. The electropolishing solution was 10% perchloric acid, 90% methanol solution, cooled to within -40°C to -50°C using a methanol bath with dry ice. A magnetic stirrer was used to create a vortex in the electropolishing solution. The face of the sample that was to be irradiated (the face polished with diamond polishing) was oriented towards the cathode, a platinum wire mesh, also submerged into the solution. And the sample was the anode. A diagram of the electropolishing set-up is shown in Figure 4.2. The samples were electropolished for approximately 15 seconds. This procedure removed an estimated 2 μm of material.

As Fe-Cr alloys are more prone to carbon uptake during irradiation, the samples with a pre-existing α' precipitate population subjected to heavy ion irradiation were additionally coated with alumina. The samples were coated after proton irradiation and before further heavy ion irradiation. The alumina coating was deposited using an atomic layer deposition machine (ALD) to a 100nm thickness. ALD is a process for depositing thin films that utilizes sequential reactions of gaseous precursors to deposit thin films one atomic layer at a time. For the deposition of alumina onto an FM steel, the steel samples were placed on a plate in the machine and the chamber sealed and purged with argon. The samples were then heated to 150°C. After the temperature stabilized, Trimethylaluminum (TMA, $Al(CH_3)_3$) was allowed into the chamber in a smaller burst. The TMA reacted with hydroxyl groups on the surface of the metal attaching the molecules to the substrate. The reaction for this process was:

$$Al(CH_3)_3 + OH \rightarrow AlO(CH_3)_2 + CH_4 \quad (4.1)$$

The TMA was then pumped out of the system before water was bubbled into the chamber. The water reacted with the methyl groups to produce more methane and new hydroxyl groups. The reaction for this step in the process was:

$$2\ H_2O + AlO(CH_3) \rightarrow AlO(CH_3)_2 + 2\ CH_4 \quad (4.2)$$

The water was then pumped out of the chamber and the process was repeated for ~980 cycles to achieve a film with a thickness of 100 nm.

Table 4.1. The composition of Fe-15Cr model alloy, in wt%.

Fe	Cr	C	O	N
Bal.	15.10	0.001	0.007	< 0.001

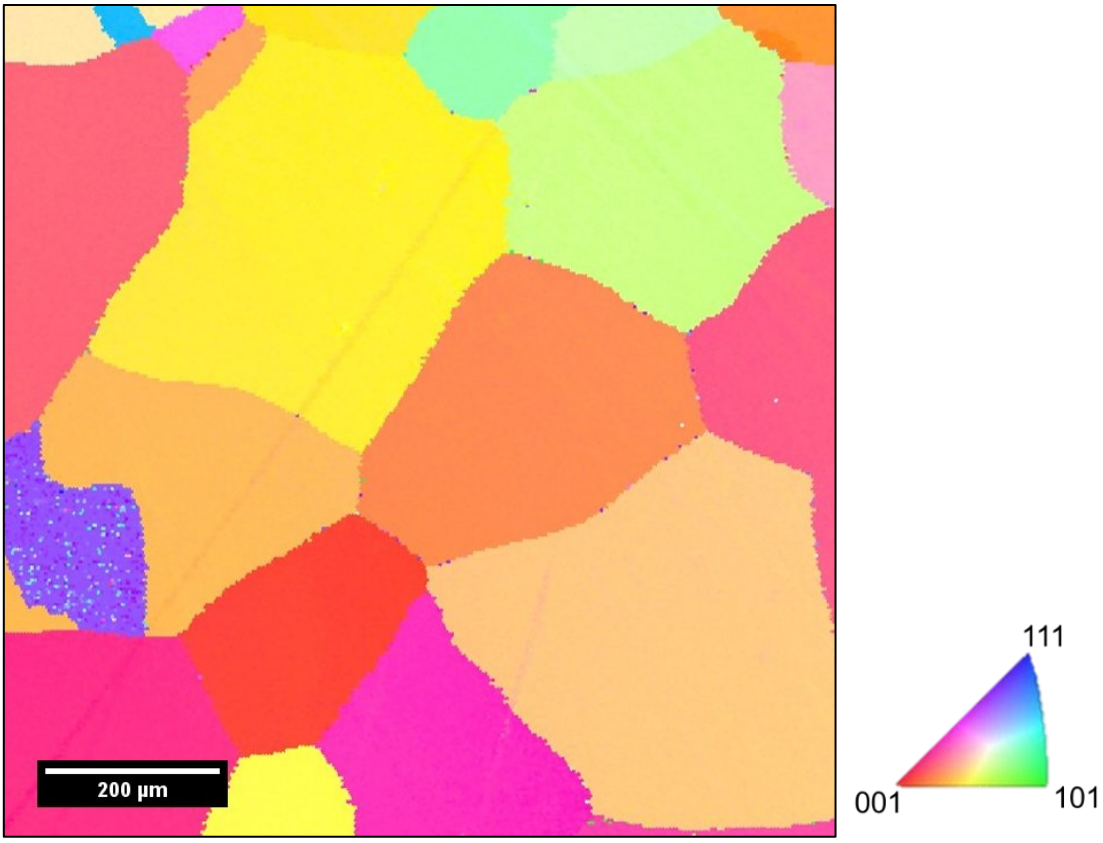

Figure 4.1. EBSD image of the unirradiated, as-received microstructure of Fe-15Cr.

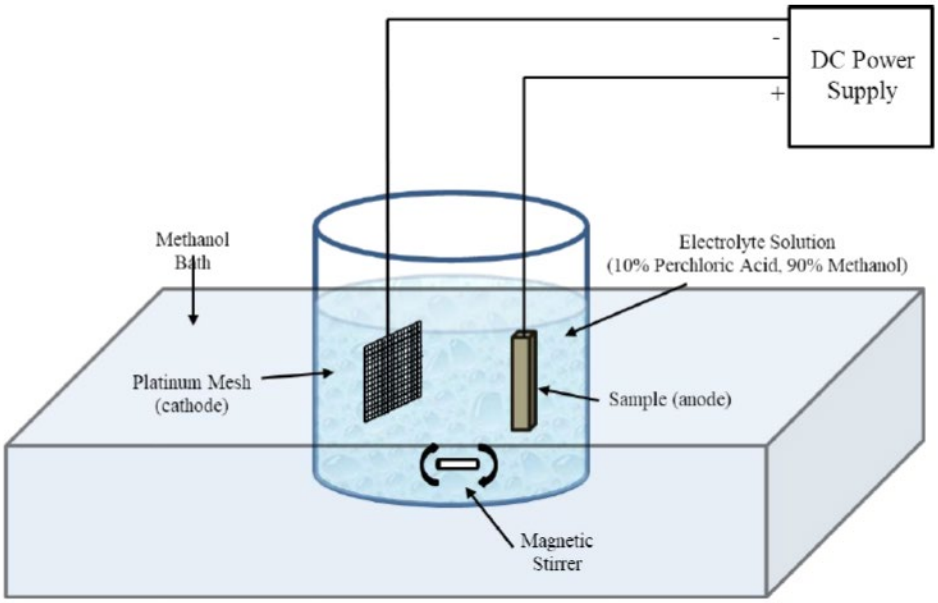

Figure 4.2 Schematic of the electropolishing set-up [1]**.**

4.1.1 Liftout preparation for electron irradiation

For electron irradiations of pre-existing α' precipitates, liftout samples were prepared from P19 and irradiated using a High Voltage Electron Microscope at Kyushu University with a 1.25 MeV electron beam at two damage rates ($1x10^{-4}$ and $1x10^{-3}$ dpa/s) to 1 dpa. Additionally, two more liftouts were irradiated at Hokkaido University with a 1.25 MeV electron beam at two damage rates ($4.6x10^{-5}$ dpa/s and $4.6x10^{-4}$ dpa/s) to 0.46 dpa. One liftout prepared from as-received Fe-15Cr was irradiated at Hokkaido University using 1.25 MeV electron beam at a damage rate of $4.6x10^{-4}$ dpa/s to 0.46 dpa. APT tips were constructed from the irradiated TEM liftouts.

The TEM liftouts were prepared from a P19 sample. The liftouts were prepared using the ThermoFisher Helios G4 PFIB UXe. The FIB utilizes an electron gun (normal to the horizontal surface) for imaging, and a gallium ion beam (at 52° from the electron beam) for imaging and milling. The current and energies of these beams could be varied. The liftouts were prepared using the process described as follows. The irradiated P19 bar was mounted irradiated side up using carbon tape on an SEM mount and placed in the FIB chamber, which was pumped down. The stage was tilted to 52° to be perpendicular to the ion beam. An appropriate area was selected in the irradiated area. A gas injector was inserted, and the ion beam was used to deposit a platinum on the target surface, in dimensions of approximately 20 x 5 μm^2 and height of 3 μm. Using a higher current, the gallium beam was used to create trenches about 25 μm deep on three sides of the platinum strip. The long sides of trenches along the platinum were cleaned using successively lower currents until the liftout reached the target thickness at 2-3 μm thick for ~20 μm deep. The stage was tilted to 0° so that the gallium beam could provide an undercut of the sample so that it was held only partially on one edge. An Omniprobe needle was inserted and slowly positioned such that it contacted the corner of the platinum deposition. A small amount of platinum was deposited (~0.5-1 μm) to weld the Omniprobe needle to the sample. The final connecting partial edge was cut away freeing the specimen from the bulk sample; the liftout Omniprobe needle was slowly lifted from the bulk sample. The SEM chamber was evacuated, and a mounted grid was placed inside; the chamber was evacuated and Omniprobe needle with liftout specimen attached re-inserted. The needle with the attached specimen was lowered to a position where it was just in contact with one of the Omniprobe grid posts. The ion beam was used to weld the specimen to the post with about 0.5-1 μm of platinum. The needle was cut free from the sample and retracted from

the chamber. Tungsten was used to further weld the specimen to the Omniprobe grid. The liftout stage was rotated 180° and tungsten was deposited on the other side to further secure the liftout to the Omniprobe grid.

For all liftouts irradiated at 10^{-3} dpa/s (for Kyushu University) or $5.4x10^{-4}$ dpa/s (for Hokkaido University) for both irradiations of the pre-existing α' precipitates and as received samples, a small slit was additionally milled in the liftouts using a low current (~0.3 nA) placed at the center of the liftout about 2-3 μm deep piercing through the liftout. This slit was used for placing the irradiation area nearby in order to better locate when making APT needles post-irradiation. Figure 4.3 shows an example SEM image of the electron irradiated liftouts. Figure 4.3(a) shows an example of the liftout with a slit in the top of the liftout, and Figure 4.3(b) does not have the slit.

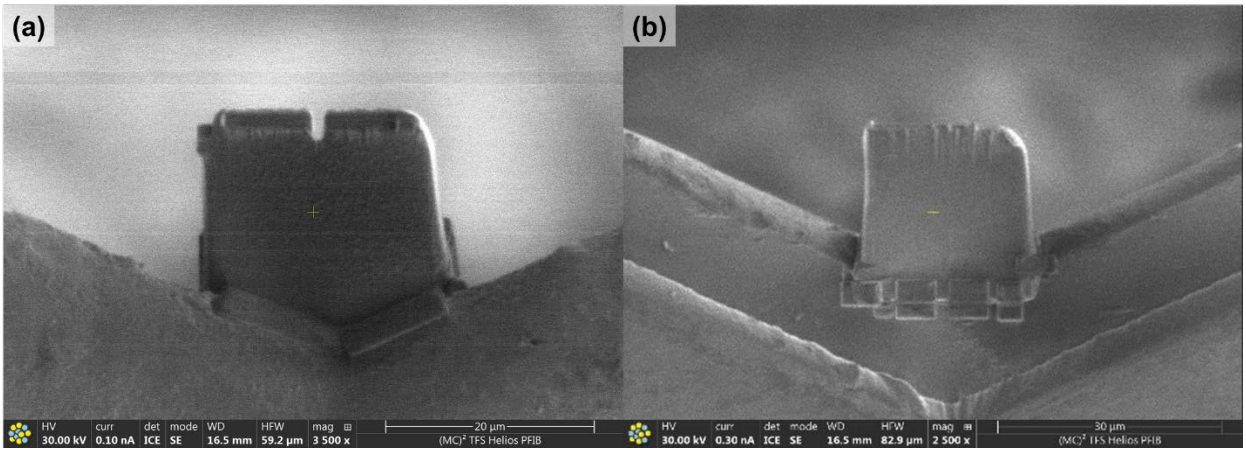

Figure 4.3 Prepared TEM liftouts for electron irradiation, where (a) has an additional slit for higher damage rate irradiations ($4.6x10^{-4}$ dpa/s, $1x10^{-3}$ dpa/s) to find the irradiated area much easier, and (b) is the lower damage rate ($1x10^{-4}$ dpa/s) liftout.

4.2 Irradiations

In order to achieve the state objective, a series of irradiations were completed. The irradiations were separated into three parts. As this thesis was aimed at studying the effect of damage rate and cascade size on the stability of existing α' precipitates, it was necessary to begin with a homogeneous α' precipitate distribution. After this distribution was created, the samples could then be further irradiated by varying the damage rate and/or cascade size. The three parts for this thesis are as follows:

Part 1: creation of initial α' precipitate microstructure in Fe-15Cr samples using proton irradiation. Two proton irradiations were conducted to induce the α' precipitate microstructure in the samples.

Part 2: variation of damage rate and cascade size in samples with initial α' precipitate microstructure. Heavy ion, proton, and electron irradiation were conducted at various damage rates and doses to observe the effects of the damage rate and cascade size on α' precipitate stability.

Part 3: variation of damage rate and cascade size in as received Fe-15Cr. Heavy ion, proton, and electron irradiation were conducted at various damage rates and doses with the primary motivation to verify the results from Part 2.

The irradiation conditions utilized for all conditions are summarized in Table 4.2-Table 4.4. All proton and heavy ion irradiations were conducted at Michigan Ion Beam Laboratory (MIBL), while all electron irradiations were conducted at Kyushu University or Hokkaido University. The following sections will discuss the unique considerations for each type of irradiation.

Table 4.2 Summary of irradiation conditions used for 2 MeV proton irradiations (creating initial α' precipitate microstructure).

Date of completion	Sample designation	Beam	Damage rate (dpa/s)	Damage (dpa)
8/24/2018	P18	2 MeV proton	$1x10^{-5}$	1
9/17/2019	P19	2 MeV proton	$1x10^{-5}$	1

Table 4.3. Summary of irradiations of pre-existing α' precipitate samples and characterization. Irradiations included heavy ion irradiation with 4.4 MeV $Fe^{2+/3+}$, proton irradiation with 1.5 MeV protons, and electron irradiation with 1.25 MeV electrons. All irradiations were at 400C.

Sample designation	Date of completion	Institution	Beam	Damage rate (dpa/s)	Damage (dpa)	Alumina coating (Y/N)	Characterization
P18+H/1e-5/1	2/22/2019	MIBL	4.4 MeV Fe^{+++}	$1x10^{-5}$	1	Y	APT
P18+H/1e-4/1 P18+H/1e-4/10	7/24/2019	MIBL	4.4 MeV Fe^{++}	$1x10^{-4}$	1 10	Y	APT
P18+H/3e-4/1dpa P18+H/3e-4/10dpa	9/11/2019	MIBL	4.4 MeV Fe^{++}	$3x10^{-4}$	1 10	Y	APT, TEM
P19+H/1e-3/1	10/18/2021	MIBL	4.4 MeV Fe^{++}	$1x10^{-3}$	1	Y	APT
P18+H/1e-3/10	10/15/2020	MIBL	4.4 MeV Fe^{++}	$1x10^{-3}$	10	N	APT
P19+P/1e-4/1 P19+P/1e-4/10	6/30/2020	MIBL	1.5 MeV H^{+}	$1x10^{-4}$	1 10	N	APT, TEM
P19+E/1e-4/1	6/2021	Kyushu University	1.25 MeV e^{-}	$1x10^{-4}$	1	N	APT
P19+E/1e-3/1	6/2021	Kyushu University	1.25 MeV e^{-}	$1x10^{-3}$	1	N	APT
P19+E/4.6e-4/0.46	6/2021	Hokkaido University	1.25 MeV e^{-}	$4.6x10^{-4}$	0.46	N	APT

Table 4.4. Summary of irradiation conditions and characterization for as received Fe-15Cr samples.

Sample designation	Date of completion	Institution	Beam	Damage rate (dpa/s)	Damage (dpa)	Alumina Coating (Y/N)	Characterization
AR+H/1.3e-5/3	9/18/2017	MIBL	4.4 MeV Fe^{+++}	$1.3x10^{-5}$	3	N	APT
AR+H/1e-4/1 AR+H/1e-4/10	4/6/2021	MIBL	4.4 MeV Fe^{++}	$1x10^{-4}$	1 10	N	APT
AR+H/1e-3/1	5/13/2019	MIBL	4.4 MeV Fe^{++}	$1x10^{-3}$	1	N	APT
AR+H/1e-3/10	6/18/2019	MIBL	4.4 MeV Fe^{++}	$1x10^{-3}$	10	N	APT
AR+P/1e-5/2	4/4/2019	MIBL	2 MeV H^{+}	$1x10^{-5}$	2	Y	APT
AR+E/4.6e-4/0.46	6/2021	Hokkaido University	1.25 MeV e^{-}	$4.6x10^{-4}$	0.46	N	APT

4.2.1 Damage calculation

Stopping and Range of Ions in Matter (SRIM) [2] was used to provide a depth-dependent estimation of the damage caused by an ion, provided its energy and the target material composition. SRIM was used to for all proton and heavy ion calculations. The SRIM damage calculations were conducted using "quick" Kinchin-Pease mode. The composition of the target material was detailed in Table 4.1. A displacement energy of 40 eV was used for both Fe and Cr. The simulation was run for 100,000 ions to obtain smooth damage curves and adequate counting statistics. Figure 4.4(a) shows the SRIM calculated profiles for proton irradiation at 2 MeV for the formation of the α' precipitate population (P18, P19) as well as one irradiation of as received 15Cr using similar conditions to a higher dose (AR+P/1e-5/2). The figure illustrates how the damage rate changes with depth for protons. The damage rate profile is mostly flat with respect to depth until the peak depth – this insured that the α' precipitate microstructure was more uniform throughout the depth as well. Figure 4.4(b) shows the profile for lower energy proton irradiation at 1.5 MeV proton. And Figure 4.4(c) shows the SRIM calculated profiles for heavy ion irradiation at 4.4 MeV used for the irradiation of both as received 15Cr and pre-existing α' precipitate samples (P18 and P19).

The SRIM damage rate was used to calculate the total irradiation time required to reach any given damage level. By making periodic measurements of the beam current, and integrating it over the time of the irradiation, and estimation of the total ion fluence was made. The equations below, Eq. (4.3) and Eq. (4.4), estimated the total dpa for a given condition (the units for each input and appropriate conversions are also given).

$$dpa = \frac{SRIM\ damage\ rate\ \cdot \sum ion\ beam\ current \cdot time}{Number\ density \cdot ion\ charge \cdot Specimen\ area\ irradiated} \tag{4.3}$$

$$\frac{disp}{atom} = \frac{\frac{disp}{\text{Å} \cdot ion} \cdot \sum \frac{\mu C}{s} \cdot s \cdot \frac{10^8 \text{Å}}{cm}}{\frac{atom}{cm^3} \cdot \frac{C}{ion} \cdot \frac{10^6\ \mu C}{C} \cdot cm^2} \tag{4.4}$$

The damage calculations for electron irradiation cannot use SRIM, but rather must use the McKinley and Feshbach approximation for the damage cross section [3]. This cross section is based on Coulomb scattering of electrons. The displacement rate was calculated as:

$$\frac{R}{N}\left[\frac{dpa}{s}\right] = \varphi\,\sigma_d(E) \tag{4.5}$$

where R is the displacement rate density (displacements/cm^{3}s), N is the atomic density, φ is the particle flux, and $\sigma_d(E)$ is the damage cross section. The cross section [4]is calculated as:

$$\begin{aligned}\sigma_d = {} & (2.5\times10^{-25})\frac{Z^2(1-\beta^2)}{\beta^4}\left\{\frac{2T_{max}}{3T_d}-(\beta^2+\pi\alpha\beta)\ln 3\right.\\ & +2\pi\alpha\beta\left[\left(\frac{T_{max}}{T_d}\right)^{\frac{1}{2}}-\left(\frac{T_{max}}{3T_d}\right)^{\frac{1}{2}}\right]\\ & -\frac{1}{2}\left[\left(\frac{T_{max}}{3T_d}\right)-1-\beta^2\ln\left(\frac{T_{max}}{3T_d}\right)\right.\\ & \left.+\pi\alpha\beta\left\{2\left[\left(\frac{T_{max}}{3T_d}\right)^{\frac{1}{2}}-1\right]-\ln\left(\frac{T_{max}}{3T_d}\right)\right\}\right]\\ & +\frac{T_{max}}{2T_d}\left[\ln\left(\frac{T_{max}}{3T_d}\right)-\left(1-\frac{3T_d}{T_{max}}\right)(\beta^2+\pi\alpha\beta)\right.\\ & \left.\left.+2\pi\alpha\beta\left[1-\left(\frac{3T_d}{T_{max}}\right)^{\frac{1}{2}}\right]\right]\right\}\end{aligned} \tag{4.6}$$

where α is $Z/137$, β is the ratio of the speed of an electron to light (v_e/c), and the remainder of the values and terms are defined in Table 4.5. The irradiations conducted at Kyushu University assumed a displacement threshold energy of 40 eV for Fe-15Cr, whereas the irradiations at Hokkaido University assumed a threshold energy of 25 eV. By correcting the threshold energy to 40 eV for Hokkaido University, the damage rate and dose achieved for each irradiation were re-calculated and reported in Table 4.6. For clarity, it is these "corrected" doses and damage rates with a threshold energy of 40 eV that is recalled throughout this thesis (including in Table 4.3 and Table 4.4).

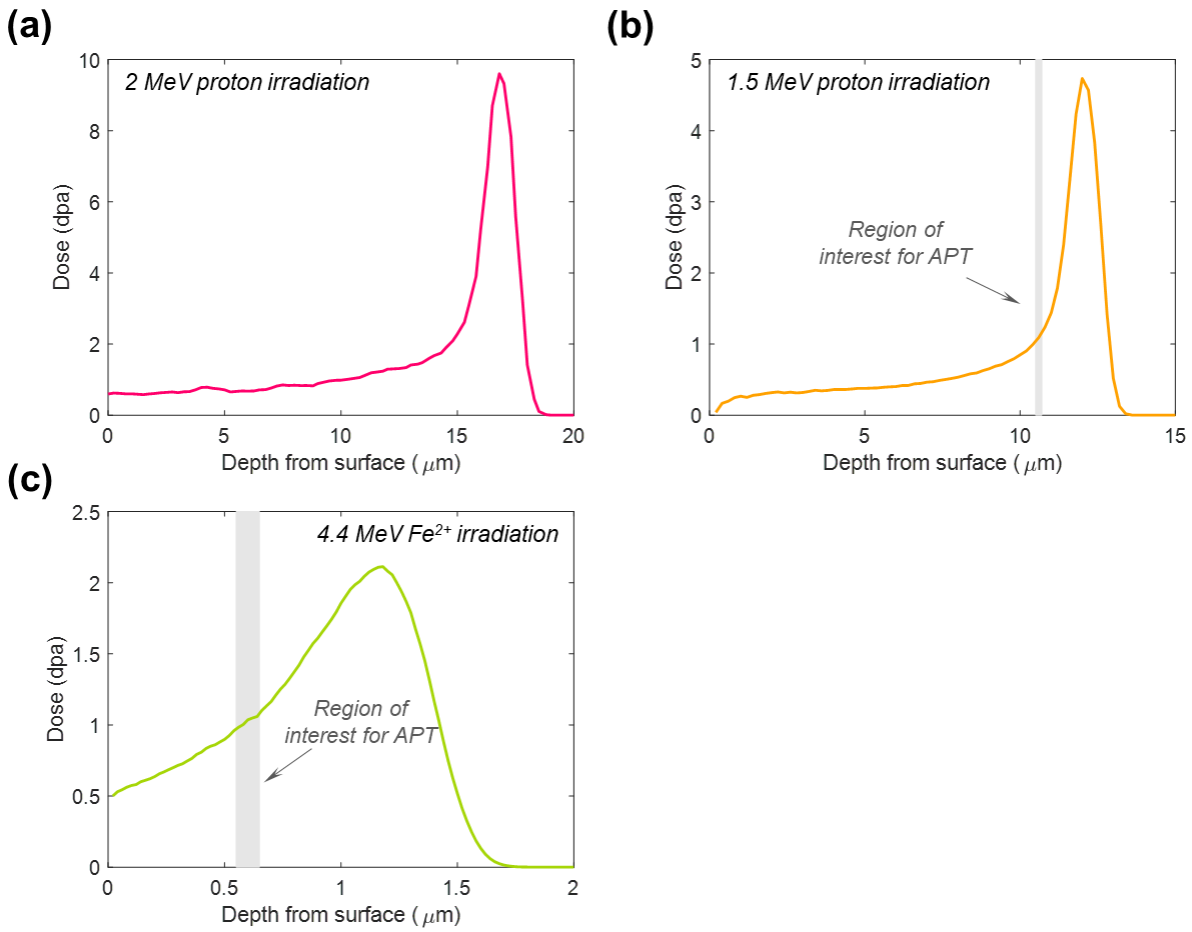

Figure 4.4. SRIM damage profile for (a) 2 MeV proton, (b) 1.5 MeV proton, and (c) 4.4 MeV Fe.

Table 4.5 Definitions and values used to calculate the damage rate for electron irradiation in Fe-15Cr.

Variable	Definition	Value
Z	Atomic number of target atom	26
E_R	Rydberg energy	13.605 *eV*
a_0	Bohr radius	5.29x10^{-11} *m*
v_e	Velocity of an electron	$c \cdot \sqrt{1 - \left(\frac{M_1 c^2}{E + M_1 c^2}\right)^2}$
c	Speed of light	2.995x10^{8} *m/s*
T_d	Displacement energy	40 *eV*
T_{max}	Maximum energy	$E_{max} = \frac{2E_0}{M_2 c^2}(E_0 + 2m_0 c^2)$
E	Energy of electrons	1-3 *MeV*
M_1	Rest mass of electron	5.486x10^{-4} *amu*
M_2	Mass of target atom (Fe)	55.845 *amu*

Table 4.6 Calculated damage cross section, damage rate, and dose for each electron irradiation condition for a threshold energy of Td of 40 eV and 25 eV.

Sample	Irradiation facilities	Beam	Td = 40 eV			Td = 25 eV		
			Cross section (m^2)	Damage rate (dpa/s)	Dose (dpa)	Cross section (m^2)	Damage rate (dpa/s)	Dose (dpa)
P19+E/1e-4/1	Kyushu University	1.25 MeV e^-	$1.96x10^{27}$	$1.0x10^{-4}$	1	--	--	--
P19+E/1e-3/1	Kyushu University	1.25 MeV e^-	$1.96x10^{27}$	$1.0x10^{-3}$	1	--	--	--
P19+E/5e-5/0.5	Hokkaido University	1.25 MeV e^-	$1.96x10^{27}$	$4.6x10^{-5}$	0.46	$4.27x10^{27}$	$1.0x10^{-4}$	1
P19+E/5e-4/0.5	Hokkaido University	1.25 MeV e^-	$1.96x10^{27}$	$4.6x10^{-4}$	0.46	$4.27x10^{27}$	$1.0x10^{-3}$	1
AR+E/5e-4/0.5	Hokkaido University	1.25 MeV e^-	$1.96x10^{27}$	$4.6x10^{-4}$	0.46	$4.27x10^{27}$	$1.0x10^{-3}$	1

4.2.2 Irradiation set-up and running the experiment

The irradiation stage builds and running of the irradiation experiment are similar between heavy ion and proton irradiations. The following sub-section will describe the irradiation process, highlighting the differences between the different types of ion irradiations.

The stages for irradiation are built differently between proton and heavy ion irradiation, largely due to the amount of beam heating one must account for under proton irradiation. For proton irradiation, a shim is fitted to a copper stage and filled with liquid indium, with an area matching the irradiation. The samples are placed on the indium (now cooled) with the guide bars on the outside. The indium facilitates the heat between the samples and stage. For heavy ion irradiation, a copper foil was placed between the samples and the stage, rather than indium. Two hold-down bars were used across the top and bottom of the samples, held down with four screws, to ensure the samples did not slip during installation or irradiation, and to prevent indium leakage. Type J thermocouples were custom built and spot-welded on the guide bars in order to calibrate the initial temperature and continue monitoring temperature throughout the irradiation. Figure 4.5 provides a schematic of the stage used for both heavy ion and proton irradiation. Figure 4.6 demonstrates a typical proton stage assembly and heavy ion stage assembly. Once the stage was built, it was sealed to the end of the ion beamline using a copper gasket and nuts and bolts. A cartridge heater was inserted into the back of the stage and airlines connected to provide cooling.

The beamline end station contains many diagnostic tools used to monitor the status of the irradiation chamber before and during the irradiation experiment. Figure 4.7 and Figure 4.8 provide a view of the end station for beamlines used for both proton and heavy ion irradiations. An Inficon ion gauge was used to read the pressure. During irradiations, the pressure is maintained below 10^{-7} torr. A CCD camera was available through a windowed port for a live view of the irradiation stage. In addition to the thermocouples, a FLIR 2D infrared thermal imager was mounted to a port to provide *in situ* temperature measurements of the sample surfaces. A custom built LabView™ program records and displays the outputs from each of these diagnostic systems.

After the stage is loaded and under vacuum, the slit aperture system was set to the desired conditions to determine the irradiation area. The aperture system consisted of four independently controlled and electronically isolated slits. The apertures measure the unsuppressed current incident on each individual slit. The slits are controlled digitally and can be moved into and out of

the beam path. The alignment of the stage was then check using a laser, which was aligned with the beam path, mounted at the end of a bending magnet near the accelerator. The laser beam was diffuse to simulate effect of raster-scanning. The alignment of the laser illuminate area was checked via CCD camera. Minor adjustments, if needed, were made via alignment screws at the end station of the beamline. Figure 4.9 shows an example of samples mounted on the beamline and aligned with the laser.

Before the beam can be placed on the samples and commence irradiation, the stage is heated to irradiation temperature (400°C) and the thermocouples are used to calibrate the FLIR pyrometer. For all irradiations using samples that had been previously irradiated, sample heat-up was conducted as quickly as possible to minimize the amount of time the samples were at high temperature without subjugation to irradiation. For proton irradiations, airlines were turned on before placing the beam on the sample, dropping the stage temperature in order to compensate for the large amount of beam heating. Once the beam was introduced, the airline was used to control the irradiation temperature fluctuations. For heavy ion irradiations, beam heating was minimal, so the airlines were not used during the irradiation, rather the cartridge heater in the back of the stage was adjusted to maintain the irradiation temperature at 400°C within ±10°C. Figure 4.10 shows a typical thermal image of the samples during irradiation, with square area of interests (AOIs) defining the areas to be monitored throughout the entire length of the irradiation. The thermocouples were still monitored in addition to the AOIs from the FLIR imager throughout the irradiation. The AOIs could also provide spatial variation of temperature across the samples as well as any potential indium leaks.

The current was monitored at all times during the experiment. The beam was raster-scanned across the samples and the slits. The both the heavy ion and proton beams were raster scanned across the samples such that it passed through each point of the irradiated area. For heavy ion irradiations, a suppressed faraday cup was periodically (every 30-45 minutes) inserted in front of the stage to measure the current impacting the stage. The balance of current values on the slits was used to realign the beam, whenever required.

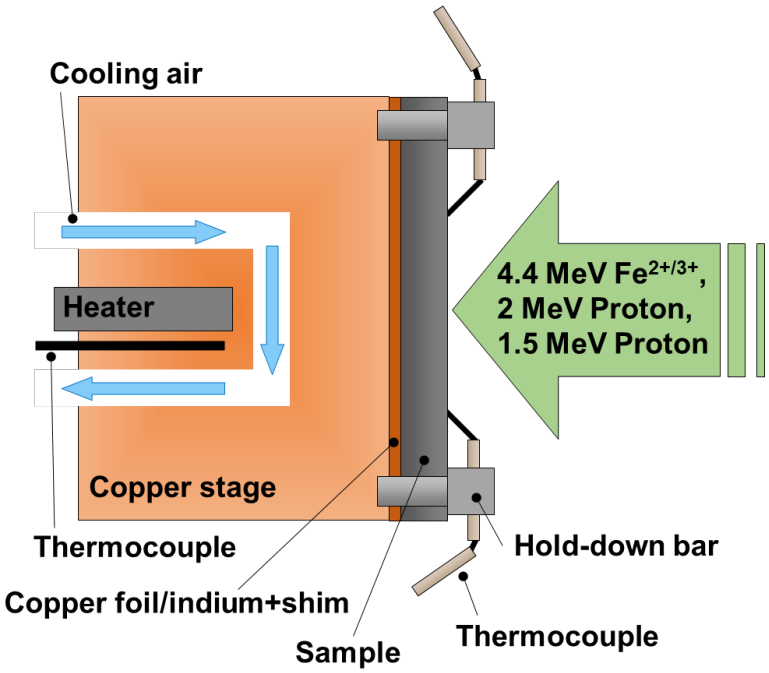

Figure 4.5 Schematic of the stage used for irradiations (proton and heavy ion irradiations).

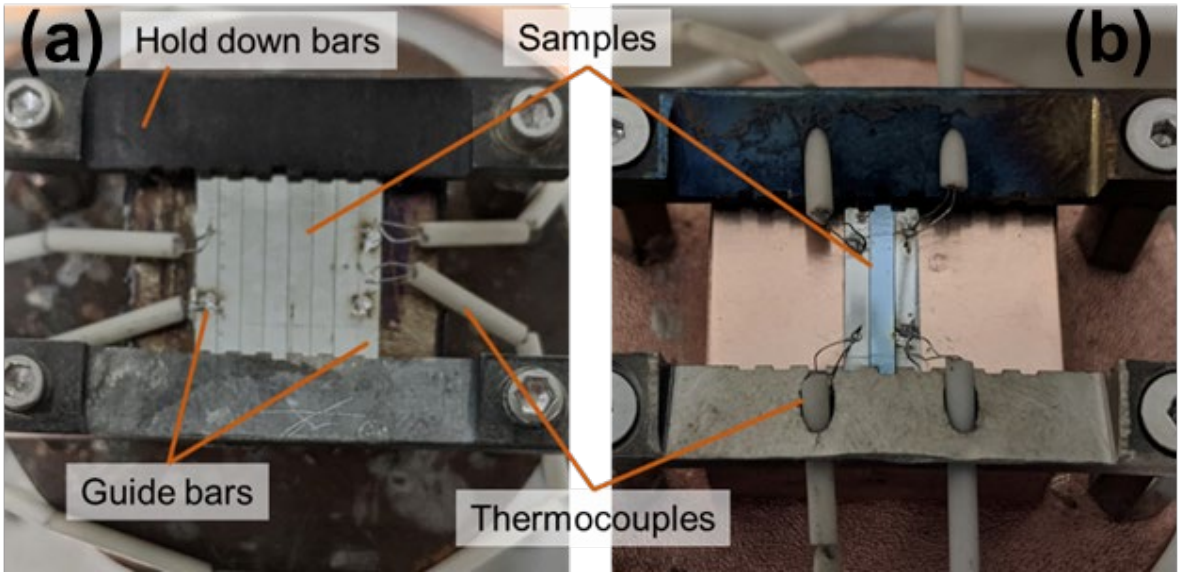

Figure 4.6 Example stage assembly for (a) proton irradiation, and (b) heavy ion irradiation.

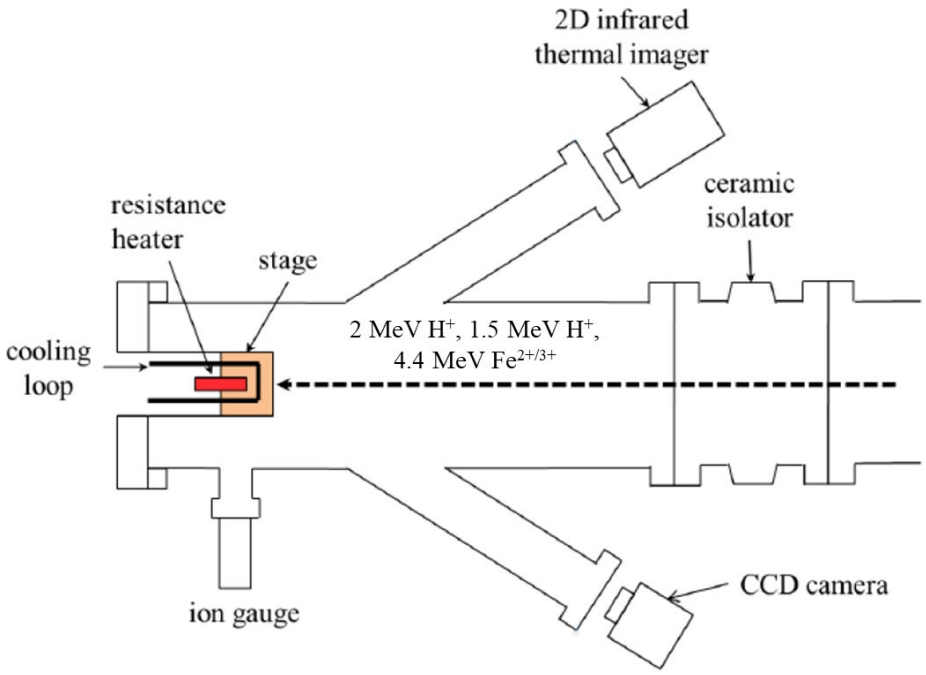

Figure 4.7 Schematic of Beamline 2 (BL2) end-station, detailing key components. Used for proton irradiations and heavy ion irradiations.

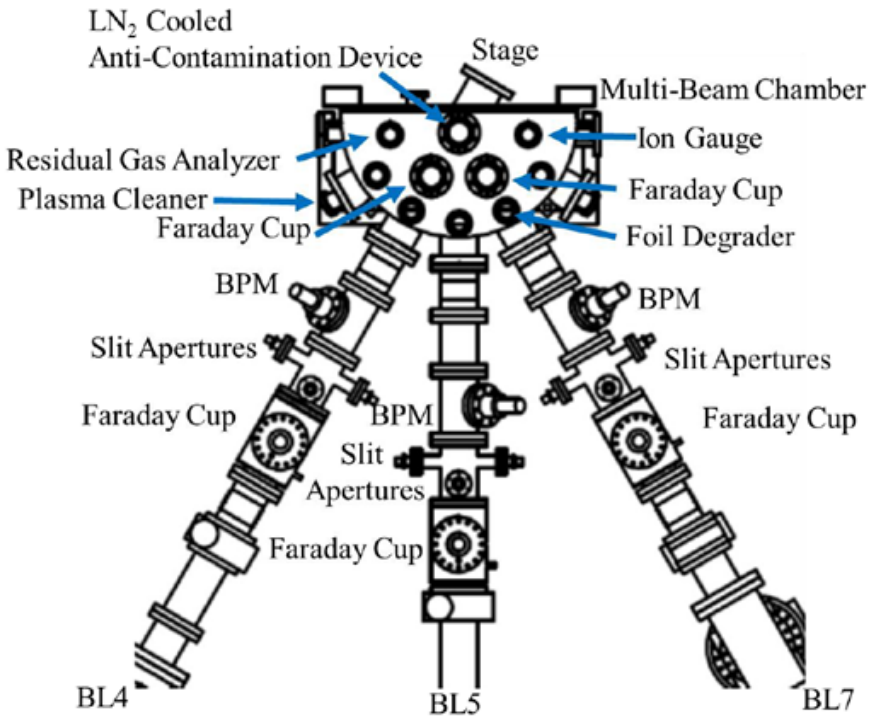

Figure 4.8 Schematic of the multi-beam chamber (MBC) with connecting beamlines and key components. For heavy ion irradiation, Beamline 7 (BL7) was used.

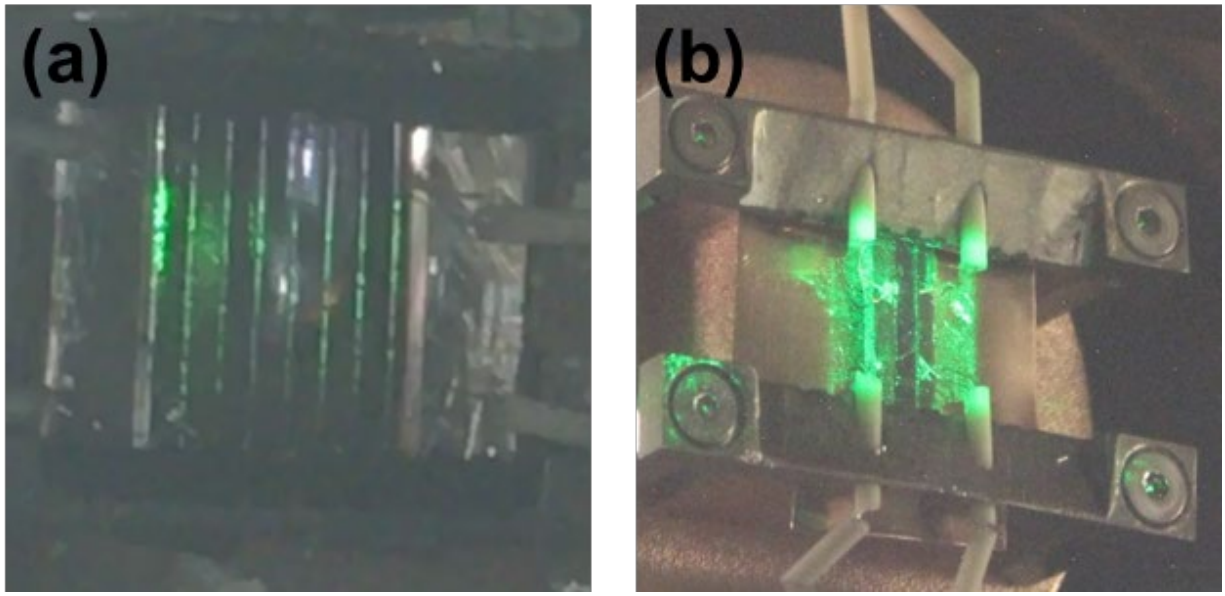

Figure 4.9 Example laser alignment on stage for (a) proton irradiation, and (b) heavy ion irradiation.

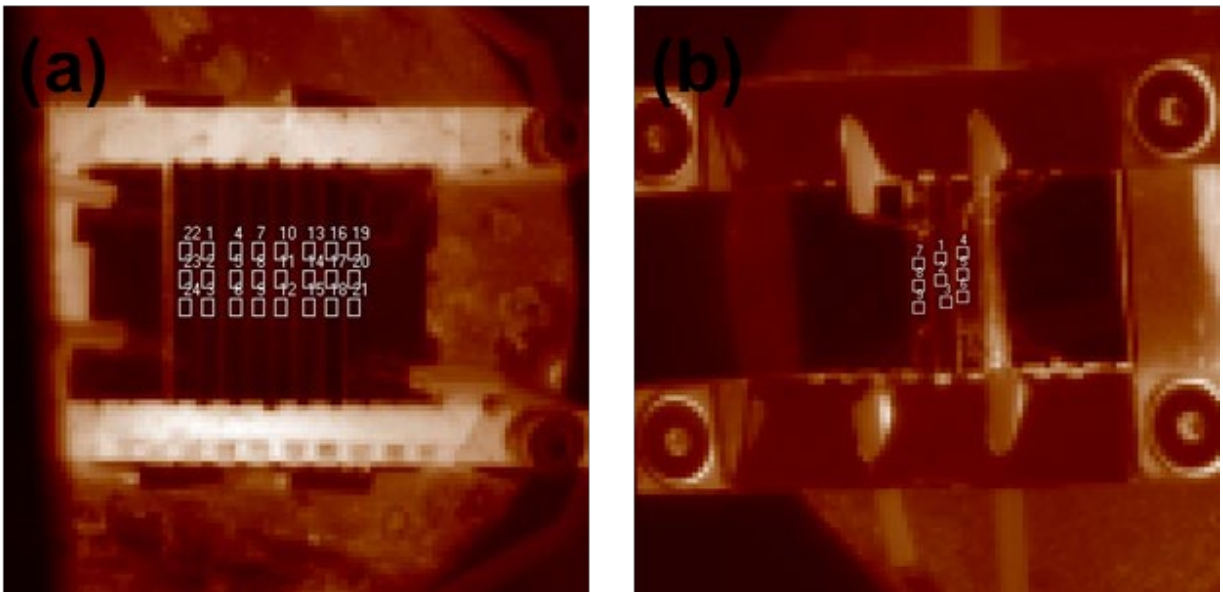

Figure 4.10 Example of a typical thermal image with AOIs on a heated stage for (a) proton irradiation, and (b) heavy ion irradiation.

4.2.3 Formation of α' precipitate distribution

In order to create the α' precipitate distribution, two proton irradiations (2 MeV) were conducted on Fe-15Cr at MIBL using the 3 MV NEC Pelletron accelerator. The samples were labeled according to the irradiation conducted: "P18" for the first proton irradiated conducted in 2018, and "P19" for the second proton irradiation conducted in 2019. Both irradiations were conducted at identical conditions: damage rate of $1x10^{-5}$ dpa/s (using SRIM quick Kinchin-Pease at 60% depth) to 1 dpa at 400°C. After irradiation, the samples were each electropolished, using the same process outlined in Section 4.1, in order to remove residual indium. APT needles were made from both P18 and P19 to characterize the initial α' microstructure.

4.2.4 Heavy ion irradiations

For each heavy ion irradiation (both irradiations of pre-existing α' precipitates and as received), samples were irradiated using either 3 MV Pelletron accelerator or 1.7 Tandetron accelerator using 4.4 MeV Fe^{2+} or Fe^{3+} at a range of damage rates $1x10^{-4}$, $3x10^{-4}$, and $1x10^{-3}$ dpa/s to 1 and 10 dpa and at $1x10^{-5}$ dpa/s to 1 dpa. APT samples were taken from each condition for characterization. Additionally, alumina coating was used for all P18 samples subjected to heavy ion irradiation. The only sample with pre-existing α' precipitate population used without alumina coating was a P19 sample irradiated at 10^{-3} dpa/s to 1 dpa (P19+H/1e-4/1). Alumina coating was not used for any heavy ion irradiations of as received samples.

4.2.5 Proton irradiations

For the proton irradiation of pre-existing α' precipitates, procedures for stage assembly, beam alignment, rastering, and temperature monitoring were identical to those used for proton irradiation used in the formation of the α' precipitate population. For each irradiation, samples were irradiated using 3 MV Pelletron accelerator at MIBL with a 1.5 MeV H^+ beam for at a damage rate of $1x10^{-4}$ dpa/s to 1 and 10 dpa. APT and TEM samples were extracted from each condition for characterization. Additionally, a proton irradiation with identical conditions to those in used to form the initial α' precipitates was conducted on as-received 15Cr alloy completed with 2 MeV

proton beam at a damage rate of $1x10^{-5}$ dpa/s to a total dose of 2 dpa. APT needles were made from this sample.

4.2.6 Electron irradiations

Electron irradiations were conducted using a High Voltage Electron Microscope (HVEM). The electron irradiations performed at Kyushu University used the JEM-1300NEF; the electron irradiations performed at Hokkaido University used the JEM-ARM-1300. Prior to starting the irradiations, the samples were heated to temperature. The electron beam current was measured using a Faraday cup, measuring the beam profile across the sample. Figure 4.11(a) shows an example image of the Faraday cup and the electron beam on the liftout sample. Figure 4.11(b) shows the measured beam profile for one of the electron irradiations, measuring the beam current in two orthogonal directions. From the beam profile, the center of the irradiation area was mostly flat, achieving a more homogeneous damage rate.

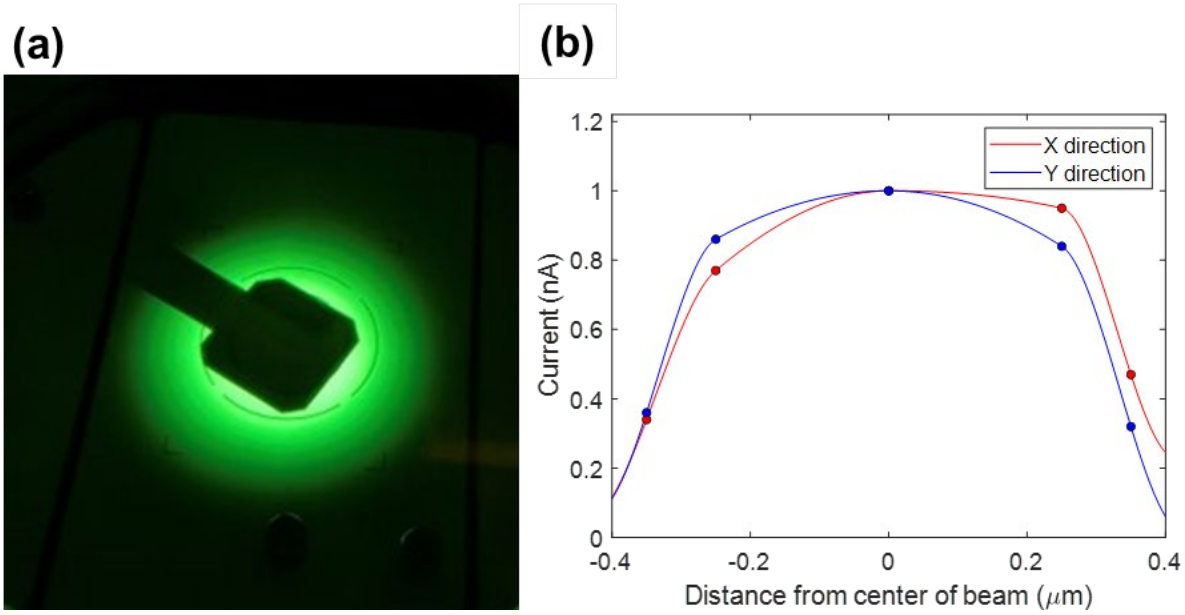

Figure 4.11 (a) Example of the Faraday cup measuring the electron beam current in the center of the beam, and (b) beam profile measured in two orthogonal directions illustrating the beam's gaussian shape with homogeneity in the center ~400nm.

4.3 Post-irradiation characterization methods

This section details the preparation and analysis methods used to examine the microstructure of the Fe-15Cr samples after irradiation. It consists of APT sample preparation, APT sample running, and reconstruction. It also consists of TEM sample preparation, imaging, and characterization.

4.3.1 APT specimen preparation

The FIB (focused ion beam) liftout method was utilized for preparing APT needles. The APT needles were prepared using the FEI Nova NanoLab^{TM} or FEI Helios NanoLab^{TM}. The FIB utilizes an electron gun (normal to the horizontal surface) for imaging, and a gallium ion beam (at 52°from the electron beam) for imaging and milling. The current and energies of these beams could be varied; the ion beam operated at energies up to 30 kV and currents up to about 7 nA. The FIB liftout method will be described below. The APT needles prepared from the 1.5 MeV proton irradiation additionally used the ThermoFisher Helios G4 PFIB UXe; the ion beam operated at currents up to 60 nA. APT needles from the samples with pre-existing α' precipitates (P18 and P19) were characterized at corresponding depths to the heavy ion, 1.5 MeV proton, and electron irradiations.

APT liftouts for the formation of α' precipitate distribution + heavy ion irradiations

The FIB liftout method utilized for characterization of 2 MeV proton irradiations and heavy ion irradiations is as follows. The irradiated bar was mounted irradiated side up using carbon tape on an SEM mount and placed in the FIB chamber, which was then pumped down. The stage was tilted to 52° to be perpendicular to the ion beam. An appropriate area was selected in the irradiated region. A gas injector was inserted, and the gallium beam was used to deposit a small amount of platinum on the target surface, in dimensions of approximately 15 x 3 μm^2 and height of 1 μm, using a current of about 0.1 nA. Using a higher current (~7 nA), the gallium beam was used to create trenches about 4 μm deep on three sides of the platinum strip. The long sides of trenches along the platinum were cleaned using a lower current (~3nA). The stage is then tilted to 22° so that the gallium beam produces an angled (or wedged) undercut. The stage is rotated 180° and the

undercut is repeated on the other side. A micromanipulator (called an Omniprobe™ needle) was inserted and slowly positioned such that it contacted the corner of the platinum deposit. A small amount of platinum was used to weld the Omniprobe™ needle to the sample. The final connecting edge was then cut using the gallium beam to free the sample from the metal bulk. The Omniprobe was slowly lifted to a safe distance above the irradiated sample surface before being removed from the chamber. The SEM chamber was evacuated, and the irradiated sample was replaced with an APT coupon. The Omniprobe needle was inserted and slowed to a position where it was just in contact with a silicon post. The gallium beam was used to weld the specimen to the post with about 0.7 μm of platinum (0.1 nA). The remaining liftout still attached to the Omniprobe needle was detached using low current (~0.5 nA). This process of mounting the needles to silicon posts and cutting away the remaining liftout was repeated until there was no usable amount of liftout remaining. The APT needles were placed on alternate silicon posts to eliminate damage from a fractured needle during the analysis process. This process typically produced 5-7 usable needles, depending on the length of the liftout.

At this point, the needles required sharpening. In order to achieve the required conical shape, successive milling is needed to be done. The APT coupon was tilted to 52° and the current set to 0.5 nA. A circular milling was used with an inner diameter of ~1 μm and an outer diameter set to cover the entire mounted specimen on the post. The milling slowly thins away the sides, forming a conical shape. The current and inner diameter were successively lowered as needed, all the while preserving the platinum layer on the sample surface. On the last milling, the current was 0.1nA with an inner diameter of 100 nm. On the lowest current and inner diameter setting, the APT needle is milling past the platinum deposit to the depth of interest. For all initial proton irradiations – P18 and P19 – and heavy ion irradiations, the process described above was used to produce the APT needles. Figure 4.12 highlights the key steps.

APT for 1.5 MeV proton irradiations

For the 1.5 MeV proton irradiations, the depth of interest was deeper than easily accessible through the FIB liftout method described above. Before proceeding with the liftout method described above, the first ~5-10 μm of sample edge were milled away using the Thermo Fisher Helios G4 PFIB UXe. The process is as follows. The irradiated bar was mounted irradiated side up using carbon tape on an SEM mount and placed in the FIB chamber, which was then pumped

down. The stage was tilted to 52° to be perpendicular to the ion beam. An appropriate area was selected in the irradiated area on the sample edge. The gas injector was inserted, and the xenon beam was used to deposit a large amount of platinum near the edge on the target surface, in dimensions of approximately 30 x 10 μm^2 and height of ~1-3 μm. Then a large section is milled on the sample side along the deposited platinum with dimensions approximately 60 x 10 μm^2 to a depth of about 30 μm, with a higher current (60 nA), careful to not mill any deposited platinum. The milled edge is cleaned up with a lower current (4 nA). The SEM chamber is vented, and the irradiated sample is turned onto the side, with the now milled side facing up and irradiated side perpendicular. The chamber is pumped back down, and the FIB liftout method, as described for heavy ion irradiation, is used, placing the platinum deposit within the milled area, parallel to the irradiated surface at the depth of interest (11 μm for 1.5 MeV proton). Figure 4.13 highlights the steps before continuing with the FIB liftout method previous described and captured in Figure 4.12.

APT for electron irradiations

For all electron irradiations, the APT needles were created from the irradiated TEM liftouts. Due to a difference in the irradiated area between higher and lower damage rates (10^{-3} dpa/s vs ~10^{-4} dpa/s) the APT needle process differs; both will be described as follows. At lower damage rates (~10^{-4} dpa/s), the irradiated area consumed the majority of the liftout. The irradiated TEM liftout was mounted in a TEM grid holder and loaded in the FIB. The irradiated area was located using corresponding images from the experimenters (Hokkaido University or Kyushu University). The irradiated area was also visible in SEM and FIB. Platinum deposition using first electron beam deposition followed by ion beam deposition (total deposition was ~0.5 μm thick) was placed on the irradiated area in order to keep track of the irradiated area throughout the APT needle process. The Ominprobe needle was inserted and slowly placed in contact with the corner of the liftout. The Omniprobe needle was welded to the liftout, and the top half of the liftout was detached using low current (~0.5 nA). The top half of the liftout was placed on another post on the TEM grid for future use. Using the remaining bottom half of the irradiated liftout, the typical FIB liftout process described above was followed, and placing the APT needles on the silicon posts. The needles were sharpened using the same process described above as well. For the liftout irradiated at Kyushu University, 7 APT needles were achieved with the bottom half the liftout. For the liftout irradiated

at Hokkaido University, 1 APT needle was achieved as the irradiated area was much smaller. Figure 4.14 illustrates the key steps of the process.

For electron irradiations at 10^{-3} dpa/s, the irradiated area was much smaller, and the target beam current was achieved in the center due to the gaussian shape of the beam. Similar to the low flux liftouts, the irradiated area was located using corresponding images from the electron irradiation. Platinum deposition was placed over the irradiated area using first electron deposition and then ion beam deposition, for total thickness ~0.5 μm. The top couple microns were milled in order to place the APT needle within about 1 μm of the center of the irradiated area. Platinum was deposited on the top of the liftout where it had been milled away to protect the top of the APT needle with a current of 0.1 nA for 1 μm thick. And from here, the same process described above was followed, targeting the center of the irradiated area, and placing the APT needle on silicon posts. The needles were sharpened using the same process described above as well, targeting the center of the irradiated area where the electron beam was greatest, and the target damage rate and damage was achieved. Only one APT needle could be achieved from these liftouts due the smaller irradiated area. Figure 4.15 illustrates the key steps of the process.

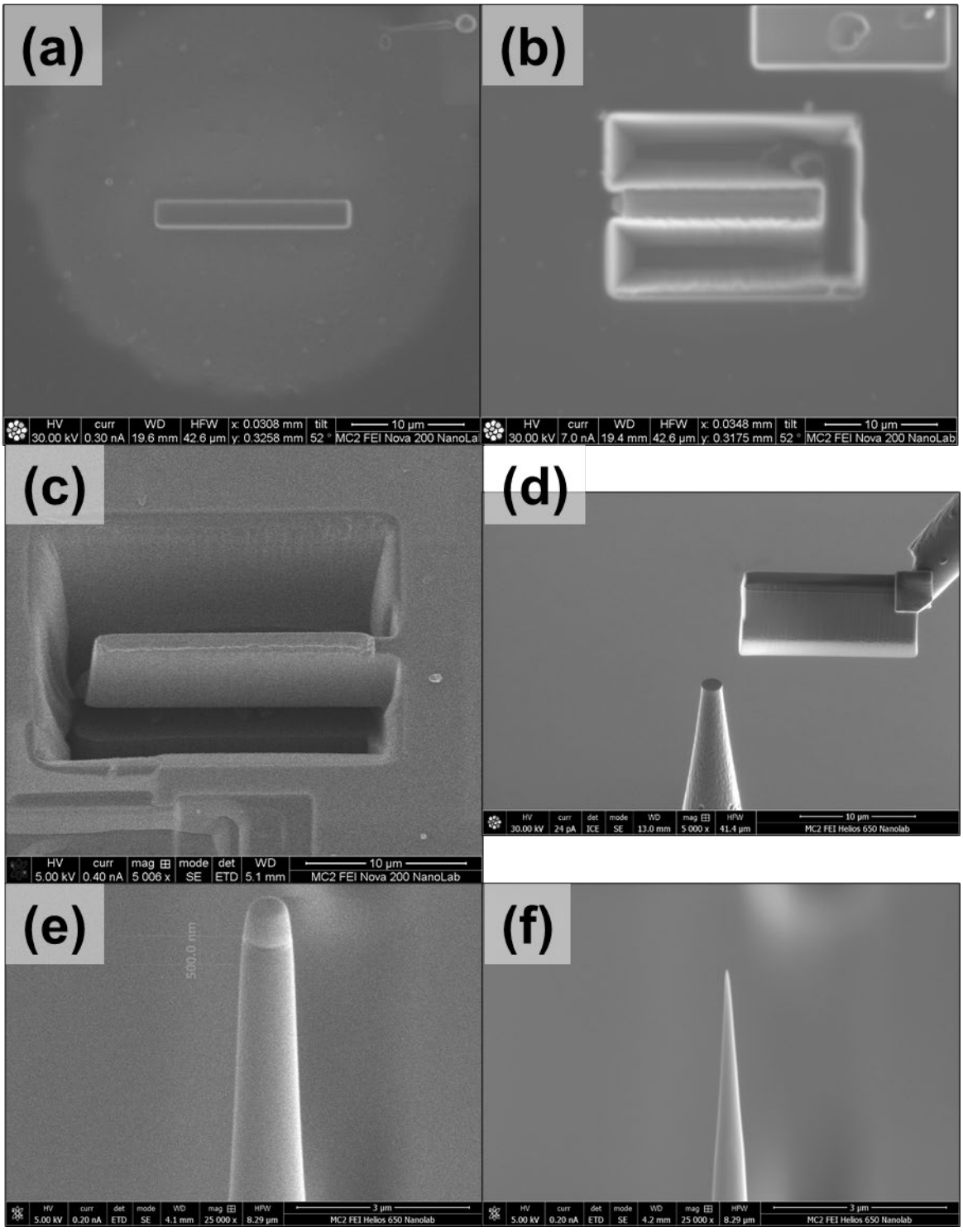

Figure 4.12 FIB liftout process used for the pre-existing α' precipitate samples and for heavy ion samples, showing (a) platinum deposition on surface, (b) trenching around the platinum deposition, (c) undercut of the sample at 22°, (d) attaching the APT needles to the Si microtips, (e) first step of sharpening APT needle where platinum is still visible, and (f) last step of APT needle sharpening where no platinum remains and the tip is at the ROI (600nm for P18, P19, and heavy ion irradiations) below the irradiated surface.

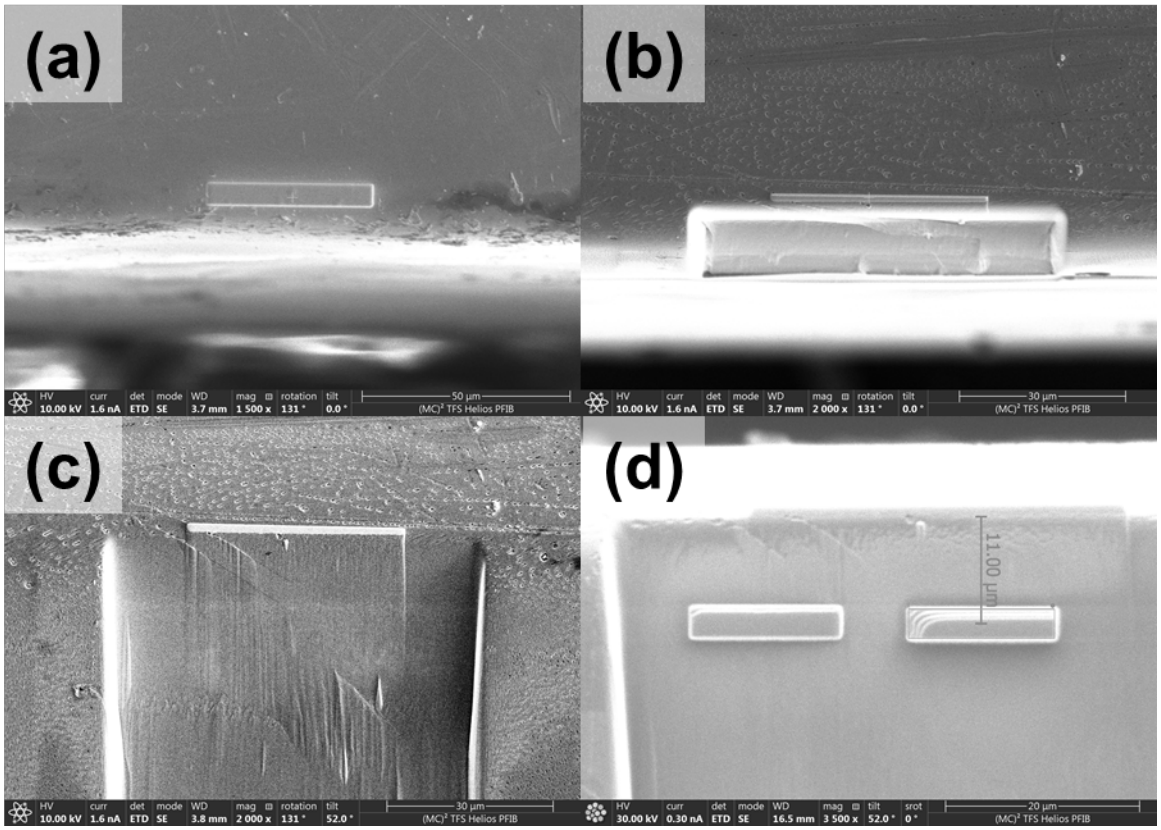

Figure 4.13 FIB liftout process used for 1.5 MeV proton irradiation of pre-existing α' precipitate samples, showing (a) the platinum deposition on the irradiated surface sample edge, (b) cutting away the sample edge while preserving the platinum deposition, (c) view of the cut away section to proceed with the FIB liftout technique, and (d) platinum deposition at ROI (11um for 1.5 MeV proton) for FIB liftout technique to produce APT needles.

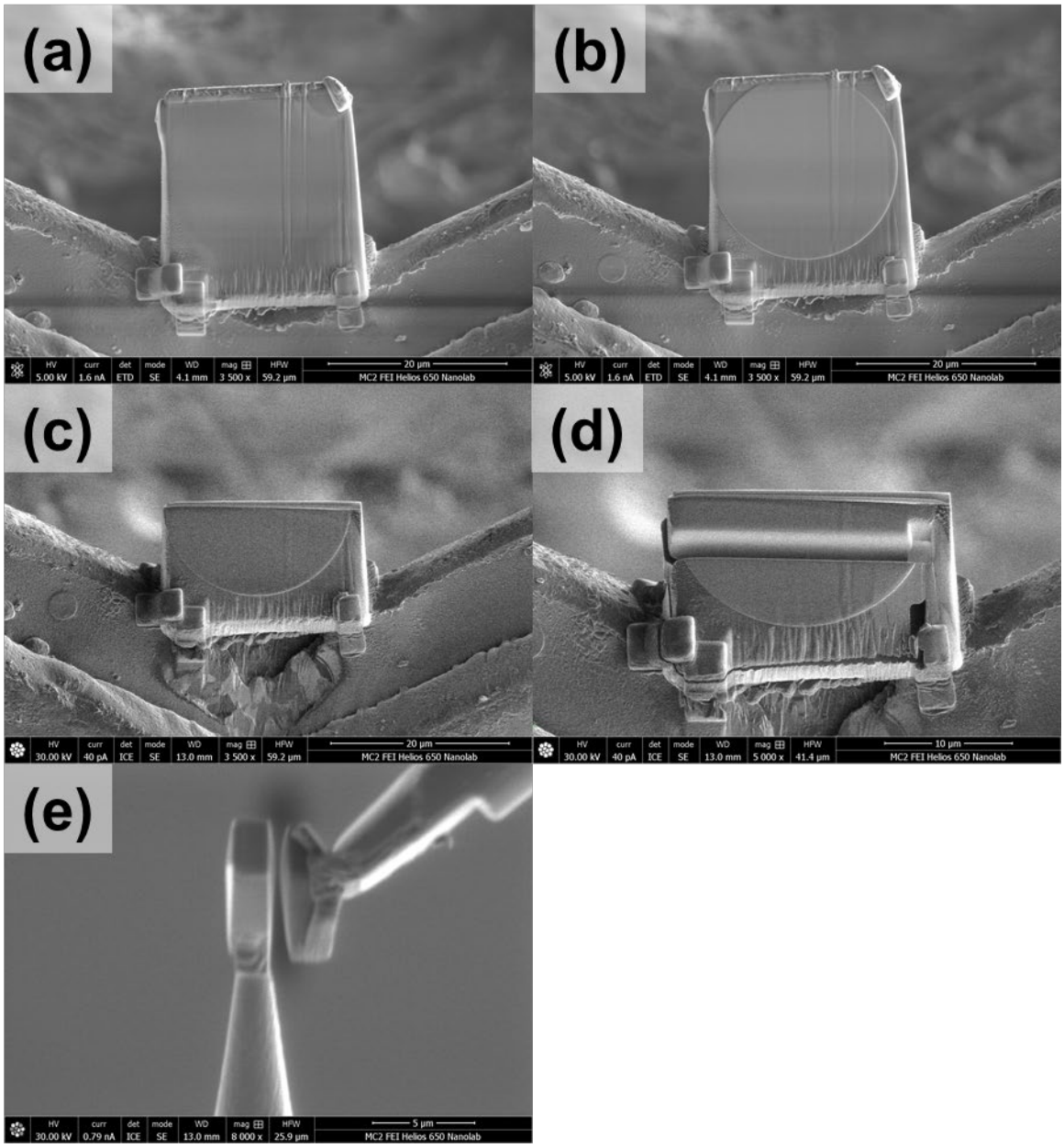

Figure 4.14 FIB liftout process used for electron irradiation samples at 10^{-4} dpa/s (P19+E/1e-4/1), showing (a) the irradiated liftout, (b) platinum deposition indicating the irradiated area, (c) the bottom half of the liftout, (d) undercuts at 22° on the bottom half of the liftout, and (e) placing the APT needles on the Si microtips.

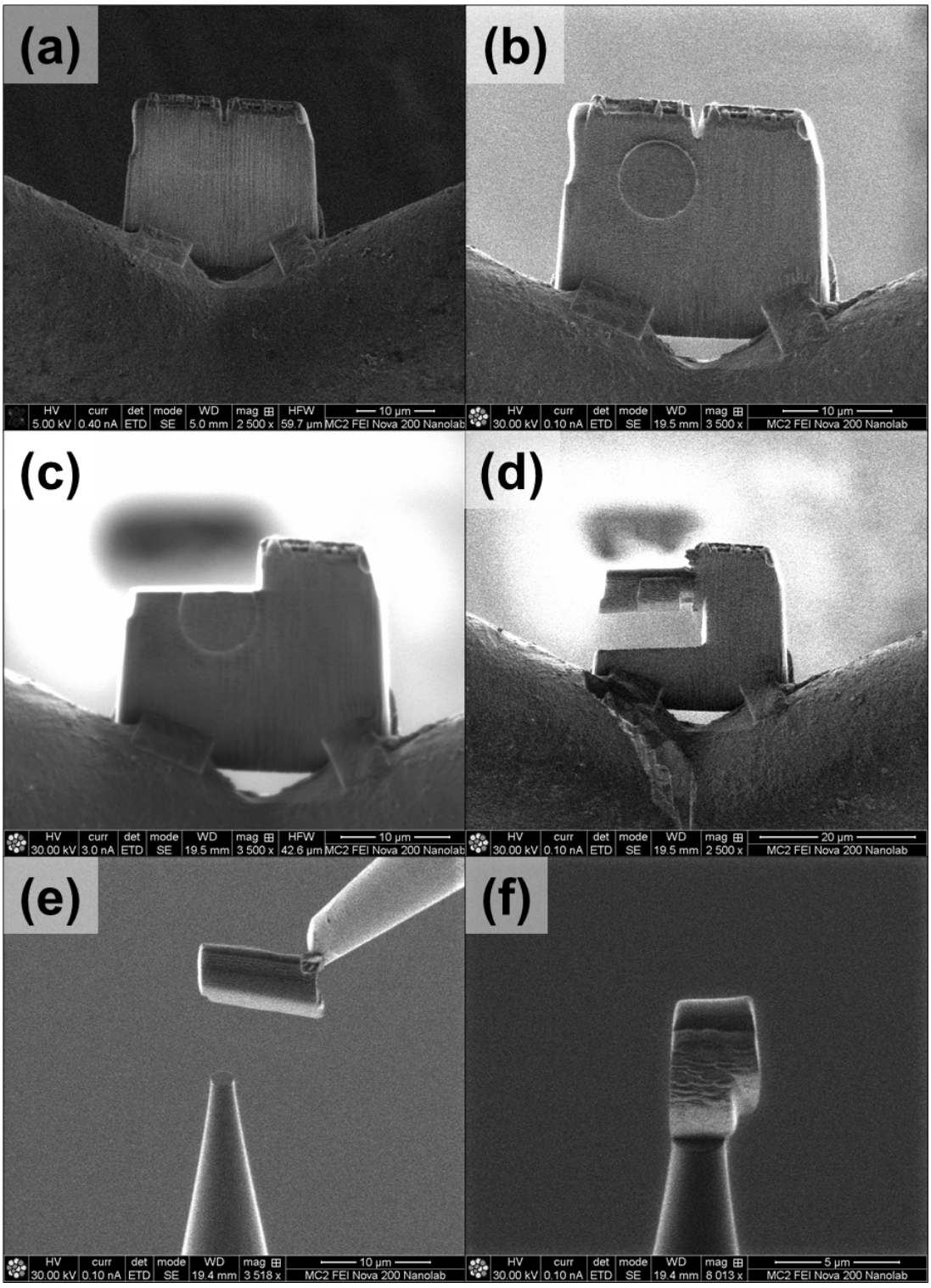

Figure 4.15 FIB liftout process used for electron irradiation samples at 10^{-3} dpa/s (P19+E/1e-3/1), showing (a) the irradiated liftout, (b) platinum deposition over irradiated area, (c) milled away top part of the irradiated area/liftout to better access the center of the irradiated area/peak damage rate, (d) undercuts at 22°, (e) placing the liftout on APT tips, (f) resulting APT needle.

4.3.2 APT data acquisition

For each irradiation condition, at least one APT needle was fabricated according to the procedures outlines in Sections 4.2.4-4.2.6 for each irradiation type. Each needle was analyzed one at a time using a Cameca LEAP 5000HR at Michigan Center for Materials Characterization ($(MC)^2$). For all specimens in this thesis, the LEAP was operated in voltage mode, except for the electron irradiated samples at higher damage rates which operated in laser mode. This was due to the limited number of tips for each electron irradiation condition and the high failure rate of APT needles in voltage mode. A series of APT needles were run with varying laser to determine the optimal laser energy. The optimal laser energy was determined to 50 pJ. For voltage mode, the APT needle was manually aligned to the local electrode prior to start, and fine-tuned upon starting acquisition using the ion collection on the detector. For laser mode, the process is similar. The APT needle is manually aligned to the electrode, followed by manually aligning the laser to the needle tip, then evaporation can proceed. In the beginning of evaporation, the needle is better aligned to the electrode, if needed, and the laser is calibrated to locate the needle tip. The laser is continually calibrated to locate the needle tip at a set time interval of 10 minutes. During evaporation, the laser power was set to 50 pJ, with a pulse rate of 200 kHz. Evaporation continued until the sample fractured due to thermal loading of the pulsing process or the preset number of ions have been collected (typically >30 million). The detector efficiency of the LEAP 5000HR is 52%. In voltage mode, the data set sizes ranged from ~1 million ions to ~15 million ions per needle. Once the sample had finished evaporation, the data set was stored as a .HITS file and was then use for analysis using a separate software package (Section 4.3.3). For both laser and voltage mode, the APT needles were cooled to 50-55K, analyzed with a pulse fraction of 20%, pulse rate of 200-250 kHz, and a detection rate of 0.005 atoms/pulse. Additionally, in laser mode, the laser pulse energy was 50 pJ.

4.3.3 APT reconstruction and analysis

The data analysis for each LEAP sample was conducted using Integrated Visualization and Analysis Software (IVAS) Version 3.8.2, and AP Suite 6. IVAS is integrated within AP Suite for data analysis in more recent reconstructions. The IVAS software enables processing of the .HITS

file from the LEAP analysis to reconstruct the original sample “atom-by-atom” and provides capabilities for cluster identification and analysis and composition analysis.

The data reconstruction process is a multi-step process. First, the ions to be used in the reconstruction were selected. Using the voltage history of the LEAP ion evaporation, a range of ions were selected. The range typically skipped the first 200,000-500,000 ions in order to remove the ions from when the needle position was more finely tuned with the electrode. And the range ended just before the tip fracture, indicated by a sharp increase in voltage on the plot. Next, the time-of-flight correction (TOF). This is an automated process within IVAS that transforms the TOF information for each atom into a mass-to-charge ratio. This then results in distribution of mass-to-charge ratios, which is next fitted. The user identifies multiple peaks in the distribution and the IVAS software than calibrated the full mass-to-charge spectrum, locating the identified peaks to their known mass-to-charge ratios and locating all remaining peaks at the best “fit” possible. Once calibrated, each peak in the mass-to-charge spectrum is indexed. For each peak, a range of ions is selected to assign the ion counts within the peak to an element. The front edge of the peak, and the back edge of the peak, was defined at edges located at double the background level. Once all peaks were identified, the tip volume is ready for reconstruction.

The aim for reconstruction is to approximate the original geometry and morphology of the sample needle as closely as possible. In order to complete needle volume reconstruction, several parameters must be identified: image compression factor (ICF), the k-factor (k), and the evaporation field (f). The k-factor is based on the tip radius, shank angle, a relative proximity to electrode during the LEAP analysis process. Since the same procedure was followed for each tip fabrication, the k-factor was assumed to be consistent and was set to the default value of 3.30. The evaporation field is dependent on the material analyzed. As the primary constituent of the Fe-Cr alloys was Fe, the evaporation field value was set to the known value for Fe for each reconstruction: 33.00 V/nm. The image compression factor played the strongest role in reconstruction and was varied until the α’ precipitates were spherical shape. If the tip reconstruction volume was large enough that the α’ precipitates were not mostly uniform in spherical shape, the reconstruction volume was broken into smaller sections and the ICF was varied accordingly for each smaller volume. The ICF values typically ranged from 1.00-1.5. It is at this point the reconstruction is created. Once the reconstruction is viewable, the morphology of the α’ precipitates is verified. If the precipitates appear elongated in the horizontal or vertical

direction, the ICF is modified accordingly, and reconstruction repeated until the α' precipitates are spherical in shape. Once satisfied with the cluster shape, the tip reconstruction is complete and cluster analysis can begin.

Analysis in this thesis used two complimentary techniques for different aspects of α' cluster analysis: (1) maximum separation method, and (2) iso-concentration (or iso-surface) method. The first method, maximum separation method (MSM), was used for calculating the cluster radii, number density, volume fraction, and matrix concentration. And the second method, the iso-concentration method, was used for identifying the cluster core concentrations values.

The MSM is based on the principle that solute-enriched regions are more densely packed together than the surrounding matrix. In this method, four parameters are used to identify the atoms in each cluster: d_{max}, N_{min}, L, and d_{ero}. First, a spherical volume with radius d_{max} is applied to each solute atom (Cr in the thesis) in the volume to search for other solute atoms. If no other solute atoms are found within the volume, the atom is considered to be in the matrix. If other solute atoms are found within the volume, the process is continued recursively until all solute atoms in the cluster are identified. And then this process is repeated for all other clusters in the analysis volume. If the d_{max} is too small, clusters may become fragmented; if d_{max} is too large, clusters may become agglomerated. Next, the N_{min} filter is applied to eliminate the random clusters, typically very small. N_{min} eliminates all clusters below a set threshold size. Finally, d_{ero} and L parameters are applied to the cluster analysis to refine the cluster definition. The envelope parameter, L, is used to determine if any matrix atoms belong within the cluster. A volume with radius of L is applied to each solute atom determined to be in a cluster, and if a matrix atom is within the volume, it is added to the cluster. The erosion parameter, d_{ero}, is then used to remove any excess atoms from the cluster. A volume with radius d_{ero} is applied to every atom in the dataset determined not to be in a cluster and are within a distance of d_{ero} from the cluster. Any cluster atom found within this volume is removed from the cluster.

In order to determine an approximate d_{max} value, the "Cluster Count Distribution Analysis" algorithm was used, with order of 5 [5]. The cluster count distribution was calculated for the analysis volume and additionally for a simulated volume, which randomized the ions in the analysis volume. The output for the randomized volume is typically a gaussian distribution. Depending on the degree of clustering, a bimodal peak is expected from analysis volume. Figure 4.16 shows an example of the output from IVAS. The d_{max} value was typically taken as the value

where the two curves first intersected, typically near the minimum on the analysis curve. This point is highlighted as a range on the figure. d_{max} values ranged from 0.30-0.34 for this thesis. The N_{min} value was determine from the "Cluster Size Distribution Analysis" algorithm from IVAS. Again, a curve was determined for the analysis volume and a randomized volume, an example of which is shown in Figure 4.17. The N_{min} value was taken to be where the analysis curve crossed the x-axis the first time. The dero and L parameters were set to half the d_{max} value. Cluster analysis outputs the .POS file and the corresponding .CSV file for the indexed clusters. The .POS file can then be opened in IVAS/AP Suite to inspect the indexed clusters. Cluster analysis was completed for a small range of d_{max} values (and corresponding N_{min}, $d_{ero,}$ L values) and the indexed cluster reconstruction volumes were compared to determine if the d_{max} value was correct based on if the clusters were separated correctly.

Once the parameters were determined to be set correctly, further cluster analysis was conducted. First, the few remaining smaller clusters that were not α' were removed. These clusters were typically very small and easy to identify as they were not spherical in shape. It was assumed these clusters were part of radiation induced segregation (RIS) as these clusters were oriented at major angles (45°, 90°) and a few were even found to outline a larger dislocation loop. These clusters were removed from all analysis, and the ion counts were added back to the matrix. Next, the clusters located on edges on the reconstruction volume were separated and indexed separately.

The IVAS cluster analysis output file (.CSV) provides the ion counts for each cluster, which was used to determine the spherical equivalent radius (R^{ppt}) given by:

$$R^{ppt} = \sqrt[3]{\frac{3\,N_{Fe+Cr}^{ppt}}{4\pi\,\rho\,Q}} \tag{4.7}$$

where N_{Fe+Cr}^{ppt} is the sum of Fe and Cr atoms in the cluster, ρ is the atomic density, and Q is the detector efficiency. The average radius and standard deviation were determined across all whole clusters (those not intersecting the edges of reconstruction volume) measured for each irradiation condition. The cluster number density (N_d^{ppt}) was determined by:

$$N_d^{ppt} = \frac{\left(N_{whole}^{ppt} + \frac{1}{2}N_{intersected}^{ppt}\right)\rho\,Q}{N_{tot}} \tag{4.8}$$

where N_{whole}^{ppt} is the number of whole clusters, $N_{intersected}^{ppt}$ is the number of incomplete clusters (those found on the edges of the reconstruction volume), and N_{tot} is the total number of ions collected in the analysis volume. The volume fraction (f) was calculated by:

$$f = \frac{\sum N_{tot}^{ppt}}{N_{tot}} \frac{\rho^{matrix}}{\rho^{\alpha'}} \tag{4.9}$$

where N_{tot}^{ppt} is the sum of all ions in the clusters, ρ^{matrix} is the atomic density of the matrix, and $\rho^{\alpha'}$ is the atomic density of α' phase.

In order to avoid the intermixing of the precipitate-matrix ions, whether due to local magnification effect or due to the nature of the α' nanoprecipitates, the iso-concentration method was used to report the Cr-rich cluster core concentration. The voxel grid was set to 0.8 nm and the d_{local} corresponding the voxel dimensions was set to 2.4 nm (or three times the value of the voxel dimension). The concentration threshold was set to minimum value at which clusters were no longer connected and the pole, if appeared in the volume, did not appear. The concentration threshold ranged between 22-35%. Proximity histograms (or proxigrams) were saved for each individual Cr-rich cluster in the reconstruction volume. The core concentration was determined by fitting an objective sigmoidal function to the proxigram, as shown in Eq. (4.10). Here $C(x)$ is the Cr concentration (in at%), x is the distance from the interface, A_{max} is the maximum concentration, A_{min} is the minimum concentration, x_0 is the position at which C is the average of A_{min} and A_{max} defining the mixing zone width. Data points in the proxigram with low count statistics were removed. Only clusters that were contained entirely within the volume were considered. Additionally, in order to remove any RIS clusters from the concentration measurements, the iso-concentration cluster coordinates were matched to MSM identified clusters; all other iso-concentration clusters were removed from concentration measurements. The average α' Cr concentration for each condition was determined to be the average of all core concentration (A_{max}) values for each condition; the error was taken as the standard deviation. Figure 4.18 shows an example of a proximity histogram from an individual Cr cluster in a reconstruction volume with the sigmoidal fit applied.

$$C(x) = A_{max} + \frac{A_{min} - A_{max}}{1 + e^{(x-x_0)/\Delta}} \tag{4.10}$$

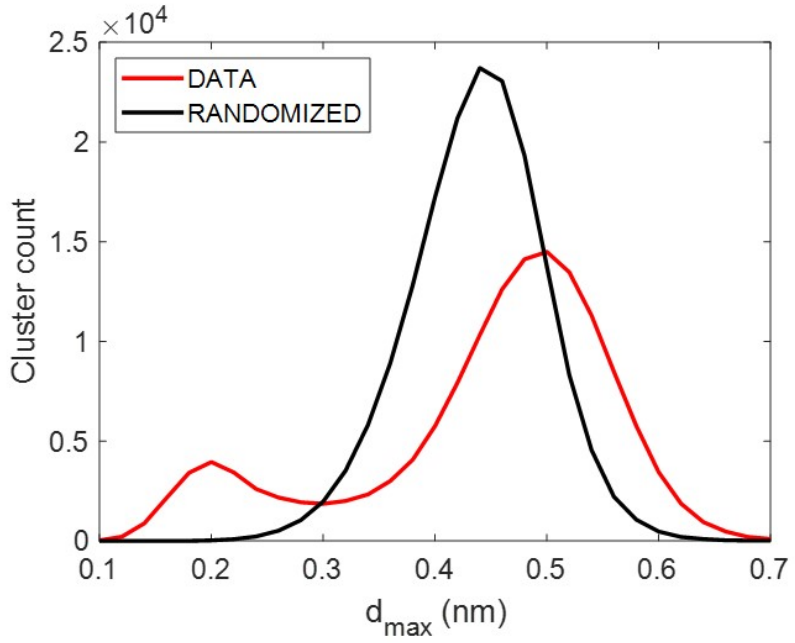

Figure 4.16 Typical "Cluster Count Distribution" output from IVAS used to determine the d_{max} parameter. Example from P18 shows defined Cr clusters in volume.

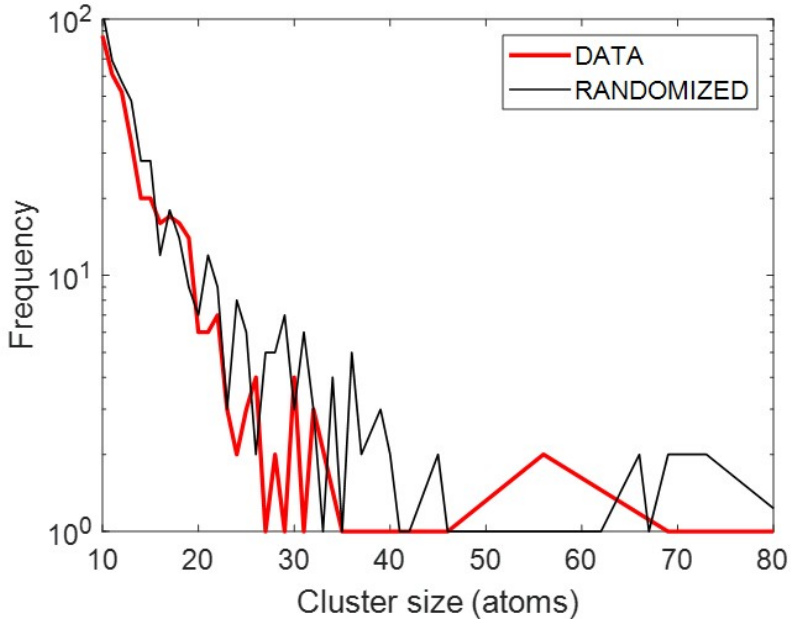

Figure 4.17 Typical "Cluster Size Distribution" output from IVAS used to determine N_{min} parameter. Example from P18.

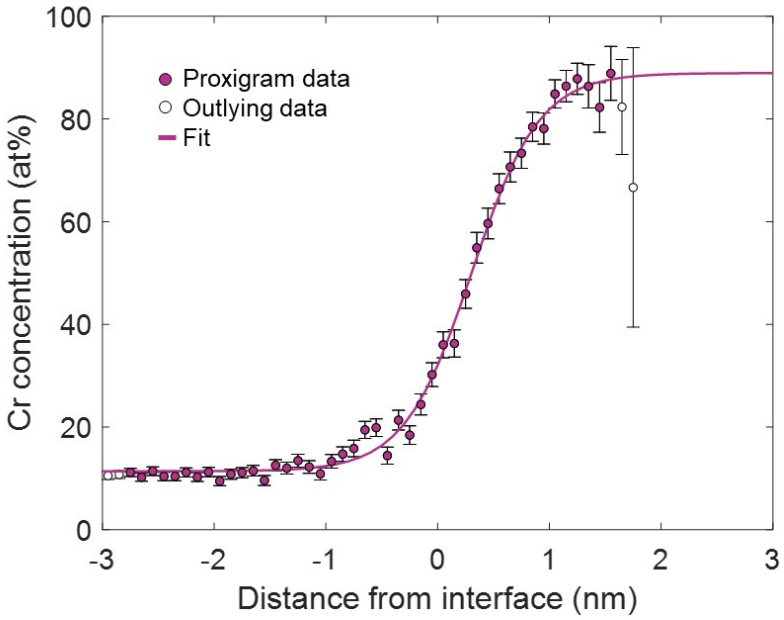

Figure 4.18 Example proximity histogram and sigmoidal fit for an α' precipitate. The obvious outlying data (open circles) due to low atom counts were removed and the remaining data was fit with a sigmoidal function (solid line).

4.4 Error analysis in ballistic dissolution parameter calculations

This section details the methods used to calculate the error for the ballistic dissolution parameter (or BDP), calculated in Chapter 6. The BDP was calculated using two methods: using the NHM equation (referred to as the NHM-based BDP) and using ballistic mixing (referred to as the ballistic mixing based BDP). The error propagation was determined using the method for non-correlated variables. The values for error associated with each variable were determined from experiments, from statistics (i.e., standard deviation), or estimations, each discussed further in this section and in Chapter 6.

The first BDP calculation method is based on the NHM equation described in Eq. (2.9). The NHM equation was solved for the ballistic dissolution parameter, φ. From this equation, six variables were determined to have error: D_{irr}, C_m, C_p, r, K_0, and $\frac{dr}{dt}$. The total error of the BDP was calculated using Eq. (4.11), which is the standard error for any function with un-correlated variables, where $\frac{\partial \varphi}{\partial D_{irr}}$, $\frac{\partial \varphi}{\partial C_m}$, $\frac{\partial \varphi}{\partial (\frac{dr}{dt})}$, $\frac{\partial \varphi}{\partial C_p}$, $\frac{\partial \varphi}{\partial r}$, and $\frac{\partial \varphi}{\partial K_0}$ are the partial derivatives of the BDP equation with respect to each term, and $\sigma_{D_{irr}}$, σ_{C_m}, $\sigma_{\frac{dr}{dt}}$, σ_{C_p}, σ_r, and σ_{K_0} are the error for each variable.

$$\sigma_\varphi{}^2 = \left(\frac{\partial \varphi}{\partial D_{irr}}\sigma_{D_{irr}}\right)^2 + \left(\frac{\partial \varphi}{\partial C_m}\sigma_{C_m}\right)^2 + \left(\frac{\partial \varphi}{\partial (\frac{dr}{dt})}\sigma_{\frac{dr}{dt}}\right)^2 + \left(\frac{\partial \varphi}{\partial C_p}\sigma_{C_p}\right)^2 + \left(\frac{\partial \varphi}{\partial r}\sigma_r\right)^2 + \left(\frac{\partial \varphi}{\partial K_0}\sigma_{K_0}\right)^2 \quad (4.11)$$

To calculate the error in D_{irr}, the error for each quantity in $D_{irr}$with an error was propagated using the method demonstrated in Eq. (4.11) for non-correlated variables. The terms D_i and D_v are dependent on temperature and the error in the temperature was determined from temperature fluctuations during the irradiation experiments. The terms C_i and C_v are dependent on the sink strength, D_i and D_v, and K_0. The sink strength error was dependent on the error in the precipitate size and number density, as well as the error in cavity sink strength, when cavities were present. The error in the damage rate was determined from the fluctuations in the current measurement during the irradiation experiment.

The errors in the terms α' terms (C_m, C_p, and r) used in the NHM-based BDP calculation were discussed previously in this chapter, in Section 4.3.3, where the errors were derived from statistical analysis.

The NHM calculation for BDP also depends on the rate of precipitate radius change ($\frac{dr}{dt}$). The precipitate radius size evolution with time was fit with a linear, polynomial, and exponential function; the derivative of this curve fit was used at the $\frac{dr}{dt}$ term. The error for the $\frac{dr}{dt}$ term was determined by placing worst fit lines (for linear fit) or curves (for polynomial and exponential fits) at the extremes of the error bars for the precipitate radius data at the minimum (0) and maximum dpa (1 or 10). Figure 4.19 shows an example. Chapter 6 will provide more information on the calculation of this term.

The second method to calculate the BDP is based on Fick's first law of diffusion. From this equation, three terms had errors: D, $\frac{dc}{dx}$, and K_0. The error was calculated using the same method as used for previous error calculations for the NHM-based BDP – the general equation for error propagation for non-correlated terms. Eq. (4.12) shows the form of this general equation applied to the ballistic mixing based BDP calculation, where $\frac{\partial \varphi}{\partial D}$, $\frac{\partial \varphi}{\partial \frac{dc}{dx}}$, and $\frac{\partial \varphi}{\partial K_0}$ are the partial derivatives of the ballistic mixing based BDP calculation with respect to each variable with error, and σ_D, $\sigma_{\frac{dc}{dx}}$, and σ_{K_0} are the errors for each variable.

$$\sigma_\varphi{}^2 = \left(\frac{\partial \varphi}{\partial D}\sigma_D\right)^2 + \left(\frac{\partial \varphi}{\partial \frac{dc}{dx}}\sigma_{\frac{dc}{dx}}\right)^2 + \left(\frac{\partial \varphi}{\partial K_0}\sigma_{K_0}\right)^2 \tag{4.12}$$

The D term was dependent on both the ballistic mixing diffusion coefficient (D_{bal}) and the RED (D_{irr}). The error associated with D_{bal} includes the damage rate and the number of replacements per atomic displacement, or "rpa". The error was assumed to be quite large as the value for heavy ion irradiation is between 30-100. For proton irradiation, the rpa is not known, but a value was assumed to be between 1 (electron irradiation) and 30 (heavy ion irradiation) so the error was again quite large. To calculate the total error for D_{irr}, the error was propagated accordingly, using the method for non-correlated terms.

The $\frac{dc}{dx}$ term was calculated from the derivative of the concentration function, $c(x,t)$ (Eq. (6.19)) from the ballistic mixing model. The variables with error for $\frac{dc}{dx}$ are c_1, c_2, and D. The error for c_1 and c_2 were based on the proximity histogram curve fits for the atom probe data used in the BDP calculation. The error for D was previously determined and described in the previous paragraph.

The error for the damage rate was calculated using the same methods as for the NHM-based BDP by using the fluctuation in the current measurements.

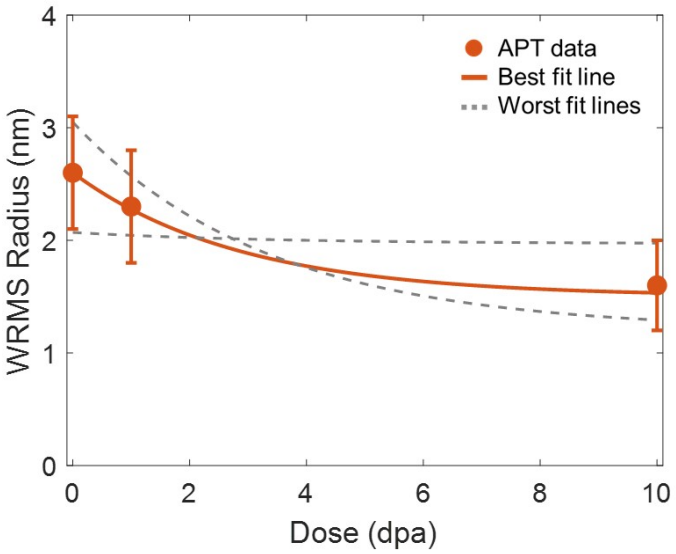

Figure 4.19 Example exponential fit (yellow solid line) with worst line fits (grey dashed lines) for error calculations of $\frac{dr}{dt}$ term in NHM-based BDP equation.

4.5 References

[1] A. Monterrosa, The Role of Pre-Implanted Helium and Carbon on Cavity Evolution in Ion-Irradiated T91, The University of Michigan, 2018. https://deepblue.lib.umich.edu/handle/2027.42/143960.

[2] J.F. Ziegler, M.D. Ziegler, J.P. Biersack, SRIM - The stopping and range of ions in matter (2010), Nucl. Instruments Methods Phys. Res. Sect. B Beam Interact. with Mater. Atoms. 268 (2010) 1818–1823. doi:10.1016/j.nimb.2010.02.091.

[3] W.A. McKinley, Jr., H. Feshbach, The Coulomb scattering of relativistic electrons by nuclei, Phys. Rev. 74 (2021) 1759–1763.

[4] P.G. Lucasson, R.M. Walker, Production and recovery of electron-induced radiation damage in a number of metals, Phys. Rev. 127 (1962) 485–500. doi:10.1103/PhysRev.127.485.

[5] D.J. Larson, T.J. Prosa, R.M. Ulfig, B.P. Geiser, T.F. Kelly, Local Electrode Atom Probe Tomography, 2013. doi:10.1007/978-1-4614-8721-0.

Chapter 5: Experimental Results

This chapter presents the results of the characterization of the irradiation experiments described in Chapter 4. The results are separated into four sections, the first based on establishing the α' precipitates in the samples and the remaining sections based upon cascade size variation. The first section describes the proton irradiations conducted to establish the α' precipitate population within the samples. The second section focuses on the heavy ion irradiations of the α' precipitate population and as received 15Cr, conducted with variated damage rate. The third section is focuses on proton irradiation of the α' precipitate population in 15Cr as well as the additional proton irradiation of as received 15Cr. And the fourth section focuses on electron irradiation of α' precipitate population and as received 15Cr.

5.1 Formation of α' precipitate distribution

A thorough analysis was conducted for the two proton irradiations conducted to establish the α' precipitate population within the samples. For both P18 and P19, APT liftouts were taken from at least two grains for variation. It was also ensured that an excess of 200-300 α' precipitates were analyzed in order to eliminate statistical variance, as it was important the starting α' precipitate microstructure was thoroughly understood. Although both proton irradiations were conducted at the same conditions, there was still variation in the precipitate microstructure between P18 and P19. For P18, the α' precipitate microstructure had an average size of 2.5±0.5nm with a density of 7.4±0.4 $x10^{23}$ m^{-3}, whereas for P19 the average radius was 2.7±0.6nm with a density of 4.7±0.2 $x10^{23}$ m^{-3}. There is no large difference in the chromium concentration of the precipitate (86.2±6.3at% and 85.3±5.7at%, respectively). Consequently, as a result in the difference of the number density, the volume fraction is also lower for P19 at 0.045 compared to 0.055 for P18. The results are shown in Table 5.1. Figure 5.1 shows representative reconstruction volumes for P18 and P19, showing the atom maps, indexed clusters, and isosurfaces each used for analysis. The

size and Cr concentration distributions for both P18 and P19 are shown in Figure 5.2. The size distributions were gaussian in shape. The core Cr concentration distribution was also gaussian.

In addition to analyzing the α' microstructure at ~600nm depth for comparison between P18 and P19, P19 was analyzed at depths corresponding to the ROIs for the 1.5 MeV proton irradiation and the 1.25 MeV electron irradiations. There were three total depths analyzed for P19, as P19 was the proton irradiation sample set that would be used for one 4.4 MeV heavy ion irradiation, all 1.5 MeV proton, and all electron irradiations. These depths, and corresponding damage rates, are provided in Table 5.2. The first depth, called "ROI 1" for this analysis, was at ~600 nm depth and corresponds to the heavy ion irradiation depths as well as approximately the depth used for P19+E/4.6e-4/0.46. ROI 1 analysis was compared to P18 in Table 5.1. The second depth analyzed, called "ROI 2" for this analysis, was at ~6 μm depth correlating to the depth for P19+E/1e-3/1. And the last depth analyzed, called "ROI 3", was at ~11 μm, correlated with the 1.5 MeV proton irradiation ROI depth as well as approximately the depth APT needles were made for P19+E/1e-4/1. The damage rate between ROI 1 and ROI 2 are similar at about 0.6-0.7x10^{-5} dpa/s and is about half that as at ROI 3 (~1.0x10^{-5} dpa/s). Figure 5.4 shows the damage rate curve produced with SRIM and the ROIs with respect to the depth of irradiation. Table 5.3 provides the APT analysis between the ROIs of interest in P19.

There is little observed difference between the initial α' microstructure in P19 between the ROIs. The average size ranged between 2.3±0.5 nm to 2.8±0.7 nm and the number density ranged from 4.1±0.4 to 8.1±0.9 x10^{23} m^{-3}. Representative APT atom maps for each ROIs are shown in Figure 5.3.

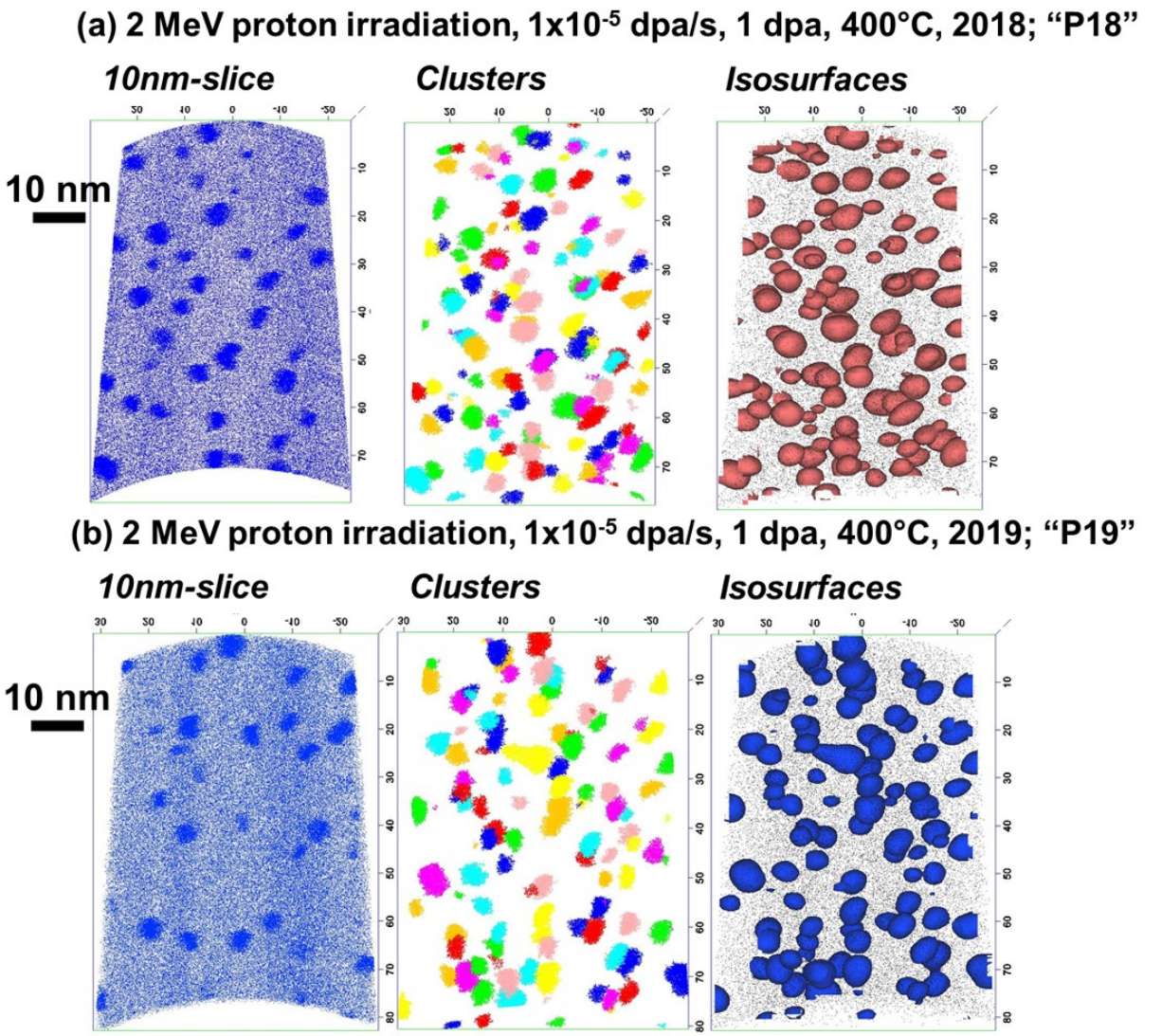

Figure 5.1. Atom probe distribution maps of α' precipitates in the established α' precipitate populations formed after 2 MeV proton irradiation at 1x10^{-5} dpa/s to 1 dpa at 400°C, where (a) is P18, and (b) is P19. The left image is an atom distribution of 100% Cr atoms in 10nm thick slice through reconstruction volume, middle image is the indexed clusters, and right image is the Cr isosurface at 30%Cr (and 0.5%Fe atom as black dots).

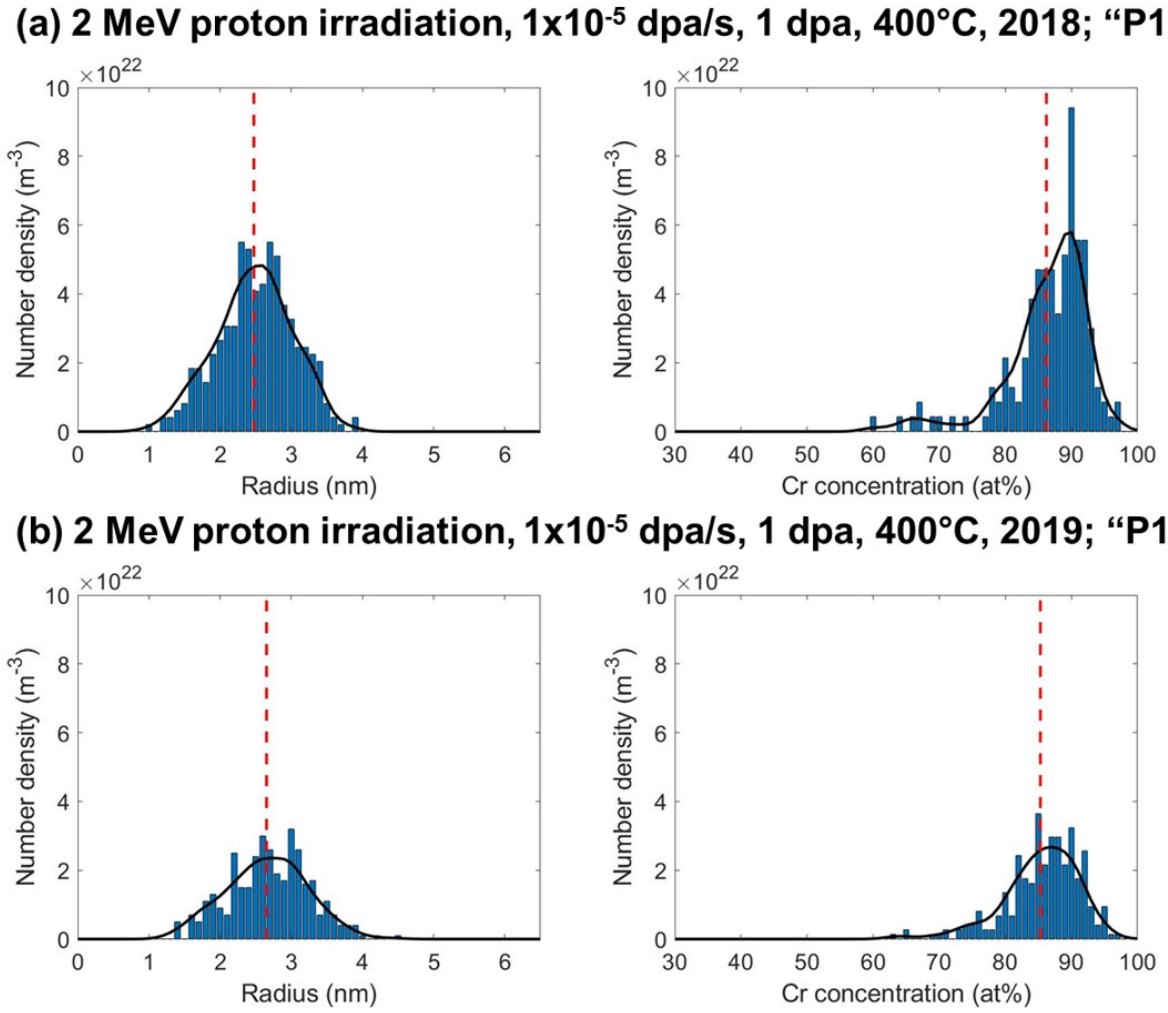

Figure 5.2. α' size and Cr concentration distributions in the established α' precipitate populations formed after 2 MeV proton irradiation at 1x10^{-5} dpa/s to 1 dpa at 400°C for (a) P18, and (b) P19. A black line shows the size distribution, and the average size or concentration is indicated as the vertical red dashed lined.

Table 5.1 Summary of α' morphology and chemistry using APT for the established α' precipitate population after 2 MeV proton irradiation at $1x10^{-5}$ dpa/s to 1 dpa at 400°C for P18 and P19.

	Formation of α' precipitate population	
Sample designation	P18	P19
Damage rate	$1x10^{-5}$ dpa/s	$1x10^{-5}$ dpa/s
Dose	1 dpa	1 dpa
# LEAP tips analyzed	6	8
# Whole clusters measured	320	260
# Total clusters measured	221	406
Analysis volume (m^{-3})	5.70×10^{-22}	1.00×10^{-21}
Average radius (nm)	2.5 ± 0.5	2.7 ± 0.6
Density ($x10^{23}$ m^{-3})	7.4 ± 0.3	4.7 ± 0.2
Volume fraction	0.054	0.044
Matrix concentration (at%)	12.2 ± 0.8	12.9 ± 0.6
α' concentration (at%)	86.2 ± 6.3	85.3 ± 5.7

Table 5.2 Description of APT analysis for P19 at other sample depths corresponding to future irradiation (heavy ion, proton, electron).

Sample descriptor	Information	Depth	Damage rate
ROI 1	Heavy ion irradiation ROIs P19+E/4.6e-4/0.46	~600 nm	~0.6×10^{-5} dpa/s
ROI 2	P19+E/1e-3/1	~6 μm	~0.7×10^{-5} dpa/s
ROI 3	1.5 MeV proton irradiation ROI P19+E/1e-4/1	~11 μm	~1.0×10^{-5} dpa/s

Table 5.3 Summary of α' morphology and chemistry using APT for P19 at varying depths of interest. ROI 1 relates to the heavy ion irradiation depth at ~600 nm below surface; ROI2 relates to electron irradiation at $1x10^{-3}$ dpa/s depth at ~6 μm below surface; and ROI 3 relates to 1.5 MeV proton irradiation depth and electron irradiation at $1x10^{-4}$ dpa/s depth at ~11 μm below the surface.

	ROI 1/ "P19" ~600 nm depth	ROI 2 ~ 6 μm depth	ROI 3 ~11 μm depth
# LEAP tips analyzed	8	1	1
# Whole clusters measured	260	79	68
# Total clusters measured	406	129	106
Analysis volume (m^{-3})	1.00×10^{-21}	$1.1x10^{-22}$	$2.5x10^{-22}$
Average radius (nm)	2.7 ± 0.6	2.3 ± 0.5	2.8 ± 0.7
Density ($x10^{23}$ m^{-3})	4.7 ± 0.2	8.1 ± 0.9	4.1 ± 0.4
Volume fraction	0.044	0.045	0.039
Matrix concentration (at%)	12.9 ± 0.6	12.4 ± 1.2	12.7 ± 1.8
α' concentration (at%)	85.3 ± 5.7	89.2 ± 5.6	83.5 ± 4.5

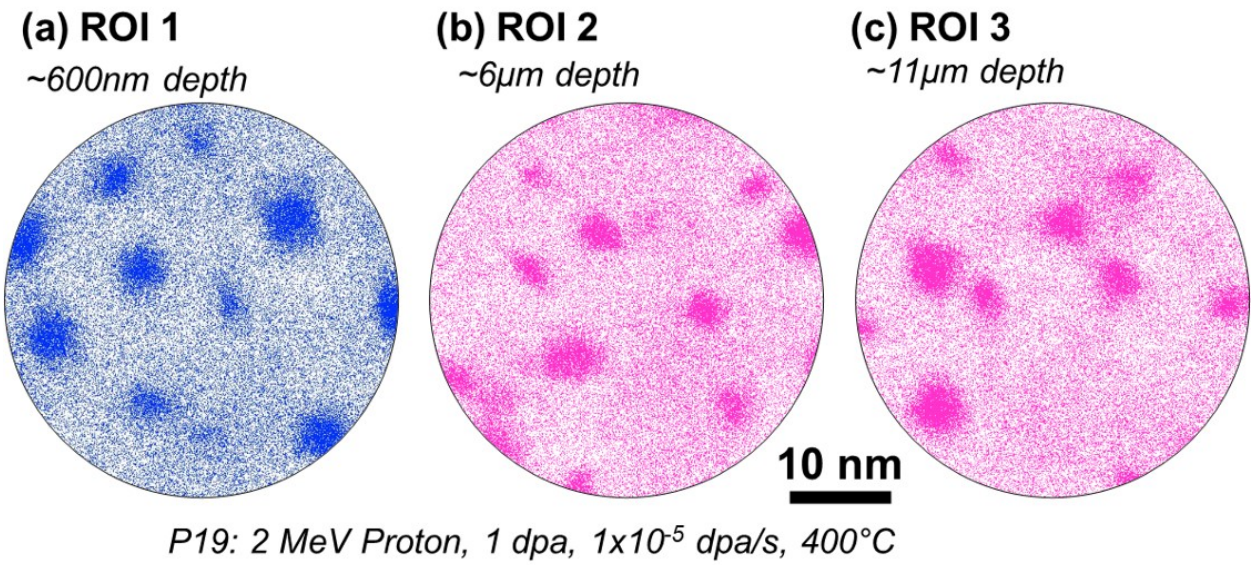

Figure 5.3 10nm thick slice Cr atom map for each region of interest for P19, where (a) is ROI 1, or about ~600nm depth, (b) is ROI 2 at about 6 um depth, (c) is ROI 3 at ~11 um depth.

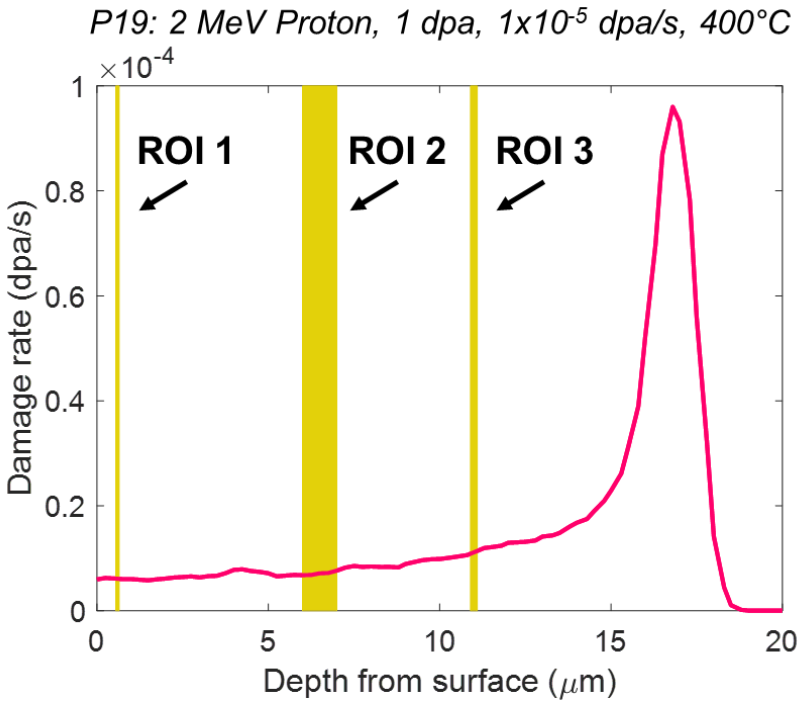

Figure 5.4 Representation of where the P19 initial microstructure was analyzed before irradiation on the damage rate curve from SRIM (pink), and highlighted areas corresponding to the depths where P19 was analyzed (yellow).

5.1.1 Other microstructural features in the initial condition

Both P18 and P19 samples were imaged using STEM-BF to observe other features in the microstructure after the initial proton irradiation to 1 dpa. Figure 5.5(a) and (b) show representative BF STEM images of the microstructure of P18. Both a<100> and a/2<111> loops were observed, with heterogeneous distribution throughout the microstructure. The average dislocation loop diameter was 14.9 ± 9.1 nm at a total density of about 6.5±0.7 $x10^{20}$ m^{-3}. The a<100> loops were found to be more ~2 times more prevalent than the a/2<111> loops.

No cavities were observed in either P18 or P19.

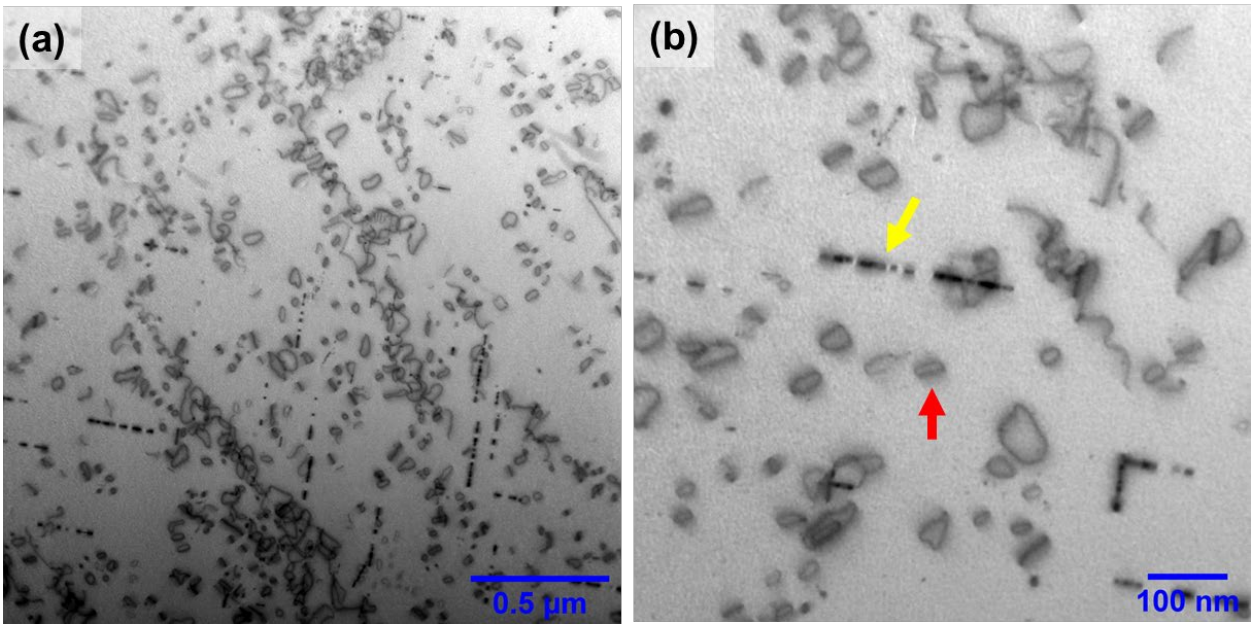

Figure 5.5 Observations of loop microstructure after 2 MeV proton irradiation at 1 dpa with STEM-BF imaging near zone axis (100) in (a), and (b) provides a closer look. An example of edge-on a<100> type dislocation loops are indicated in the yellow arrow and a/2<111> type dislocation loops are indicated in the red arrow.

5.2 Heavy ion irradiation

This section will be further divided into two sections: the effect of heavy ion damage and damage rate on α' stability and the effect of heavy ion damage and damage rate on α' precipitation.

5.2.1 α' stability under heavy ion irradiation

As the P18 samples were alumina coated in addition to use of the cold trap during irradiation as carbon uptake preventative measures, there was minimal carbon uptake observed and no major carbon clustering. Additionally, there were no other clusters observed or clustering of other solutes associated with the α'.

The average α' cluster size for each heavy ion irradiation is provided in Table 5.4. After 1 dpa for all damage rates, the average α' radius decreased to a similar size. But by 10 dpa, the α' was completely dissolved at the higher damage rates (P18+H/3e-4/10 and P18+H/1e-3/10), whereas the lowest damage rate (P18+H/1e-4/10) the α' was significantly reduced in size to 1.5±0.4 nm. Figure 5.6 shows the size distribution for each condition. Additionally, a red dashed line indicates the average precipitate size. The number density and volume fraction are also calculated and given in Table 5.4. Under heavy ion irradiation, the number density increases slightly, and volume fraction decreases at 1 dpa; by 10 dpa, the volume fraction is reduced even more so, and the number density has increased, where sample P18+H/1e-4/10 (at 10^{-4} dpa/s) a volume fraction of 0.018 and number density of 10.1±0.6 x10^{23} m^{-3}. The average α' core concentration is also provided in Table 5.4. Figure 5.7 shows the core concentration distributions for each heavy ion irradiation of pre-existing α' precipitates, again with distributions shown in black lines and the red dashed line representing the average Cr concentration. After 1 dpa, the core Cr concentration was significantly affected for all damage rates, broadening of the distribution, but retaining the gaussian shape. For all damage rates (10^{-5}-10^{-3} dpa/s) at 1 dpa, the average core Cr concentration was similar ranging from 67.2at% Cr to 84.0at% Cr. By 10 dpa at 10^{-4} dpa/s (sample P18+H/1e-4/10), the average core Cr concentration was 55.7±6.5 at%, and the distribution was retained the gaussian shape, becoming more prominent at 10 dpa. Figure 5.8 shows the evolution of the radius, number density, volume fraction, average core Cr concentration and matrix concentration with dose.

For samples P18+H/3e-4/10 and P18/1e-3/10 where there was no α' remaining in the samples, there were Cr-rich clusters determined to be radiation induced segregation (RIS). As described in Section 4.3.2, these RIS clusters were not similar to α' in morphology and were between 20-35at% Cr. In the APT atom maps for these samples in Figure 5.12 and Figure 5.13, there appears to be clustering, but it is the RIS observed in the samples. This RIS was observed in all irradiation cases, including proton and electron.

Figure 5.10-Figure 5.13 show the representative atom probe volume for each heavy ion irradiation of pre-existing α' precipitates, illustrating three cluster visualization techniques: (1) 3D atom maps of Cr, (2) isosurface construction with threshold set at 30at% Cr, (3) indexed clusters from MSM.

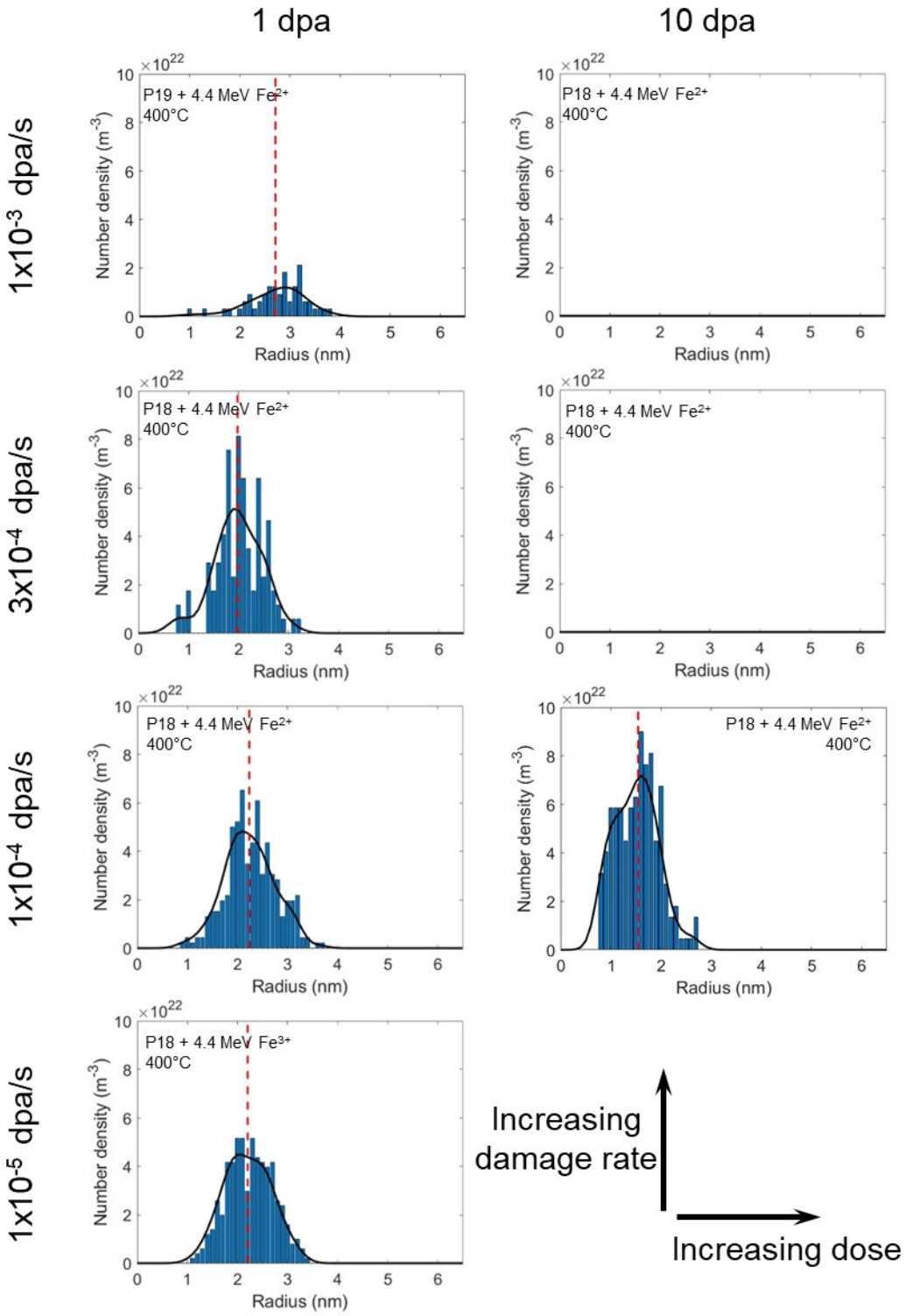

Figure 5.6 α' size distribution after heavy ion irradiation of pre-existing α' precipitates with varying damage rate and dose. A black line shows the size distribution, and the average size is indicated as the vertical dashed lined. All samples were P18+H, except for the sample at 1x10^{-3} dpa/s, 1 dpa which was P19 (P19+H/1e-3/1).

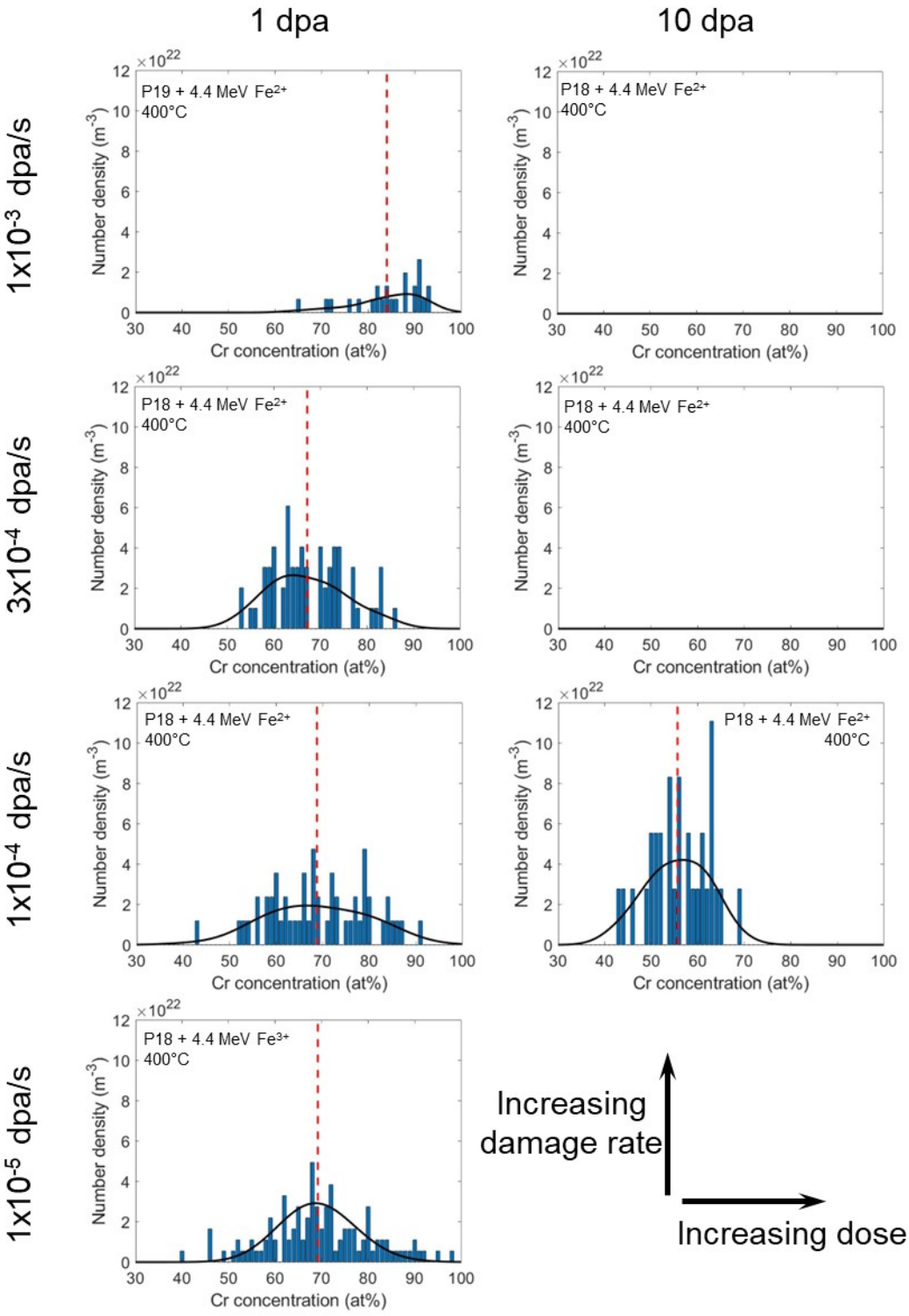

Figure 5.7 α' Cr concentration distribution for heavy ion irradiation of pre-existing α' precipitates with varying damage rate and dose. The black line shows the size distribution, and the average concentration is indicated as the vertical dashed lined. All samples were P18+H, except for the sample at 1x10^{-3} dpa/s, 1 dpa which was P19 (P19+H/1e-3/1).

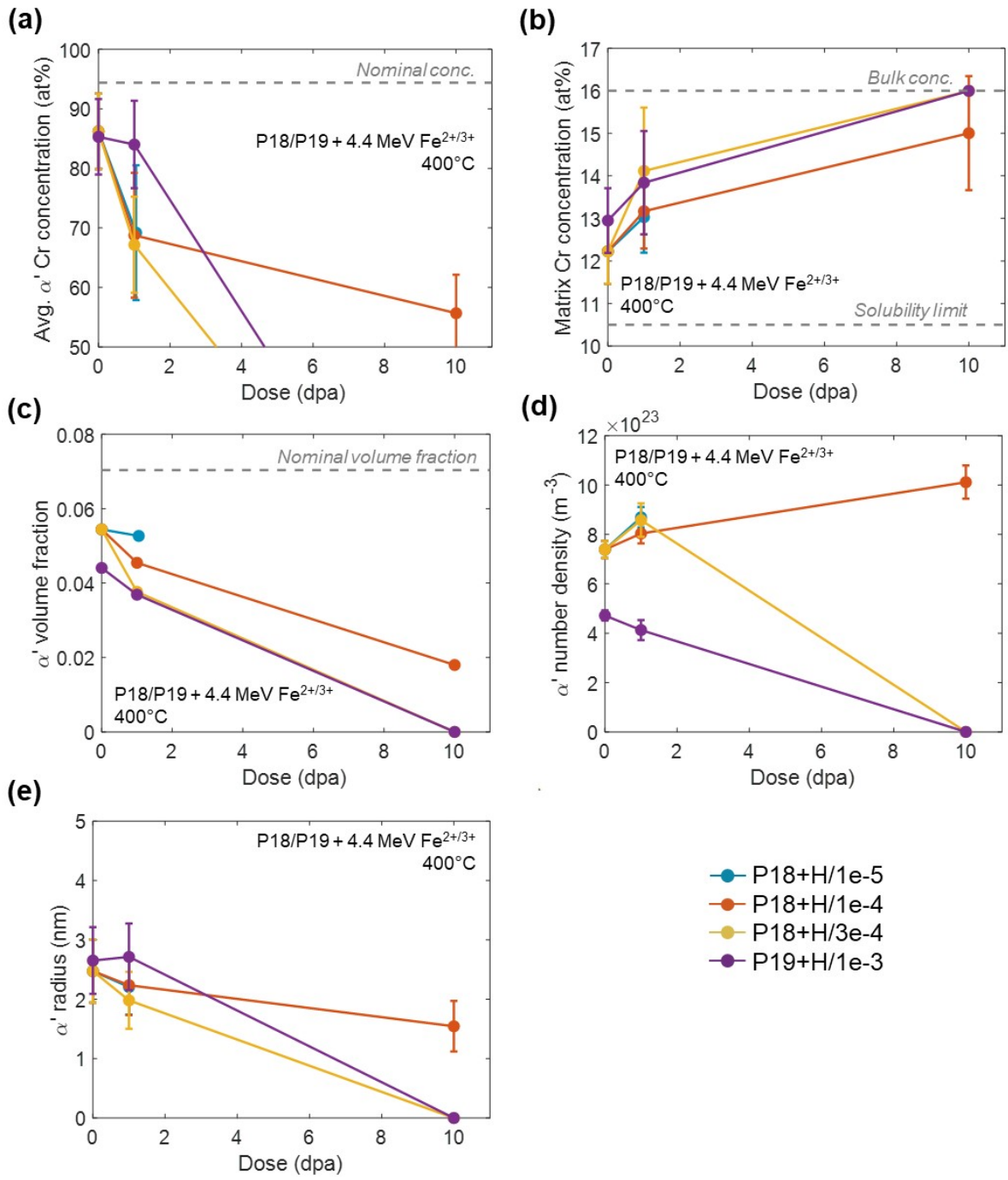

Figure 5.8 Precipitate evolution with dose under heavy ion irradiation, where (a) shows the average α' precipitate concentration, (b) shows the matrix concentration, (c) shows the volume fraction, (d) shows the number density, and (e) shows the average radius.

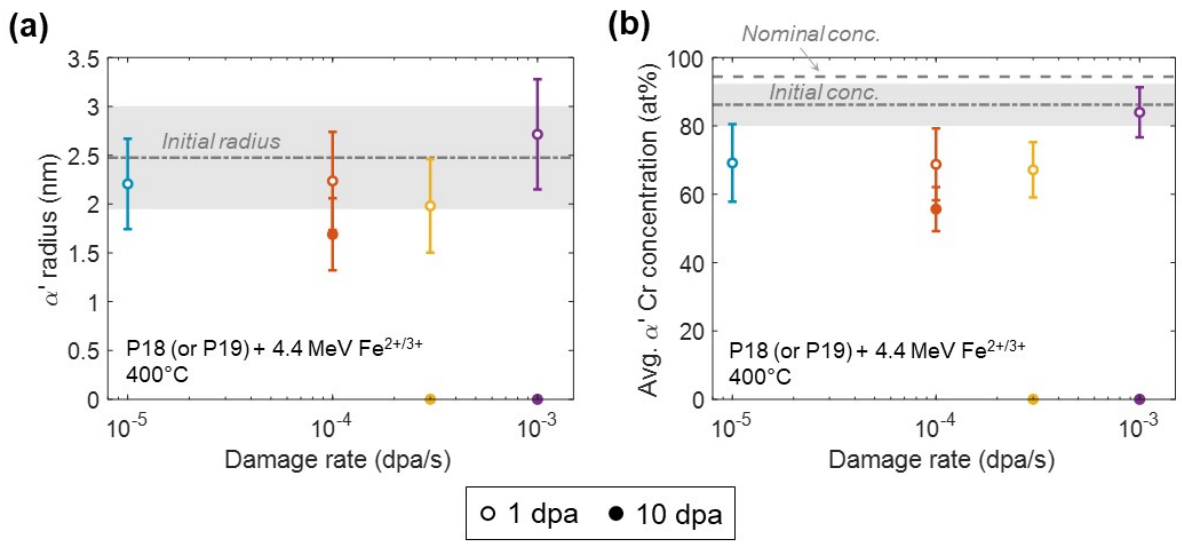

Figure 5.9 Precipitate evolution with damage rate under heavy ion irradiation, where (a) shows the average radius, and (b) shows the average α' precipitate concentration. The initial precipitate size/concentration is shown in the gray dash-dot line with error represented as the gray highlighted area. The data at 1 dpa is represented by open circles; data at 10 dpa represented by a filled circle.

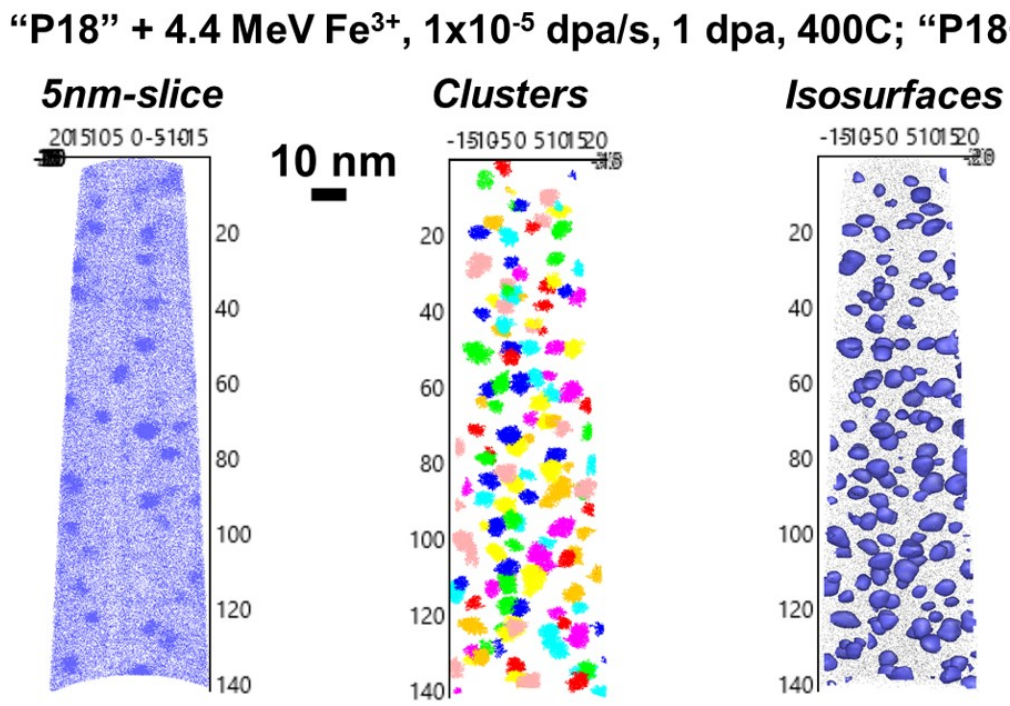

Figure 5.10 Representative atom probe volumes for P18+H/1e-5/1 (pre-existing α' precipitate microstructure subjected to 4.4 MeV Fe^{3+} irradiation at $1x10^{-5}$ dpa/s to 1 dpa), where (left) is an atom distribution of 100% Cr atoms in 5nm thick slice through reconstruction volume, (middle) image is the indexed clusters, and (right) image is the Cr isosurface at 30%Cr (and 0.5%Fe atom as black dots).

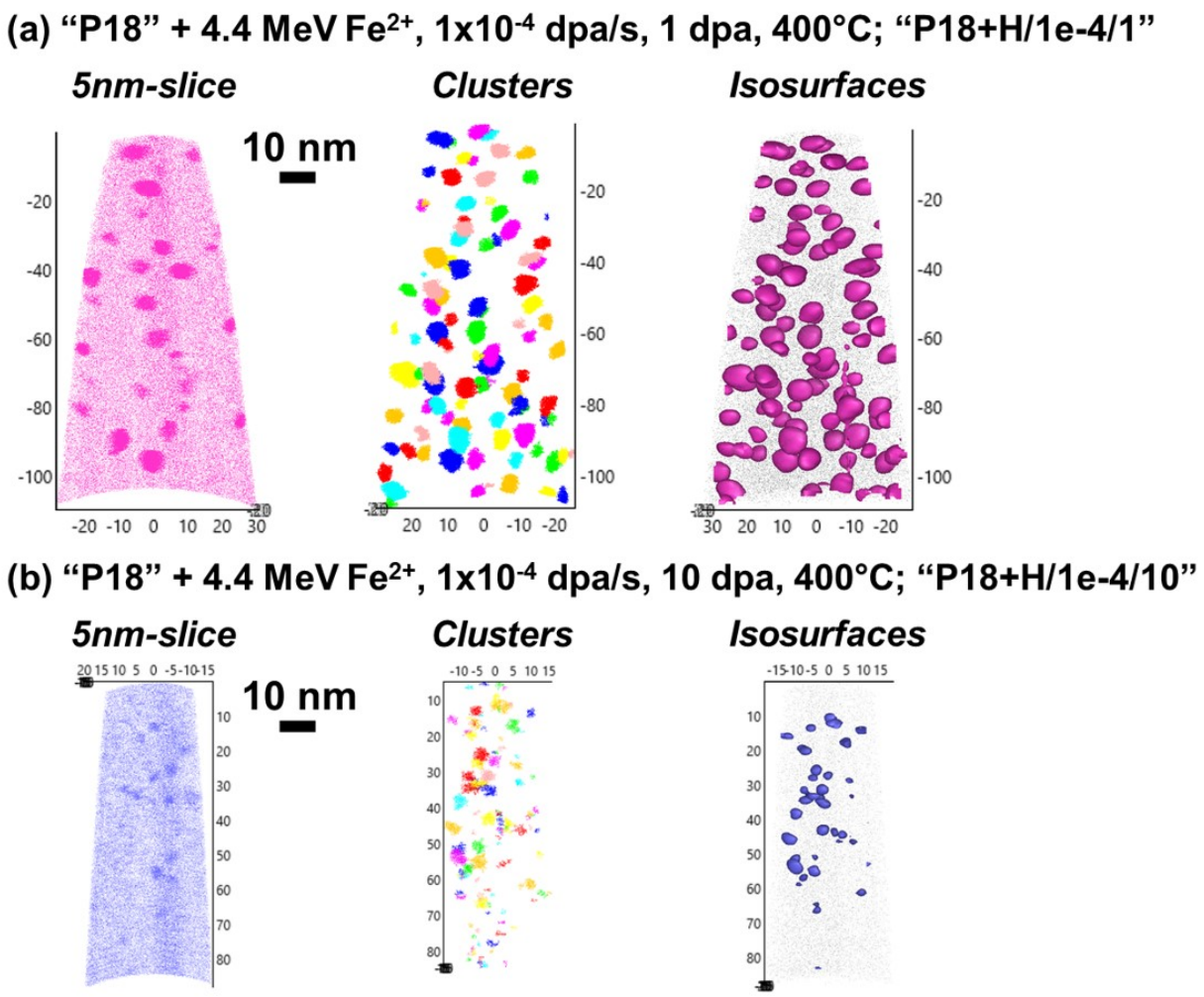

Figure 5.11 Representative atom probe volumes for (a) P18+H/1e-4/1, and (b) P18+H/1e-4/10 (pre-existing α' precipitate microstructure subjected to 4.4 MeV Fe^{2+} irradiation at $1x10^{-4}$ dpa/s), where (left) is an atom distribution of 100% Cr atoms in 5nm thick slice through reconstruction volume, (middle) image is the indexed clusters, and (right) image is the Cr isosurface at 30%Cr (and 0.5%Fe atom as black dots).

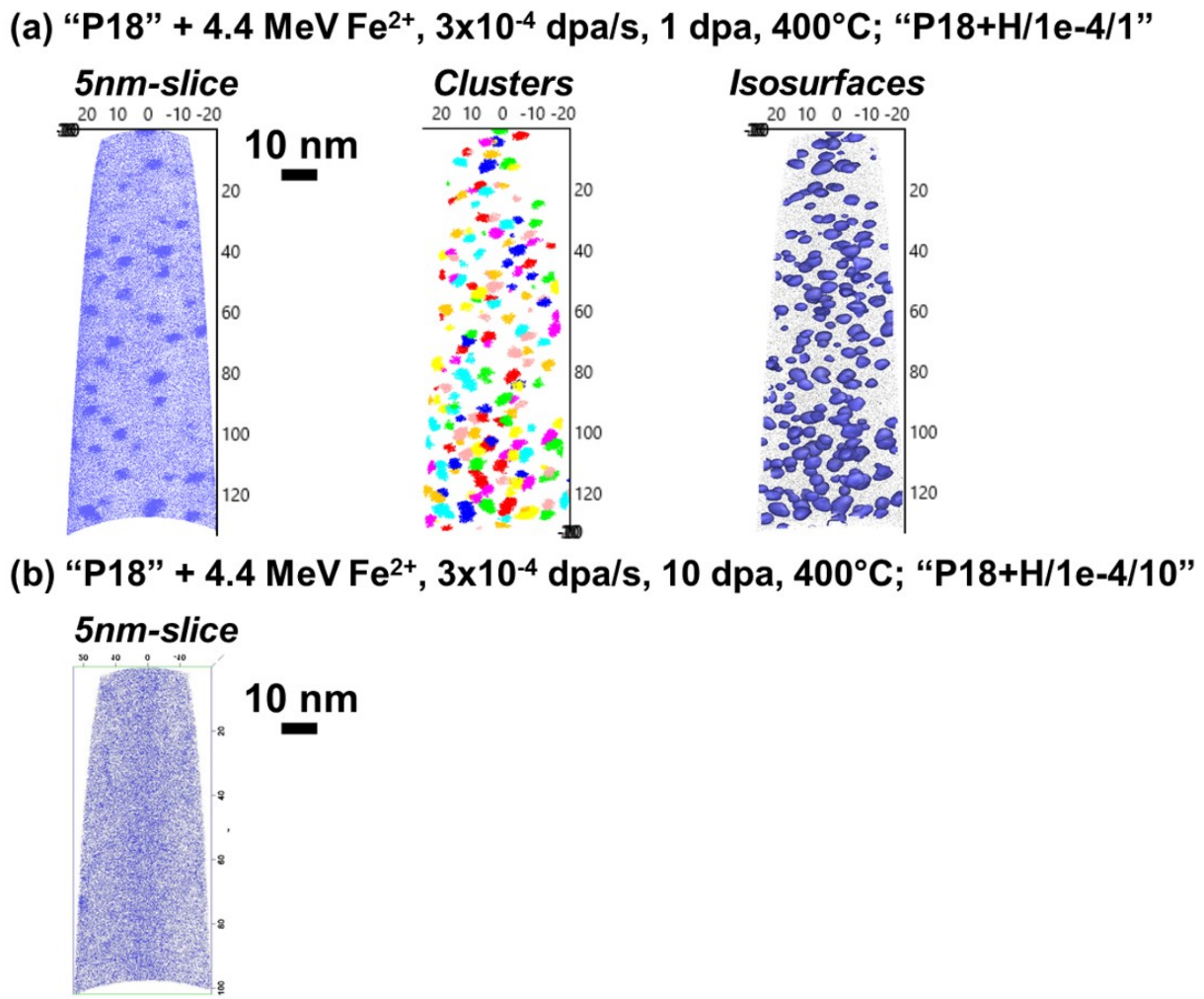

Figure 5.12 Representative atom probe volumes for (a) P18+H/3e-4/1, and (b) P18+H/3e-4/10 (pre-existing α' precipitate microstructure subjected to 4.4 MeV Fe^{2+} irradiation at $3x10^{-4}$ dpa/s), where (left) is an atom distribution of 100% Cr atoms in 5nm thick slice through reconstruction volume, (middle) image is the indexed clusters, and (right) image is the Cr isosurface at 30%Cr (and 0.5%Fe atom as black dots).

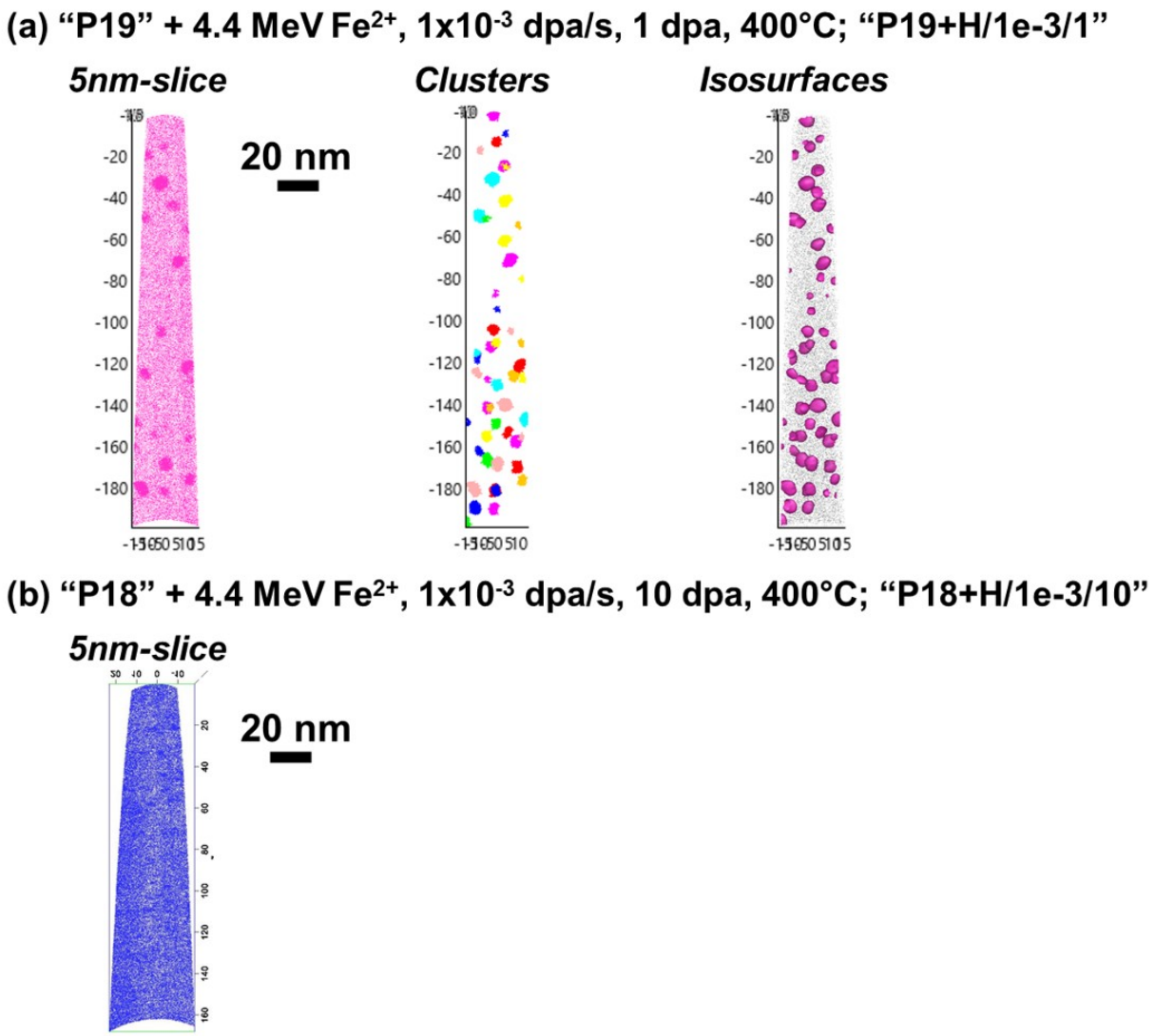

Figure 5.13 Representative atom probe volumes for (a) P19+H/1e-3/1, and (b) P18+H/1e-3/10 (pre-existing α' precipitate microstructure subjected to 4.4 MeV Fe^{2+} irradiation at $1x10^{-3}$ dpa/s), where (left) is an atom distribution of 100% Cr atoms in 5nm thick slice through reconstruction volume, (middle) image is the indexed clusters, and (right) image is the Cr isosurface at 30%Cr (and 0.5%Fe atom as black dots).

5.2.2 α' precipitation under heavy ion irradiation

As received samples subjected to similar heavy ion irradiation conditions were used to validate the results of the irradiated pre-existing α' population. Under heavy ion irradiation, the α' precipitates were observed to form and grow in the as-received Fe-15Cr samples at damage rates of $1x10^{-5}$ dpa/s and $1x10^{-4}$ dpa/s (AR+H/1.3e-5/3, AR+H/1e-4/1 and AR+H/1e-4/10). The α' precipitates were observed to be stable at $1x10^{-5}$ dpa/s with an average radius of 1.6±0.3 nm. At a damage rate of $1x10^{-4}$ dpa/s, the α' precipitates were observed to grow from an average size of 1.2±0.3 nm to 1.4±0.4 nm. Similarly, the solute concentration increased with dose increasing from 46.1±7.9 to 52.0±6.5. At a higher damage rate, the α' precipitates were not observed in the microstructure, matching that observed in Section 5.2.1 with the heavy ion irradiation of the pre-existing α' precipitate population at the same irradiation conditions. Table 5.4 lists the precipitate characteristics for the heavy ion irradiation of as received 15Cr, including the average size, number density, average concentration, matrix concentration, and volume fraction. Figure 5.14 shows a representative atom probe volume from each of the irradiation conditions.

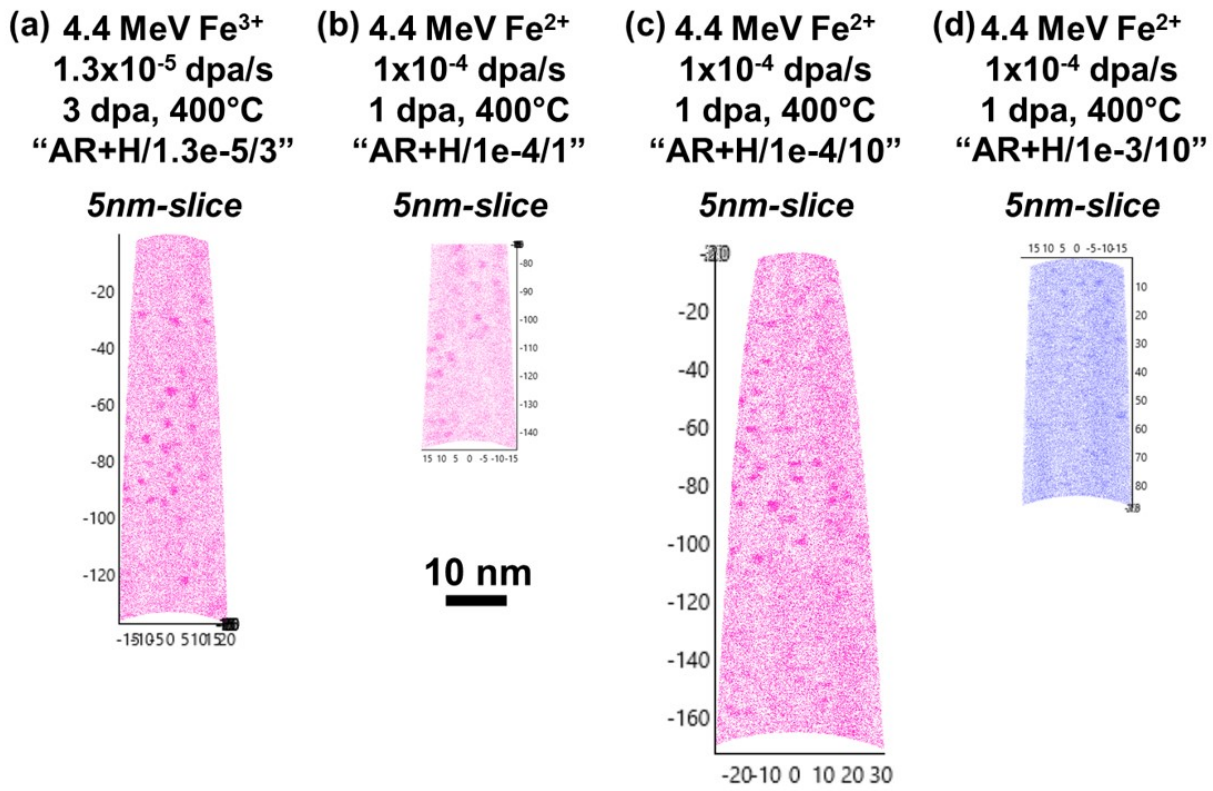

Figure 5.14 Representative atom probe volumes for 4.4 MeV $Fe^{3+/2+}$ irradiation of as-received Fe-15Cr sample at 400°C, showing 100% Cr atoms present in 5nm thick volume atom distribution for (a) AR+H/1.3e-5/3, (b) AR+H/1e-4/1, (c) AR+H/1e-4/10 (30% Cr atoms present), and (d) AR+H/1e-3/10.

Table 5.4 Summary of nanocluster morphology and chemistry using APT for heavy ion irradiation with 4.4 MeV Fe^{2+} at 400°C (P18+H/1e-5/1 was irradiated with 4.4 MeV Fe^{3+}) where samples either had pre-existing α' precipitates from P18 (or P19) or were as received condition.

	Pre-existing α'		Irradiation of pre-existing α' precipitates							Irradiation of as-received 15Cr			
Sample designation	P18	P19	P18+H/1e-5/1	P18+H/1e-4/1	P18+H/3e-4/1	P19+H/1e-3/1	P18+H/1e-4/10	P18+H/3e-4/10	P18+H/1e-3/10	AR+H/1e-5/3	AR+H/1e-4/1	AR+H/1e-4/10	AR+H/1e-3/10
Damage rate (dpa/s)	$1x10^{-5}$ dpa/s	$1x10^{-5}$ dpa/s	$1x10^{-5}$	$1x10^{-4}$	$3x10^{-4}$	$1x10^{-3}$	$1x10^{-4}$	$3x10^{-4}$	$1x10^{-3}$	$1x10^{-5}$	$1x10^{-4}$	$1x10^{-4}$	$1x10^{-3}$
Dose (dpa)	--	--	1 dpa	1 dpa	1 dpa	1 dpa	10 dpa	10 dpa	10 dpa	3 dpa	1 dpa	10 dpa	10 dpa
# LEAP tips analyzed	6	8	6	2	1	3	3	2	3	1	1	2	3
# Whole clusters measured	320	260	307	289	108	73	191	0	0	49	25	117	N.A.
# Total clusters measured	221	406	570	450	187	135	259	0	0	62	30	155	N.A.
Analysis volume ($x10^{-22}$ m^3)	5.7	10.0	5.0	4.6	1.7	2.5	2.2	2.0	3.6	0.8	0.2	1.0	N.A.
Average radius (nm)	2.5 ± 0.5	2.7 ± 0.6	2.2 ± 0.5	2.2 ± 0.5	2.0 ± 0.5	2.7 ± 0.6	1.5 ± 0.4	N.A.	N.A.	1.6 ± 0.3	1.2 ± 0.3	1.4 ± 0.4	N.A.
Density ($x10^{23}$ m^{-3})	7.4 ± 0.3	4.7 ± 0.2	8.7 ± 0.4	8.0 ± 0.4	8.6 ± 0.6	4.1 ± 0.4	10.1 ± 0.6	N.A.	N.A.	6.3 ± 0.8	17.1 ± 3.3	13.8 ± 1.2	N.A.
Volume fraction	0.054	0.044	0.053	0.046	0.038	0.041	0.018	N.A.	N.A.	0.011	0.012	0.019	N.A.
Matrix concentration (at%)	12.2 ± 0.8	12.9 ± 0.6	13.0 ± 0.8	13.2 ± 0.9	14.1 ± 1.5	13.8 ± 1.2	15.0 ± 1.3	N.A.	N.A.	16.0 ± 2.3	15.8 ± 5.1	15.3 ± 2.0	N.A.
α' concentration (at%)	86.2 ± 6.3	85.3 ± 5.7	69.2 ± 11.3	68.8 ± 10.5	67.2 ± 8.1	84.0 ± 7.4	55.7 ± 6.5	N.A.	N.A.	56.2 ± 7.1	46.1 ± 7.9	52.0 ± 6.5	N.A.

5.2.3 Other microstructural features after heavy ion irradiation

Various samples were imaged using TEM to observe other features in the heavy ion irradiated microstructure. Figure 5.15 and Figure 5.16 are representative STEM-BF images of the microstructure after heavy ion irradiation. In Figure 5.15(a) and (b) shows sample P18+H/3e-4/1 tilted off a (100) zone, highlighting the dislocation microstructure. It is clear after 1 dpa, the dislocation loop density increases, and the average size has decreased. There is an inhomogeneous spatial distribution of the loops, with small loops decorating other large dislocations. Figure 5.16(a) and (b) show sample P18+H/3e-4/10 tilted off a (100) zone, highlighting the dislocation microstructure evolution, which is similar in nature with the inhomogeneous clustering remaining. The average dislocation loop size for P18+H/3e-4/10 was 8.2 ± 4.4 nm with a total density of 8.2±1.6 $x10^{21}$ m^{-3}. The a<100> loops were found to be more ~2 times more prevalent than the a/2<111> loops.

EDS intensity maps were also collected for multiple damage rates to identify radiation induced segregation to dislocation loops or lines. Figure 5.17 is a representative EDS intensity map from P18+H/1e-3/10. The intensity maps confirm the presence of the Cr-rich clusters in the alloy after α' is dissolved, as indicated in APT. The concentration is low, typically ~25-35at%, and located on dislocation loops, similar to the results found with APT discussed in Section 5.2.1.

Cavities were not observed in any heavy ion irradiated condition.

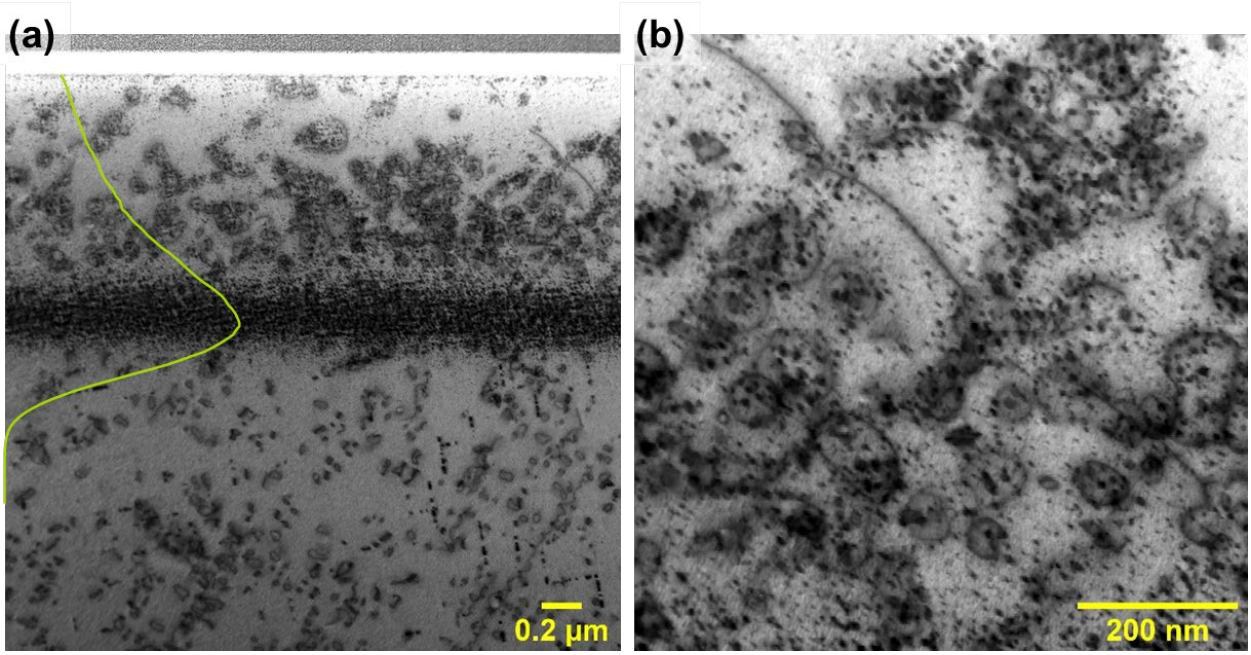

Figure 5.15 Observations of loop microstructure after heavy ion irradiation in sample P18+H/3e-4/1 with STEM-BF imaging near a (100) zone axis in (a), and (b) provides a closer look. The damage profile (green line) is overlaid on (a).

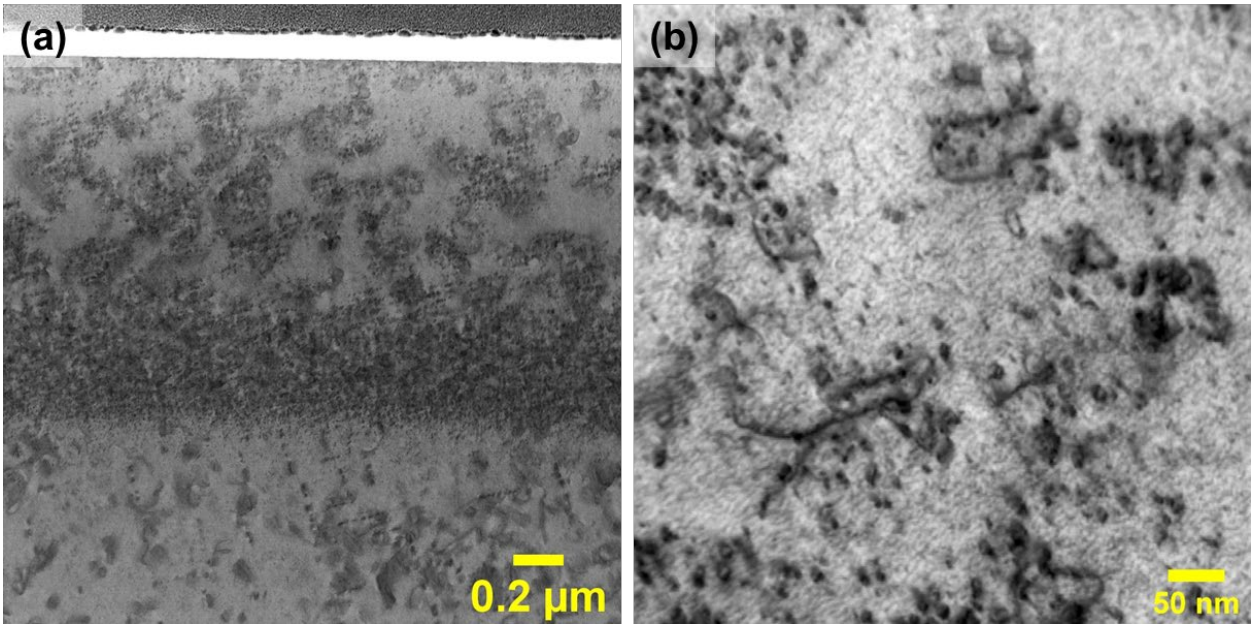

Figure 5.16 Observations of loop microstructure after heavy ion irradiation in sample P18+H/3e-4/10 with STEM-BF imaging near zone axis (100) in (a), and (b) provides a closer look.

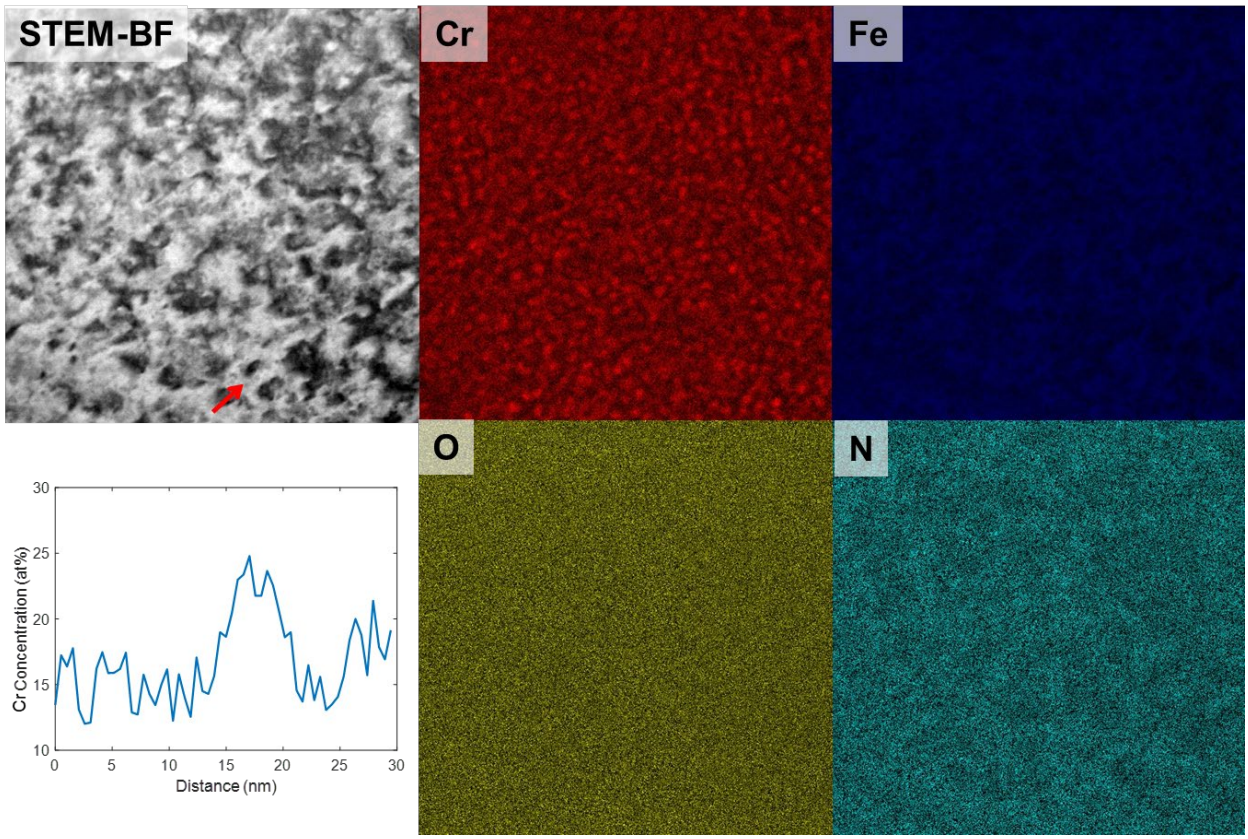

Figure 5.17 Respective STEM-BF image and Kα X-ray spectra maps for Cr and Fe in P18+H/1e-3/10.

5.3 Proton irradiations

The α' precipitate microstructure was observed to change substantially after proton irradiation with 1.5 MeV proton at $1x10^{-4}$ dpa/s. The α' precipitates in sample P19+P/1e-4/1 grew a small amount in size to 2.7±0.7 nm and the density decreased to 2.5±0.2 $x10^{23}$ m^{-3}. From sample P19+P/1e-4/10, the remaining α' had grown significantly in size to 3.7±1.1 nm and the density likewise dropped to 5.1±0.9 $x10^{22}$ m^{-3}. The size distributions are shown in Figure 5.18. The core Cr concentration increased with dose, increasing to 86.6±7.1at% at 1 dpa and to 89.8±5.8at%. The volume fraction correspondingly decreased, to 0.026 at 1 dpa to 0.016 at 10 dpa. The values are shown in Table 5.5.

The only proton irradiation of an as-received 15Cr sample was at $1x10^{-5}$ dpa/s to 2 dpa, AR+H/1e-5/2. The results were similar to the α' precipitate population established in 15Cr for P18 and P19 using similar conditions (except to 1 dpa). The average radius for AR+H/1e-5/2 was 2.2±0.5 nm with a density of 9.0±0.6 $x10^{23}$ m^{-3}. The average radius was smaller than that of P18 and P19 with a higher density, but all within error. The volume fraction is 0.056, which matches that of P18. The matrix concentration was 12.4±1.2at% and average α' core Cr concentration was 88.1±6.6at%, which is all within range of the 1 dpa conditions of P18 and P19. The values are provided in Table 5.5.

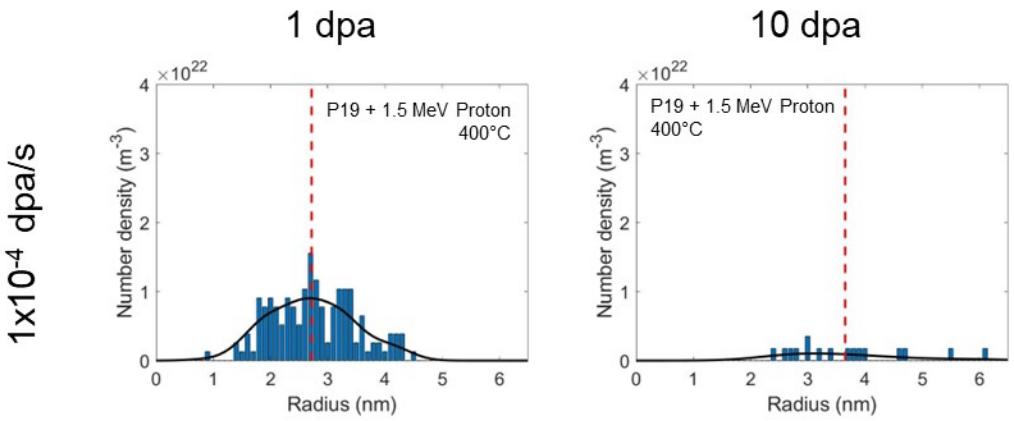

Figure 5.18 α' precipitate size distribution after proton irradiation of the pre-existing α' precipitate population at 1x10^{-4} dpa/s at (left) 1 dpa, (right) 10 dpa. Black line is the size distribution and red dashed line is the average size.

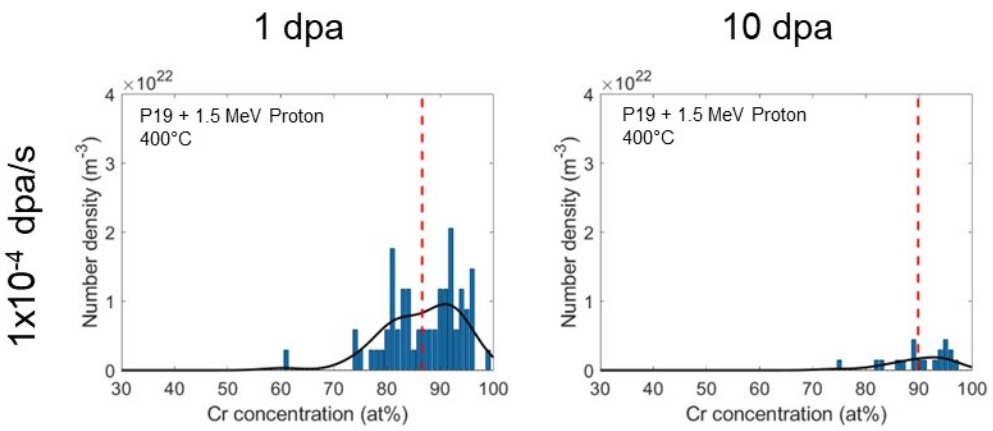

Figure 5.19 α' precipitate Cr concentration distribution after proton irradiation of the pre-existing α' precipitate population at 1x10^{-4} dpa/s at (left) 1 dpa, (right) 10 dpa. Black line is the size distribution and red dashed line is the average concentration.

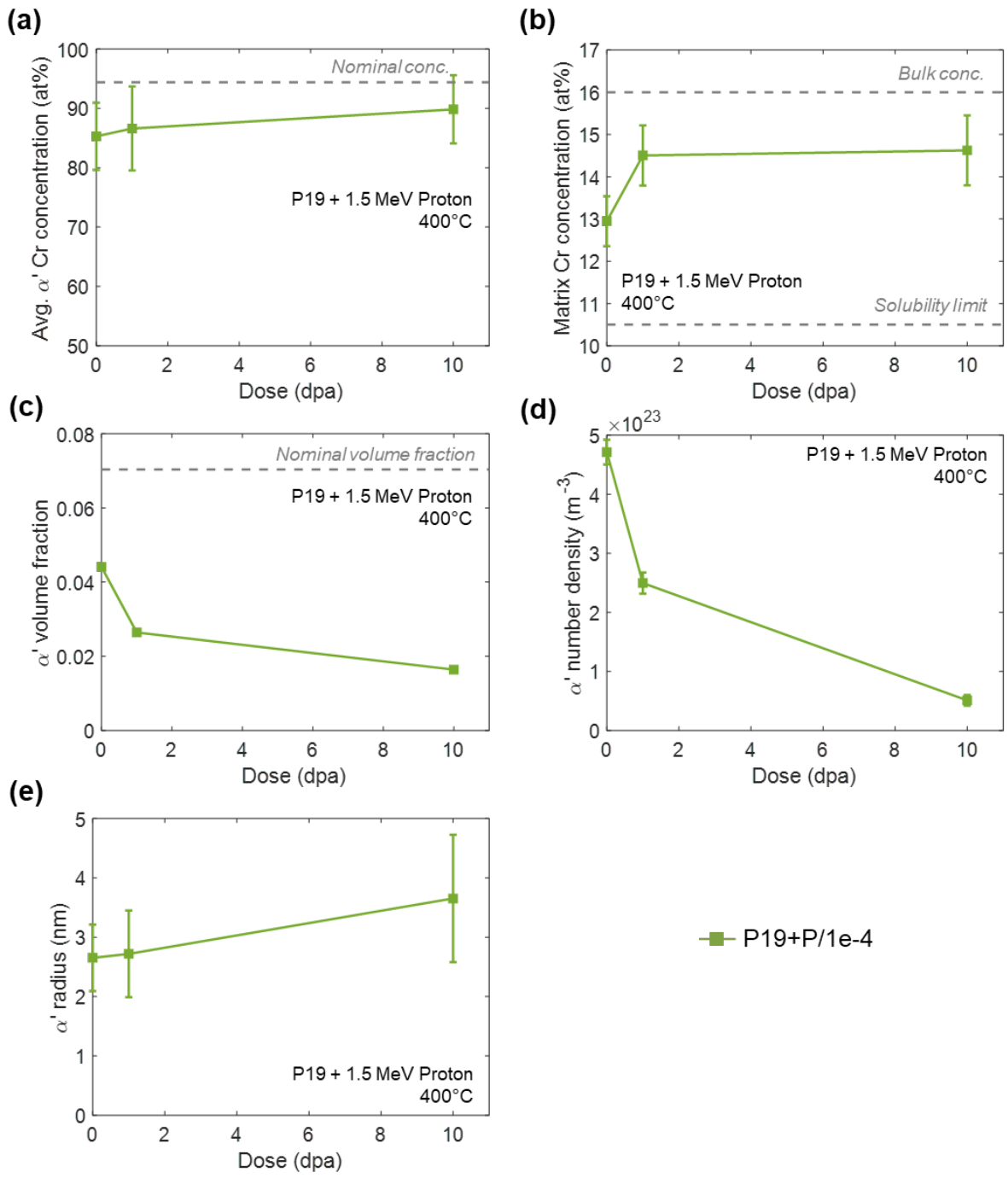

Figure 5.20 Precipitate evolution with dose under proton irradiation, where (a) shows the average α' precipitate concentration, (b) shows the matrix concentration, (c) shows the volume fraction, (d) shows the number density, and (e) shows the average radius.

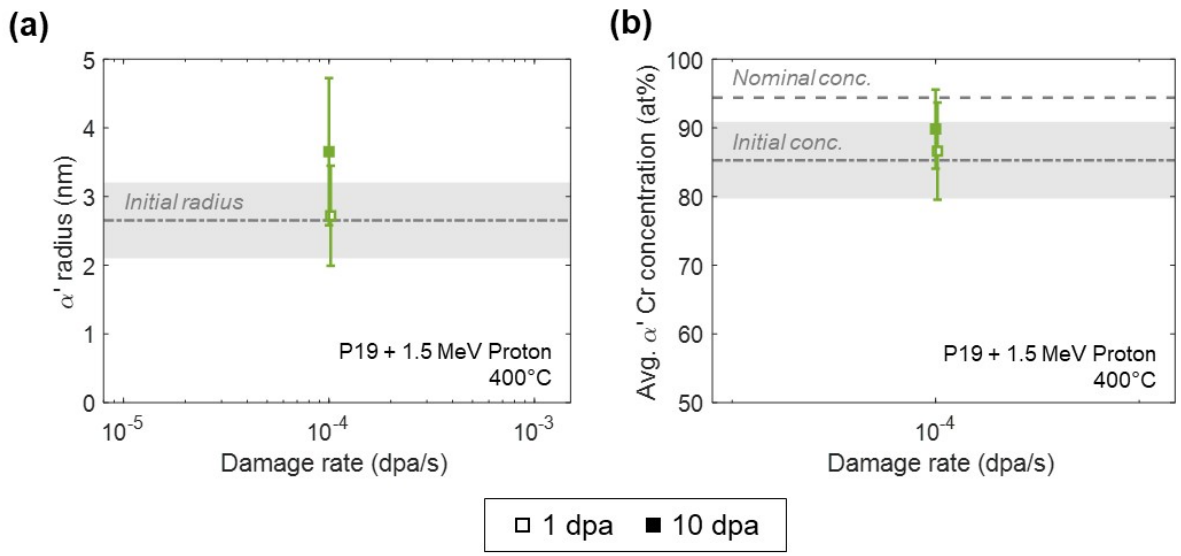

Figure 5.21 Precipitate evolution with damage rate under proton irradiation, where (a) shows the average radius, and (b) shows the average α' precipitate concentration. The initial precipitate size/concentration is shown in the gray dash-dot line with error represented as the gray highlighted area. The data at 1 dpa is represented by open square; data at 10 dpa represented by a filled square.

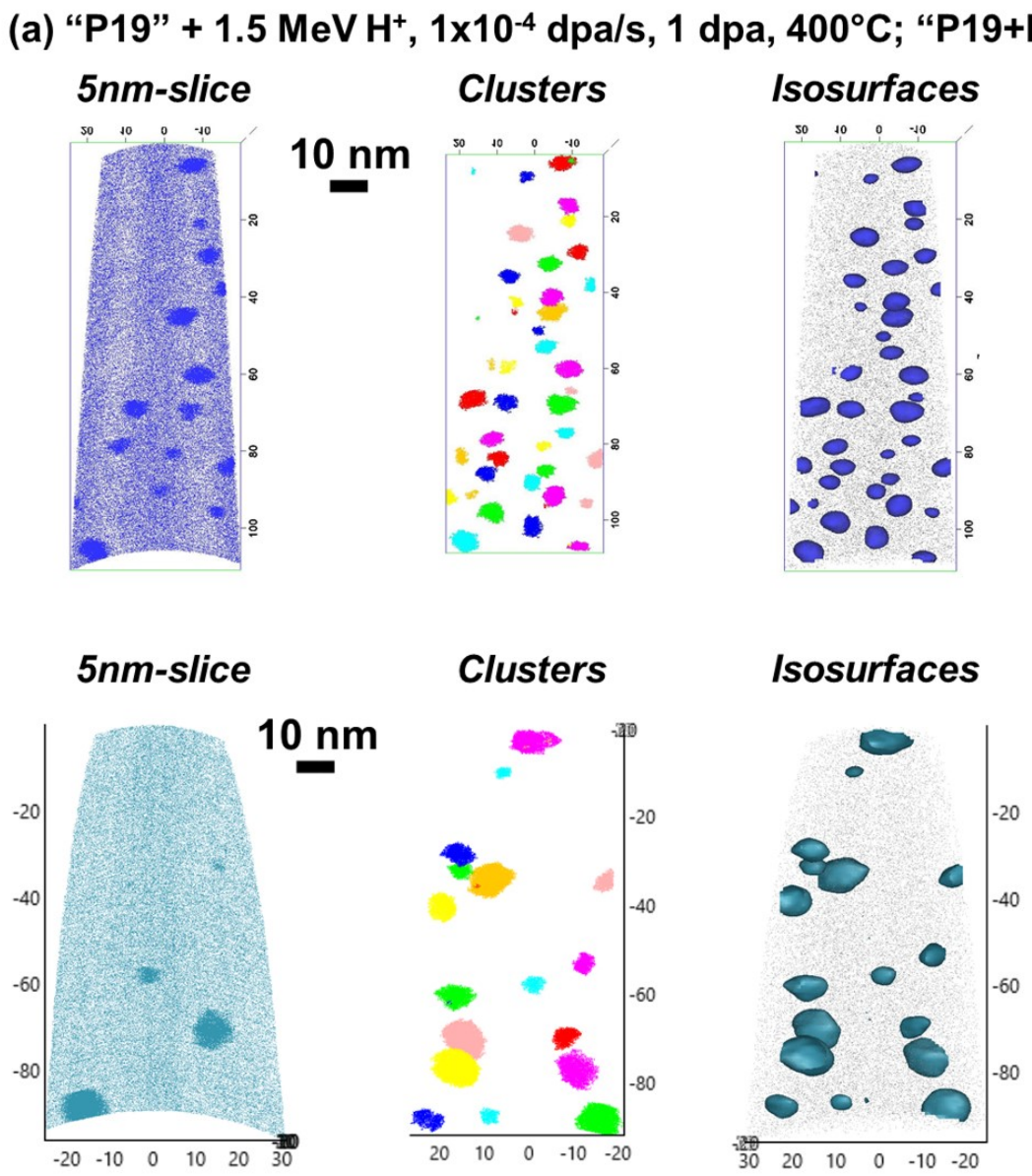

Figure 5.22 Atom probe distribution maps of α' precipitates in Fe-15Cr with an initial α' precipitate population after proton irradiation with 1.5 MeV protons at $1x10^{-4}$ dpa/s to (1) 1 dpa, and (b) 10 dpa, where (left) is an atom distribution of 100% Cr atoms in 5nm thick slice through reconstruction volume, (middle) image is the indexed clusters, and (right) image is the Cr isosurface at 35%Cr (and 0.5%Fe atom as black dots).

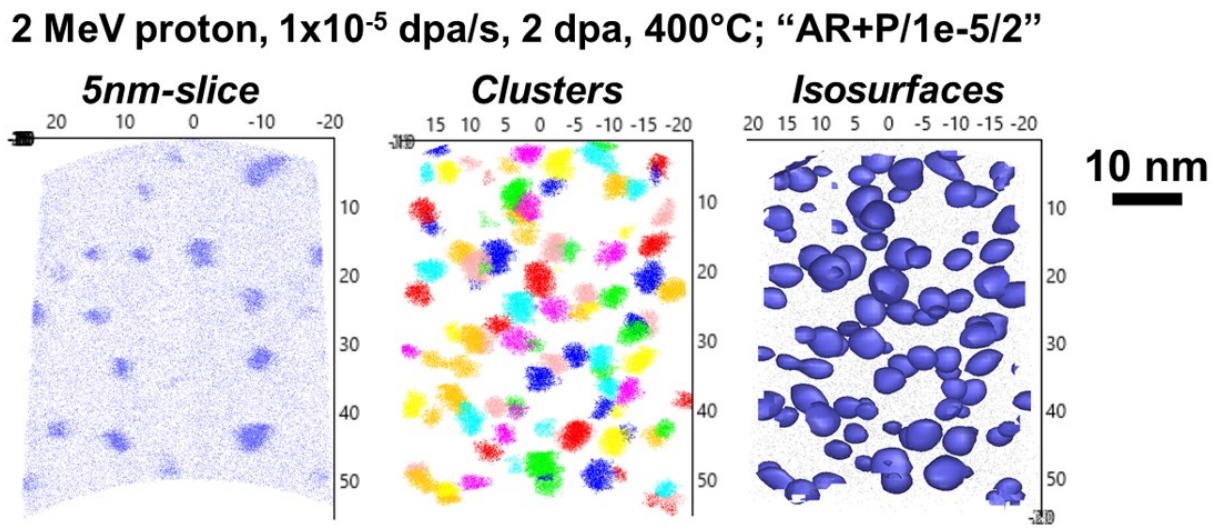

Figure 5.23 Atom probe distribution maps of α' precipitates in Fe-15Cr irradiated with 2 MeV protons at $1x10^{-5}$ dpa/s to 2 dpa at 400°C, where (left) is an atom distribution of 100% Cr atoms in 5nm thick slice through reconstruction volume, (middle) image is the indexed clusters, and (right) image is the Cr isosurface at 30%Cr (and 0.5%Fe atom as black dots).

Table 5.5 Summary of nanocluster morphology and chemistry using APT for proton irradiation of as received Fe-15Cr and pre-existing α' precipitates. The as received 15Cr was irradiated with 2 MeV protons at $1x10^{-5}$ dpa/s to 2 dpa at 400°C; the pre-existing α' precipitates were irradiated with 1.5 MeV protons at $1x10^{-4}$ dpa/s to 1 and 10 dpa at 400°C.

	Pre-existing α' precipitates	Irradiation of pre-existing α' population		Irradiation of as received 15Cr
Sample designation	P19	P19+P/1e-4/1	P19+P/1e-4/10	AR+P/1e-5/2
Damage rate (dpa/s)	$1x10^{-5}$	$1x10^{-4}$	$1x10^{-4}$	$1x10^{-5}$
Dose (dpa)	--	1	10	2
# LEAP tips analyzed	8	5	5	4
# Whole clusters measured	260	145	19	124
# Total clusters measured	406	240	26	275
Analysis volume ($x10^{-22}$ m^3)	10.0	5.7	3.8	2.2
Average radius (nm)	2.7 ± 0.6	2.7 ± 0.7	3.7 ± 1.1	2.2 ± 0.5
Density ($x10^{23}$ m^{-3})	4.7 ± 0.2	2.5 ± 0.2	0.51 ± 0.09	9.0 ± 0.6
Volume fraction	0.044	0.027	0.017	0.056
Matrix concentration (at%)	12.9 ± 0.6	14.5 ± 0.7	14.6 ± 0.8	12.4 ± 1.2
α' concentration (at%)	85.3 ± 5.7	86.6 ± 7.1	89.8 ± 5.8	88.1 ± 6.6

5.3.1 Other microstructural features under proton irradiation

After proton irradiation, TEM was used to observe the microstructural evolution in the samples. Primarily, cavities were the main feature observed. EDS mapping and dislocation images were also completed.

Cavities were observed to form under proton irradiation in samples P19+P/1e-4/1 and P19+P/1e-4/10. The cavities were observed to be faceted in shape when imaged on the zone axis. Figure 5.24 shows examples of the faceted cavities in sample P19+P/1e-4/10 with the incident beam on two different zones resulting in different observed shapes of the cavities. There was no variation in shape or truncation with size. For sample P19+P/1e-4/1, the average cavity diameter was 8.0±4.0 nm and reached an average of 19.8±10.6 by 10 dpa in sample P19+P/1e-4/10. Table 5.6 shows the measured cavity characteristics for samples P19+P/1e-4/1 and P19+P/1e-4/10 and Figure 5.25 shows the corresponding cavity distribution.

STEM-BF imaging revealed the dislocation microstructure. After proton irradiation at $1x10^{-4}$ dpa/s, the dislocations were largely composed of strings of loops. Figure 5.26(a) shows a representative micrograph for P19+P/1e-4/1 on a (100) zone, showing the long strings of loops and dislocation lines; and in Figure 5.26(b) is tilted slightly off a (110) zone also showing long strings of loops.

EDS intensity maps were also collected for P19+P/1e-4/10 to identify RIS. Figure 5.27 is a representative EDS intensity map highlighting a faceted cavity. EDS scans and intensity mapping indicated no signs of RIS to any cavities. The Cr and Fe maps indicate a heterogeneous distribution of α' precipitates in microstructure.

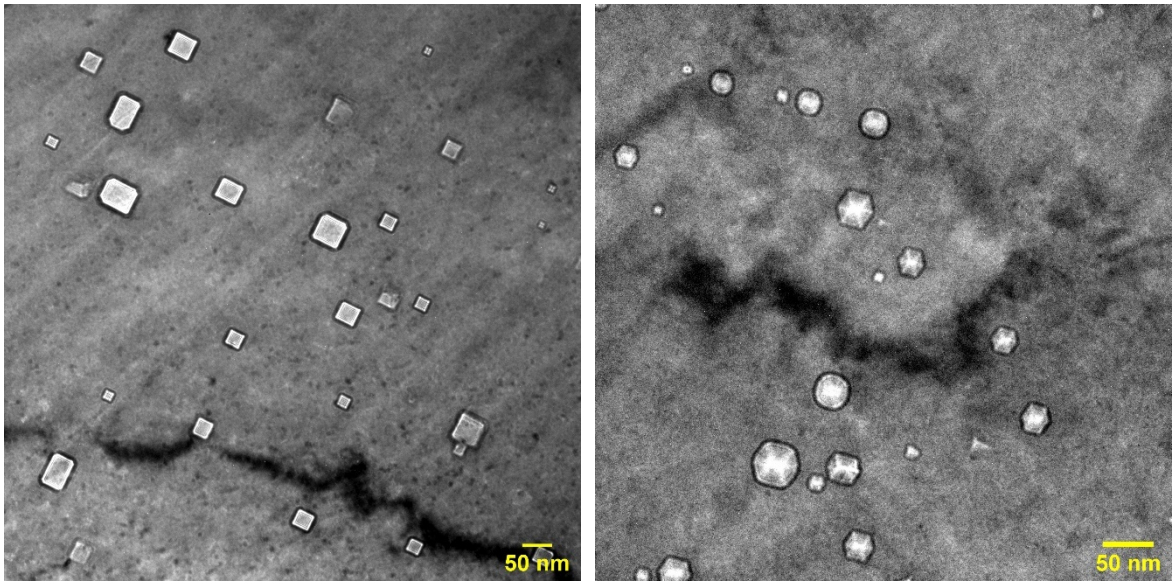

Figure 5.24 Examples of faceted cavities after 1.5 MeV proton irradiation at $1x10^{-4}$ dpa/s to 10 dpa of pre-existing α' precipitate population. (left) the incident beam is on the [100] resulting in square shape; (right) the incident beam is on the [110] resulting in the hexagonal appearance.

Table 5.6 Summary of cavity characteristics for proton irradiation of pre-existing α' precipitates at $1x10^{-4}$ dpa/s (P19+P/1e-4/1 and P19+P/1e-4/10).

Sample	# Cavities examined	Average diameter (nm)	Number density (m^{-3})	Sink Strength (m^{-2})
P19+P/1e-4/1	101	8.0 ± 4.0	2.5×10^{21}	1.5×10^{14}
P19+P/1e-4/10	519	19.6 ± 11.9	4.6×10^{20}	6.3×10^{13}

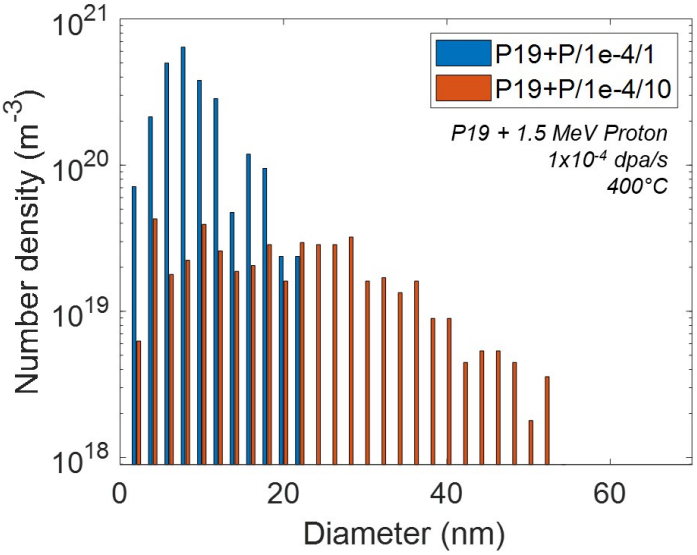

Figure 5.25 Cavity size distribution for 1.5 MeV proton irradiation of pre-existing α' precipitates at 1x10^{-4} dpa/s to 1 dpa (P19+P/1e-4/1, in blue) and 10 dpa (P19+P/1e-4/10, in 10 dpa).

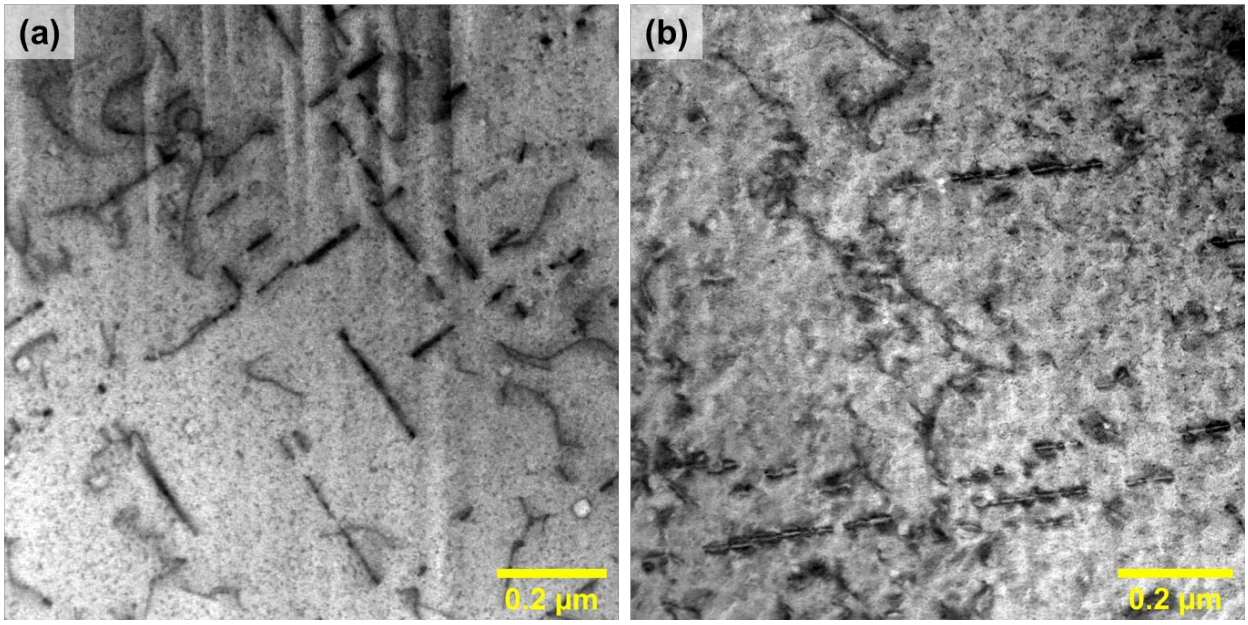

Figure 5.26 Representative STEM-BF imaging of the dislocation microstructure for 1.5 MeV proton irradiation of pre-existing α' precipitates at $1x10^{-4}$ dpa/s to (a) 1 dpa (P19+P/1e-4/1) exhibited tilted off a (100) zone, and (b) 10 dpa (P19+P/1e-4/10) exhibited tilted off a (110) zone.

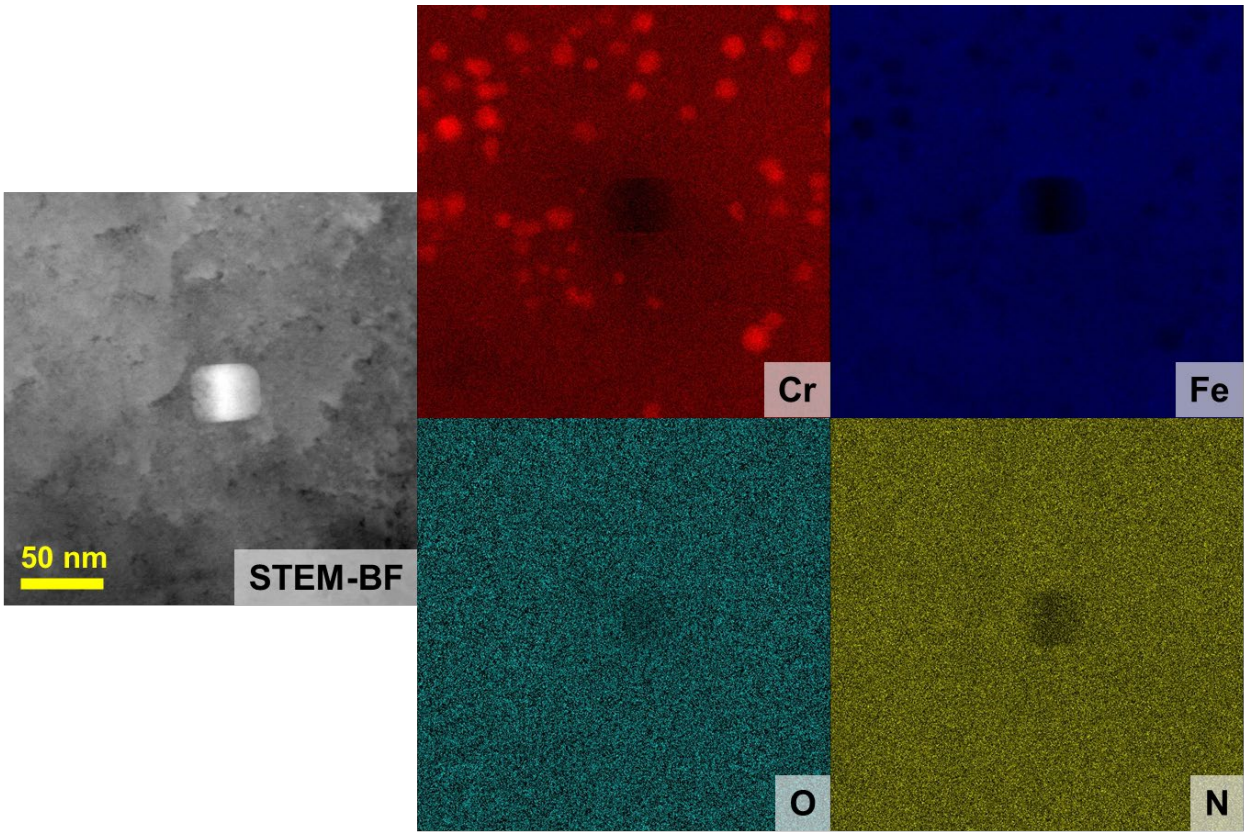

Figure 5.27 Respective STEM-BF image and Kα X-ray spectra maps for Cr, Fe, O, and N for 1.5 MeV proton irradiation of pre-existing α' precipitates at $1x10^{-4}$ dpa/s to 10 dpa (P19+P/1e-4/10).

5.4 Electron irradiations

For the electron irradiated samples, it was more desirable to run the APT needles in laser mode as opposed to voltage mode due to the high rate of early failure in voltage mode. In order to determine the parameters selected for laser mode were comparable to those used in voltage mode a series of tips were run in laser mode with varied laser energy. The base temperature, detection rate, and pulse rate remained constant between laser mode and voltage mode. Three laser pulse energies were tested: 40, 50, and 60 pJ. The samples used were from the electron irradiated sample P19+E/1e-4/1. The large irradiation area on the TEM liftout provided many APT needles which could be used to validate laser mode conditions. Figure 5.28 shows a comparison between the atom probe conditions in the iso-surface constructions. The size distribution and concentration distribution are shown in Figure 5.29, comparing voltage mode to the three laser energy modes used. Table 5.7 presents the APT analysis comparison for voltage mode and various laser modes. There was no significant difference in the distributions and the resulting chemical analysis between voltage mode and the variation in laser pulse energies. Moving forward, the remaining electron irradiated APT needles used a pulse energy of 50 pJ. Additionally, the data from voltage and laser mode collected for this sample was combined for future analysis and comparison with other irradiation conditions.

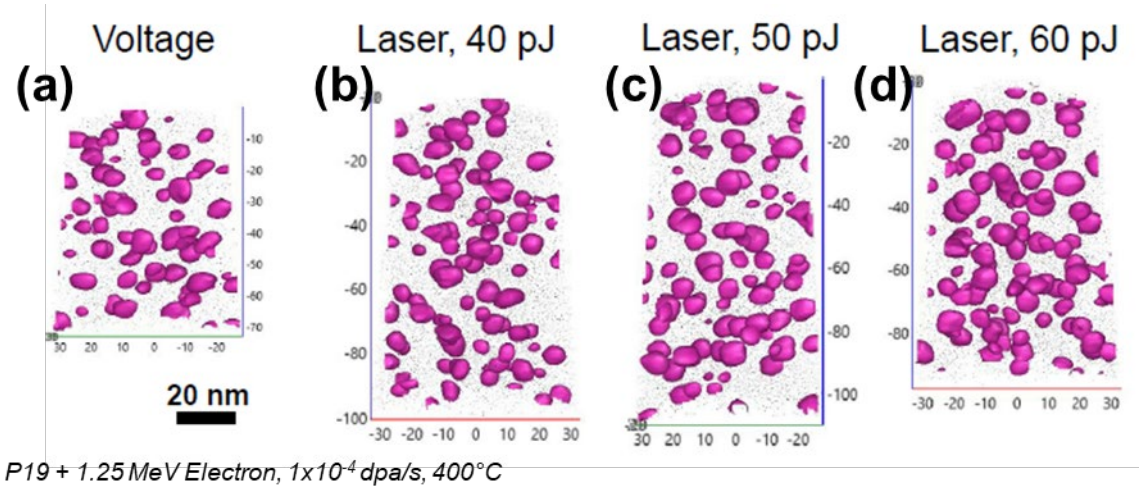

Figure 5.28. Representative atom probe volume for each analysis condition, where (a) is voltage mode, (b) is laser mode with energy 40 pJ, (c) laser mode with energy 50 pJ, and (d) is laser mode with energy 60 pJ. Iso-concentration surface is at 35%Cr; black dots are 0.2% of the Fe atoms. APT needles were from 1.25 MeV electron irradiated pre-existing α' precipitates at 1x10^{-4} dpa/s to 1 dpa at 400°C (P19+E/1e-4/1).

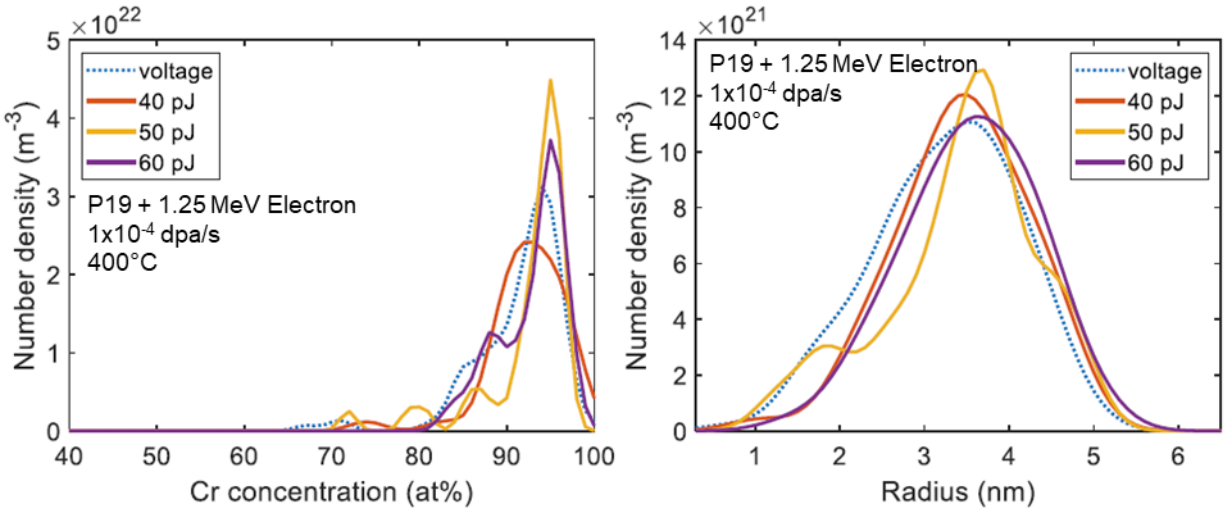

Figure 5.29. Comparison of APT analysis mode (voltage vs laser) in addition to laser energy variation, where the left image is the size distribution, and the right figure is the concentration distribution for α' precipitates. APT needles were from 1.25 MeV electron irradiated pre-existing α' precipitates at 1x10^{-4} dpa/s to 1 dpa at 400°C (P19+E/1e-4/1).

Table 5.7 Summary of nanocluster morphology and chemistry using APT comparing voltage mode to various laser mode conditions used. APT needles were from the same liftout from 1.25 MeV electron irradiated pre-existing α' precipitates at $1x10^{-4}$ dpa/s to 1 dpa at 400°C (P19+E/1e-4/1).

	Voltage mode	Laser mode, 40 pJ	Laser mode, 50 pJ	Laser mode, 60 pJ
# LEAP tips analyzed	2	1	1	1
# Whole clusters measured	139	65	41	64
# Total clusters measured	252	97	72	101
Analysis volume ($x10^{-22}$ m^3)	5.2	2.5	2.3	2.5
Average radius (nm)	3.2 ± 0.8	3.4 ± 0.7	3.4 ± 0.9	3.5 ± 0.8
Density ($x10^{23}$ m^{-3})	3.6 ± 0.3	3.2 ± 0.3	3.1 ± 0.3	3.3 ± 0.3
Volume fraction	0.036	0.040	0.039	0.043
Matrix concentration (at%)	11.9 ± 1.4	11.7 ± 1.1	12.0 ± 1.2	12.3 ± 1.2
α' concentration (at%)	91.4 ± 5.2	92.4 ± 4.3	92.4 ± 5.3	92.8 ± 3.7

5.4.1 α' stability under electron irradiation

The pre-existing α' precipitates were observed to grow after electron irradiation by 1 dpa. For all damage rates (P19+E/1e-4/1, P19+E/4.6e-4/0.46, and P19+E/1e-3/1), the α' increased in size, volume fraction, α' core Cr concentration and decreased in number density. Comparing P19+E/1e-4/1 to P19+E/1e-3/1 shows that at the higher damage rate, the α' was slightly smaller at 3.0±0.8 nm compared to 3.3±0.8 nm. The volume fraction is also reduced at 0.053 compared to 0.063. All the values are within error between the conditions, but P19+E/1e-3/1 shows a slightly stunted α' growth under electron irradiation in comparison to the other two conditions. Table 5.8 provides the α' characterization values for each electron irradiation condition for the irradiation of pre-existing α' precipitates and irradiation of as received samples. The corresponding size and Cr concentration distributions are shown in Figure 5.30 and Figure 5.31, respectively. And Figure 5.32 shows the precipitate evolution trends for average α' concentration, matrix concentration, volume fraction, and number density for each electron irradiation.

Table 5.8 Summary of nanocluster morphology and chemistry using APT for electron irradiation with 1.25 MeV electrons at 400°C. Table includes data for irradiation of 15Cr samples with pre-existing α' and as received 15Cr.

	Pre-existing α' precipitates	Irradiation of pre-exiting α' precipitates			Irradiation of as received 15Cr
		Kyushu University	Kyushu University	Hokkaido University	Hokkaido University
Sample designation	P19	P19+E/1e-4/1	P19+E/1e-3/1	P19+E/4.6e-4/0.46	AR+E/4.6e-4/0.46
Damage rate (dpa/s)	$1x10^{-5}$ dpa/s	$1x10^{-4}$	$1x10^{-3}$	$4.6x10^{-4}$	$4.6x10^{-4}$
Dose (dpa)	--	1	1	0.46	0.46
# LEAP tips analyzed	8	5	1	1	1
# Whole clusters measured	260	324	73	68	123
# Total clusters measured	406	540	118	114	188
Analysis volume ($x10^{-22}$ m^3)	10.0	12.5	2.5	2.8	0.5
Average radius (nm)	2.7 ± 0.6	3.3 ± 0.8	3.0 ± 0.8	3.3 ± 0.6	1.5 ± 0.4
Density ($x10^{23}$ m^{-3})	4.7 ± 0.2	3.4 ± 0.2	3.9 ± 0.4	2.7 ± 0.3	2.9 ± 0.2
Volume fraction	0.044	0.063	0.053	0.067	0.054
Matrix concentration (at%)	12.9 ± 0.6	10.9 ± 0.5	11.1 ± 1.1	10.6 ± 1.0	12.2 ± 2.5
α' concentration (at%)	85.3 ± 5.7	92.0 ± 4.9	92.6 ± 5.7	90.3 ± 6.8	76.4 ± 11.9

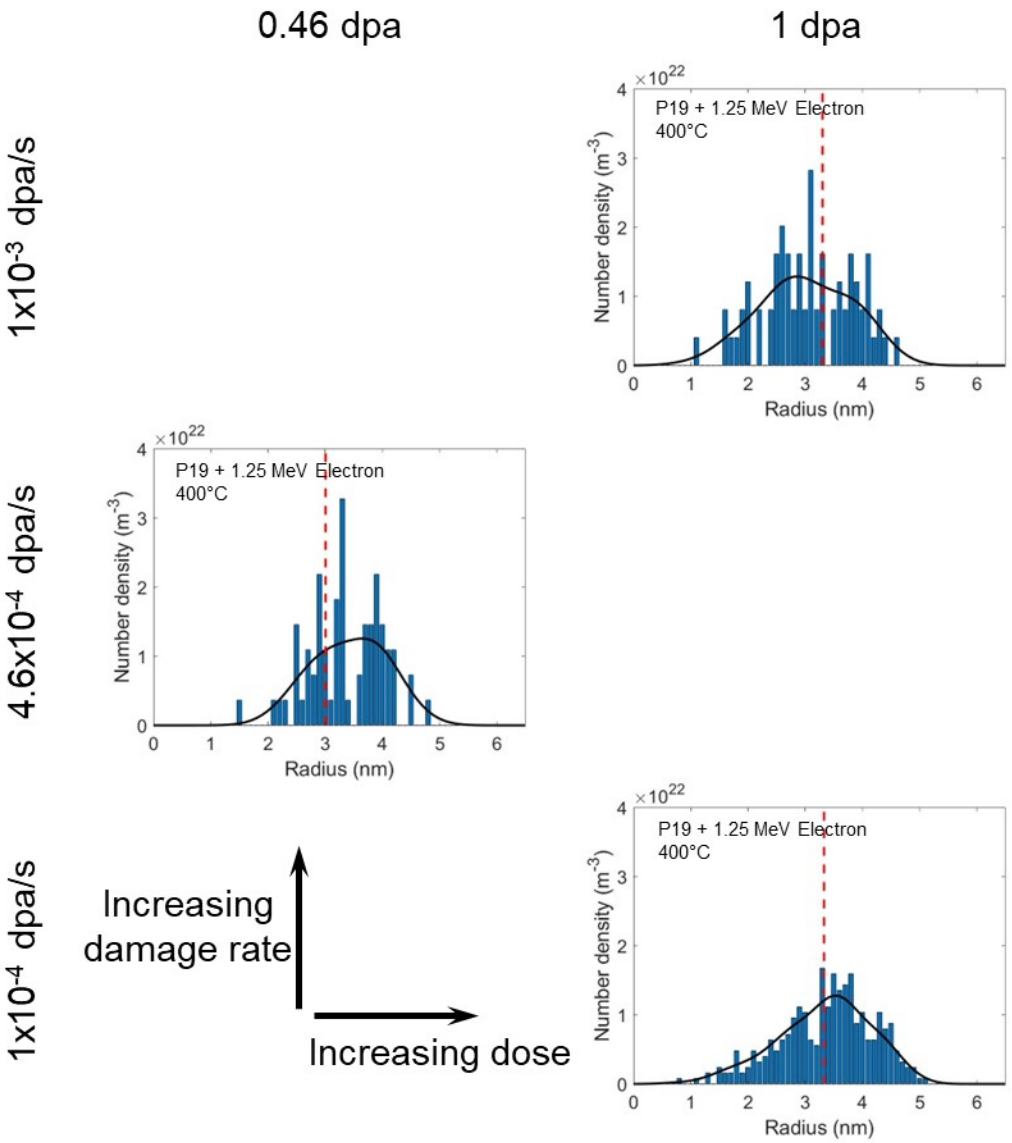

Figure 5.30. α' precipitate size distribution after electron irradiation with 1.25 MeV electrons of the pre-existing α' population at varying doses and damage rates.

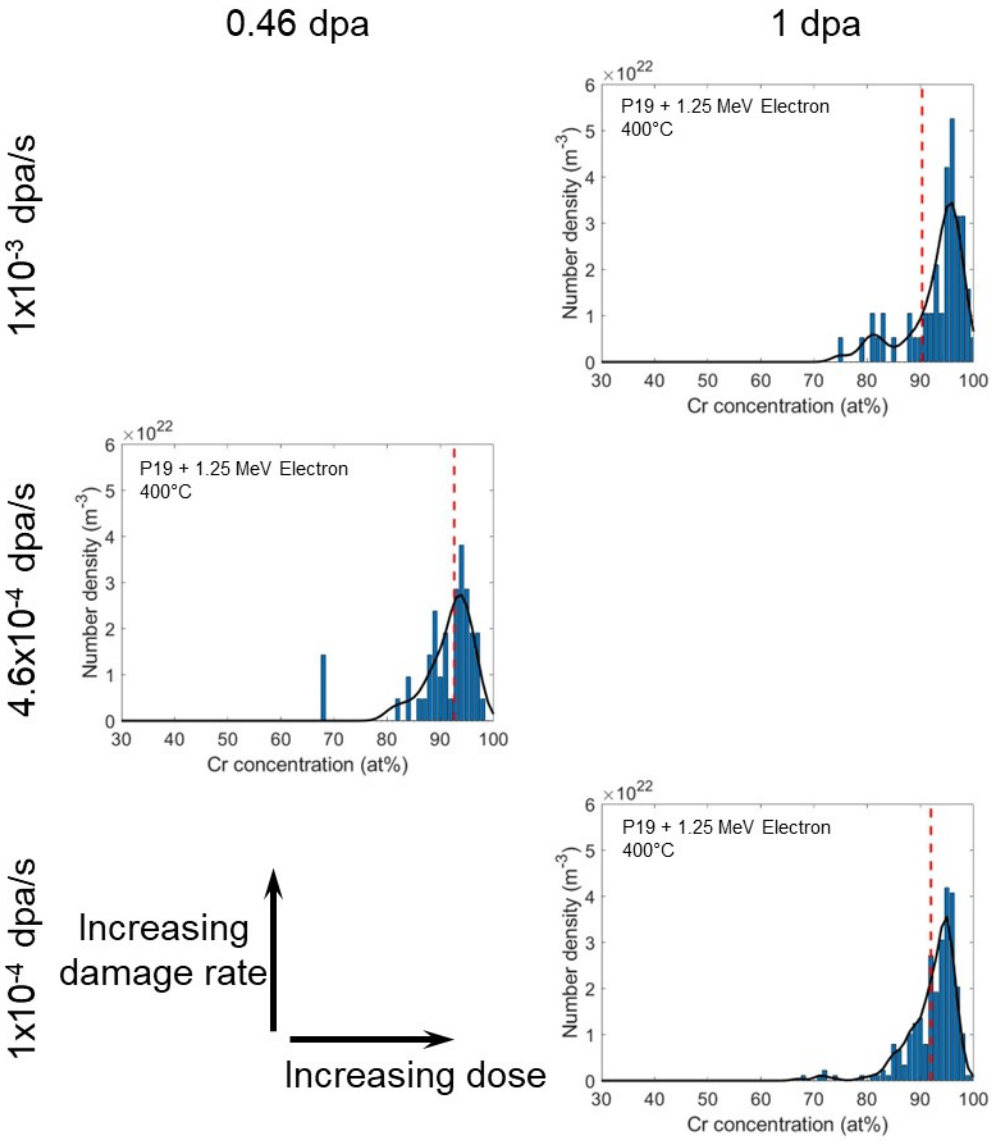

Figure 5.31. α' precipitate Cr concentration distribution after electron irradiation with 1.25 MeV electrons of the pre-existing α' population at varying doses and damage rates at 400°C.

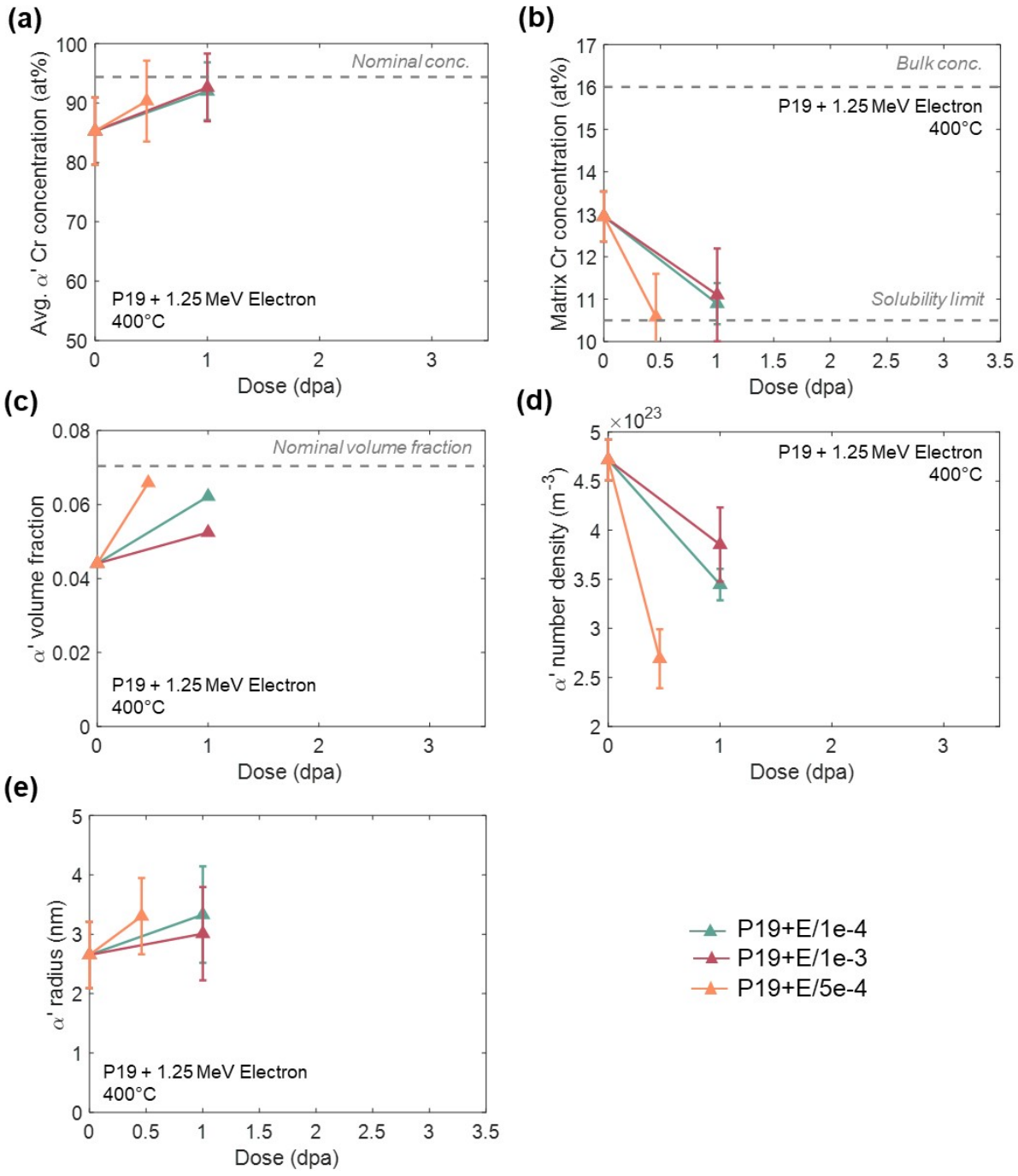

Figure 5.32 Precipitate evolution with dose after electron irradiation with 1.25 MeV electrons of the pre-existing α' population at varying damage rates at 400°C, where (a) shows the average α' precipitate concentration, (b) shows the matrix concentration, (c) shows the volume fraction, (d) shows the number density, and (e) shows the average radius.

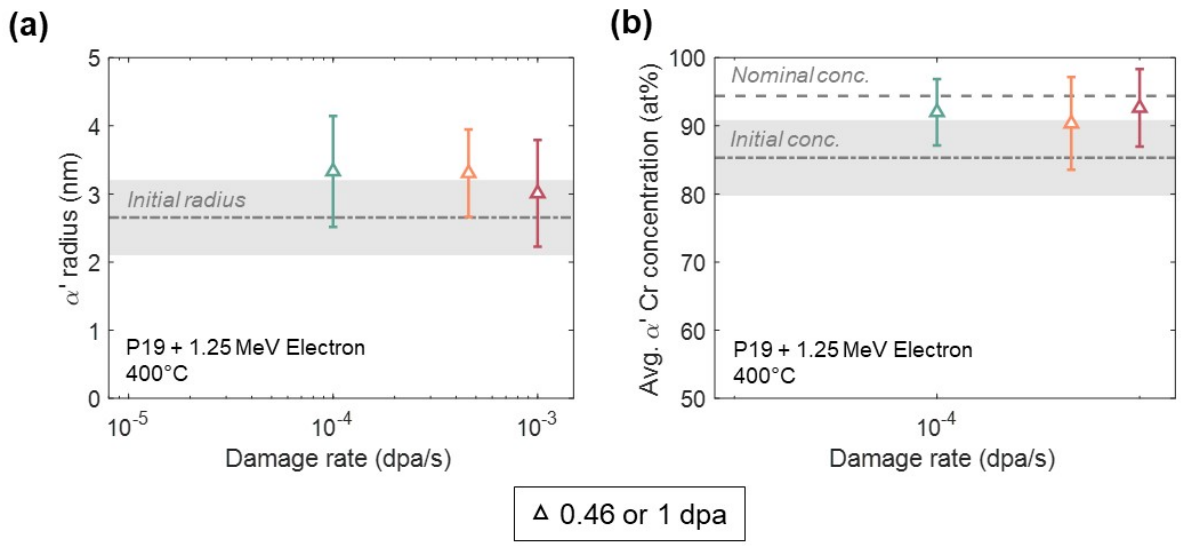

Figure 5.33 Precipitate evolution of the pre-existing α' population with damage rate under electron irradiation with 1.25 MeV electrons at 400°C, where (a) shows the average radius, and (b) shows the average α' precipitate concentration. The initial precipitate size/concentration is shown in the gray dash-dot line with error represented as the gray highlighted area. The data at 0.46 dpa or 1 dpa is represented by open triangles.

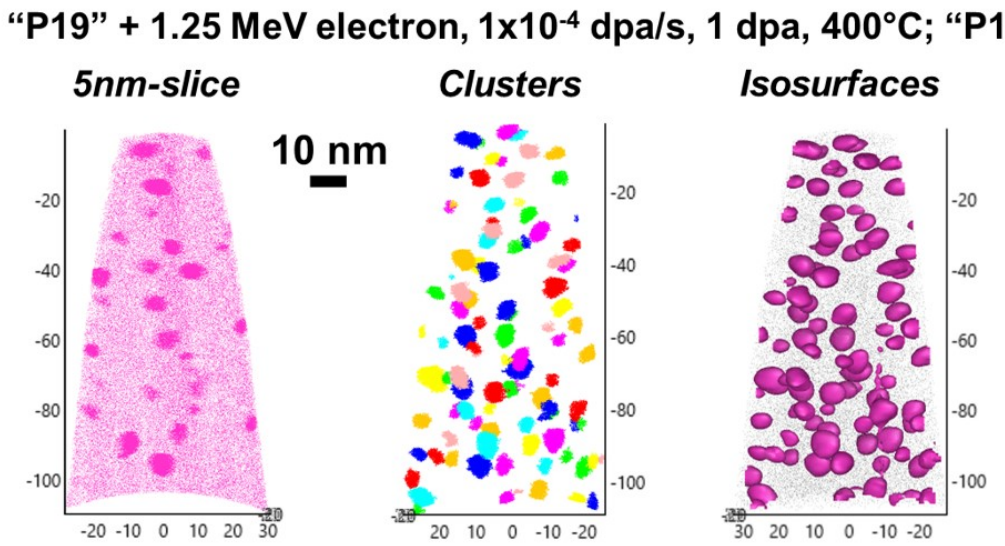

Figure 5.34 Representative atom probe volumes of the electron irradiation of pre-existing α' precipitates (P19) with 1.25 MeV electrons at $1x10^{-4}$ dpa/s to 1 dpa at 400°C, where (left) is an atom distribution of 100% Cr atoms in 5nm thick slice through reconstruction volume, (middle) image is the indexed clusters, and (right) image is the Cr isosurface at 30%Cr (and 0.5%Fe atom as black dots).

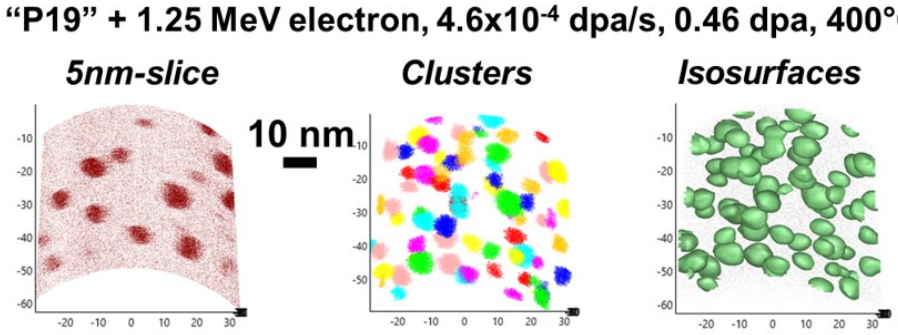

Figure 5.35 Representative atom probe volumes of the electron irradiation of pre-existing α' precipitates (P19) with 1.25 MeV electrons at 4.6x10^{-4} dpa/s to 0.46 dpa at 400°C, where (left) is an atom distribution of 100% Cr atoms in 5nm thick slice through reconstruction volume, (middle) image is the indexed clusters, and (right) image is the Cr isosurface at 30%Cr (and 0.5%Fe atom as black dots).

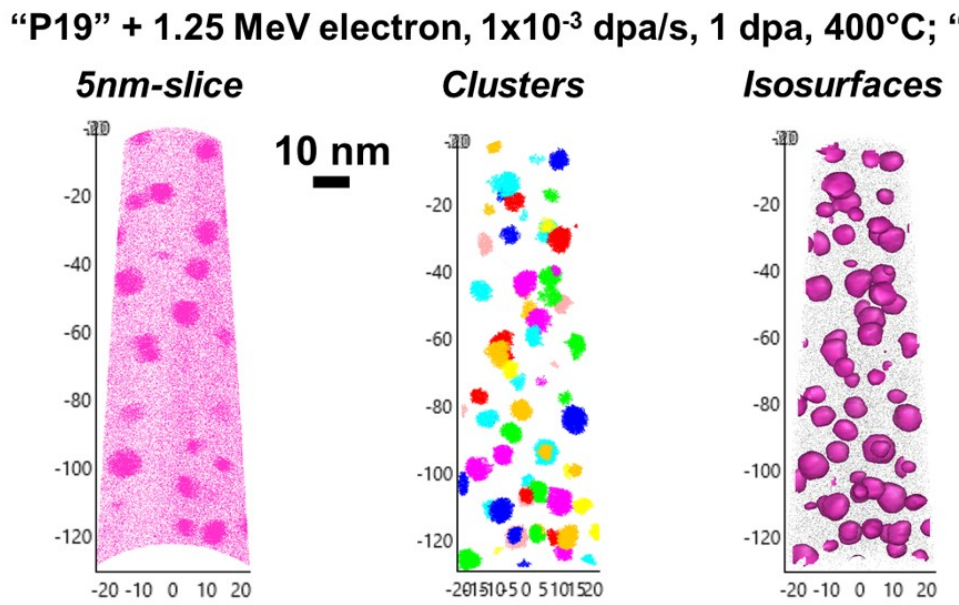

Figure 5.36 Representative atom probe volumes of the electron irradiation of pre-existing α' precipitates (P19) with 1.25 MeV electrons at $1x10^{-3}$ dpa/s to 1 dpa at 400°C, where (left) is an atom distribution of 100% Cr atoms in 5nm thick slice through reconstruction volume, (middle) image is the indexed clusters, and (right) image is the Cr isosurface at 30%Cr (and 0.5%Fe atom as black dots).

5.4.2 α' precipitation under electron irradiation

As received Fe-15Cr was also electron irradiated in order to validate results observed from the electron irradiated pre-existing α' precipitates. Under electron irradiation, the α' precipitates were observed to form and grow in the as-received Fe15Cr at a damage rate of $4.6x10^{-4}$ dpa/s to 0.46 dpa (AR+E/4.6e-4/0.46). The α' precipitates had an average radius of 1.5±0.4 nm, smaller than those observed after electron irradiation of the pre-existing α' precipitates. The solute concentration was also lower than those from the electron irradiation of the pre-existing α' precipitates, at 76.4±11.9 at%. Table 5.8 lists the precipitate characteristics for the electron irradiation of the as received Fe-15Cr sample, including the average size, number density, average concentration, matrix concentration, and volume fraction. Figure 5.37 shows a representative atom probe volume for AR+E/4.6e-4/0.46.

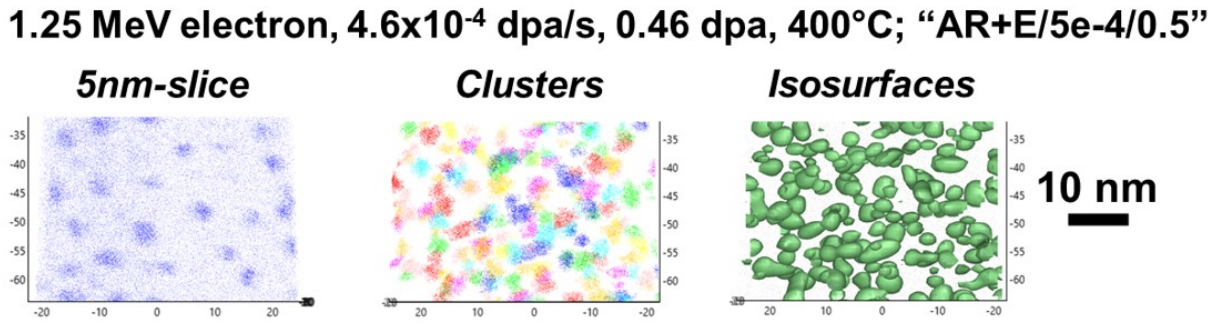

Figure 5.37 Representative atom probe volumes of the electron irradiation of as received Fe-15Cr sample with 1.25 MeV electrons at $4.6x10^{-4}$ dpa/s to 0.46 dpa at 400°C (AR+E/0.46e-4/0.46), where (left) is an atom distribution of 100% Cr atoms in 5nm thick slice through reconstruction volume, (middle) image is the indexed clusters, and (right) image is the Cr isosurface at 30%Cr (and 0.5%Fe atom as black dots).

Chapter 6: Discussion

Discussion of results from Chapter 5 will be presented in four sections: In Section 6.1, the precipitate evolution models discussed in Section 2.4 will be used to describe the precipitate size dependence on cascade size and damage rate including the calculation of the ballistic dissolution parameter; Section 6.2 will address the dependence of the α' precipitate solute concentration on cascade size and damage rate, including calculating the ballistic dissolution parameter through a second method; Section 6.3 will use both methods of calculating the ballistic dissolution parameter for α' from irradiated as-received 15Cr; lastly, Section 6.4 will focus on the role of damage rate and cascade size on the α' precipitate size and solute concentration.

6.1 Determination of BDP using the NHM model

This section will discuss the α' precipitate size evolution dependence on the damage rate and cascade size using the NHM [1] and Chen-modified NHM [2] equations. First, the growth term in both models will be validated using the electron irradiation data, as there is no cascade dissolution under electron irradiation – only radiation enhanced dissolution. Then, using the NHM model, the ballistic dissolution parameter, BDP – referred to as the NHM-based BDP – will be calculated for both proton and heavy ion irradiation, in which radiation enhanced diffusion and ballistic dissolution occur simultaneously. The BDP will be calculated for multiple irradiation cases and compared across damage rates and dose.

6.1.1 Calculation of BDP

The NHM model and Chen-modified NHM model were introduced in Section 2.4. These models describe the change in the precipitate radius over time. As discussed previously, the NHM model is composed of two terms to describe the precipitate size evolution: one is the growth term,

and the other is the dissolution term. The growth term should describe the precipitate evolution in the absence of irradiation. The growth term presented in Section 2.4 is written as:

$$\frac{dr}{dt} = \frac{D_{irr}(C_m - C_e)}{rC_p} \tag{6.1}$$

where D_{irr} is the radiation enhanced diffusion coefficient, r is the precipitate radius, and C_p is the precipitate concentration. The total concentration of solute does not change, and so a conservation condition can be applied such that:

$$C_b = \frac{4}{3}n\pi r^3 C_p + C_m\left(1 - \frac{4}{3}\pi r^3 n\right) \tag{6.2}$$

where C_b is the bulk concentration of the solute, n is the precipitate number density. Eq. (6.2) relies on multiple APT determined values (radius, number density and precipitate concentration) to calculate the matrix concentration. For this thesis, the matrix concentration measured from APT was used, negating Eq. (6.2) altogether.

The growth term for the Chen-modified NHM model is based on the Gibbs-Thomson effect to better account for nanoprecipitate interface [2], rewritten here:

$$\frac{dr}{dt} = \frac{D_{irr}}{r} \cdot \frac{C_m - C_r}{C_p - C_r} \tag{6.3}$$

Here, C_m is the solute concentration in the matrix, C_p is the solute concentration in the dispersoid, and C_r is:

$$C_r = C_\infty \exp\left(\frac{2\gamma_i V_{at}}{kTr}\right) \tag{6.4}$$

where C_∞ is the solubility limit at a flat interface of the two phases, γ_i is the interfacial energy at the precipitate-matrix interface, V_{at} is the average atomic volume of the precipitate, T is the temperature, and k is the Boltzmann constant.

The dissolution term describes the dissolution of the precipitate due to irradiation. This term is dependent on the ballistic dissolution parameter, BDP or φ, a constant describing the ballistically-induced atom flux from the precipitate per dpa:

$$\frac{dr}{dt} = -\frac{\varphi K_0}{N_{at}} \tag{6.5}$$

where K_0 is the defect production rate, and N_{at} is the atomic density.

Under irradiation, both the thermal effects of growth, enhanced by irradiation, and the dissolution by irradiation are coupled together to produce the full NHM and Chen-modified NHM equations:

$$NHM: \quad \frac{dr}{dt} = \frac{D_{irr}(C_m - C_e)}{rC_p} - \frac{\varphi K_0}{N_{at}} \tag{6.6}$$

$$CHEN: \quad \frac{dr}{dt} = \frac{D_{irr}}{r} \cdot \frac{C_m - C_r}{C_p - C_r} - \frac{\varphi K_0}{N_{at}} \tag{6.7}$$

The growth term for the NHM models depends on the radiation-enhanced diffusion (D_{irr}). This term represents the non-equilibrium concentration of the vacancy and interstitial defects in the material enhancing the mobility of diffusing solutes. The radiation-enhanced diffusion (RED) rate of solutes is generally expressed as:

$$D_{irr} = D_v C_v^{irr} + D_i C_i^{irr} + D_{eq} \tag{6.8}$$

where D_v and D_i are the diffusion rates of vacancies and interstitials, respectively, and C_v^{irr} and C_i^{irr} are the concentration of vacancies and interstitials due to irradiation, respectively. D_{eq} is the equilibrium diffusion coefficient. At high temperatures, the effect of irradiation is overcome. The vacancies and interstitial diffusion coefficient are described by Eq. (6.9) and Eq. (6.10) respectively:

$$D_v = {a_0}^2 \nu \exp\left(-{E_m^v}/{kT}\right) \tag{6.9}$$

$$D_i = {a_0}^2 \nu \exp\left(-{E_m^i}/{kT}\right) \tag{6.10}$$

where the E_m^v is the vacancy migration energy (0.62 eV) and E_m^i is the interstitial migration energy (0.34 eV). The migration energies used were calculated for Fe-16Cr using a composition weighted average of the migration energies for pure Cr and pure Fe [3]. The point defect concentrations under irradiation are much higher than under equilibrium. In order to determine the fraction of defects lost to recombination compared to sinks, the analysis from Ref. [4] was used:

$$f_{recom} = \frac{RC_iC_v}{{k_s}^2(total)D_v + K_{iv}C_iC_v} \tag{6.11}$$

$$f_{sinks} = \frac{{k_s}^2(total)D_v}{{k_s}^2(total) + RC_iC_v} \tag{6.12}$$

where f_{recom} is the fraction of defects lost to recombination and f_{sinks} is the fraction of defects lost to sinks. For these calculations, Eq. (6.13) and Eq. (6.14) were used for C_v^{irr} and C_i^{irr},

respectively, in which $K_i = k_s^2(total)D_i$, $K_v = k_s^2(total)D_v$, $R = 4\pi r_c(D_i + D_v)N_{at}$, K_0 is the defect production rate, and ξ is the production efficiency term.

The production efficiency term was set to 0.1 for heavy ion irradiation [5–7], 0.8 for proton irradiation [8], and 1 for electron irradiation [8–10]. The defect production efficiency governed by the fraction of defects that spontaneously recombine, which is larger with larger cascade size. Heavy ion irradiation was shown to have an efficiency ~0.3 with early molecular dynamic simulations that weren't conducted for long enough time [8–10]. Recent studies have shown this asymptotic value is closer to ~0.1 [5–7].

The total sink strength, $k_s^2(total)$, given by Eq. (6.15), is the sum of the sink strengths of the α' precipitates, dislocations loops, and the cavities. The sink strength of the α' precipitates, $k_s^2(\alpha')$, is $4\pi rn$. The spontaneous recombination radius is taken to be 0.3x10^{-9} m [11,12].

$$C_v^{irr} = -\frac{K_i}{2R} + \sqrt{\frac{{K_i}^2}{4R^2} + \frac{\xi K_0 K_i}{R\,K_v}} \tag{6.13}$$

$$C_i^{irr} = -\frac{K_v}{2R} + \sqrt{\frac{{K_v}^2}{4R^2} + \frac{\xi K_0 K_v}{R\,K_i}} \tag{6.14}$$

$$k_s^2(total) = k_s^2(\alpha') + k_s^2(dislocations) + k_s^2(cavities) \tag{6.15}$$

The fraction of defect loss was calculated for each irradiation condition. The sink strength for dislocations was assumed to be ~3x10^{14} m^{-2} for heavy ion irradiation. – a value based on TEM characterization of P18+H/3e-4/10. This value is relatively low compared to the sink strength of α' precipitates and it matches other literature values and assumptions well [11,13–15]. The sink strengths for dislocations under proton and electron irradiation were assumed to be lower. A value of ~3x10^{13} m^{-2} was determined from TEM characterization of the initial α' precipitate microstructure (P18). This value was used for all proton and electron irradiation calculations. Figure 6.1 shows the comparison for defect concentration loss for electron, proton, and heavy ion irradiation. The loss to recombination was determined to be insignificant for all irradiation conditions and that the microstructure was sink dominant. Although the loss to recombination is insignificant, Eq. (6.13) and Eq. (6.14) were used to calculate the defect concentration, as these equations accounted for both recombination and sinks.

There were no observations that α' was associated with cavities or loops for either proton or heavy ion irradiation. Under proton irradiation of the pre-existing α' precipitates, TEM examination showed there was no RIS to the cavity surfaces. Additionally, the α' appeared to be distributed homogeneously for both proton and heavy ion irradiations. Under both heavy ion and proton irradiation, some clustering of Cr was observed in both TEM and APT that may or may not be associated with dislocation loops. Cavities and loops were used primarily to calculate the sink strength which was used for the calculation of radiation enhanced diffusion.

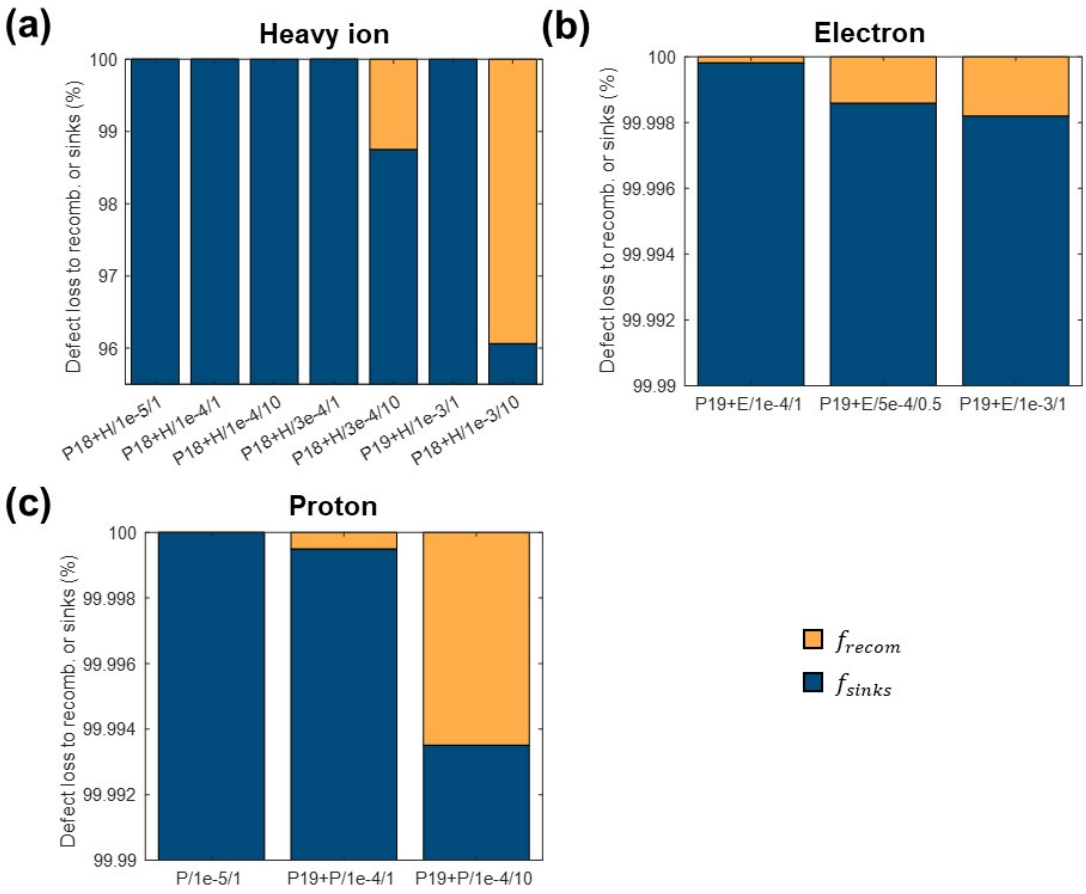

Figure 6.1 Fraction of defects lost to mutual recombination and sinks for (a) heavy ion irradiation, (b) proton irradiation, and (c) electron irradiation.

6.1.2 Precipitate evolution under electron irradiation

The precipitate size evolution was described for each electron irradiation condition using both the NHM model and the Chen-modified NHM model. Under electron irradiation, radiation enhanced diffusion is expected to be the only mechanism because only isolated point defects are produced [11,16–18], so only the growth term was used for each model. The α' precipitate size evolution was determined by calculating the growth rate over incremental time steps. The change in precipitate radius was then calculated for the time corresponding to the applied dpa. The sink strength and the D_{irr} were also recalculated for damage step. The precipitate concentration, number density, and matrix concentration (C_p, n, and C_m, respectively) were interpolated between the starting condition and the experimental value at 1 dpa (or 0.46 dpa). The starting condition for the models was the initial condition for the samples: proton irradiated (P19). Values used to calculate the α' precipitate evolution under electron irradiation are shown in Table 6.1 and Table 6.2.

APT data were shown to match the NHM and Chen-modified NHM model well. Figure 6.2 shows that the precipitate size evolution predicted by both models was very similar, as indicated by overlap in the figure. Moreover, the predicted precipitate size at 1 (or 0.46) dpa was close to the experimentally observed average α' precipitate size. There were small differences between the growth terms modeled, primarily exhibited in the growth rate shown in Figure 6.3; at high doses (and low growth rates), the two models diverge. Figure 6.3 depicts the experimentally observed linear growth rate ($\frac{\Delta r}{\Delta t}$ between 0-1 dpa conditions). This data shows that the models yield results with the correct order of magnitude and that precipitates do not grow linearly with dose. From both Figure 6.2 and Figure 6.3, it is clear that electron irradiation is adequately described with only the growth term, thereby substantiating the assumption that electron irradiation produces only isolated point defects and no ballistic dissolution. Given the agreement between the NHM and Chen-modified growth NHM model, future work in remaining sections will use only the simpler NHM model.

Table 6.1 NHM model calculations for electron irradiation of pre-existing α' precipitates over a range of damage rates. Table provides the data inputs and outputs for conditions at 0, 0.46 and 1 dpa. Bold values represent the outputs from the model or were calculated using an output (such as the radius).

	Definition	Units	P+E/1e-4/1		P+E/0.46e-4		P+E/1e-3	
			0 dpa	1 dpa	0 dpa	0.46 dpa	0 dpa	1 dpa
K_0	Damage rate	dpa/s	$1x10^{-4}$	$1x10^{-4}$	$4.6x10^{-4}$	$4.6x10^{-4}$	$1x10^{-3}$	$1x10^{-3}$
C_e	Solubility limit	atomic fraction	0.105	0.105	0.105	0.105	0.105	0.105
C_m	Matrix concentration	atomic fraction	0.129	0.109	0.129	0.106	0.129	0.111
C_p	α' concentration	atomic fraction	0.853	0.920	0.853	0.903	0.853	0.926
r	α' radius	nm	2.65	**3.33**	2.65	**2.99**	2.65	**3.35**
n	α' number density	m^{-3}	$4.71x10^{23}$	$3.44x10^{23}$	$4.71x10^{23}$	$2.69x10^{23}$	$4.71x10^{23}$	$3.85x10^{23}$
$k_s^2(\alpha')$	α' sink strength	m^{-2}	$1.57x10^{16}$	$\mathbf{1.44x10^{16}}$	$1.57x10^{16}$	$\mathbf{1.01x10^{16}}$	$1.57x10^{16}$	$\mathbf{1.62x10^{16}}$
D_{irr}	RED	m^2/s	$1.27x10^{-20}$	$\mathbf{1.39x10^{-20}}$	$5.86x10^{-20}$	$\mathbf{8.90x10^{-20}}$	$1.27x10^{-19}$	$\mathbf{1.23x10^{-19}}$
ξ	Efficiency	unitless	1	1	1	1	1	1

Table 6.2 Chen-modified NHM model calculations for electron irradiation of pre-existing α' precipitates over a range of damage rates. Table provides the data inputs and outputs for conditions at 0, 0.46 and 1 dpa. Bold values represent the outputs from the model or were calculated using an output (such as the radius)

	Definition	Units	P+E/1e-4/1		P+E/4.6e-4		P+E/1e-3	
			0 dpa	1 dpa	0 dpa	0.46 dpa	0 dpa	1 dpa
K_0	Damage rate	dpa/s	$1x10^{-4}$	$1x10^{-4}$	$4.6x10^{-4}$	$4.6x10^{-4}$	$1x10^{-3}$	$1x10^{-3}$
C_e	Solubility limit	atomic fraction	0.105	0.105	0.105	0.105	0.105	0.105
C_m	Matric concentration	atomic fraction	0.129	0.109	0.129	0.106	0.129	0.111
C_p	α' concentration	atomic fraction	0.853	0.920	0.853	0.903	0.853	0.926
γ_i	α'-matrix interfacial energy	J/m^2	0.183	0.229	0.183	0.222	0.183	0.232
C_∞	Solubility limit at flat surface	atomic fraction	0.09	0.09	0.09	0.09	0.09	0.09
C_r	Solute conc. at interface	atomic fraction	0.107	**0.107**	0.107	**0.107**	0.107	**0.107**
r	α' radius	m	2.65	**3.33**	2.65	**2.95**	2.65	**3.35**
n	α' number density	m^{-3}	$4.71x10^{23}$	$3.44x10^{23}$	$4.71x10^{23}$	$2.69x10^{23}$	$4.71x10^{23}$	$3.85x10^{23}$
$k_s^2(\alpha')$	α' sink strength	m^{-2}	$1.57x10^{16}$	$\mathbf{1.44x10^{16}}$	$1.57x10^{16}$	$\mathbf{9.97x10^{15}}$	$1.57x10^{16}$	$\mathbf{1.62x10^{16}}$
D_{irr}	RED	m^2/s	$1.273x10^{-20}$	$\mathbf{1.39x10^{-20}}$	$5.859x10^{-20}$	$\mathbf{9.03x10^{-20}}$	$1.273x10^{-19}$	$\mathbf{1.23x10^{-19}}$
ξ	Efficiency	unitless	1	1	1	1	1	1

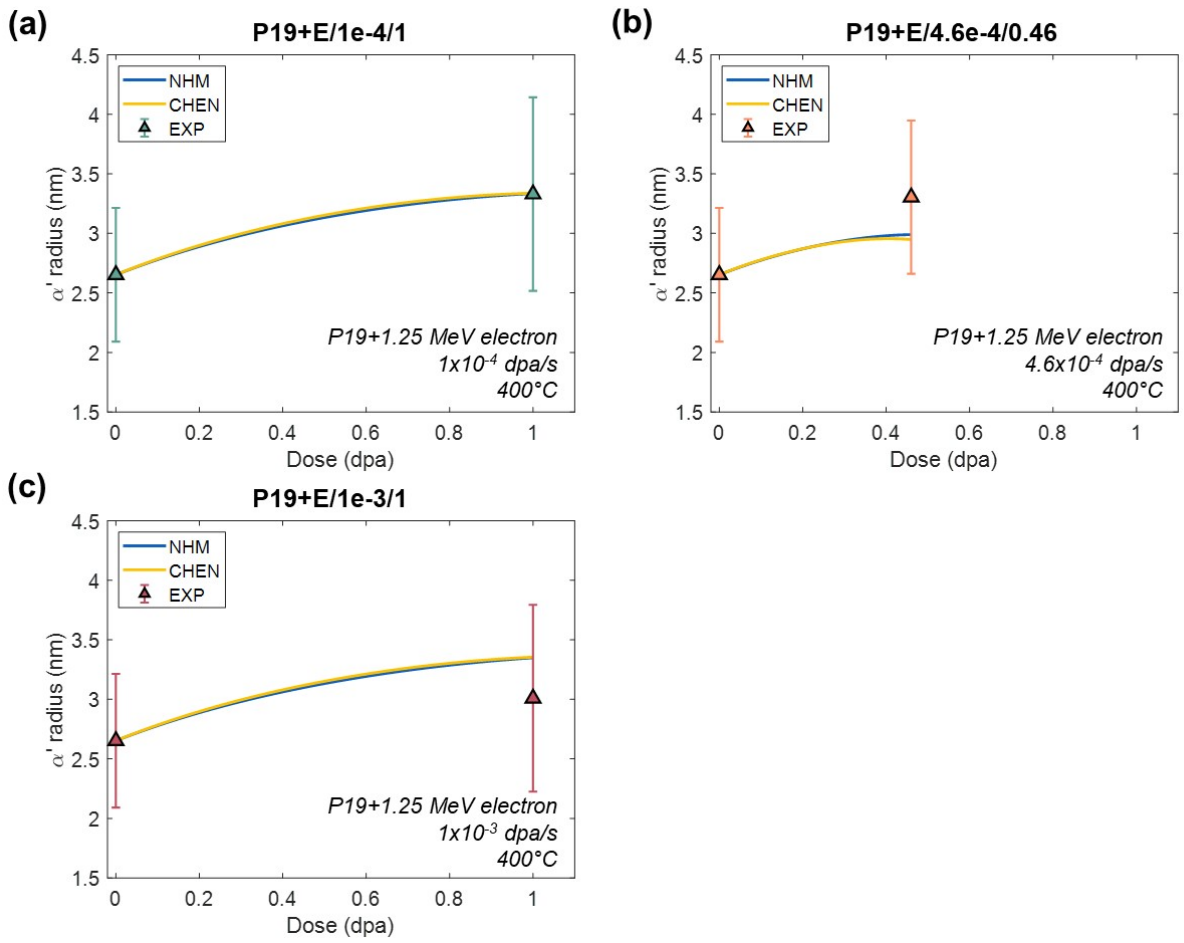

Figure 6.2 Precipitate evolution predictions for the NHM (blue curves) and Chen-modified NHM model (yellow curves) compared to the experimental value for the electron irradiation of pre-existing α' precipitates (filled triangles) at a damage rate of (a) $1x10^{-4}$ dpa/s (P19+E/1e-4/1), (b) $4.6x10^{-4}$ dpa/s (P19+E/4.6e-4/0.46), and (c) $1x10^{-3}$ dpa/s (P19+E/1e-3/1).

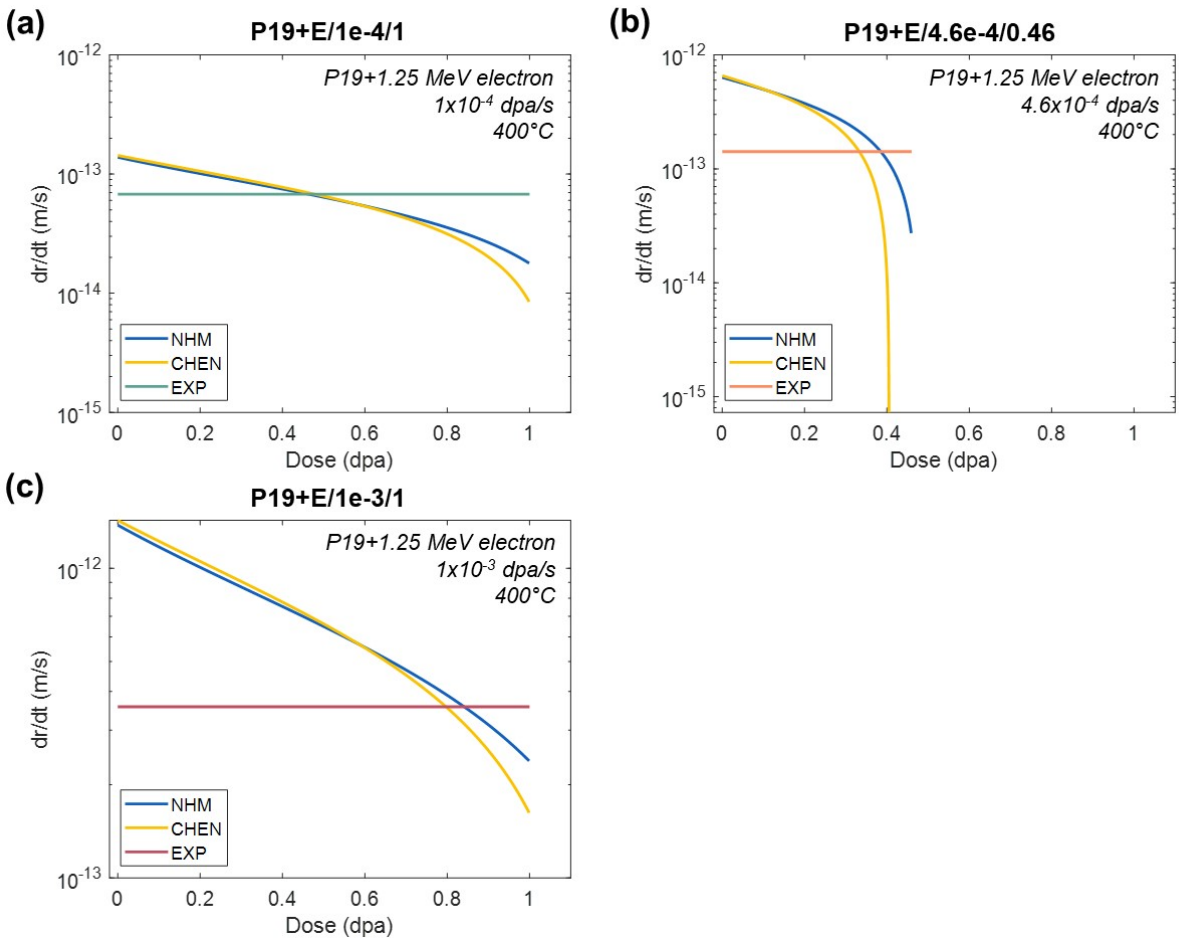

Figure 6.3 Growth rate from the NHM model (blue curves), Chen-modified NHM model (yellow curves), and experiment $\frac{\Delta r}{\Delta t}$ (straight lines) for electron irradiation of pre-existing α' precipitates (filled triangles) at a damage rate of (a) 1x10^{-4} dpa/s (P19+E/1e-4/1), (b) 4.6x10^{-4} dpa/s (P19+E/4.6e-4/0.46), and (c) 1x10^{-3} dpa/s (P19+E/1e-3/1).

6.1.3 Calculation of the BDP for proton irradiation

Ballistic dissolution is expected under proton irradiation and as such, the full NHM model, which includes both a growth term and dissolution term, was used.

Solving the NHM equation for the ballistic dissolution parameter, or BDP (φ) gives:

$$\varphi = \frac{N_{at}}{\xi K_0}\left[\frac{D_{irr}(C_m - C_e)}{r\, C_p} - \frac{dr}{dt}\right] \tag{6.16}$$

where N_{at} is the atomic density, ξ is the efficiency, K_0 is the damage rate, C_e is the solubility limit, and $\frac{dr}{dt}$ is the growth rate. C_m, C_p, and r are the matrix Cr concentration, α' precipitate Cr concentration, and the α' average precipitate radius, respectively, all of which were determined from APT analysis. The D_{irr} term was calculated as discussed in Section 6.1.1. There is no nucleation term in the NHM equation. In reality, the radius, number density, matrix concentration, and precipitate concentration evolve together, and new precipitates may be nucleated. But the BDP is calculated at a given dose with a given α' microstructure, and under these conditions neglecting nucleation will not alter the result.

The NHM equation, as described in Eq. (2.3), relates the dissolution volume to the surface area of the precipitate. To arrive at a representative precipitate size from the α' precipitate size distribution, a weighted root mean square (WRMS) radius was determined for each irradiation condition. Table 6.3 shows the WRMS radius values for the proton irradiation conditions compared to the average precipitate radius reported in Section 5.3.

The growth rate term, $\frac{dr}{dt}$, represents the instantaneous growth rate of the α' precipitates. To determine the growth rate at each dose, a fit was applied to the α' precipitate WRMS radius. The derivative of the fit describing the precipitate evolution provided the instantaneous slope at a given dose.

In order to best capture the precipitate evolution, three fitting techniques were applied to the precipitate WRMS radius, and the growth rate term was calculated as the instantaneous slope from the applied fit. The first fit applied was a simple linear fit with intervals between the data points: 0 to 1 dpa and 1 to 10 dpa. Realistically, α' precipitates do not grow linearly, as was demonstrated in Section 6.1.2, with the growth term applied to radiation enhanced precipitate growth under electron irradiation. But the linear fits will provide a good first approximation of the $\frac{dr}{dt}$ value and thus an approximate BDP value. Precipitate evolution under irradiation is further

described by a polynomial, or quadratic fit. The third fit applied was exponential. This fit assumes that a steady state precipitate size will be achieved by some dose as it asymptotes, which follows the expectation of the NHM model and previous experiments with α' [1,19]. The exponential fit may be more closely related to what is occurring in the system under irradiation.

For analysis of proton irradiation of pre-existing α' precipitates at $1x10^{-4}$ dpa/s (P19+P/1e-4), the linear fit was applied over the intervals of 0 to 1 dpa and 1 to 10 dpa. $\frac{dr}{dt}$ was derived from the derivative of the linear fit (i.e., the slope). Figure 6.4(a) shows the linear fits applied to the WRMS radius of the proton irradiated pre-existing α' precipitates. Figure 6.4(b) shows the corresponding growth rate, and the values of the growth rate used for the $\frac{dr}{dt}$ term, represented as data points. In addition to the linear fits, another data point was used at 10 dpa based on the assumption the α' precipitates had reached steady state by 10 dpa ($\frac{dr}{dt}$(t=0 dpa) = 0 m/s). From this figure, the growth rate increases with dose, which is unexpected. Even under electron irradiation, where there was no dissolution, the growth of the precipitate slowed. This may mean that there is an error in the average size determined for the proton irradiated α' precipitates, which is not wholly unexpected as the number density is much lower and the counting statistics are significantly lower.

The polynomial fit was applied to the WRMS radius over all three data points, from 0-10 dpa. The polynomial fit was a quadradic function, $r(t) = a(t-b)^2 + c$, where the parameters b and c coordinate to the vertex of the parabola, (b, c), and a dictates the curvature of the parabola. For the 1.5 MeV proton irradiation of pre-existing α' precipitates at $1x10^{-4}$ dpa/s, the vertex was set to the precipitate size at 10 dpa and the curvature adjusted to drive the parabola through the initial WRMS radius. Figure 6.5(a) shows the polynomial fit for proton irradiation at $1x10^{-4}$ dpa/s. The growth rate was derived from the derivative of the polynomial fit, $\frac{dr}{dt}(t) = 2a(t-b)$. The value of $\frac{dr}{dt}$ used for the BDP calculation was determined from this equation at the given dose. Figure 6.5(b) shows the corresponding growth rate for proton irradiation of α' precipitates, including the experimental average dissolution rate, $(\mathrm{r_2} - \mathrm{r_1})/(\mathrm{t_2} - \mathrm{t_1})$, and fit average dissolution rate, which is described by:

$$fit\ avg\ rate = \frac{1}{t_2 - t_1}\int_{t_1}^{t_2} 2a(t-b)dt \tag{6.17}$$

The experimental average growth rate matches that from the linear fits and shows the unexpected trend of increasing growth rate with dose. The fit average growth rate for the polynomial fit shows

a decreasing average growth rate with dose, which matches the expected trend. This suggests the polynomial approach may be better suited for fitting this data.

Lastly, the exponential fit was applied to the WRMS radius over all three data points, from 0, 1, and 10 dpa. The exponential fit, $r(t) = a\exp(bt) + c$, is dependent on three fitting parameters: a, the pre-exponential term; b, which dictates the curvature; and c, which sets the steady-state precipitate size. The growth rate was derived from the derivative of the exponential fit, $\frac{dr}{dt}(t) = ab\exp(bt)$. Parameters were set to minimize the difference between the experimental average growth rate and the exponential fit average growth rate, while also placing the exponential fit through the initial WRMS point:

$$fit\ avg\ rate = \frac{1}{t_2 - t_1}\int_{t_1}^{t_2} ab\exp(bt)\,dt \tag{6.18}$$

Figure 6.6(a) shows the exponential fit to the WRMS radius for proton irradiation of pre-existing α' precipitates at $1\text{x}10^{-4}$ dpa/s; Figure 6.6 (b) shows the corresponding growth rate from the exponential fit as well as the experimental average growth rate (dashed black line) and the fit average growth rate (black line). The experimental average growth rate matches that from the linear fits and shows the non-physical trend of increasing growth rate with dose. The fit average growth rate for the exponential fit shows a decreasing average growth rate with dose, which matches the expected trend. This shows that the exponential fit may be better suited for proton irradiation data.

The BDP was calculated using the linear, polynomial, and exponential fits for proton irradiation of the pre-existing α' precipitates at $1\text{x}10^{-4}$ dpa/s. BDP values for each fit are provided in Table 6.4. Full details regarding the input parameters for the BDP calculations for each fit are provided in Appendix A. BDPs for all fits were observed to increase in size, with similar values. Additionally, the BDP calculated for each dose was similar between fits. The BDP is expected to be a constant, independent of damage rate and dose. However, with increasing dose, BDP is observed to increase. For the linear fit, the growth rate is similar between 0 to 1 dpa and 1 to 10 dpa presenting similar values of the BDP at 1 dpa for each fit. The growth rate from the linear fit from 1-10 is also increasing (higher than the growth rate for 0-1 dpa), so the linear fit BDP values for 1 and 10 dpa are higher than the expected BDP value for proton irradiation. The BDP was also calculated assuming the α' precipitates had achieved a steady state size by 10 dpa (i.e., growth rate of 0 m/s). The resulting BDP was similar to the linear fit BDP at 10 dpa ($8.15\pm9.02\ \text{x}10^{20}$

atoms/m^2·dpa compared to 8.04±3.88 x10^{20} atoms/m^2·dpa, respectively). Although the fit average growth rates were decreasing with dose as expected, unlike the linear fit, the BDPs calculated with the polynomial and exponential fit were similar in value and increased with dose. This is attributed to the low accuracy of the precipitate size determination which results from the low number density and counting statistics.

The BDP that best represents proton irradiation is at 0 dpa because there was the highest number of α' precipitates analyzed at this dose providing for high accuracy, at 8.6 ± 6.2x10^{19} atoms/m^2·dpa. At the higher doses of 1 and 10 dpa, the BDP is increasing – not constant. This is due the increasing matrix concentration and positive growth rate of the precipitates under irradiation, as the terms are summed in the NHM equation (Eq. (6.16)). This suggests there is either an error in the matrix concentration or the NHM model is not well suited to the conditions presented in proton irradiation at 1 and 10 dpa. The BDP for proton irradiation is approximately 8.6 ± 6.2x10^{19} atoms/m^2·dpa. This value was calculated using the exponential fit, as this approach more accurately described the precipitate evolution under irradiation. The BDP calculated using the linear fits at 0 dpa was similar in magnitude (at 9.6 ± 15.4x10^{19} atoms/m^2·dpa).

Table 6.3 WRMS radius for initial (P19) and proton irradiation (1.5 MeV proton irradiation of pre-existing α' precipitates at $1x10^{-4}$ dpa/s at 400°C to 1 and 10 dpa) used for BDP calculations compared to the average radius of the distribution.

	Units	P19	P19+P/1e-4/1	P19+P/1e-4/10
WRMS	nm	2.8 ± 0.6	2.9 ± 0.7	3.9 ± 1.3
Avg. radius	nm	2.7 ± 0.6	2.7 ± 0.7	3.7 ± 1.1

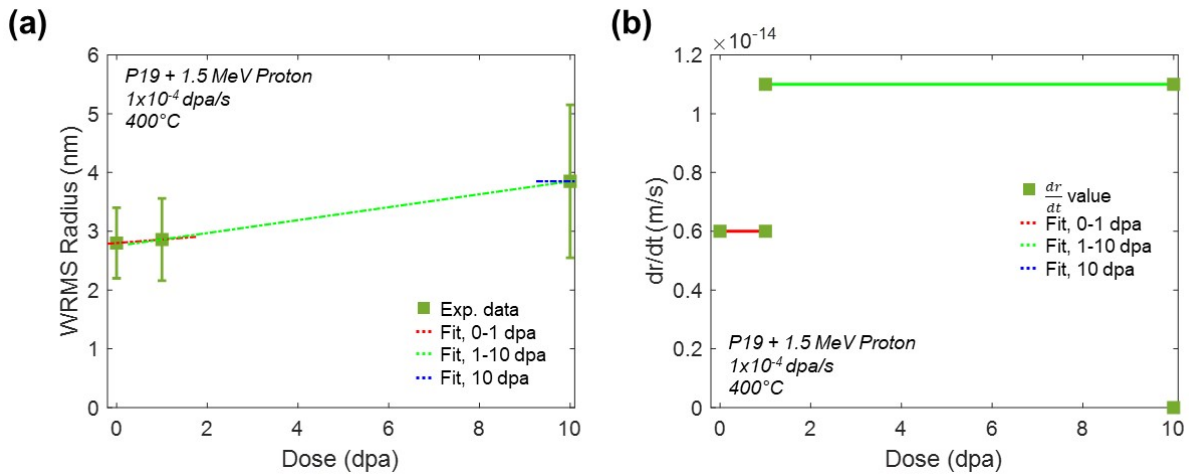

Figure 6.4 (a) Linear fits to the WRMS radius from the proton irradiation of pre-existing α' precipitates at 1x10^{-4} dpa/s (P19+P/1e-4/1 and P19+P/1e-4/10) with a fit for the interval from 0 to 1 dpa (red dashed line), a fit for the interval from 1 to 10 dpa (green dashed line), and a linear fit at 10 dpa (blue dashed line) assuming steady state has been achieved. (b) Corresponding growth rate for the linear fits. Green squares represent $\frac{dr}{dt}$ values used at the corresponding doses.

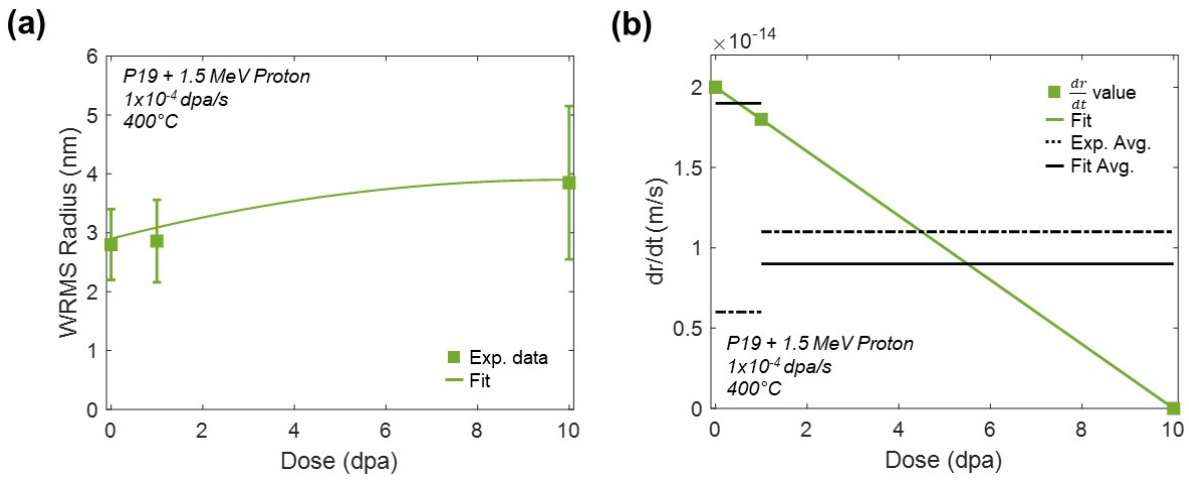

Figure 6.5 Polynomial fit to the WRMS radius from the proton irradiation of pre-existing α' precipitates at $1x10^{-4}$ dpa/s (P19+P/1e-4/1 and P19+P/1e-4/10) for (a) and (b) is the corresponding derivative of the polynomial fit showing the growth rate of the α' precipitates under proton irradiation at $1x10^{-4}$ dpa/s. Additionally, the experimental average growth rate (dashed black line) and the fit average growth rate (solid black line) are shown for the intervals of 0 to 1 dpa and 1 to 10 dpa to depict the quality of the polynomial fit parameters. Green squares represent the values of $\frac{dr}{dt}$ used to calculate BDP.

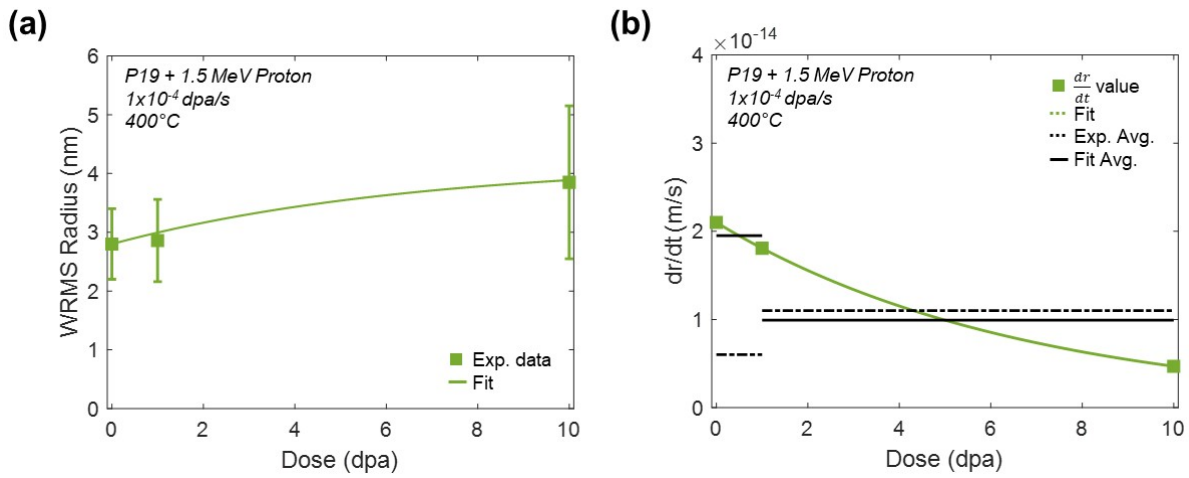

Figure 6.6 (a) Exponential fit to the WRMS radius from the proton irradiation of pre-existing α' precipitates at 1x10^{-4} dpa/s (P19+P/1e-4/1 and P19+P/1e-4/10). (b) The corresponding derivative of the exponential fit shows the growth rate of the α' precipitates under proton irradiation at 1x10^{-4} dpa/s. Additionally, the experimental average growth rate (dashed black line) and the fit average growth rate (solid black line) are shown for the intervals of 0 to 1 dpa and 1 to 10 dpa to depict the quality of the exponential fit parameters; the squares represent the values of $\frac{dr}{dt}$ used at those doses to calculate BDP.

Table 6.4 Comparison of the NHM-based BDP calculated for 1.5 MeV proton irradiation of pre-existing α' precipitates at $1x10^{-4}$ dpa/s at 400°C with various fits used to describe the precipitate evolution.

α' evolution fit	Units	0 dpa	1 dpa	10 dpa
Linear, 0-1 dpa fit	atoms/m^2·dpa	9.63 ± $15.4x10^{19}$	2.92 ± $11.9x10^{20}$	--
Linear 1-10 dpa fit	atoms/m^2·dpa	--	2.92 ± $11.8x10^{20}$	8.04 ± $3.88x10^{20}$
Steady state at 10 dpa	atoms/m^2·dpa	--	--	8.15 ± $9.02x10^{20}$
Polynomial fit	atoms/m^2·dpa	8.57 ± $6.51x10^{19}$	2.84 ± $1.48x10^{20}$	8.15 ± $3.96x10^{20}$
Exponential fit	atoms/m^2·dpa	8.60 ± $6.20x10^{19}$	2.85 ± $1.47x10^{20}$	8.10 ± $3.96x10^{20}$

6.1.4 Calculation of the BDP for heavy ion irradiation

Ballistic dissolution and radiation enhanced dissolution play a role on the α' precipitate microstructure under heavy ion irradiation, so the BDP was calculated using the NHM model, as done for proton irradiation, as described in Eq. (6.15). As with proton irradiation, the weighted root mean square (WRMS) radius was used for the α' precipitate radius, r, in the BDP calculations. The WRMS radius values used for the BDP calculations are provided in Table 6.5.

The precipitate WRMS radius evolution was fit using three different fits in an effort to best capture the precipitate evolution under heavy ion irradiation: linear, polynomial, and exponential. The fits were used to determine growth rate term, or dissolution rate now with negative growth rate, ($\frac{dr}{dt}$) at each dose (0, 1, or 10 dpa) using the instantaneous slope of the fit. The first fit applied was the linear fit with intervals between the data points: 0 to 1 dpa and 1 to 10 dpa. The linear fit provides a good first approximation of the BDP value for each dose. At 1 dpa for all damage rates (except at 1x10^{-5} dpa/s) there are two linear fits through this point and thus two slopes for $\frac{dr}{dt}$. This is the slowing of the precipitate dissolution from the 0-1 dpa interval to the 1-10 dpa interval, where there is slower dissolution. Figure 6.7 shows the linear fits for each of the heavy ion irradiation conditions, with the linear fits extended past the region to illustrate differences in slope between the intervals. Figure 6.8 presents the dissolution rate for each condition with data points for each value used at each dose. At 1 dpa, the true BDP value is expected to fall between the values calculated at the intervals 0-1 dpa and 1-10 dpa. The interval from 0 to 1 dpa shows significant dissolution, and the dissolution rate should be slowing by 1 dpa. The interval from 1 to 10 dpa will also include the range at which a steady state has been achieved, so the dissolution rate is much lower than that in the first interval. The value at 10 dpa for 1x10^{-4} dpa/s (P+H/1e-4/10) was also calculated twice for the linear fit: one calculation used the slope from the 1 to 10 dpa linear fit, and the second calculation assumed a steady state had been achieved ($\frac{dr}{dt}(t$ = 10 dpa) = 0 m/s). Realistically, α' precipitates are not dissolving linearly with time, but the linear fits and combined assumed steady state at 10 dpa provide a good approximation of the $\frac{dr}{dt}$ value and thus an approximate BDP value.

The polynomial fit was applied to the WRMS radius over all three data points, from 0-10 dpa. The polynomial fit was a quadradic function: $r(t) = a(t-b)^2 + c$, with a corresponding dissolution rate of $\frac{dr}{dt}(t) = 2a(t-b)$. This fit could not be applied at the damage rate of 1x10^{-5}

dpa/s as there were only two data points and at least three are required for a quadratic fit. For experimental sets at damage rates of $1x10^{-4}$ dpa/s and $3x10^{-4}$ dpa/s, the vertex of the parabola was set to the precipitate radius at 10 dpa. This condition set steady state at 10 dpa. Heavy ion irradiations of as received 15Cr at the same damage rates confirmed that steady state is achieved between 1 and 10 dpa. The polynomial fit is expected to better describe the data, especially at 0 and 1 dpa, but may not be as reliable at 10 dpa. For $1x10^{-3}$ dpa/s, the WRMS radius difference between 0 and 1 dpa was small, so the vertex (i.e., the steady state) of the parabola was placed at 0 dpa to achieve the best fit. Figure 6.9 shows the polynomial fit to the heavy ion irradiation conditions and Figure 6.10 shows the corresponding dissolution rate for each heavy ion irradiation condition. For the dissolution graphs, the experimental average dissolution rate and fit average dissolution rates are also presented on the graph, with the points indicating the values used for the $\frac{dr}{dt}$ term at each dose.

The exponential fit was applied to the WRMS radius over all three (or two in the case of P18+H/1e-5/1) data points, from 0, 1, and 10 dpa. The exponential fit was selected because it has an asymptotic behavior, which is well suited to describe the α' precipitate evolution under heavy ion irradiation, as described by the NHM model [1] and as previously observed in Fe-Cr alloys [19]. The growth rate was derived from the derivative of the exponential fit, $\frac{dr}{dt}(t) = ab\exp(bt)$. The c parameter for exponential fit sets the steady state value or asymptote. For heavy ion irradiation conditions at $3x10^{-4}$ and $1x10^{-3}$ dpa/s the c parameter was set to 0 and for heavy ion irradiation at $1x10^{-4}$ dpa/s, the c parameter was set to 1.5 nm. Heavy ion irradiations of as-received 15Cr at the same damage rate and to 10 dpa showed a similar microstructure, thus the α' was likely at a steady state by 10 dpa. For the heavy ion irradiation condition at $1x10^{-5}$ dpa/s (P18+H/1e-5/1), there were only two data points (0 and 1 dpa). But there was an additional experiment on as-received 15Cr at approximately ~$1x10^{-5}$ dpa/s to 3 dpa (AR+H/1.3e-5/3) where α' was observed. The steady state size (i.e., the c parameter for the exponential fit) for $1x10^{-5}$ dpa/s was estimated from the WRMS size from AR+H/1e-5/3. The a parameter, or pre-exponential term, was adjusted such that the fit went through the initial WRMS radius. Lastly, the b parameter was adjusted to minimize the difference between the experimental average growth rate and the exponential fit average growth rate.

The BDP was calculated for each heavy ion irradiation condition at 0, and 1 dpa, and 10 dpa for $1x10^{-4}$ dpa/s for the linear, polynomial, and exponential fits. BDP values calculated from

each condition are shown in Table 6.6, and Figure 6.13 depicts calculated BDPs for each damage rate and type of fit as a function of dose. The BDP values from linear fits for each heavy ion irradiation were similar to BDP values from both exponential and polynomial fits, showing the linear fit was a good approximation. For the linear fit, the value in $\frac{dr}{dt}$ drops when switching from the 0-1 dpa interval to the 1-10 dpa interval. This leads to the spread in the BDP values expected at 1 dpa, which is depicted in the figure. Similarly, at 10 dpa there is a gap between the BDPs from the linear fit (for 1-10 dpa) and the assumed steady state BDP value.

The BDPs from the polynomial and exponential fits were similar to the linear fit BDPs, with values falling between the linear fit BDPs for most heavy ion irradiation conditions. This suggests that the polynomial and exponential fits serve as a more accurate method for describing the precipitate evolution and dissolution rates. Overall, the exponential and polynomial fits yield similar results to the linear fits, with values falling between the linear fit extremes, except at $1\text{x}10^{-3}$ dpa/s, where the exponential fit is higher.

The BDP is expected to be independent of dose and damage rate. Here, the BDP calculated using multiple fitting techniques was constant over the dose range for each damage rate. The calculated BDPs were also similar across damage rates.

The BDP that best represents heavy ion irradiation is the BDP calculated using the exponential fit for P18+H/1e-4/10 at 0 dpa. This value is approximately $3.8 \pm 2.3\text{x}10^{20}$ atoms/m^2·dpa. For this condition, it is the same damage rate and dose as the selected BDP for proton irradiation. Additionally, there are a large number of α' precipitates analyzed for this condition and the exponential fit better describes precipitate evolution under irradiation better than a linear fit or polynomial fit.

Table 6.5 WRMS radius for heavy ion irradiation conditions used for NHM based BDP calculations compared to the average radius reported in Chapter 5.

	Units	P18+H/1e-5/1	P18+H/1e-4/1	P18+H/1e-4/10	P18+H/3e-4/1	P19+H/1e-3/1
WRMS	nm	2.3 ± 0.5	2.3 ± 0.5	1.6 ± 0.4	2.1 ± 0.5	2.8 ± 0.6
Avg. radius	nm	2.2 ± 0.5	2.2 ± 0.5	1.7 ± 0.4	2.0 ± 0.5	2.7 ± 0.6

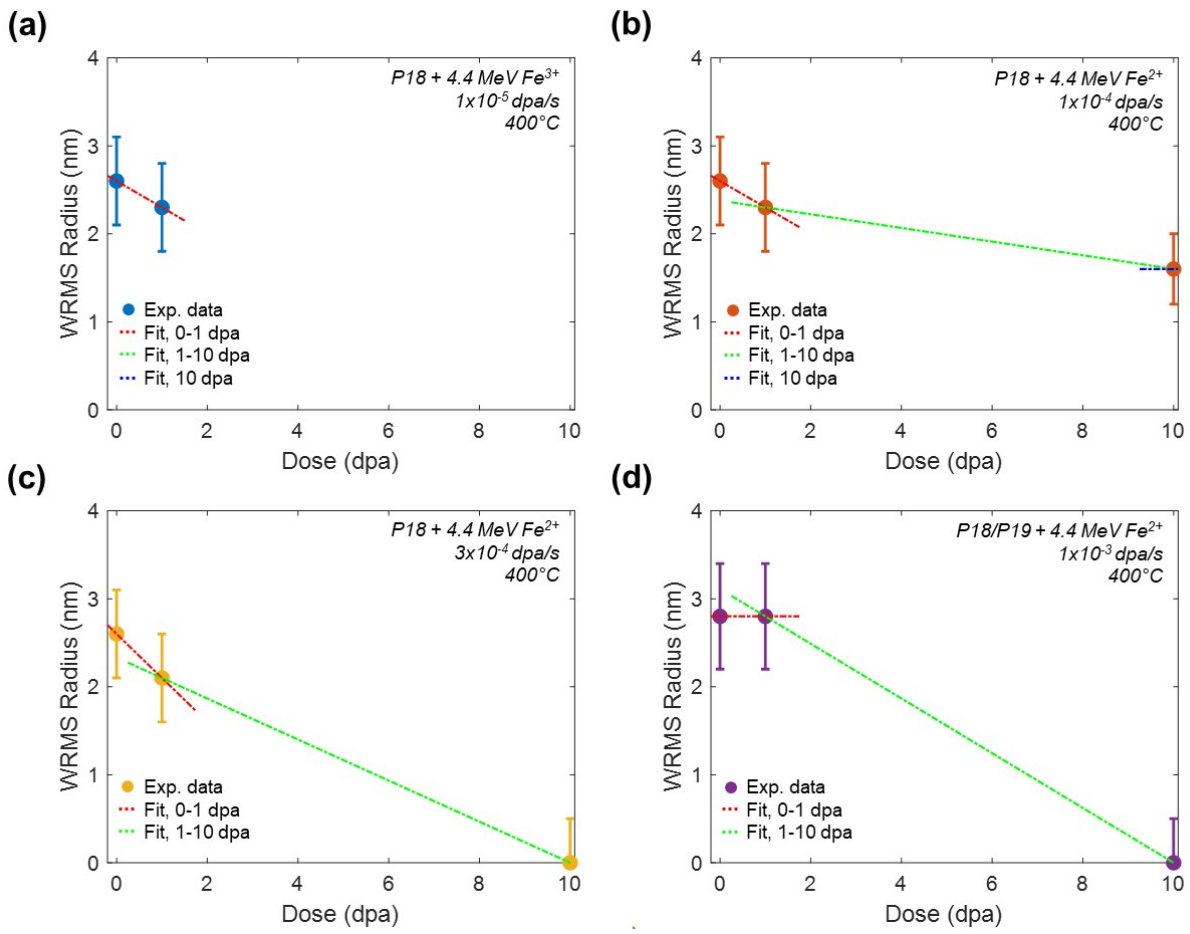

Figure 6.7 Linear fits to the WRMS radius from the heavy ion irradiation of pre-existing α' precipitates with a fit for the interval from 0 to 1 dpa (red dashed line), a fit for the interval from 1 to 10 dpa (green dashed line), and a linear fit at 10 dpa (blue dashed line) assuming steady state has been achieved (only for P18+H/1e-4/10) where (a) is at $1x10^{-5}$ dpa/s, (b) is $1x10^{-4}$ dpa/s, (c) is $3x10^{-4}$ dpa/s, and (d) is $1x10^{-3}$ dpa/s.

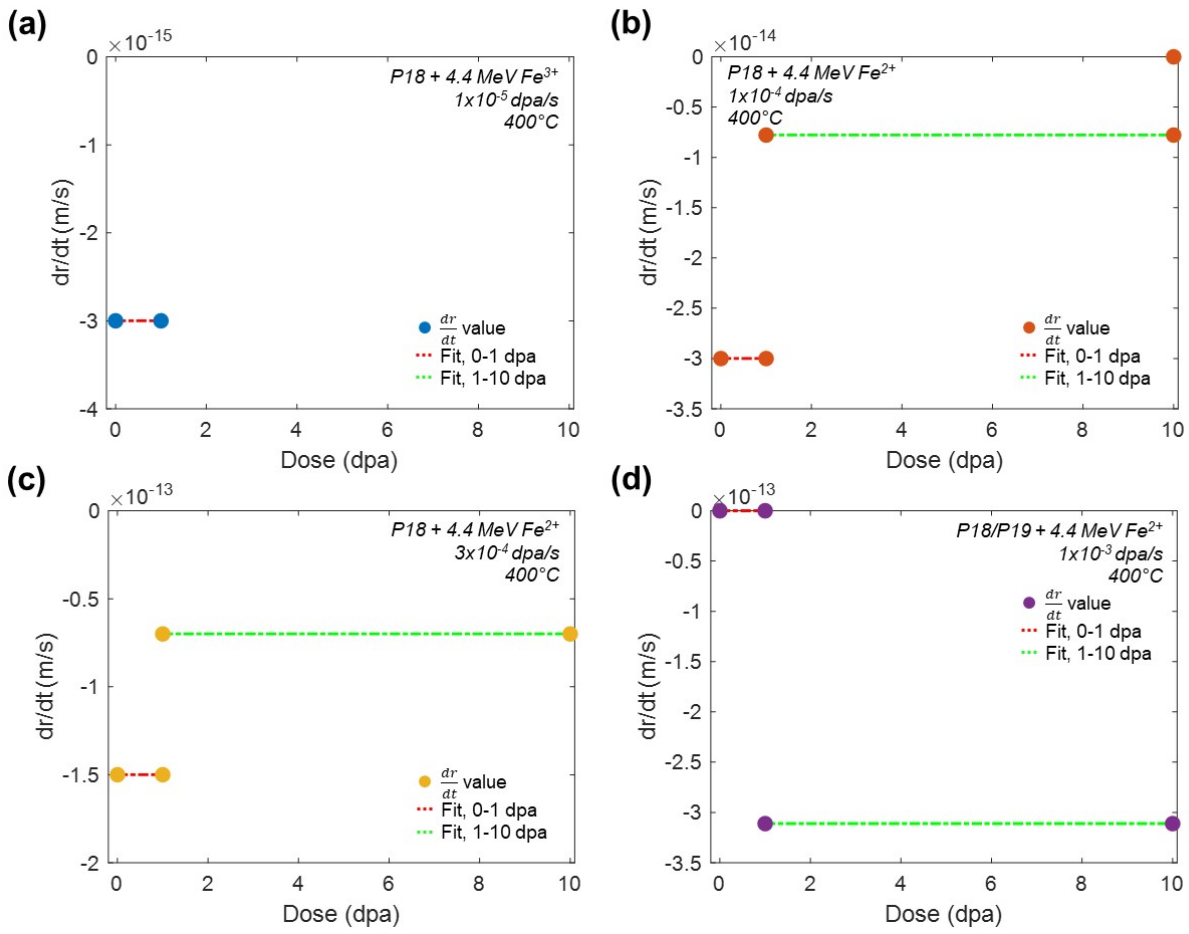

Figure 6.8 Corresponding growth (or dissolution) rates for heavy ion irradiation of pre-existing α' precipitates with linear fit the interval from 0 to 1 dpa (red dashed line), a fit for the interval from 1 to 10 dpa (green dashed line), and a point at 10 dpa assuming steady state has been achieved (only for P18+H/1e-4/10) where (a) is at $1x10^{-5}$ dpa/s, (b) is $1x10^{-4}$ dpa/s, (c) is $3x10^{-4}$ dpa/s, and (d) is $1x10^{-3}$ dpa/s.

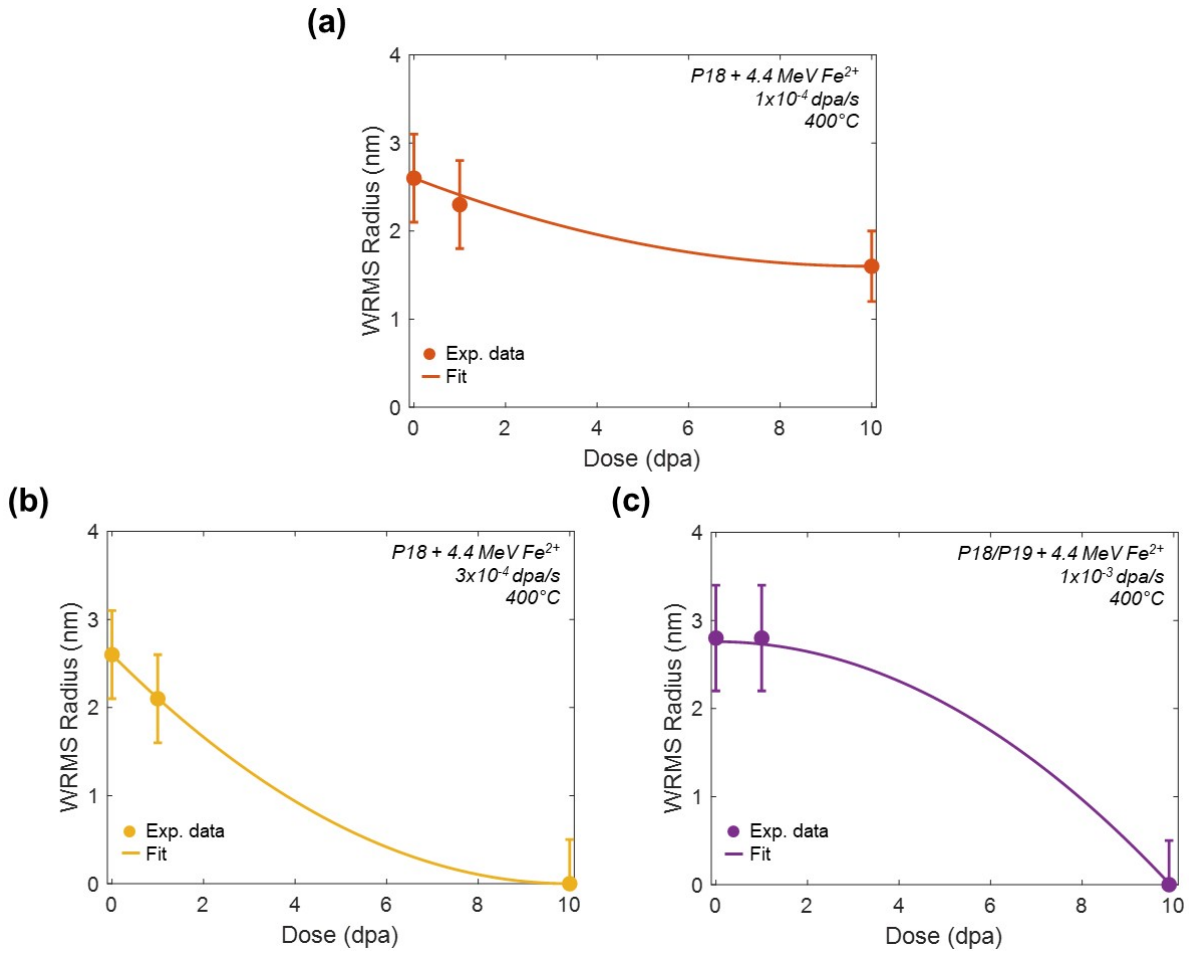

Figure 6.9 Polynomial fit to the WRMS radius from the heavy ion irradiation of pre-existing α' precipitates at (a) $1x10^{-4}$ dpa/s, (b) $3x10^{-4}$ dpa/s, and (c) $1x10^{-3}$ dpa/s.

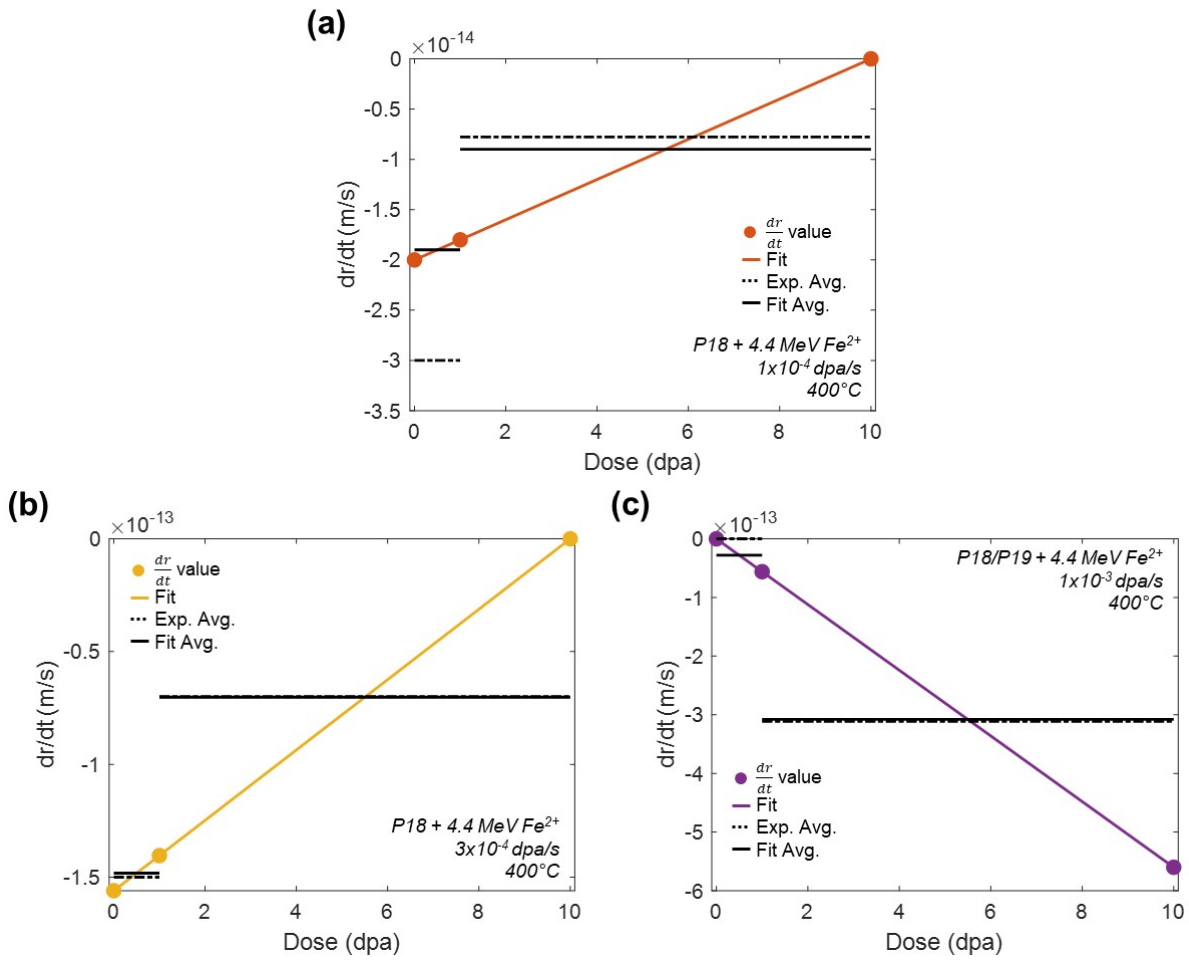

Figure 6.10 Corresponding growth (or dissolution) rate for the heavy ion irradiation of pre-existing α' precipitates at (a) $1x10^{-4}$ dpa/s, (b) $3x10^{-4}$ dpa/s, and (c) $1x10^{-3}$ dpa/s. Additionally, the experimental average growth rate (dashed black line) and the fit average growth rate (solid black line) are shown for the intervals of 0 to 1 dpa and 1 to 10 dpa to depict the quality of the polynomial fit parameters. Circles represent the values of $\frac{dr}{dt}$ used to calculate BDP.

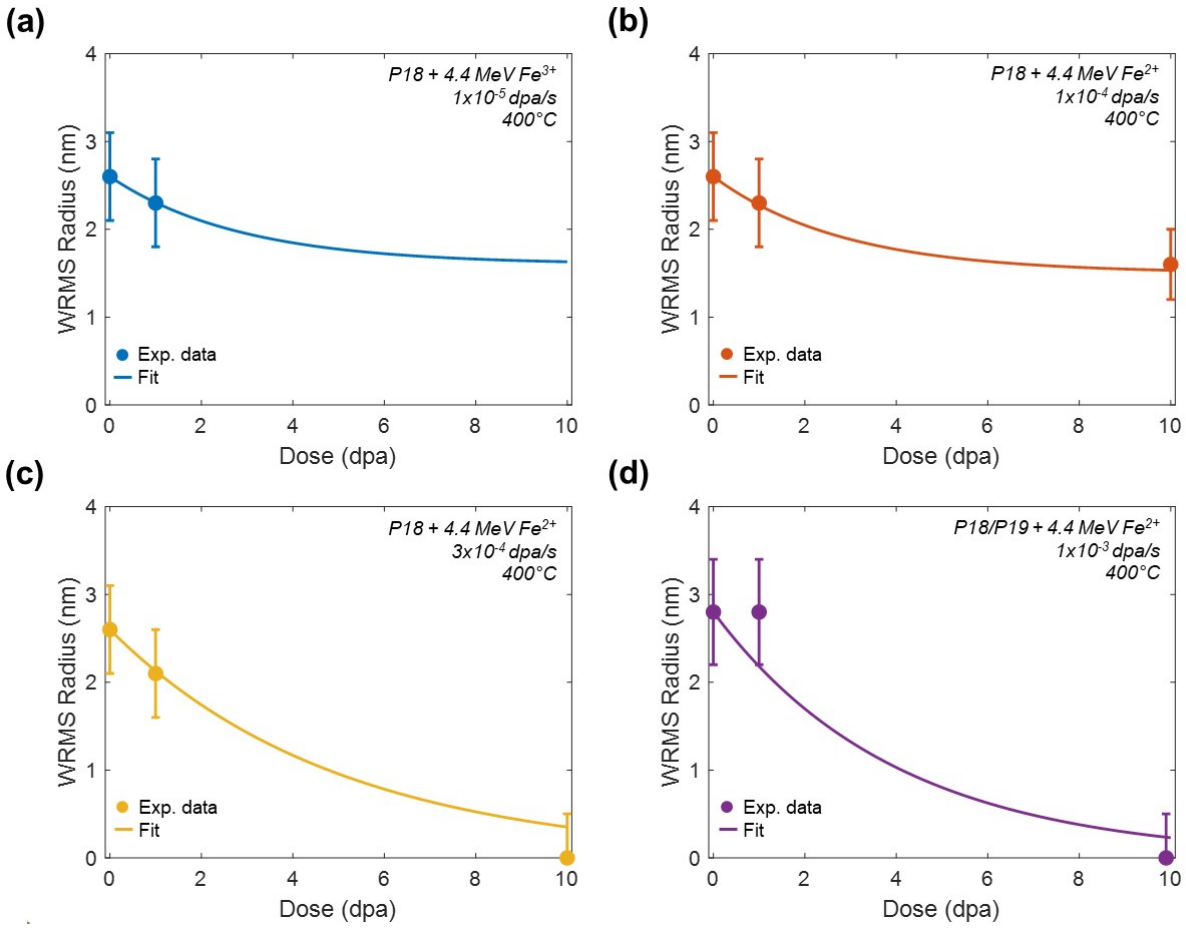

Figure 6.11 Exponential fit to the WRMS radius from the heavy ion irradiation of pre-existing α' precipitates at (a) $1x10^{-5}$ dpa/s, (b) $1x10^{-4}$ dpa/s, (c) $3x10^{-4}$ dpa/s, and (d) $1x10^{-3}$ dpa/s.

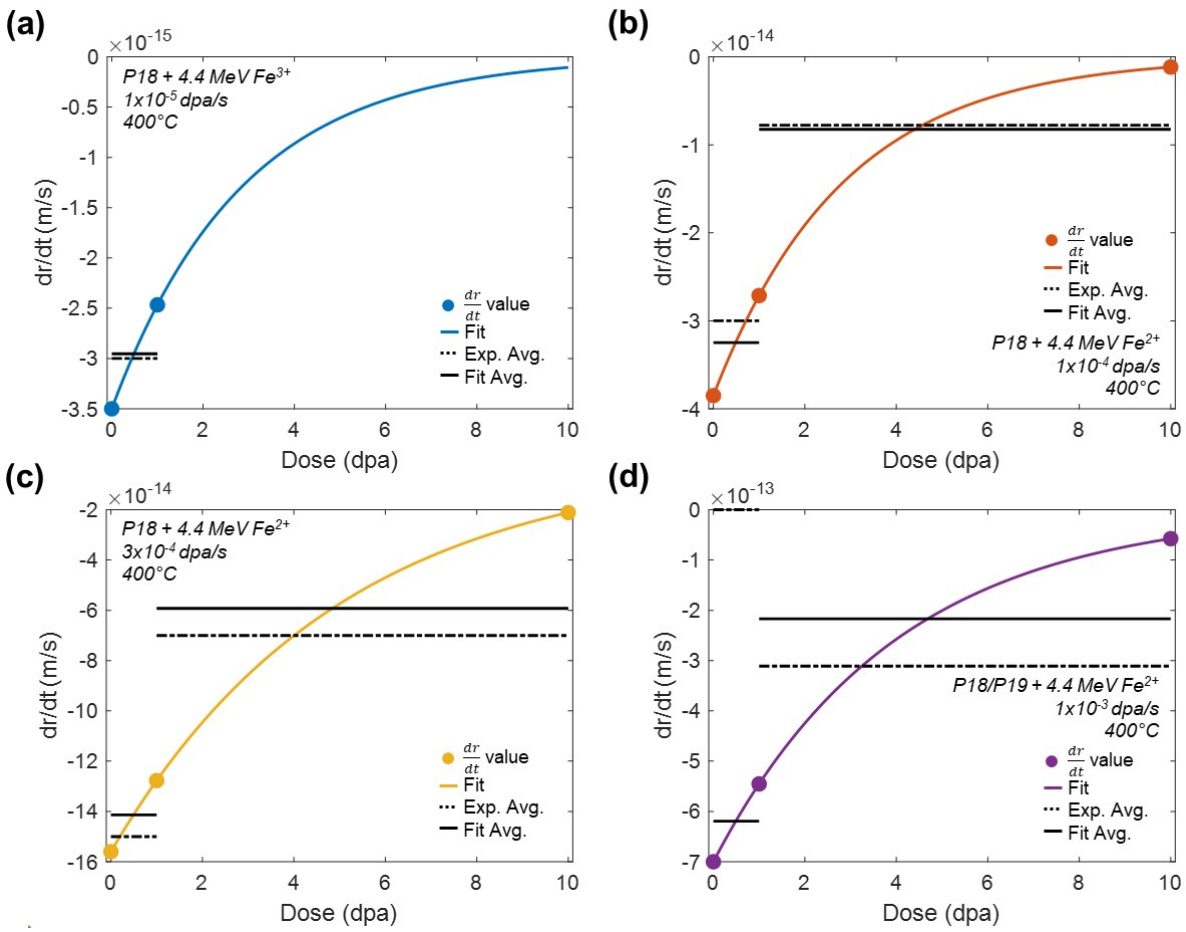

Figure 6.12 Corresponding growth (or dissolution) rate for the heavy ion irradiation of pre-existing α' precipitates at (a) $1x10^{-5}$ dpa/s, (b) $1x10^{-4}$ dpa/s, (c) $3x10^{-4}$ dpa/s, and (d) $1x10^{-3}$ dpa/s. Additionally, the experimental average growth rate (dashed black line) and the fit average growth rate (solid black line) are shown for the intervals of 0 to 1 dpa and 1 to 10 dpa to depict the quality of the exponential fit parameters. Circles represent the values of $\frac{dr}{dt}$ used to calculate BDP.

Table 6.6 Comparison of the NHM-based BDP calculated for 4.4 MeV Fe^{2+} irradiation of pre-existing α' precipitates at $1x10^{-4}$ dpa/s at 400°C with various fits used to describe the precipitate evolution. Irradiation at $1x10^{-5}$ dpa/s used 4.4 MeV Fe^{3+}.

α' evolution fit	Units	Dose (dpa)	BDP (P18+H/1e-5)	BDP (P18+H/1e-4)	BDP (P18+H/3e-4)	BDP (P19+H/1e-3)
Linear, 0-1 dpa fit	atoms/m^2·dpa	0	$2.56 \pm 6.13x10^{20}$	$2.58 \pm 8.75x10^{20}$	$4.92 \pm 8.97x10^{20}$	$0.61 \pm 0.64x10^{20}$
Linear, 0-1 dpa fit	atoms/m^2·dpa	1	$3.41 \pm 11.4x10^{20}$	$3.26 \pm 11.33x10^{20}$	$6.35 \pm 13.48x10^{20}$	$1.17 \pm 0.96x10^{20}$
Linear, 1-10 dpa fit	atoms/m^2·dpa	1	N.A.	$1.96 \pm 6.78x10^{20}$	$4.02 \pm 12.41x10^{20}$	$4.20 \pm 11.93x10^{20}$
Linear 1-10 dpa fit	atoms/m^2·dpa	10	N.A.	$5.12 \pm 2.37x10^{20}$	N.A.	N.A.
Steady state at 10 dpa	atoms/m^2·dpa	10	N.A.	$4.42 \pm 4.95x10^{20}$	N.A.	N.A.
Polynomial fit	atoms/m^2·dpa	0	N.A.	$2.27 \pm 1.37x10^{20}$	$5.00 \pm 1.90x10^{20}$	$1.08 \pm 12.4x10^{20}$
Polynomial fit	atoms/m^2·dpa	1	N.A.	$2.79 \pm 1.52x10^{20}$	$5.98 \pm 2.31x10^{20}$	$2.10 \pm 12.3x10^{20}$
Polynomial fit	atoms/m^2·dpa	10	N.A.	$4.42 \pm 2.22x10^{20}$	N.A.	N.A.
Exponential fit	atoms/m^2·dpa	0	$3.81 \pm 1.94x10^{20}$	$3.83 \pm 2.28x10^{20}$	$4.94 \pm 5.57x10^{20}$	$5.27 \pm 2.56x10^{20}$
Exponential fit	atoms/m^2·dpa	1	$3.99 \pm 1.99x10^{20}$	$3.56 \pm 1.92x10^{20}$	$5.57 \pm 2.70x10^{20}$	$5.13 \pm 2.08x10^{20}$
Exponential fit	atoms/m^2·dpa	10	N.A.	$4.52 \pm 2.23x10^{20}$	N.A.	N.A.

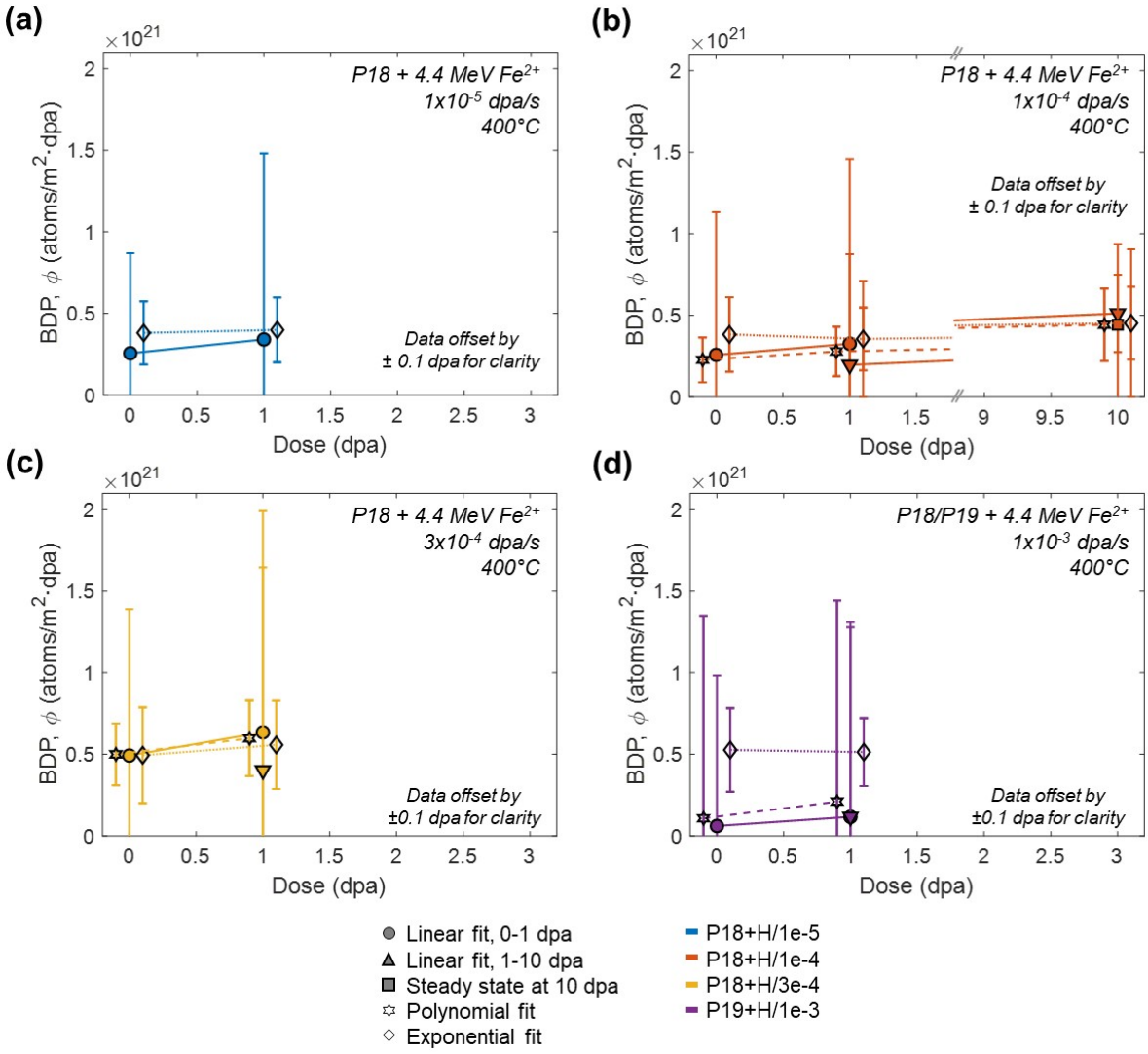

Figure 6.13 Comparison of BDP calculated for heavy ion irradiated pre-existing α' precipitates for a linear fit, polynomial, and exponential fit to the precipitate evolution to determine the dissolution term, where (a) is at $1x10^{-5}$ dpa/s, (b) is at $1x10^{-4}$ dpa/s, (c) is at $3x10^{-4}$ dpa/s, and (d) is at $1x10^{-3}$ dpa/s. The BDP calculated using linear fits to the precipitate evolution are shown in the solid symbols and solid line, polynomial fit is the open star symbol and dashed line, and exponential fit is the open diamond symbol and dotted line.

6.2 Determination of the BDP using α' precipitate Cr concentration

This section will discuss the effects of ballistic mixing and dependence of mixing on the cascade size and damage rate. First, the combination of Fick's second law and APT proximity histogram curves will be used to illustrate the ballistic mixing of the α' precipitate under heavy ion irradiation. Then the ballistic mixing models are used in combination with Fick's first law to calculate the BDP (referred to as the mixing based BDP).

6.2.1 Application of the ballistic mixing model to heavy ion irradiation

When ballistic mixing is dominant over radiation enhanced diffusion, mixing resulting from the irradiation cascades leads to blurring of the precipitate-matrix interface, leading to a decrease in solute concentration in a precipitate. This may be described by Fick's second law of diffusion:

$$c(x,t) = c_1 + \frac{c_2 + c_1}{2} \cdot \left[1 - erf\left(\frac{x}{\sqrt{4Dt}}\right)\right] \tag{6.19}$$

where c_1 and c_2 are the precipitate and matrix concentration, respectively [17]. The critical temperature determines when to apply the mixing model, and in this case, it applies to the heavy ion irradiation conditions. The critical temperature depends on the total diffusion coefficient, described in Eq. (2.13), and repeated as:

$$D = D_{bal} + D_{irr} \exp\left({}^{-Q}/_{kT}\right) \tag{6.20}$$

The total diffusion coefficient is composed of both a ballistic mixing term and the radiation enhanced diffusion term. The ballistic mixing term is described as:

$$D_{bal} \cong \frac{1}{6}\lambda^2 \eta K \tag{6.21}$$

where λ is jump length (or lattice parameter), K is the defect production rate, and η is the number of replacements per displacement (or rpa) [20]. The radiation enhanced diffusion term D_{irr} was thoroughly described in Section 6.1.1. Lastly, $Q = E_m^v/2$.

Interface mixing under heavy ion irradiation at 1 dpa and 10 dpa at a damage rate of $1\text{x}10^{-4}$ dpa/s was captured with the mixing model presented. For these calculations, the total diffusion coefficient is given by Eq. (6.20). The concentration terms (c_1 and c_2) were from the sigmoidal

fitting of the proximity histogram (or proxigram) discussed previously in Chapter 4 as the method used to determine Cr concentration in α' precipitates. The proxigram used for the mixing model was the average proxigram for the condition. The proxigram was also selected to ensure that the plateau, or precipitate core, extended beyond the mixing zone for optimal fitting. The time variable was adjusted to fit the model curve best to the proxigram. R^2 value of 0.997 for both 1 and 10 dpa suggest the fits provide a good match. Figure 6.14 shows the mixing model applied to the APT proxigram and Table 6.7 provides the corresponding data in mixing model.

The mixing model also captures the ballistic mixing at 1 dpa at other damage rates under heavy ion irradiation. In the same process for P18+H/1e-4, the concentration terms (c_1 and c_2) were from the sigmoidal fitting of the proxigram, the diffusion coefficient was calculated using the APT values for the given condition using Eq. (6.19), and the time, t, used in the mixing model was adjusted to fit the model curve best to the proxigram. Figure 6.15 shows the mixing model applied to the APT proxigrams for each heavy ion irradiation at 1 dpa and the values used to calculate the mixing model in Table 6.8. Again, the R^2 values were near unity for all conditions, supporting the quality of the fit between the mixing model and the APT proxigrams. The mixing model provides a suitable match to the proxigrams obtained from APT, suggesting that α' precipitates are subjected to ballistic mixing which leads to the dissolution or reduction in solute concentration and ultimately the steady state Cr concentration lower than the equilibrium value that was observed in this thesis, and has been reported in other works [19,21–23].

A material with nanoprecipitates is known to encounter trajectory aberrations with atom probe, leading to blurring of the matrix-precipitate interface [24,25]. This effect is due to the lower evaporation field of Cr compared to Fe leading to artificially high densities of Cr in the α' [26]. This is primarily a problem with small precipitates, in which the interface blurring consumes the precipitate core. This artifact was not a concern when applying the mixing model for multiple reasons. First, the proxigrams were ensured to be large enough that the core concentration was prominent. This was evident by the plateau of Cr concentration within the precipitate. Second, the proxigram of α' observed in electron irradiated as-received 15Cr (AR+E/4.6e-4/0.46) showed the mixing zone, defined as the width between the maximum Cr concentration and the minimum Cr concentration, was ~1.5-2nm (Figure 6.16). The mixing zone can be artificially broadened by trajectory aberrations. This was minimized by using optimal APT parameters (e.g., low temperature to minimize preferential field evaporation and lower pulse repetition to prevent large

multi-heat events on the detector). Recent simulation work by Liao, et al [27] on the irradiation of pre-existing α' precipitates in Fe-15Cr-8Al alloy has shown a similar mixing effect on the concentration profile after irradiation, where the precipitate-matrix interface has become mixed. Additionally, the mixing width was shown to be ~1.5-2nm independent of the initial α' size. This supports the assertion the APT observations of widths of the same order may actually be ballistic mixing.

The mixing based BDP can be determined from the Cr concentration profiles in the precipitates using Fick's first law:

$$J_{recoil} = D\frac{\Delta C}{\Delta x}N_{at} \tag{6.22}$$

where $\frac{\Delta C}{\Delta x}$ is the difference in c_1 and c_2 over the distance of the interface (Δx). This method was also used in Ref. [28] and discussed in Section 2.4 A variation can be made by replacing $\frac{\Delta C}{\Delta x}$ with the instantaneous slope at the precipitate-matrix interface, $\frac{dC}{dx}(0,t)$. Eq. (6.23) is the derivative of Eq. (6.19) used to calculate the instantaneous slope at the interface:

$$\frac{dc}{dx}(x,t) = \frac{(c_1 - c_2)\exp\left(-x^2/4Dt\right)}{2\sqrt{\pi}\sqrt{Dt}} \tag{6.23}$$

and gives the flux of atoms leaving the precipitate, J_{recoil}, as:

$$J_{recoil} = D\frac{\Delta C}{\Delta x}N_{at} = D\frac{dc}{dx}(0,t)N_{at} \tag{6.24}$$

Therefore, the BDP is the quotient of the flux of atoms leaving the precipitate, now modified to be Eq. (6.24), and the defect production rate:

$$\varphi = \frac{J_{recoil}}{\xi K_0} \tag{6.25}$$

The mixing BDP for heavy ion irradiation is taken as 1.5 ± 0.7 x10^{20} atoms/m^2·dpa, the value at 1x10^{-4} dpa/s at 1 dpa. The mixing based BDP was constant for all damage rates at 1 dpa under heavy ion irradiation. The comparison is made in Figure 6.17, showing the calculated values for the heavy ion irradiation conditions. Table 6.9 shows the resulting values for the mixing BDP for each heavy ion irradiation condition, as well as a comparison to the other NHM-based BDP values. Additionally, at 10 dpa, the mixing BDP is approximately the same value at 1.7 ± 0.7 x10^{20} atoms/m^2·dpa, compared to 1.5 ± 0.7 x10^{20} atoms/m^2·dpa at 1 dpa.

The mixing based BDP was similar in value to the NHM-based BDP, showing that the BDP can be calculated through multiple methods. The connection between the two BDP values

also shows a connection between the different processes occurring under irradiation: the precipitate size evolution described by the NHM model, and the Cr concentration evolution described by the mixing model. The NHM-based BDP was calculated primarily using the precipitate size evolution and dissolution or growth rate under irradiation, whereas the mixing based BDP was determined based on the Cr concentration evolution under irradiation. Figure 6.18 shows the comparison between both the mixing based and NHM-based BDP at 1 dpa, with the NHM-based BDP (exponential fit) in orange and the mixing based BDP in green. Although the NHM based BDP value was approximated at 0 dpa for the $1x10^{-4}$ dpa/s condition, the values for each damage rate at 1 dpa are present for a better comparison to the mixing model based BDP at 1 dpa (as the mixing BDP cannot be calculated at 0 dpa). From the figure, it is apparent that the values are within error and are separated by a factor of ~2. The heavy ion irradiation BDP can be estimated to be ~$3x10^{20}$ atoms/m^2·dpa, a value between the NHM-based and mixing based BDPs.

The BDP determined for heavy ion irradiation are similar to previously determined values and estimates for the BDP. For this work, the BDP for heavy ion irradiation was between 1.5-$4.5x10^{20}$ atoms/m^2·dpa between the two different approaches to calculate it, which was taken to be ~$3x10^{20}$ atoms/m^2·dpa. Previous values for the heavy ion irradiation BDP, estimated through a method similar to the mixing model, showed values between ~$2x10^{19}$-$1.4x10^{20}$ atoms/m^2·dpa [19,29] for heavy ion irradiation. The mixing based BDP from this work was very similar, at ~$1.5x10^{20}$ atoms/m^2·dpa. Other BDP values from literature determined through other methods for neutron and heavy ion irradiation include ~10^{18} atoms/m^2·dpa [1], ~$3x10^{19}$ atoms/m^2·dpa [30], and ~$1.17x10^{21}$ atoms/m^2·dpa [19]. The BDP, at ~$3x10^{20}$ atoms/m^2·dpa, is well within the expected range from literature. Zhao, et al [19] calculated the BDP ($1.4x10^{20}$ atoms/m^2·dpa and $1.17x10^{21}$ atoms/m^2·dpa) with application to heavy ion irradiation of Fe-18Cr, similar to 15Cr used in this work, and found these values were either an underestimate or overestimate and ultimately used a value of ~$8x10^{20}$ atoms/m^2·dpa, only two times higher than the value calculated in this work. The BDP calculated for experiments for heavy ion irradiation matches suitably to literature values.

While the BDP value for heavy ion irradiation corresponded well to the literature values, a simple calculation was completed to determine if this BDP was on the right order of magnitude. For a precipitate with a 2.5 nm radius (# atoms in precipitate = $4\pi r^3 N_{at}/3$), assuming spherical precipitate with an atomic density of $8.43x10^{28}$ atoms/m^3, there are ~5,500 atoms. In the case for heavy ion irradiation, a BDP ranging from 1.5-$3.8x10^{20}$ atoms/m^2·dpa ejects ~11,000-30,000

atoms per dpa from a 2.5 nm radius precipitate (# atoms ejected = $4\pi r^2 \cdot \varphi$). Considering the irradiation condition at 10^{-4} dpa/s, the number of atoms returning to the precipitate can be estimated from the growth of an α' precipitate under electron irradiation, where there was no ballistic dissolution to impede the growth. The precipitate volumetric growth was calculated as $\Delta V = 4\pi(r_o^3 - r_i^3)N_{at}/3$, where r_o was the precipitate size at 1 dpa and r_i was the initial precipitate size. From ΔV at 10^{-4} dpa/s under electron irradiation, the number of atoms returning to the precipitate in 1 dpa can be estimated as ~7,000 atoms (# atoms $\Delta V = \Delta V \cdot N_{at}$). By balancing the number of atoms leaving and entering a 2.5 nm radius in 1 dpa, there is a net loss of -1,500 to -22,000 atoms. The dissolution of 1,500 atoms results in the complete dissolution or reduction to 4,000 atoms, or ~1.6 nm radius precipitate after 1 dpa of irradiation, which matches the experimental results at 10 dpa of irradiation, the steady state size. These estimates show that the BDP very good match to the value expected based on the experiments for heavy ion irradiation.

Table 6.7 Mixing model calculations for heavy ion irradiation at $1x10^{-4}$ dpa/s for 1 and 10 dpa.

Term	Definition	Units	P18+H/1e-4/1	P18+H/1e-4/10
t	Time	dpa	0.80	0.25
c_1	α' precipitate conc.	atomic fraction	0.814	0.586
c_2	Matrix conc.	atomic fraction	0.121	0.145
D	Total diffusion coefficient	m^2/s	$7.14x10^{-23}$	$7.55x10^{-23}$

Table 6.8 Mixing model calculations for heavy ion irradiation at each damage rate at 1 dpa.

Term	Definition	Units	P18+H/1e-5/1	P18+H/1e-4/1	P18+H/3e-4/1	P18+H/1e-3/1
t	Time	dpa	0.28	0.80	0.85	0.40
c_1	α' precipitate conc.	atomic fraction	0.778	0.814	0.819	0.84
c_2	Matrix conc.	atomic fraction	0.112	0.121	0.124	0.134
D	Total diffusion coefficient	m^2/s	7.12×10^{-24}	7.14×10^{-23}	2.14×10^{-22}	7.27×10^{-22}

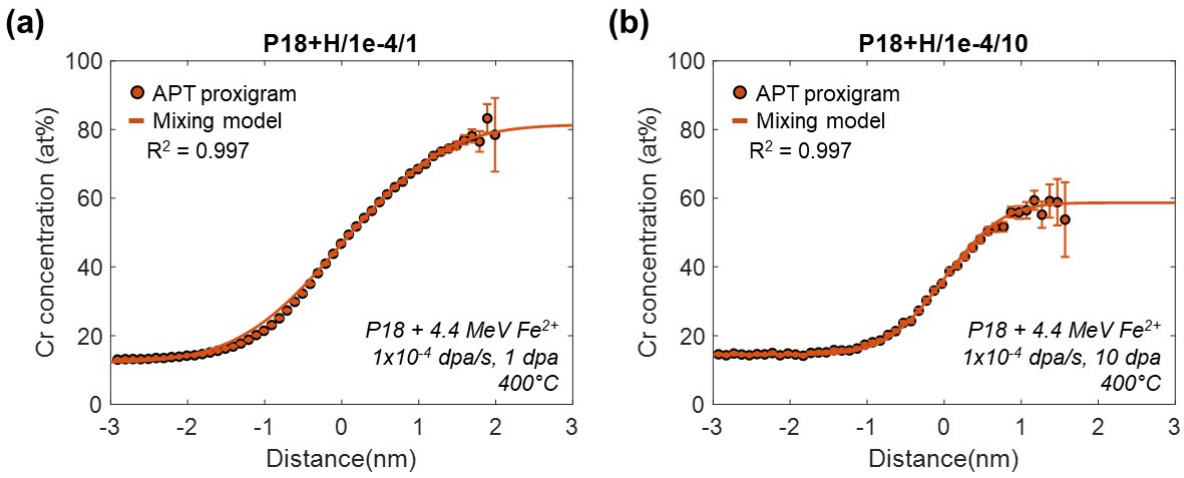

Figure 6.14 APT proxigram overlaid with the ballistic mixing model results for heavy ion irradiation at 1x10^{-4} dpa/s at (a) 1 dpa and (b) 10 dpa.

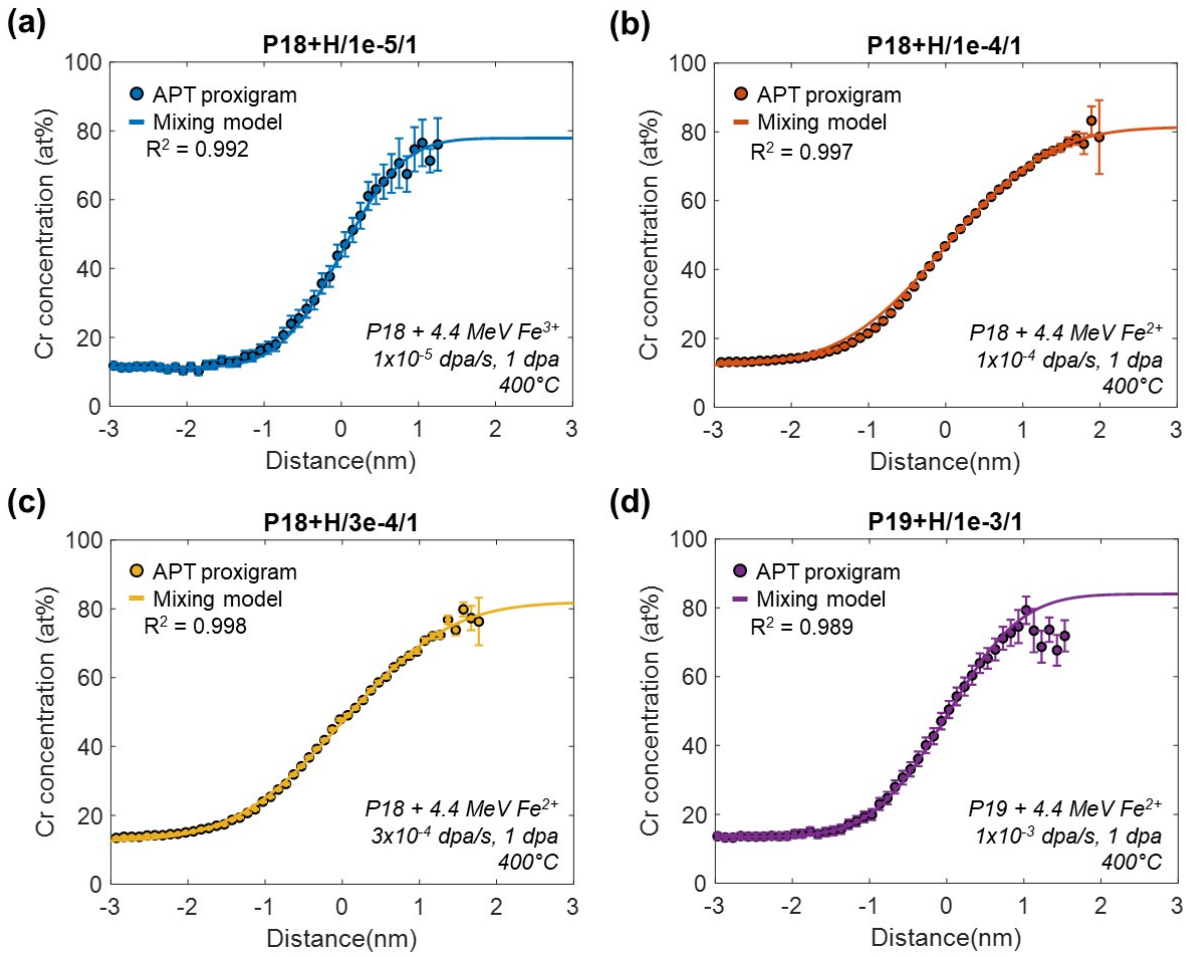

Figure 6.15 APT proxigram overlaid with the ballistic mixing model results for heavy ion irradiation at 1 dpa for (a) $1x10^{-5}$ dpa/s, (b) $1x10^{-4}$ dpa/s, (c) $3x10^{-4}$ dpa/s, and (d) $1x10^{-3}$ dpa/s.

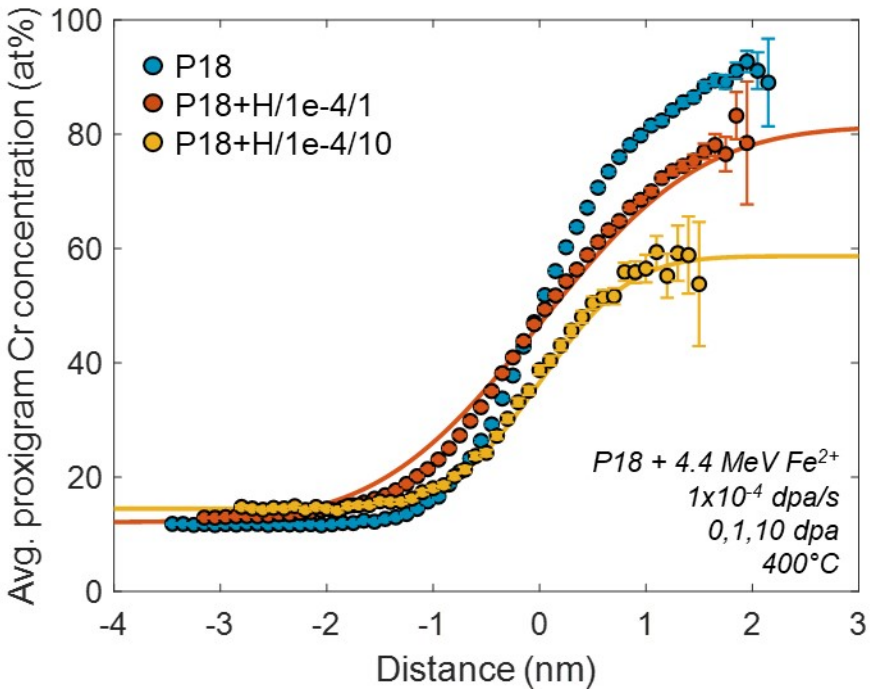

Figure 6.16 Proxigram comparison of P18 (initial, blue) to the heavy ion irradiated conditions P18+H/1e-4/1 (orange) and P18+H/1e-4/10 (yellow) alongside the mixing model for heavy ion irradiation condition to highlight the trajectory aberrations versus ballistic mixing.

Table 6.9 Comparison of mixing based BDP to NHM-based BDP (with multiple fits) calculations for heavy ion irradiation at each damage rate at 1 and 10 dpa.

	Units	P18+H/1e-5/1	P18+H/1e-4/1	P18+H/1e-4/10	P18+H/3e-4/1	P18+H/1e-3/1
Damage rate	dpa/s	$1x10^{-5}$	$1x10^{-4}$	$1x10^{-4}$	$3x10^{-4}$	$1x10^{-3}$
Dose	dpa	1	1	10	1	1
Mixing-based BDP	atoms/m^2dpa	$2.50 \pm 1.15\ x10^{20}$	$1.54 \pm 0.71\ x10^{20}$	$1.76 \pm 0.72\ x10^{20}$	$1.50 \pm 0.69\ x10^{20}$	$2.24 \pm 1.03\ x10^{20}$
NHM-based BDP: linear fit, 0-1 dpa	atoms/m^2dpa	$3.41 \pm 11.4\ x10^{20}$	$3.26 \pm 11.33\ x10^{20}$	N.A.	$6.35 \pm 13.48\ x10^{20}$	$1.17 \pm 0.96\ x10^{20}$
NHM-based BDP: linear fit, 1-10 dpa	atoms/m^2dpa	N.A.	$1.96 \pm 6.78\ x10^{20}$	$5.12 \pm 2.37\ x10^{20}$	$4.02 \pm 12.41\ x10^{20}$	$4.20 \pm 11.93\ x10^{20}$
NHM-based BDP: steady state at 10 dpa	atoms/m^2dpa	N.A.	N.A.	$4.42 \pm 4.95\ x10^{20}$	N.A.	N.A.
NHM-based BDP: polynomial fit	atoms/m^2dpa	N.A.	$2.79 \pm 1.52\ x10^{20}$	$4.42 \pm 2.22\ x10^{20}$	$5.98 \pm 2.31\ x10^{20}$	$2.10 \pm 12.3\ x10^{20}$
NHM-based BDP: exponential fit	atoms/m^2dpa	$3.99 \pm 1.99\ x10^{20}$	$3.56 \pm 1.92\ x10^{20}$	$4.52 \pm 2.23\ x10^{20}$	$5.57 \pm 2.70\ x10^{20}$	$5.13 \pm 2.08\ x10^{20}$

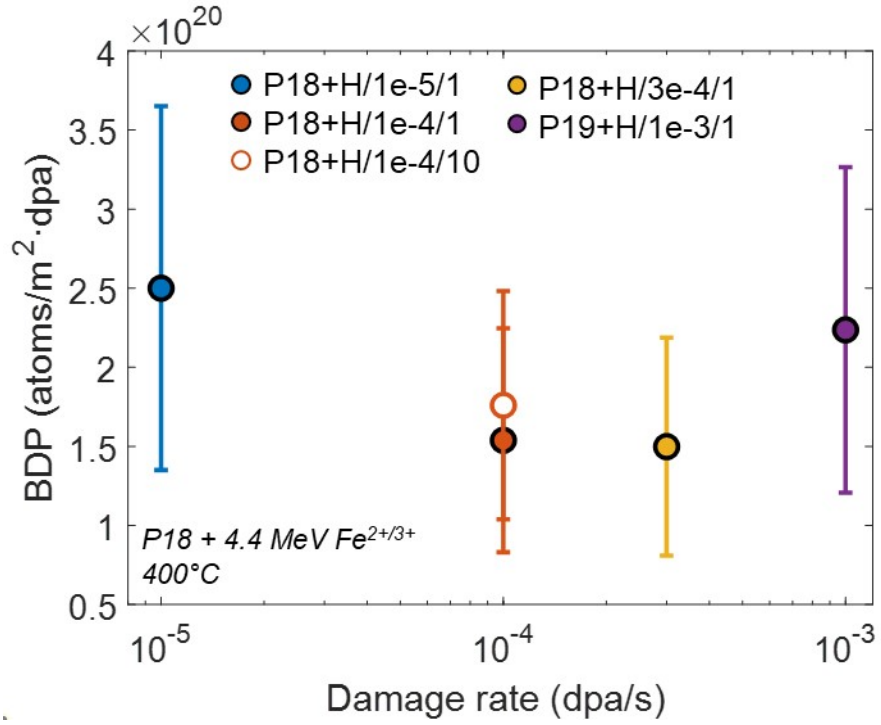

Figure 6.17 Mixing based BDP for heavy ion irradiation for each damage rate at 1 dpa and $1x10^{-4}$ dpa/s at 10 dpa (open orange circle).

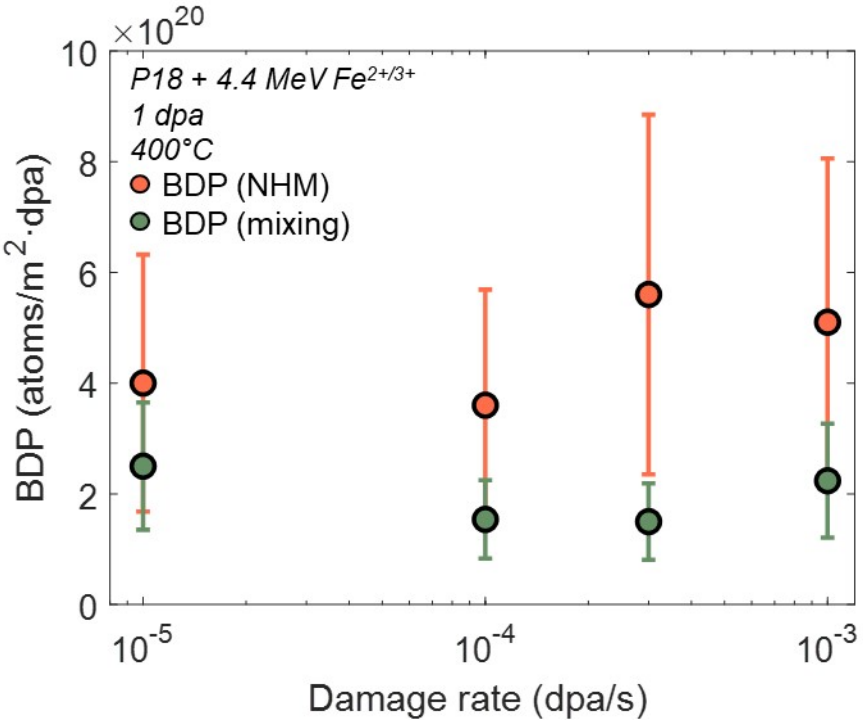

Figure 6.18 Comparison of the NHM-based BDP (exponential fit) to the mixing based BDP for heavy ion irradiation at each damage rate at 1 dpa.

6.2.2 Application of the ballistic mixing model to proton irradiation

As proton irradiation is also subject to a ballistic mixing, interface mixing can also be captured using the mixing model presented in Section 6.2.1. The mixing model was applied to the proton irradiation of pre-existing α' precipitates at 1 dpa and 10 dpa at a damage rate of $1x10^{-4}$ dpa/s. For these calculations, the total diffusion coefficient was calculated using Eq. (6.20). The concentration terms (c_1 and c_2) were from the sigmoidal fitting of the proxigrams. The proxigram used for the mixing model was the average proxigram for the condition, ensuring that the core concentration was representative for the condition and that the proxigram plateau extended beyond the mixing zone. For both 1 and 10 dpa condition (P19+P/1e-4/1, P19+P/1e-4/10), the time was adjusted to fit the model curve best to the proxigram. R^2 values of 0.991 and 0.998 for 1 and 10 dpa, respectively, suggest the fits provide a good match. Figure 6.14 shows the mixing model applied to the APT proxigram and Table 6.7 provides the corresponding data in mixing model.

The mixing based BDP for proton irradiation was similar in value to the 0 dpa condition for the NHM-based BDP, 2.3-6.8x10^{19} atoms/m^2·dpa and 8.6 ± 6.2 x10^{19} atoms/m^2·dpa, respectively. The NHM-based BDP increasing with dose is attributed to low APT statistics making it poorly suited as the BDP is expected to be a constant value independent to dose and damage rate. Whereas the mixing based BDP determined a BDP for 1 and 10 dpa for proton irradiation that was similar to the 0 dpa condition for the NHM-based BDP. The increase in NHM-based BDP with dose was errant and the value at 0 dpa is a suitable value for the BDP for proton irradiation. A comparison between the NHM-based BDP and the mixing-based BDP is shown in Figure 6.20 and in Table 6.11.

The BDP values from literature are for neutron and heavy ion irradiation and has not been calculated for proton irradiation. Due to the smaller cascade size of proton irradiation, the BDP is expected to be smaller. As discussed in the previous section, the literature values for heavy ion and neutron BDP ranges from 10^{18}-10^{21} atoms/m^2·dpa. In this thesis work the proton irradiation BDP was between 2-9x10^{19} atoms/m^2·dpa, below most reported values for heavy ion and neutron irradiation BDP values, as expected. These values are ~4-5 times smaller than the heavy ion irradiation BDP, consistent with the smaller damage cascade exhibited by proton irradiation.

While the BDP value for proton irradiation was below most literature values as expected, a simple calculation was completed to determine if this BDP near the right value. The BDP value

for proton irradiation was determined to be suitable by estimating the number of atoms dissolved per dpa from a precipitate. For a precipitate with a 2.5 nm radius (# atoms in precipitate = $4\pi r^3 N_{at}/3$), assuming spherical precipitate with an atomic density of 8.43×10^{28} atoms/m^3, there are ~5,500 atoms. Considering the proton irradiation condition at 10^{-4} dpa/s, a BDP between 2.3-8.6×10^{19} atoms/m^2·dpa dissolves ~5,000-5,700 atoms per dpa from a 2.5 nm radius precipitate (# atoms ejected = $4\pi r^2 \cdot \varphi$). The number of atoms dissolved per dpa for proton irradiation is approximately 2-5 times smaller than the number of atoms dissolved under heavy ion irradiation (~11,000-30,000), corresponding to the same size difference in the BDP for proton and heavy ion irradiation. The number of atoms returning to the precipitate can be estimated from the growth of an α' precipitate under electron irradiation, where there was no ballistic dissolution to impede the growth. The precipitate volumetric growth was calculated as $\Delta V = 4\pi(r_o^3 - r_i^3)N_{at}/3$, where r_o was the precipitate size at 1 dpa and r_i was the initial precipitate size. From ΔV at 10^{-4} dpa/s under electron irradiation, the number of atoms returning to the precipitate in 1 dpa can be estimated as ~7,000 atoms (# atoms $\Delta V = \Delta V \cdot N_{at}$). By balancing the number of leaving and entering a 2.5 nm radius in 1 dpa, there is a net gain of 1,300 to 2,000 atoms. This yields a precipitate growth to a size of ~2.7-3.1 nm radius, which matches the experimental results with the small amount of precipitate growth observed after 1 dpa under proton irradiation. These estimates show that the BDP very good match to the value expected based on the experiments for heavy ion irradiation.

Table 6.10 Mixing model calculations for proton irradiation at $1x10^{-4}$ dpa/s for 1 and 10 dpa.

Term	Definition	Units	P19+P/1e-4/1	P19+P/1e-4/10
t	Time	dpa	0.5	0.17
c_1	α' precipitate conc.	atomic fraction	0.900	0.903
c_2	Matrix conc.	atomic fraction	0.139	0.141
D	Total diffusion coefficient	m^2/s	$5.13x10^{-23}$	$1.56x10^{-22}$
φ	BDP	atoms/m^2dpa	$2.27 \pm 0.70\ x10^{19}$	$6.78 \pm 2.31\ x10^{19}$

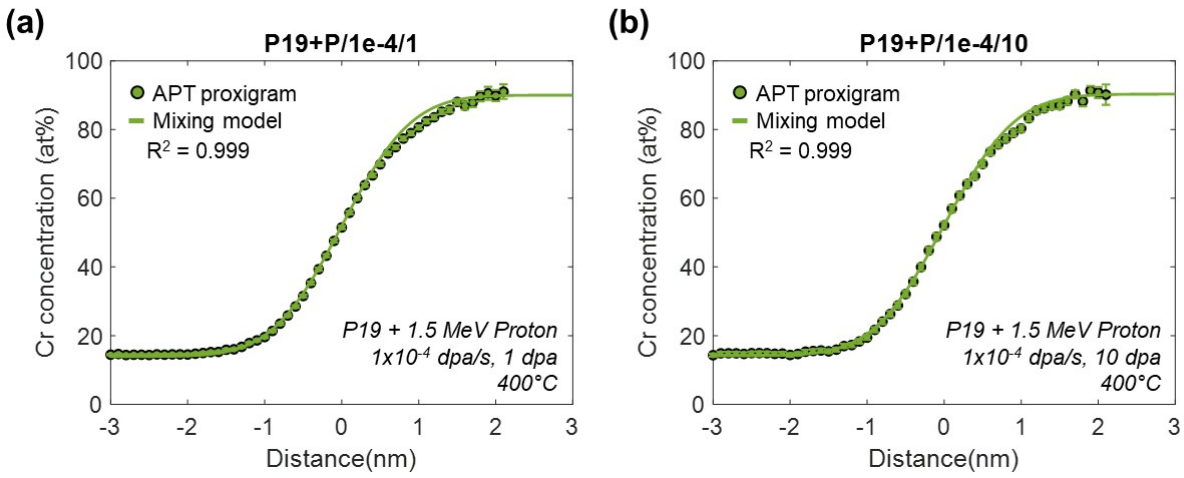

Figure 6.19 APT proxigram overlaid with the ballistic mixing model results for proton irradiation at 1x10^{-4} dpa/s at (a) 1 dpa and (b) 10 dpa.

Table 6.11 Comparison of the mixing-based BDP to NHM-based BDP (with multiple fits) calculated for 1.5 MeV proton irradiation of pre-existing α' precipitates at $1x10^{-4}$ dpa/s at 400°C.

α' evolution fit	Units	0 dpa	1 dpa	10 dpa
Mixing-based BDP	atoms/m^2·dpa	--	2.27 ± 0.70 $x10^{19}$	6.78 ± 2.31 $x10^{19}$
Linear, 0-1 dpa fit	atoms/m^2·dpa	$9.63 \pm 15.4x10^{19}$	$2.92 \pm 11.9x10^{20}$	--
Linear 1-10 dpa fit	atoms/m^2·dpa	--	$2.92 \pm 11.8x10^{20}$	$8.04 \pm 3.88x10^{20}$
Steady state at 10 dpa	atoms/m^2·dpa	--	--	$8.15 \pm 9.02x10^{20}$
Polynomial fit	atoms/m^2·dpa	$8.57 \pm 6.51x10^{19}$	$2.84 \pm 1.48x10^{20}$	$8.15 \pm 3.96x10^{20}$
Exponential fit	atoms/m^2·dpa	$8.60 \pm 6.20x10^{19}$	$2.85 \pm 1.47x10^{20}$	$8.10 \pm 3.96x10^{20}$

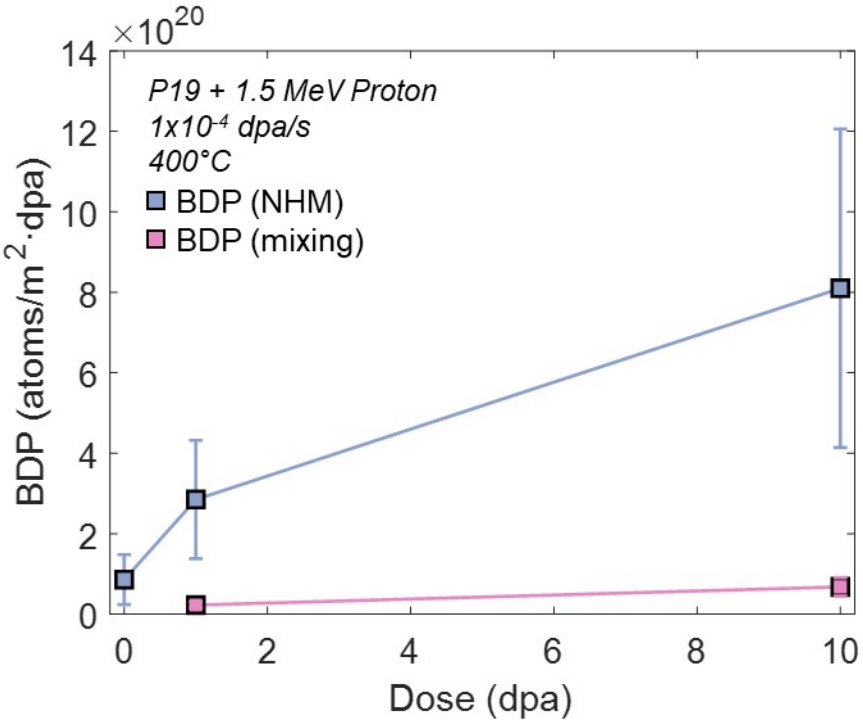

Figure 6.20 Comparison of the NHM-based BDP (exponential fit) to the mixing based BDP for proton irradiation at $1x10^{-4}$ dpa/s.

6.3 Calculation of the BDP for α' nucleation

The primary focus of this thesis work was understanding the α' precipitate stability under irradiation and connecting the BDP to the precipitate stability. To confirm the long-term stability of α' precipitates under heavy ion irradiation, an as-received Fe-15Cr sample was irradiated at $1x10^{-4}$ dpa/s to 1 and 10 dpa, as presented in Section 5.2, referred to as AR+H/1e-4/1 and AR+H/1e-4/10.

The BDP was calculated for AR+H/1e-4/1 and AR+H/1e-4/10 using the NHM model. The exponential fit method from Section 6.1.4 was used here, with modification to describe α' precipitate growth under heavy ion irradiation, rather than dissolution. Figure 6.21(a) shows the exponential fit applied to the WRMS radii. Figure 6.21(b) shows the growth rate, including the average experimental growth rate and the average fit growth rate. The c parameter for the steady state for AR+H/1e-4 was determined by comparing the heavy ion irradiation of the as-received sample to the heavy ion irradiated pre-existing α' precipitates. The evolution of the α' precipitates, either from nucleation or from the pre-existing α' precipitates, evolves toward a steady state at ~1.5 nm radius, shown in Figure 6.22. Exponential fits are applied to P18+H/1e-4 and AR+H/1e-4 to better illustrate the precipitate evolution. From this result, it is apparent that a steady state has been reached at $1x10^{-4}$ dpa/s under heavy ion irradiation by 10 dpa.

The NHM based BDP was calculated to be $2.2 \pm 5.1x10^{20}$ atoms/m^2·dpa and $3.7 \pm 1.8x10^{20}$ atoms/m^2·dpa for 1 and 10 dpa, respectively, for heavy ion irradiation of as-received 15Cr at $1x10^{-4}$ dpa/s. The BDP at 10 dpa is similar to the BDP at P18+H/1e-4/10 ($4.5 \pm 2.2x10^{20}$ atoms/m^2·dpa). This is because the α' precipitates have reached a steady state by 10 dpa and have a similar microstructure.

The mixing model was applied to the as-received sample to determine the BDP at 10 dpa. Unlike the α' precipitates in Section 6.2.1, which started at higher Cr concentration and were subjected to ballistic mixing to reach a steady state Cr concentration under heavy ion irradiation, the α' precipitates in the as-received 15Cr were competing with ballistic mixing to nucleate and enrich in Cr concentration. The time, t, in the mixing model was set to a time that gave a good match to the proxigram. Concentration values, c_1 and c_2, were determined from the proxigram. The diffusion coefficient was calculated based on the APT data at AR+H/1e-4/10. Figure 6.23

shows the mixing model overlaid with the APT proxigram for AR+H/1e-4/10. Table 6.13 provides the data used to calculate the mixing based BDP for AR+H/1e-4/10.

The NHM-based BDPs and the mixing based BDP for AR+H/1e-4 exhibit good agreement. Figure 6.24 shows the NHM-based BDP tabulated for AR+H/1e-4/1 and AR+H/1e-4/10 from the exponential fit and the mixing based BDP for AR+H/1e-4/10 in comparison to the previously calculated NHM and mixing based BDPs for P18+H/1e-4/1 and P18+H/1e-4/10. The values at 10 dpa for the NHM based model match well. This is because the α' precipitates have reached a steady state and have a similar microstructure between the two conditions. The mixing based BDP for AR+H/1e-4/10 is also similar to the NHM based BDPs at 10 dpa, or about double the value for the mixing based BDP for P18+H/1-4/10.

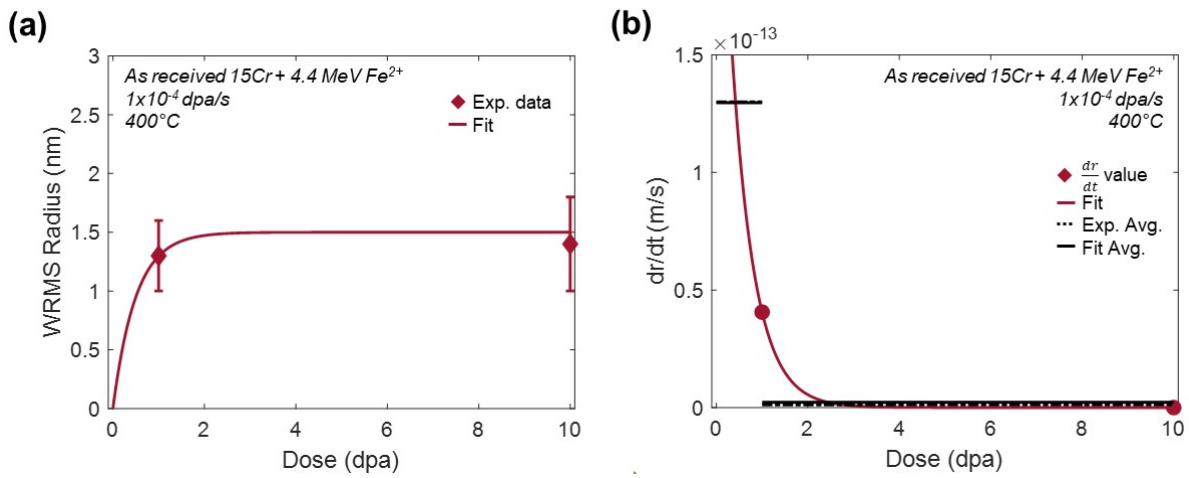

Figure 6.21 (a) Exponential fit to the WRMS radius from the heavy ion irradiation of as-received 15Cr, and (b) the corresponding growth rate (red), experimental average growth rate (dashed black line) and the fit average growth rate (solid black line) are shown for the intervals of 0 to 1 dpa and 1 to 10 dpa to depict the quality of the exponential fit parameters. Circles represent the values of $\frac{dr}{dt}$ used at those doses to calculate BDP.

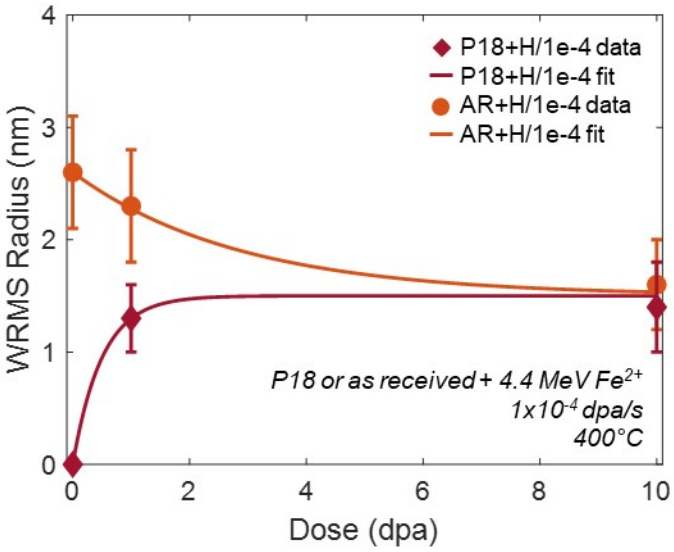

Figure 6.22 Comparison of the heavy ion irradiation of as-received 15Cr and the pre-existing α' precipitates at $1x10^{-4}$ dpa/s. The exponential fits are included to emphasize the steady state has been achieved by 10 dpa for as-received and pre-existing α' precipitates.

Table 6.12 BDP calculated from the NHM model for as-received 15Cr under heavy ion irradiation at 1x10^{-4} dpa/s at 10 dpa.

	Definition	Units	P18+H/1e-4/1	P18+H/1e-4/10
C_e	Solubility limit	at. fraction	0.105	0.105
C_m	Matrix conc.	at. fraction	0.158	0.153
C_p	α' conc.	at. fraction	0.461	0.520
r	α' WRMS radius	m	1.2x10^{-9}	1.4x10^{-9}
n	α' number density	m^{-3}	1.7x10^{23}	1.4x10^{23}
${k_s}^2(\alpha')$	α' sink strength	m^{-2}	2.7x10^{16}	3.2x10^{16}
${k_s}^2(dislocations)$	Dislocation sink strength	m^{-2}	3.0x10^{14}	3.0x10^{14}
${k_s}^2(cavities)$	Cavities sink strength	m^{-2}	0	0
${k_s}^2(total)$	Total stink strength	m^{-2}	2.7x10^{16}	3.2x10^{16}
ξ	Efficiency	unitless	0.1	0.1
K_0	Damage rate	dpa/s	1x10^{-4}	1x10^{-4}
D_{irr}	RED	m^2/s	8.17x10^{-22}	6.99x10^{-22}
$\frac{dr}{dt}$	Growth/dissolution rate	m/s	4.06x10^{-14}	6.18x10^{-22}
φ	Ballistic dissolution parameter	atoms/m^{2}s	2.97 ± 4.96 x10^{20}	3.71 ± 1.84 x10^{20}

Table 6.13 Mixing model calculations for as-received 15Cr under heavy ion irradiation at $1x10^{-4}$ dpa/s at 10 dpa.

Term	Definition	Units	AR+H/1e-4/10
t	Time	dpa	0.1
c_1	α' precipitate conc.	atomic fraction	0.579
c_2	Matrix conc.	atomic fraction	0.139
D	Total diffusion coefficient	m^2/s	$2.42 \pm x10^{-22}$
φ	Ballistic dissolution parameter	$atoms/m^2s$	$5.01 \pm 2.14\ x10^{20}$

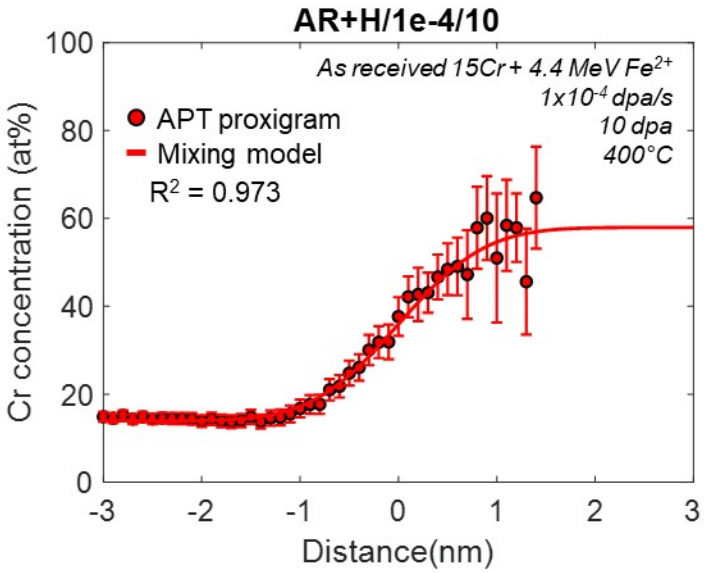

Figure 6.23 APT proxigram overlaid with the ballistic mixing model results for heavy ion irradiation of as-received 15Cr at 10 dpa (AR+H/1e-4/10).

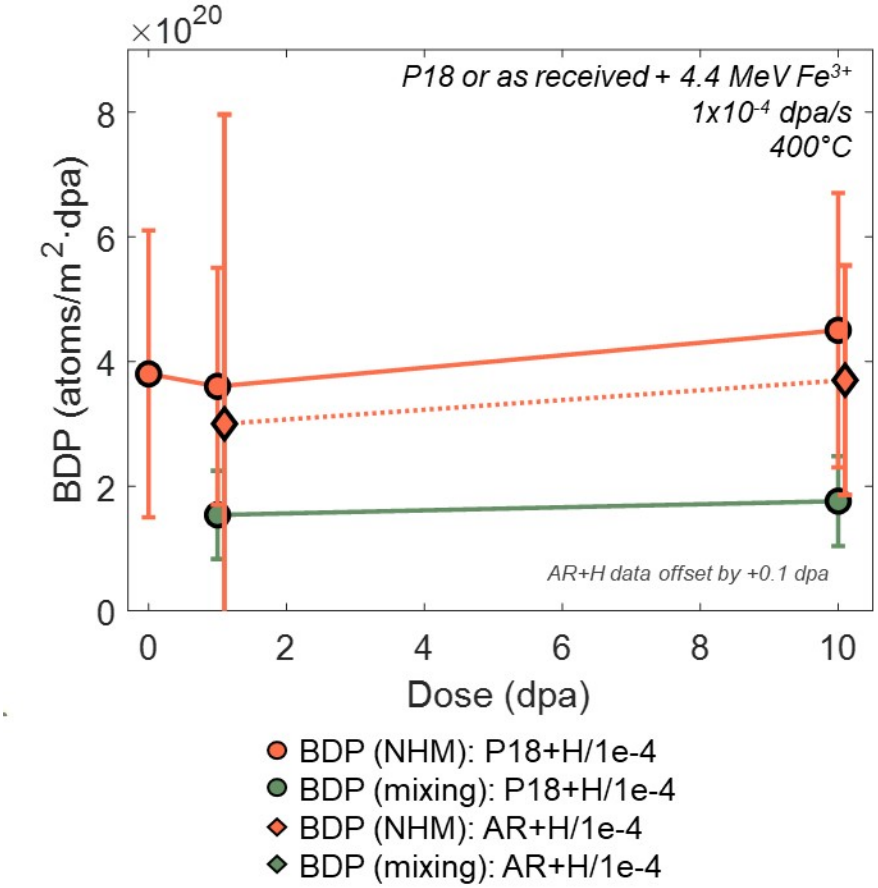

Figure 6.24 Comparison of NHM BDP (orange) and mixing BDP (green) for heavy ion irradiation at 1x10^{-4} dpa/s. Irradiated samples with pre-existing α' are in circles and as-received samples are diamonds. AR+H/1e-4/10 (diamonds) are offset to better show the overlapping datapoints.

6.4 Role of damage rate and cascade size in α' stability

The balance between ballistic mixing and radiation enhanced diffusion is most evident in the evolution of the α' precipitate size and solute concentration. Figure 6.25 shows the evolution of the α' precipitate average radius with dose under heavy ion (a), proton (b), and electron irradiation (c). The average α' precipitate size under heavy ion irradiation decreases or completely dissolves by 10 dpa. Both ballistic mixing and RED are present in heavy ion irradiation, with ballistic mixing playing a strong role in the dissolution of the α' precipitates. Furthermore, the damage rate also clearly plays a role in the rate of dissolution of the α' precipitate, where a faster damage rate leads to a faster dissolution of the α' precipitate. Conversely, under electron irradiation, α' precipitates grow. Only RED is present with electron irradiation leading to the growth of α' precipitates. This was confirmed in Section 6.1.2 through the NHM model (and Chen-modified NHM model), showing that with RED only, the predicted α' precipitate size matches to that experimentally observed with electron irradiation. Under proton irradiation, the α' precipitate size increased with dose, but not to the same extent as electron irradiation. The α' precipitates grew in size due to the enhanced diffusion but were limited to an extent by the ballistic mixing of the small cascades in proton irradiation. Figure 6.25(d) shows a comparison of each type of irradiation at the same damage rate ($1x10^{-4}$ dpa/s) illustrating the balance between ballistic mixing and RED on the precipitate size evolution. Figure 6.25(e) and (f) show α' precipitate evolution under heavy ion and electron with respect to time, highlighting the effects of damage rate. Under heavy ion irradiation, the increasing damage rate led to a faster rate of dissolution of the α' precipitates. Similarly, under electron irradiation, the damage rate is controlling the rate of precipitate growth.

The BDP is another way to describe the degree of ballistic dissolution on the α' precipitate stability. In Section 6.1.4, the NHM based BDP calculated represents the flux of atoms ballistically ejected from the precipitate per dpa. The BDP is representative of the cascade size of the irradiation particle as that plays a role in the degree of ballistic dissolution, where the smaller BDP value for proton irradiation is due to the smaller cascade size and lesser degree of ballistic dissolution. The larger BDP for heavy ion irradiation is due to the larger cascade size and a higher degree of ballistic dissolution. The BDP for heavy ion irradiation was calculated to be ~4-5 times larger than the BDP for proton irradiation, confirming that a higher degree of ballistic dissolution is expected for heavy ion irradiation due to the larger, denser cascades. The cascade size for 2 MeV proton and 4.4 MeV

heavy ion irradiation were calculated using MD simulations [31] to be ~2.3 nm and ~8.6 nm in diameter, respectively. Simulations were completed using a Wigner-Seitz defect analysis. The cascade diameters were calculated from the average volume, which was calculated from the average of 15-20 simulations for each condition, with conditions including more than one direction. Figure 6.25 shows the trend where under heavy ion irradiation, the precipitates are shrinking due to the ballistic dissolution. Under proton irradiation, by contrast, growth of the α' precipitates are stunted by ballistic dissolution, but to a lesser extent than heavy ion irradiation due to the cascade size.

The α' Cr concentration evolution also demonstrates the balance between ballistic mixing and enhanced diffusion. Figure 6.26 shows the evolution of the α' precipitate Cr concentration under heavy ion irradiation (a), proton irradiation (b), and electron irradiation (c). Under electron irradiation (Figure 6.26 (c)), the α' precipitates increase in Cr concentration, due to the enhanced diffusion, approaching the nominal α' Cr concentration predicted by the phase diagram. For heavy ion irradiation, the (Figure 6.26 (a)), α' Cr concentration decreases with increasing dose, and decreasing at a faster rate with for higher damage rates. The decrease in Cr concentration is due to the mixing of the matrix and precipitate from the irradiation cascades with a small degree of recovery from RED leading to a steady state concentration lower than the initial concentration and lower than the Cr concentration expected based on the phase diagram. At higher damage rates, the ballistic mixing overtakes the recovery by RED leading to the complete dissolution of α'. This is corroborated by faster decrease in Cr concentration for higher damage rates. Under proton irradiation, the α' Cr concentration increased with dose, but at a slower rate than the electron irradiation. Although ballistic mixing is not expected to play a dominant role (as shown through the critical temperature in the following Section 6.4.1), it still plays a small role, as evident in Figure 6.26(b) and (d), when compared to electron irradiation at the same damage rate. Figure 6.26(d) compares between the cascades sizes at the same damage rate ($1x10^{-4}$ dpa/s), demonstrating the balance between ballistic mixing and RED on the precipitate Cr concentration. Figure 6.26(e) and (f) show α' precipitate Cr concentration evolution with respect to time, highlighting the effects of damage rate. Under heavy ion irradiation (Figure 6.26(e)), the increasing damage rate led to a faster dissolution and mixing of the α' precipitates and therefore a faster decrease in Cr concentration. Under electron irradiation, (Figure 6.26(f)), the damage is also

controlling the rate of Cr concentration increase in the α' precipitates, where all are increasing at a similar rate due to no restrictions of ballistic mixing.

The dependence of Cr concentration on the cascade size also follows the trends expected by literature. Figure 2.6 from Chapter 2 was updated to include the data from heavy ion, proton, and electron irradiation experiments from this thesis and presented again to produce Figure 6.27. The heavy ion irradiation data presented is P18+H/1e-4/10, where a steady state has been achieved in the α' precipitates, the proton irradiation data is AR+P/1e-5/2 and P19+P/1e-4/10, and all three electron irradiations of pre-existing α' precipitates are presented. The figure shows that under electron irradiation, the α' precipitate solute concentration is at or near the nominal concentration across the temperatures. Whereas under heavy ion irradiation, the fraction of solute concentration in the α' precipitate is much lower, and is additionally affected by temperature, showing a clear linear trend between 300-450°C. This shows that the ballistic mixing plays a smaller role with increasing temperatures as the α' precipitate solute concentration is able to recover and attain a higher concentration at higher temperatures. Figure 2.5 from the Chapter 2 was also updated with heavy ion, proton, and electron data presented in this thesis and included in Figure 6.28 to compare to literature showing the Cr concentration dependence on the cascade size and damage rate. This figure shows the heavy ion irradiation of pre-existing α' precipitates for all damage rates at 10 dpa (no $1x10^{-5}$ dpa/s), proton irradiation at 10 dpa and as-received proton irradiated at 2 dpa, and all three electron irradiation data points. The figure is primarily exhibiting data irradiated at around ~300°C, with outliers from Zhao, et al [19] at 350°C and 450°C and this thesis work at 400°C. Comparing the electron irradiation at different damage rates and temperatures, α' achieved the nominal solute concentration expected by the phase diagram by <1 dpa. The proton irradiation is shown to have approximately the nominal concentration at both 10^{-5} and 10^{-4} dpa/s and are set slightly below electron irradiation, as expected as there is a small amount of ballistic dissolution affecting the α' precipitates. Comparing the heavy ion irradiation across damage rates and temperatures, the solute concentration is lower than dictated by the phase diagram at ~0.4-0.6. This thesis work established a stability limit between $1\text{-}3x10^{-4}$ dpa/s for α' precipitates in Fe-15Cr. Similarly, for 18Cr, there is a boundary by ~10^{-3} dpa/s. Comparing with literature data at $1x10^{-4}$ dpa/s, expected nominal α' solute concentration for 400°C follows the trend set from Zhao, et al, with 18Cr at 350°C and 450°C. This figure demonstrates the heavy ion irradiation data follows the expected trends from literature.

The effects of ballistic dissolution are determined primarily by the effects on the α' precipitate radius and α' Cr concentration throughout this work. Ballistic dissolution can be observed through other microstructural features such as the matrix concentration or volume fraction. The two models selected to calculate the BDP primarily focused on the α' precipitate size and Cr concentration. Size and Cr concentration of the α' are expected to have less variation between reconstructed volumes for each irradiation condition, whereas matrix concentration, volume fraction, and number density may vary more between volumes due multiple factors including the α' distribution throughout the microstructure.

The effect of cascade size and damage rate on α' Cr concentration and α' precipitate size is shown in Figure 6.29. Because experiments were conducted at different temperatures, the α' concentration reported in Figure 6.29(a) was the concentration reported in the experiment normalized to the equilibrium α' concentration expected based on the phase diagram. All literature data is for nucleation of α', whereas all data presented from this work is from pre-existing α'. However, it was shown in Section 6.3 that the stability of the precipitates determined here agrees with their formation as determined by irradiation of as-received samples.

For electron irradiation, where there is no cascade size, the α' precipitates are all at 100% of the expected α' concentration, with no damage rate effects. The relatively small cascade size in proton irradiation produced α' precipitates at ~90% of the maximum concentration expected by the phase diagram, again with no observable damage rate effects. The large cascade size from neutron and heavy ion irradiation, produced α' with even lower Cr concentrations. The cascade size shows a strong influence on the precipitate concentration and no influence of the damage rate on the precipitate concentration.

The cascade size strongly influences the precipitate size with damage rate playing little to no role, as shown in Figure 6.29(b). For Electron irradiation results in the largest increase in radius, for which there is little effect of damage rate. For proton irradiation, the precipitates are smaller in size due to of ballistic mixing. The large cascade size of neutron and heavy ion irradiation led to the smallest α' precipitates. For all three particles, the dominant effect on precipitate size is the size of the cascade, with little damage rate influence.

This work demonstrates the differences between electron, proton, and heavy ion irradiation on the evolution of α' precipitates under irradiation. This work provided guidance for cascade size

and damage rate at which to produce desired α' properties, including emulating neutron irradiation, which is recommended with heavy ion irradiation at low damage rates, where α' is stable.

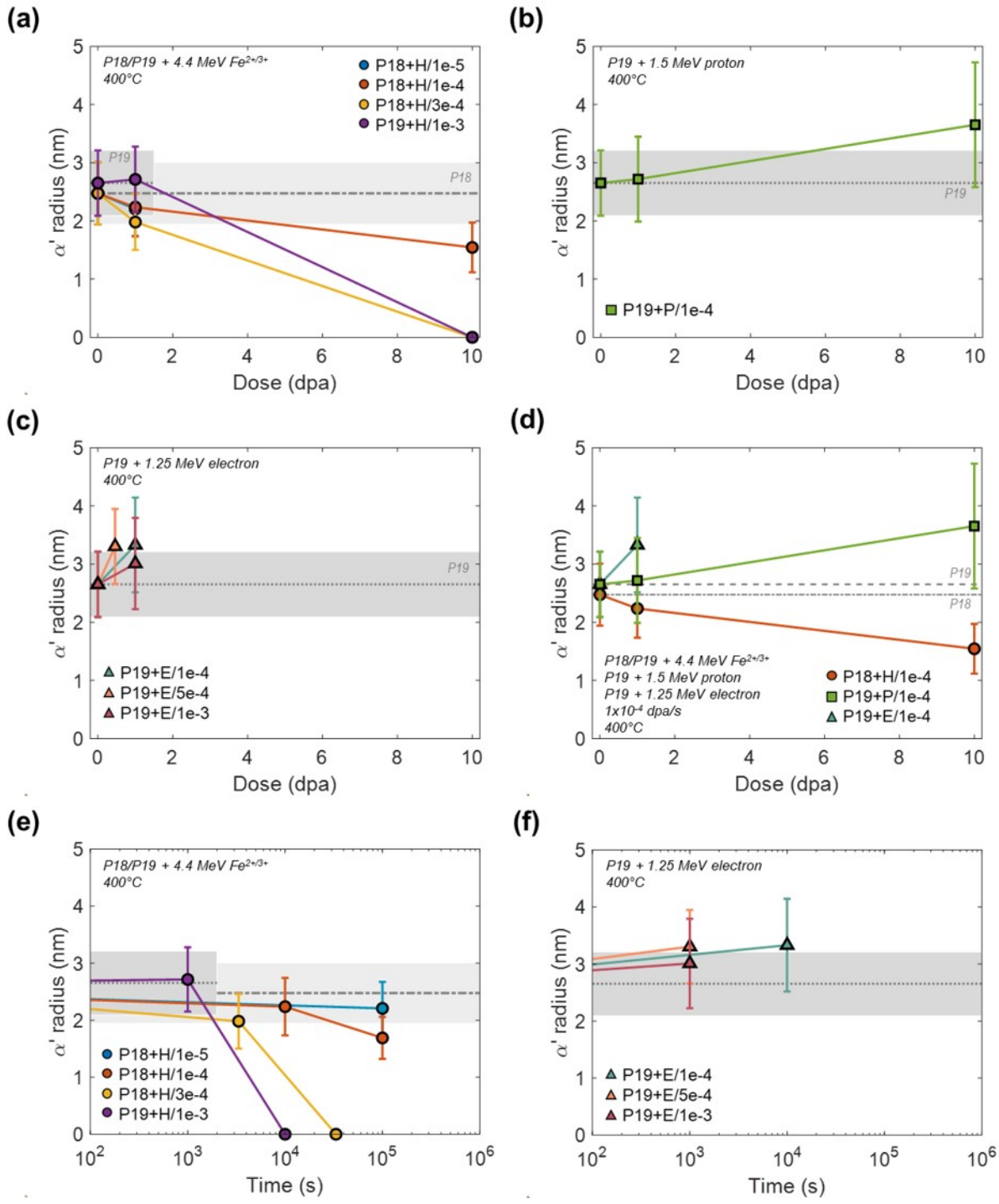

Figure 6.25 Comparison of α' precipitate radius changes with damage rate between types of irradiation (i.e., cascade size) with respect to dose, where (a) is heavy ion irradiation, (b) is proton irradiation, (c) is electron irradiation, and (d) is a comparison of cascade size at 10^{-4} dpa/s. The radius changes with damage rate with respect to time are also shown, where (e) is heavy ion irradiation and (f) is electron irradiation.

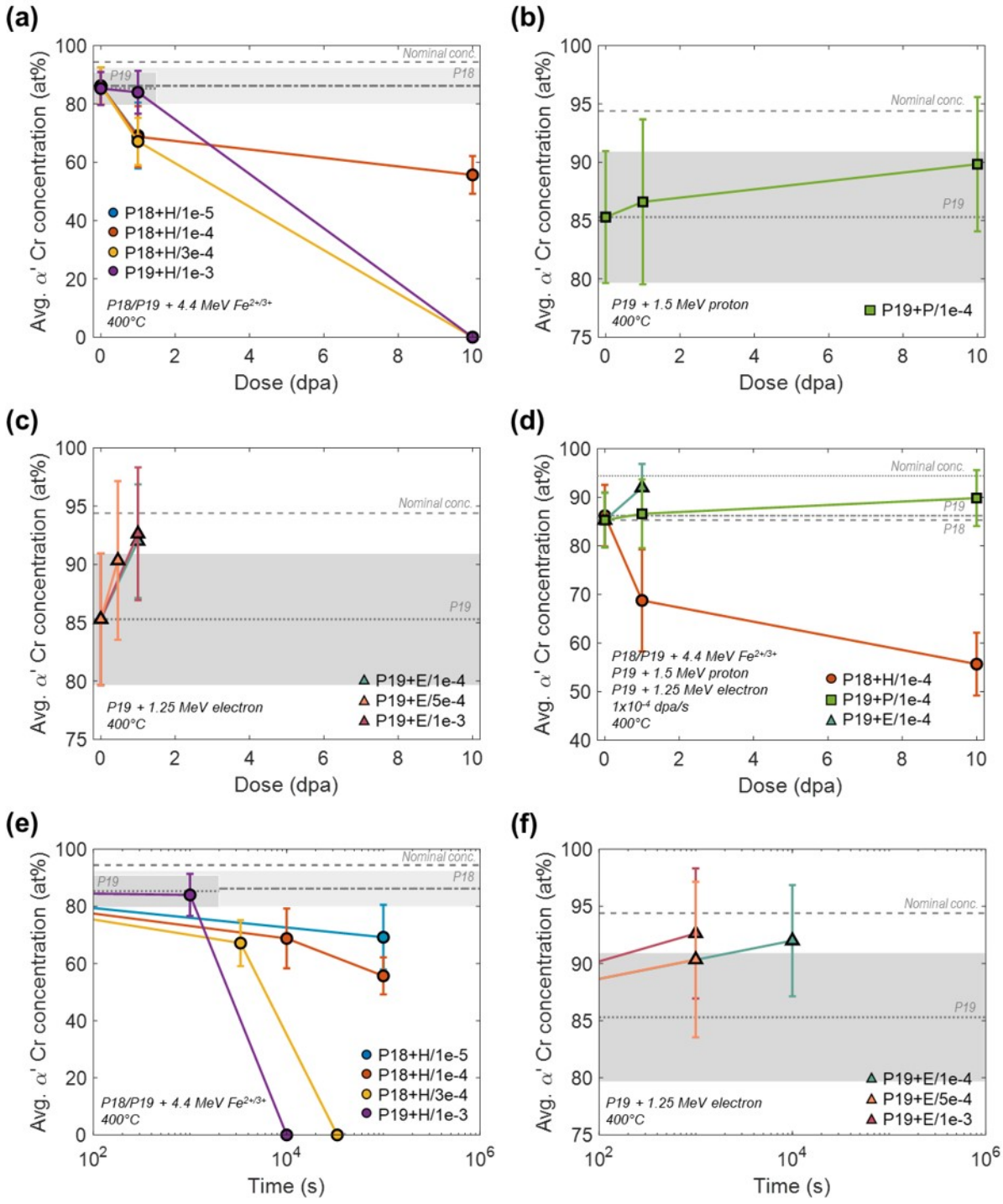

Figure 6.26 Comparison of α' precipitate Cr concentration changes with damage rate between types of irradiation (i.e., cascade size) with respect to dose, where (a) is heavy ion irradiation, (b) is proton irradiation, (c) is electron irradiation, and (d) is a comparison of cascade size at 10^{-4} dpa/s. The Cr concentration changes with damage rate with respect to time are also shown, where (e) is heavy ion irradiation and (f) is electron irradiation.

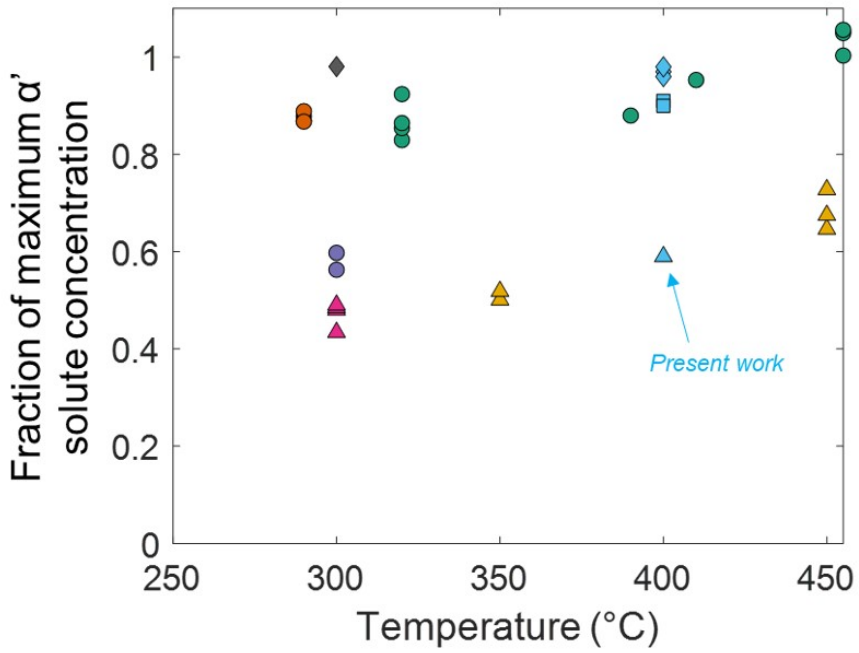

○ Neutron irradiation
△ Heavy ion irradiation
□ Proton irradiation
◇ Electron irradiation
● Fe-(9,12,15,18)Cr, ATR, 3.4×10^{-7} dpa/s, 1.82 dpa, Bachhav, et al. (2014) [33]
● Fe-(9,12)Cr, BR2, 0.6 dpa, Kuksenko, et al. (2013) [34]
● Fe-(9,12,15,18)Cr, ATR, ~3.5×10^{-7} dpa/s, 7 dpa, Reese, et al. (2018) [25]
Fe-12Cr, BOR-60, 7×10^{-7} dpa/s, 17 dpa, Reese, et al. (2018) [25]
▲ Fe-15Cr, JANNuS-Saclay facility, 3.5-6.1×10^{-5} dpa/s, 0.5-1 dpa, Tissot, et al. (2016) [21]
▲ Fe-18Cr, MIBL facility, 1×10^{-4}-1×10^{-3} dpa/s, 0.37 & 3.7 dpa, Zhao, et al. (2022) [19]
◆ Fe-15Cr, HVEM-Saclay facility, 3.5×10^{-5} dpa/s, 0.012-0.7 dpa, Tissot, et al. (2016) [16]
▲ Fe-15Cr, MIBL facility, 1×10^{-4} dpa/s, 10 dpa (present work)
■ Fe-15Cr, MIBL facility, 1×10^{-5}-1×10^{-4} dpa/s, 1-10 dpa (present work)
◆ Fe-15Cr, Hokkaido Univ. HVEM facility, 1×10^{-4}-1×10^{-3} dpa/s, 0.46-1 dpa (present work)

Figure 6.27 Comparison of the results from this thesis to the literature work showing the effect of temperature and cascade size on the fraction of nominal α' solute concentration after irradiation. Work presented in this thesis is represented in the light blue. Triangles represent heavy ion irradiation, squares represent proton irradiation, diamonds represent electron irradiation, and circles represent neutron irradiation.

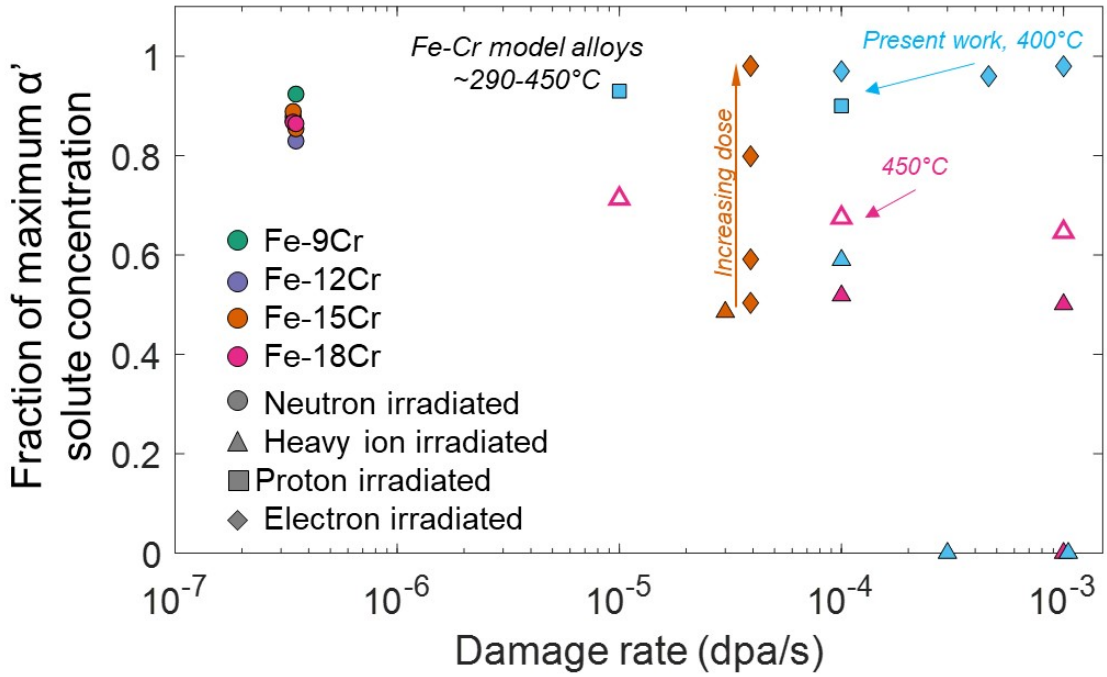

- Fe-(9,12,15,18)Cr, ATR, 290°C, 3.4x10^{-7} dpa/s, 1.82 dpa, Bachhav, et al. (2014) [33]
- Fe-(9,12,15,18)Cr, ATR, 320°C, ~3.5x10^{-7} dpa/s, 7 dpa, Reese, et al. (2018) [25]
- Fe-15Cr, JANNuS-Saclay facility, 300°C, 3.5-6.1x10^{-5} dpa/s, 0.5-1 dpa, Tissot, et al. (2016) [21]
- Fe-15Cr, HVEM-Saclay facility, 300°C, 3.5x10^{-5} dpa/s, 0.012-0.7 dpa, Tissot, et al. (2016) [16]
- Fe-18Cr, MIBL facility, 300-450°C, 10^{-5}-10^{-3} dpa/s, 0.37 dpa, Zhao, et al. (2022) [19]
- Fe-15Cr, MIBL facility, 400°C, 1x10^{-4} dpa/s & 1x10^{-3} dpa/s, 10 dpa (present work)
- Fe-15Cr, MIBL facility, 400°C, 1x10^{-4} dpa/s, 10 dpa (present work)
- Fe-15Cr, Hokkaido Univ. HVEM Facility, 400°C, 1x10^{-4} dpa/s & 1x10^{-3} dpa/s, 1 dpa (present work)
- Fe-15Cr, Kyushu Univ. HVEM Facility, 400°C, 4.6x10^{-4} dpa/s, 0.46 dpa (present work)

Figure 6.28 Comparison of the results from this thesis to literature work showing the effect of damage rate and cascade size on fraction of the nominal α' solute concentration after irradiation. Work presented in this thesis is represented in light blue. Triangles represent heavy ion irradiation, squares represent proton irradiation, diamonds represent electron irradiation, and circles represent neutron irradiation. Most data are presented at ~300°C, with other temperatures presented noted.

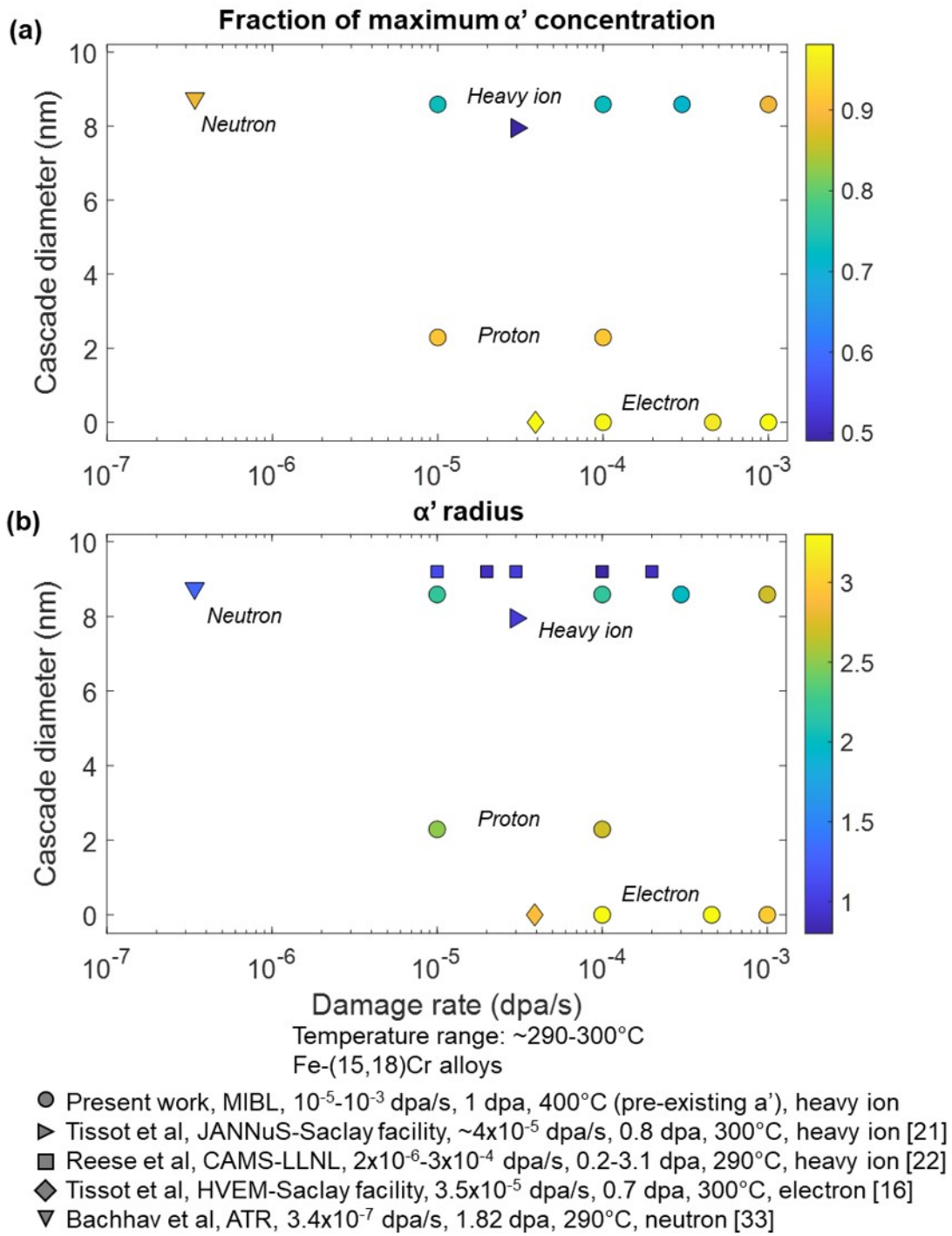

Figure 6.29 Cascade size and damage rate effects on (a) fraction of maximum α' concentration, and (b) α' precipitate radius in literature data and thesis work in Fe-15Cr and Fe-18Cr model alloys at ~300°C (400°C for thesis work).

6.4.1 Correlation between ballistic mixing and the critical temperature

The α' precipitate concentration varies between cascade size and damage rate. This was observed in Section 5.2.1, where under heavy ion irradiation the α' concentration decreases with dose and at $1x10^{-4}$ dpa/s at 10 dpa, the Cr concentration was much lower than the initial concentration and the equilibrium concentration for α' phase. In contrast, under proton and electron irradiation, the α' precipitate Cr concentration increases. The difference in Cr concentration may be explained by presence of ballistic mixing resulting from irradiation cascades. Heavy ion irradiation has larger, denser cascades than proton irradiation, and electron irradiation produces Frenkel pairs.

There exists a narrow temperature range separating the temperature independent ballistic mixing and the Arrhenius-type radiation-enhanced diffusion. The onset of RED is shown as Eq. (2.14), shown here again as Eq. (6.26), describes the critical temperature. Below this critical temperature, ballistic mixing is the primary contributor to diffusion and above this temperature, RED is the primary contributor to diffusion.

$$T_C = \frac{Q}{k\ ln\left({D_{irr}}/{D_{bal}}\right)} \tag{6.26}$$

The ballistic mixing term was calculated for electron, proton, and heavy ion irradiation. The jump length was approximated to be equal to the lattice parameter. The number of replacements per displacement for electrons was 1 and for heavy ions was 50 [11]. The rpa value for proton irradiation is not widely established, and so a value of 5 was used as it is an order of magnitude lower than the rpa for heavy ions and larger than electron irradiation.

The critical temperature for heavy ion irradiation was significantly greater than the experiment temperature, whereas the critical temperature of electron and proton irradiation are below the experimental temperature. A comparison of the critical temperatures between electron, proton, and heavy ion irradiation can be made from Table 6.14. The table shows critical temperatures at a damage rate of $1x10^{-4}$ dpa/s for the 0 and 1 dpa conditions. Experimental temperature exceeding T_C indicates radiation enhanced diffusion is playing a greater role than ballistic dissolution for proton and electron irradiation. However, T_C(proton) > T_C(electron) indicates that ballistic dissolution does play a role, though small, in proton irradiation. This is experimentally supported by observation of increasing precipitate concentration and precipitate

size under both proton and electron irradiation. Under heavy ion irradiation, opposite trends, decreasing precipitate concentration and size, are observed. With the critical temperature higher than the experiment temperature, ballistic mixing is dominant over RED for heavy ion irradiation. In the case of heavy ion irradiation, there is greater competition between ballistic mixing breaking apart the α' precipitates and radiation enhanced diffusion assembling the α' precipitates.

Table 6.14 Critical temperature calculation for electron, proton, and heavy ion irradiation of pre-existing α' precipitates at 1x10^{-4} dpa/s at 0 and 1 dpa.

Terms	Definition	Units	P19+E/1e-4		P19+P/1e-4		P18+H/1e-4	
Dose	--	dpa	0	1	0	1	0	1
η	Lattice parameter	unitless	1	1	5	5	50	50
ξ	efficiency	unitless	1	1	0.8	0.8	0.1	0.1
${k_s}^2(total)$	Total sink strength	m^{-2}	$1.58x10^{16}$	$1.44x10^{16}$	$1.58x10^{16}$	$8.78x10^{15}$	$1.58x10^{16}$	$2.27x10^{16}$
$D_{irr} \cdot \exp\left({}^{-Q}/_{kT}\right)$	RED term	m^2/s	$3.30x10^{-23}$	$3.62x10^{-23}$	$2.64x10^{-23}$	$4.75x10^{-23}$	$3.30x10^{-24}$	$2.3x10^{-24}$
D_{bal}	Ballistic mixing diffusion term	m^2/s	$1.38x10^{-24}$	$1.38x10^{-24}$	$6.91x10^{-24}$	$6.91x10^{-24}$	$6.91x10^{-23}$	$6.91x10^{-23}$
T_C	Critical temperature	°C	166	161	276	235	1104	1300

6.5 References

[1] R.S. Nelson, J.A. Hudson, D.J. Mazey, The stability of precipitates in an irradiation environment, J. Nucl. Mater. 44 (1972) 318–330. doi:10.1016/0022-3115(72)90043-8.

[2] T. Chen, J.G. Gigax, L. Price, D. Chen, S. Ukai, E. Aydogan, S.A. Maloy, F.A. Garner, L. Shao, Temperature dependent dispersoid stability in ion-irradiated ferritic-martensitic dual-phase oxide-dispersion-strengthened alloy: Coherent interfaces vs. incoherent interfaces, Acta Mater. 116 (2016) 29–42. doi:10.1016/j.actamat.2016.05.042.

[3] J.P. Wharry, The Mechanism of Radiation-Induced Segregation in Ferritic-Martensitic Steels, University of Michigan, 2012.

[4] S. Taller, V. Pauly, Z. Jiao, R. Hanbury, G.S. Was, Solute segregation and precipitation across damage rates in dual-ion–irradiated T91 steel, J. Nucl. Mater. 563 (2022) 153626. doi:10.1016/j.jnucmat.2022.153626.

[5] S.J. Zinkle, B.N. Singh, Analysis of displacement damage and defect production under cascade damage conditions, J. Nucl. Mater. 199 (1993) 173–191. doi:10.1016/0022-3115(93)90140-T.

[6] S. Zinkle, Y.R. Lin, Y. Zhao, S. Levine, Y. Li, Z. Qi, A. Bhattacharya, S. Agarwal, Recent Progress in Understanding Fundamental Radiation Processes, in *TMS2022*, February 27-March 3, Anaheim, CA (2022).

[7] K. Nordlund, S.J. Zinkle, A.E. Sand, F. Granberg, R.S. Averback, R.E. Stoller, T. Suzudo, L. Malerba, F. Banhart, W.J. Weber, F. Willaime, S.L. Dudarev, D. Simeone, Primary radiation damage: A review of current understanding and models, J. Nucl. Mater. 512 (2018) 450–479. doi:10.1016/j.jnucmat.2018.10.027.

[8] L. Malerba, Molecular dynamics simulation of displacement cascades in α-Fe: A critical review, J. Nucl. Mater. 351 (2006) 28–38. doi:10.1016/j.jnucmat.2006.02.023.

[9] R.S. Averback, Ion-irradiation studies of cascade damage in metals, J. Nucl. Mater. 108–109 (1982) 33–45. doi:10.1016/0022-3115(82)90469-X.

[10] R.S. Averback, T. Diaz de la Rubia, Displacement Damage in Irradiated Metals and Semiconductors, ACADEMIC PRESS, 1998. doi:10.1016/S0081-1947(08)60193-9.

[11] J.H. Ke, E.R. Reese, E.A. Marquis, G.R. Odette, D. Morgan, Flux effects in precipitation under irradiation – Simulation of Fe-Cr alloys, Acta Mater. 164 (2019) 586–601.

doi:10.1016/j.actamat.2018.10.063.

[12] N. Soneda, Embrittlement correlation methods to identify trends in embrittlement in reactor pressure vessels (RPVs), 2015. doi:10.1533/9780857096470.3.333.

[13] M. Hernández-Mayoral, C. Heintze, E. Oñorbe, Transmission electron microscopy investigation of the microstructure of Fe–Cr alloys induced by neutron and ion irradiation at 300 °C, J. Nucl. Mater. 474 (2016) 88–98. doi:10.1016/j.jnucmat.2016.03.002.

[14] J.J. Kai, R.L. Klueh, Microstructural analysis of neutron-irradiated martensitic steels, J. Nucl. Mater. 230 (1996) 116–123.

[15] M. Hernández-Mayoral, Z. Yao, M.L. Jenkins, M. a. Kirk, Heavy-ion irradiations of Fe and Fe–Cr model alloys Part 2: Damage evolution in thin-foils at higher doses, Philos. Mag. 88 (2008) 2881–2897. doi:10.1080/14786430802380477.

[16] O. Tissot, C. Pareige, E. Meslin, B. Decamps, J. Henry, Kinetics of α′ precipitation in an electron-irradiated Fe15Cr alloy, Scr. Mater. 122 (2016) 31–35. doi:10.1016/j.scriptamat.2016.05.021.

[17] G.S. Was, Fundamental of Radiation Materials Science, 2nd ed., Springer, New York, 2017.

[18] G.S. Was, T.R. Allen, Radiation-induced segregation in multicomponent alloys: Effect of particle type, Mater. Charact. 32 (1994) 239–255. doi:10.1016/1044-5803(94)90101-5.

[19] Y. Zhao, A. Bhattacharya, C. Pareige, C. Massey, P. Zhu, J.D. Poplawsky, J. Henry, S.J. Zinkle, Effect of heavy ion irradiation dose rate and temperature on α precipitation in high purity Fe-18 % Cr alloy R, Acta Mater. 231 (2022) 117888. doi:10.1016/j.actamat.2022.117888.

[20] F. Soisson, E. Meslin, O. Tissot, Atomistic modeling of α' precipitation in Fe-Cr alloys under charged particles and neutron irradiations: Effects of ballistic mixing and sink densities, J. Nucl. Mater. 508 (2018) 583–594.

[21] O. Tissot, C. Pareige, E. Meslin, B. Décamps, J. Henry, Influence of injected interstitials on α′ precipitation in Fe–Cr alloys under self-ion irradiation, Mater. Res. Lett. 3831 (2016) 1–7. doi:10.1080/21663831.2016.1230896.

[22] E.R. Reese, N. Almirall, T. Yamamoto, S. Tumey, G. Robert Odette, E.A. Marquis, Dose rate dependence of Cr precipitation in an ion-irradiated Fe18Cr alloy, Scr. Mater. 146 (2018) 213–217. doi:https://doi.org/10.1016/j.scriptamat.2017.11.040.

[23] O.A. Korchuganova, M. Thuvander, A.A. Aleev, S. V. Rogozhkin, T. Boll, T. V. Kulevoy, Microstructural evolution of Fe-22%Cr model alloy under thermal ageing and ion irradiation conditions studied by atom probe tomography, J. Nucl. Mater. 477 (2016) 172–177. doi:10.1016/j.jnucmat.2016.05.007.

[24] M.K. Miller, M.G. Hetherington, Local magnification effects in the atom probe, Surf. Sci. 246 (1991) 442–449. doi:10.1016/0039-6028(91)90449-3.

[25] E.R. Reese, M. Bachhav, P. Wells, T. Yamamoto, G. Robert Odette, E.A. Marquis, On α′ precipitate composition in thermally annealed and neutron-irradiated Fe- 9-18Cr alloys, J. Nucl. Mater. 500 (2018) 192–198. doi:10.1016/j.jnucmat.2017.12.036.

[26] F. Vurpillot, A. Bostel, D. Blavette, Trajectory overlaps and local magnification in three-dimensional atom probe, Appl. Phys. Lett. 76 (2000) 3127–3129. doi:10.1063/1.126545.

[27] X. Liao, Y. Chen, H. Gong, T. Liu, H. Deng, W. Hu, F. Gao, The stability and behavior of Cr-rich α' precipitates under cascade damage in Fe-15Cr-8Al ternary alloys: An atomic-scale simulation study, J. Nucl. Mater. 570 (2022) 153955. doi:10.1016/j.jnucmat.2022.153955.

[28] A.D. Marwick, Solute segregation and precipitate stability in irradiated alloys, Nucl. Instruments Methods. 182–183 (1981) 827–843. doi:10.1016/0029-554X(81)90815-6.

[29] K.L. Rusbridge, Modification of near-surface precipitation in Al-Ge alloy by ion irradiation, J. Nucl. Instruments Methods Phys. Res. B. 182/183 (1981) 521–529.

[30] A.L. Chang, M. Baron, Particle redistribution and phase stability in ion and neutron irradiated gamma prime strengthened Fe-Cr-Ni based alloys, J. Nucl. Mater. 83 (1979) 214–222.

[31] M. Higgins, F. Gao, Cascade size calculation in Fe-15Cr, (2018), unpublished.

[32] M.J. Swenson, J.P. Wharry, Nanocluster irradiation evolution in Fe-9%Cr ODS and ferritic-martensitic alloys, J. Nucl. Mater. 496 (2017) 24–40. doi:10.1016/j.jnucmat.2017.08.045.

[33] M. Bachhav, G. Robert Odette, E.A. Marquis, α′ precipitation in neutron-irradiated Fe-Cr alloys, Scr. Mater. 74 (2014) 48–51. doi:10.1016/j.scriptamat.2013.10.001.

[34] V. Kuksenko, C. Pareige, P. Pareige, Cr precipitation in neutron irradiated industrial purity Fe-Cr model alloys, J. Nucl. Mater. 432 (2013) 160–165. doi:10.1016/j.jnucmat.2012.07.021.

Chapter 7: Conclusions and Future Work

The following conclusions have been reached in this thesis:

Ballistic dissolution was confirmed to play no role in electron irradiation. Electron irradiations of pre-existing α' precipitates over a range of damage rates combined with modeling work showed that the evolution of α' precipitates with dose can be fully accounted for by radiation enhanced diffusion, as evidenced by the accelerated precipitate growth. The NHM model and the Chen-modified NHM model growth terms were validated by modeling the growth of α' precipitates under electron irradiation over a range of damage rates up to 1 dpa. The critical temperature was also used to showed that ballistic dissolution plays no role in the α' precipitate stability under electron irradiation.

Ballistic dissolution was confirmed to play a role in the α' precipitate stability under proton irradiation. Calculation of the ballistic dissolution parameter was determined using the NHM model and gave a BDP of ~8.6 ± 6.2x10^{19} atoms/m^2·dpa, smaller than the heavy ion irradiation BDP, thus revealing the cascade size effect of ballistic dissolution. Furthermore, the critical temperature demonstrated that the ballistic dissolution did play a part in the α' precipitate stability. Experiments also demonstrated the role of ballistic dissolution in α' stability in proton irradiation, where α' precipitates exhibited a slower growth rate in comparison to electron irradiation, where there is no ballistic dissolution.

Ballistic mixing plays a stronger role under heavy ion irradiation, in comparison to electron and proton irradiation, leading to the reduced α' precipitate sizes and reduced chromium concentrations in the α' precipitates, or complete dissolution. Calculation of the ballistic dissolution parameter was determined using both the NHM and mixing models and gave a BDP in the range of 1.5-5x10^{20} atoms/m^2·dpa. Moreover, the NHM-based BDP for heavy ion irradiation was ~4-5 larger than that calculated for proton irradiation, revealing the effect of the cascade size

on the ballistic dissolution of α' precipitates under irradiation. Also, the application of the mixing model to experimental results from heavy ion irradiation revealed the effects of precipitate-matrix mixing, eventually leading to the decrease in chromium concentration or complete dissolution in α' precipitates. Additionally, the critical temperature was calculated for heavy ion and proton irradiation demonstrating a stronger role of ballistic dissolution for heavy ion irradiation than for proton irradiation. The critical temperature also demonstrated that the ballistic dissolution played a stronger role than radiation enhanced diffusion under heavy ion irradiation, whereas under proton irradiation, the radiation enhanced diffusion was the dominant mechanism for atom transport.

Cascade size dictates stability of α' precipitates and damage rate dictates the rate at which α' precipitates grow or dissolve. Under heavy ion irradiation where there is a strong role of ballistic dissolution, α' precipitates dissolved at a rate dependent on the damage rate. However, under electron irradiation where ballistic dissolution is absent, the α' precipitates grew in concentration and size. Under proton irradiation where there is a smaller role of ballistic dissolution, the α' precipitates grew in size and concentration, but at a reduced rate due to the ballistic dissolution.

A threshold damage rate was established under heavy ion irradiation, below which α' precipitates remain stable in solution and above which α' dissolve or does not grow. Heavy ion irradiations were completed over a range of damage rates, from 10^{-5} to 10^{-3}. Pre-existing α' precipitates were completely dissolved by 10 dpa at damage rates of $3x10^{-4}$ dpa/s and 10^{-3} dpa/s, yet remained stable at a lower damage rate of 10^{-4} dpa/s. This establishes the threshold damage rate boundary for 15Cr at 400°C between 1-$3x10^{-4}$ dpa/s.

While there are notable conclusions in this work, there remains some unanswered questions that deserve future attention:

The role of ballistic mixing in proton irradiation. There remains unresolved work understanding the effect of proton irradiation on the α' precipitate stability. This thesis work provided a cascade size variation between heavy ion, proton, and electron irradiation at a single damage rate and temperature, and this work did show that proton irradiation is subject to ballistic mixing. Further, by comparing results from this work to literature, the effects of ballistic mixing

from heavy ion irradiation can be observed over a range of damage rates and temperatures, but this picture is incomplete for proton irradiation. Additional studies with higher damage rates may identify the rate at which precipitate dissolution occurs, revealing more on the role of ballistic dissolution under proton irradiation.

The effect of microstructure and alloy. Most α' studies have used Fe-Cr model alloys to study α' under irradiation, this work included. But now as α' has been successfully observed under a range of irradiation conditions and the mechanisms of which are better understood, the next step is to use a commercial alloy. A rigorous study focusing on damage rate and cascade size, especially coupled with pre-existing α' precipitates, in a high Cr F-M commercial alloy could provide new, real-world insight into the stability and evolution of α' precipitates.

The role of temperature. In this work, the experiments were completed at one temperatures: 400°C. The role of ballistic dissolution is expected to increase with decreasing temperature. A previous study also suggested that as ballistic dissolution decreases, the dose required to achieve a steady state α' precipitate microstructure increases. Further ion irradiation studies at various temperatures would help understand how ballistic dissolution effect α' precipitates, including the dose at which steady state is achieved by coupling ion irradiations of as received alloys with pre-existing α' precipitates.

Appendices

Appendix A: BDP Calculations

The input values for NHM-based and mixing-based BDP calculations for proton and heavy ion irradiation. Tables for both linear and exponential fits are included in this appendix.

Table A.1 NHM based BDP at 0 dpa for proton irradiation of pre-existing α' precipitates at $1x10^{-4}$ dpa/s with a linear fit for the precipitate evolution.

	Definition	Units	P19+P/1e-4, 0 dpa		
α' evolution fit	N.A.	N.A.	Linear fit, 0-1 dpa	Exponential fit	Polynomial fit
C_e	Solubility limit	at. fraction	0.105	0.105	0.105
C_m	Matrix conc.	at. fraction	0.129	0.129	0.129
C_p	α' conc.	at. fraction	0.853	0.853	0.853
r	α' WRMS radius	m	$2.8x10^{-9}$	$2.8x10^{-9}$	$2.8x10^{-9}$
n	α' number density	m^{-3}	$4.72x10^{23}$	$4.72x10^{23}$	$4.72x10^{23}$
${k_s}^2(\alpha')$	α' sink strength	m^{-2}	$1.6x10^{16}$	$1.6x10^{16}$	$1.6x10^{16}$
${k_s}^2(disl)$	Dislocation sink strength	m^{-2}	$3.0x10^{13}$	$3.0x10^{13}$	$3.0x10^{13}$
${k_s}^2(cavities)$	Cavities sink strength	m^{-2}	0	0	0
${k_s}^2(total)$	Total stink strength	m^{-2}	$1.6x10^{16}$	$1.6x10^{16}$	$1.6x10^{16}$
ξ	Efficiency	unitless	0.8	0.8	0.8
K_0	Damage rate	dpa/s	$0.9 \pm 0.1x10^{-4}$	$0.9 \pm 0.1x10^{-4}$	$0.9 \pm 0.1x10^{-4}$
D_{irr}	RED	m^2/s	$9.27x10^{-21}$	$9.27x10^{-21}$	$9.27x10^{-21}$
$\frac{dr}{dt}$	Growth/dissolution rate	m/s	$1.05x10^{-14}$	$1.97x10^{-14}$	$1.13x10^{-14}$
$\varphi\ (BDP)$	Ballistic dissolution parameter	$atoms/m^2 \cdot dpa$	$9.63 \pm 15.4x10^{19}$	$8.60 \pm 6.20x10^{19}$	$8.57 \pm 6.51x10^{19}$

Table A.2 NHM based BDP at 1 dpa for proton irradiation of pre-existing α' precipitates at $1x10^{-4}$ dpa/s with a linear fit for the precipitate evolution.

	Definition	Units	P19+P/1e-4/1			
α' evolution fit	N.A.	N.A.	Linear fit, 0-1 dpa	Linear fit, 1-10 dpa	Exponential fit	Polynomial fit
C_e	Solubility limit	at. fraction	0.105	0.105	0.105	0.105
C_m	Matrix conc.	at. fraction	0.145	0.145	0.145	0.145
C_p	α' conc.	at. fraction	0.898	0.898	0.898	0.898
r	α' WRMS radius	m	$2.9x10^{-9}$	$2.9x10^{-9}$	$2.9x10^{-9}$	$2.9x10^{-9}$
n	α' number density	m^{-3}	$2.5x10^{23}$	$2.5x10^{23}$	$2.5x10^{23}$	$2.5x10^{23}$
${k_s}^2(\alpha')$	α' sink strength	m^{-2}	$9.0x10^{15}$	$9.0x10^{15}$	$9.0x10^{15}$	$9.0x10^{15}$
${k_s}^2(disl)$	Dislocation sink strength	m^{-2}	$3.0x10^{13}$	$3.0x10^{13}$	$3.0x10^{13}$	$3.0x10^{13}$
${k_s}^2(cavities)$	Cavities sink strength	m^{-2}	$1.5x10^{14}$	$1.5x10^{14}$	$1.5x10^{14}$	$1.5x10^{14}$
${k_s}^2(total)$	Total stink strength	m^{-2}	$9.4x10^{15}$	$9.4x10^{15}$	$9.4x10^{15}$	$9.4x10^{15}$
ξ	Efficiency	unitless	0.8	0.8	0.8	0.8
K_0	Damage rate	dpa/s	$0.9 \pm 0.1x10^{-4}$	$0.9 \pm 0.1x10^{-4}$	$0.9 \pm 0.1x10^{-4}$	$0.9 \pm 0.1x10^{-4}$
D_{irr}	RED	m^2/s	$1.68x10^{-20}$	$1.68x10^{-20}$	$1.68x10^{-20}$	$1.68x10^{-20}$
$\frac{dr}{dt}$	Growth/dissolution rate	m/s	$1.05x10^{-14}$	$1.10x10^{-14}$	$1.70x10^{-14}$	$1.11x10^{-14}$
$\varphi\ (BDP)$	Ballistic dissolution parameter	$atoms/m^2 \cdot dpa$	$2.92 \pm 11.9x10^{20}$	$2.92 \pm 11.8x10^{20}$	$2.85 \pm 1.47x10^{20}$	$2.84 \pm 1.48x10^{20}$

Table A.3 NHM based BDP at 10 dpa for proton irradiation of pre-existing α' precipitates at $1x10^{-4}$ dpa/s with a linear fit for the precipitate evolution

	Definition	Units	P19+P/1e-4/10			
α' evolution fit	N.A.	N.A.	Linear fit, 1-10 dpa	Steady state at 10 dpa	Exponential fit	Polynomial
C_e	Solubility limit	at. fraction	0.105	0.105	0.105	0.105
C_m	Matrix conc.	at. fraction	0.146	0.146	0.146	0.146
C_p	α' conc.	at. fraction	0.898	0.898	0.898	0.898
r	α' WRMS radius	m	$3.9x10^{-9}$	$3.9x10^{-9}$	$3.9x10^{-9}$	$3.9x10^{-9}$
n	α' number density	m^{-3}	$5.09x10^{22}$	$5.09x10^{22}$	$5.09x10^{22}$	$5.09x10^{22}$
${k_s}^2(\alpha')$	α' sink strength	m^{-2}	$2.5x10^{15}$	$2.5x10^{15}$	$2.5x10^{15}$	$2.5x10^{15}$
${k_s}^2(disl)$	Dislocation sink strength	m^{-2}	$3.0x10^{13}$	$3.0x10^{13}$	$3.0x10^{13}$	$3.0x10^{13}$
${k_s}^2(cavities)$	Cavities sink strength	m^{-2}	$6.3x10^{13}$	$6.3x10^{13}$	$6.3x10^{13}$	$6.3x10^{13}$
${k_s}^2(total)$	Total stink strength	m^{-2}	$2.8x10^{15}$	$2.8x10^{15}$	$2.8x10^{15}$	$2.8x10^{15}$
ξ	Efficiency	unitless	0.8	0.8	0.8	0.8
K_0	Damage rate	dpa/s	$1.0 \pm 0.1x10^{-4}$	$1.0 \pm 0.1x10^{-4}$	$1.0 \pm 0.1x10^{-4}$	$1.0 \pm 0.1x10^{-4}$
D_{irr}	RED	m^2/s	$6.43x10^{-20}$	$6.43x10^{-20}$	$6.43x10^{-20}$	$6.43x10^{-20}$
$\frac{dr}{dt}$	Growth/dissolution rate	m/s	$1.10x10^{-14}$	0	$4.64x10^{-15}$	$9.70x10^{-15}$
$\varphi\ (BDP)$	Ballistic dissolution parameter	atoms/m^2·dpa	$8.04 \pm 3.88x10^{20}$	$8.15 \pm 9.02x10^{20}$	$8.10 \pm 3.96x10^{20}$	$8.15 \pm 3.96x10^{20}$

Table A.4 NHM based BDP at 0 dpa for heavy ion irradiation of pre-existing α' precipitates at various damage rates with a linear fit for the precipitate evolution.

	Units	P18+H/1e-5	P18+H/1e-4	P18+H/3e-4	P19+H/1e-3
α' evolution fit	N.A.	Linear fit, 0-1 dpa	Linear fit, 0-1 dpa	Linear fit, 0-1 dpa	Linear fit, 0-1 dpa
C_e	at. fraction	0.105	0.105	0.105	0.105
C_m	at. fraction	0.122	0.122	0.122	0.13
C_p	at. fraction	0.862	0.862	0.862	0.853
r	m	$2.6\text{x}10^{-9}$	$2.6\text{x}10^{-9}$	$2.6\text{x}10^{-9}$	$2.8\text{x}10^{-9}$
n	m^{-3}	$7.4\text{x}10^{23}$	$7.4\text{x}10^{23}$	$7.4\text{x}10^{23}$	$4.7\text{x}10^{23}$
${k_s}^2(\alpha')$	m^{-2}	$2.6\text{x}10^{16}$	$2.6\text{x}10^{16}$	$2.6\text{x}10^{16}$	$1.6\text{x}10^{16}$
${k_s}^2(disl)$	m^{-2}	$3.0\text{x}10^{14}$	$3.0\text{x}10^{14}$	$3.0\text{x}10^{14}$	$3.0\text{x}10^{14}$
${k_s}^2(cavities)$	m^{-2}	0	0	0	0
${k_s}^2(total)$	m^{-2}	$2.6\text{x}10^{16}$	$2.6\text{x}10^{16}$	$2.6\text{x}10^{16}$	$1.6\text{x}10^{16}$
ξ	unitless	0.1	0.1	0.1	0.1
K_0	dpa/s	$1.38 \pm 0.2\text{x}10^{-5}$	$1.0 \pm 0.1\text{x}10^{-4}$	$2.9 \pm 0.7\text{x}10^{-4}$	$1.0 \pm 0.1\text{x}10^{-3}$
D_{irr}	m^2/s	$1.81\text{x}10^{-22}$	$9.00\text{x}10^{-22}$	$2.46\text{x}10^{-21}$	$1.27\text{x}10^{-20}$
$\frac{dr}{dt}$	m/s	$-3.85\text{x}10^{-15}$	$-2.36\text{x}10^{-14}$	$-1.43\text{x}10^{-13}$	$5.67\text{x}10^{-14}$
$\varphi\ (BDP)$	atoms/m^2·dpa	$3.21 \pm 6.13\text{x}10^{20}$	$2.58 \pm 8.75\text{x}10^{20}$	$4.75 \pm 8.97\text{x}10^{20}$	$6.12 \pm 92.2\text{x}10^{19}$

Table A.5 NHM based BDP at 1 dpa for heavy ion irradiation of pre-existing α' precipitates at various damage rates with a linear fit for the precipitate evolution.

	Units	P18+H/1e-5	P18+H/1e-4		P18+H/3e-4		P18+H/1e-3	
α' evolution fit	N.A.	Linear fit, 0-1 dpa	Linear fit, 0-1 dpa	Linear fit, 1-10 dpa	Linear fit, 0-1 dpa	Linear fit, 1-10 dpa	Linear fit, 0-1 dpa	Linear fit, 1-10 dpa
C_e	at. fraction	0.105	0.105	0.105	0.105	0.105	0.105	0.105
C_m	at. fraction	0.130	0.131	0.131	0.141	0.141	0.138	0.138
C_p	at. fraction	0.692	0.687	0.687	0.671	0.671	0.84	0.84
r	m	$2.3\text{x}10^{-9}$	$2.3\text{x}10^{-9}$	$2.3\text{x}10^{-9}$	$2.1\text{x}10^{-9}$	$2.1\text{x}10^{-9}$	$2.8\text{x}10^{-9}$	$2.8\text{x}10^{-9}$
n	m^{-3}	$8.7\text{x}10^{23}$	$8.04\text{x}10^{23}$	$8.04\text{x}10^{23}$	$8.58\text{x}10^{23}$	$8.58\text{x}10^{23}$	$4.13\text{x}10^{23}$	$4.13\text{x}10^{23}$
${k_s}^2(\alpha')$	m^{-2}	$2.5\text{x}10^{16}$	$2.4\text{x}10^{16}$	$2.4\text{x}10^{16}$	$2.2\text{x}10^{16}$	$2.2\text{x}10^{16}$	$1.5\text{x}10^{16}$	$1.5\text{x}10^{16}$
${k_s}^2(disl)$	m^{-2}	$3.0\text{x}10^{14}$	$3.0\text{x}10^{14}$	$3.0\text{x}10^{14}$	$3.0\text{x}10^{14}$	$3.0\text{x}10^{14}$	$3.0\text{x}10^{14}$	$3.0\text{x}10^{14}$
${k_s}^2(cavities)$	m^{-2}	0	0	0	0	0	0	0
${k_s}^2(total)$	m^{-2}	$2.5\text{x}10^{16}$	$2.4\text{x}10^{16}$	$2.4\text{x}10^{16}$	$2.3\text{x}10^{16}$	$2.3\text{x}10^{16}$	$1.5\text{x}10^{16}$	$1.5\text{x}10^{16}$
ξ	unitless	0.1	0.1	0.1	0.1	0.1	0.1	0.1
K_0	dpa/s	$1.38 \pm 0.2\text{x}10^{-5}$	$1.0 \pm 0.1\text{x}10^{-4}$	$1.0 \pm 0.1\text{x}10^{-4}$	$2.9 \pm 0.7\text{x}10^{-4}$	$2.9 \pm 0.7\text{x}10^{-4}$	$1.0 \pm 0.1\text{x}10^{-3}$	$1.0 \pm 0.1\text{x}10^{-3}$
D_{irr}	m^2/s	$1.75\text{x}10^{-22}$	$9.10\text{x}10^{-22}$	$9.10\text{x}10^{-22}$	$2.62\text{x}10^{-21}$	$2.62\text{x}10^{-21}$	$1.42\text{x}10^{-20}$	$1.42\text{x}10^{-20}$
$\frac{dr}{dt}$	m/s	$-3.85\text{x}10^{-15}$	$-2.36\text{x}10^{-14}$	$-8.24\text{x}10^{-15}$	$-1.43\text{x}10^{-13}$	$-6.67\text{x}10^{-14}$	$5.67\text{x}10^{-14}$	$-3.13\text{x}10^{-15}$
$\varphi\ (BDP)$	atoms/m^2·dpa	$4.05 \pm 11.4\text{x}10^{20}$	$3.26 \pm 11.33\text{x}10^{20}$	$1.96 \pm 6.78\text{x}10^{20}$	$6.18 \pm 13.48\text{x}10^{20}$	$3.94 \pm 12.41\text{x}10^{20}$	$1.17 \pm 11.6\text{x}10^{20}$	$4.20 \pm 11.93\text{x}10^{20}$

Table A.6 NHM based BDP at 10 dpa for heavy ion irradiation of pre-existing α' precipitates at various damage rates with a linear fit for the precipitate evolution.

	Units	P18+H/1e-5	P18+H/1e-4		P18+H/3e-4	P18+H/1e-3
α' evolution fit	N.A.	N.A.	Linear fit, 1-10 dpa	Assume Steady State	N.A.	N.A.
C_e	at. fraction	N.A.	0.105	0.105	N.A.	N.A.
C_m	at. fraction	N.A.	0.155	0.155	N.A.	N.A.
C_p	at. fraction	N.A.	0.556	0.556	N.A.	N.A.
r	m	N.A.	$1.6\text{x}10^{-9}$	$1.6\text{x}10^{-9}$	N.A.	N.A.
n	m^{-3}	N.A.	$1.0\text{x}10^{24}$	$1.0\text{x}10^{24}$	N.A.	N.A.
${k_s}^2(\alpha')$	m^{-2}	N.A.	$2.0\text{x}10^{16}$	$2.0\text{x}10^{16}$	N.A.	N.A.
${k_s}^2(disl)$	m^{-2}	N.A.	$3.0\text{x}10^{14}$	$3.0\text{x}10^{14}$	N.A.	N.A.
${k_s}^2(cavities)$	m^{-2}	N.A.	0	0	N.A.	N.A.
${k_s}^2(total)$	m^{-2}	N.A.	$2.1\text{x}10^{16}$	$2.1\text{x}10^{16}$	N.A.	N.A.
ξ	unitless	N.A.	0.1	0.1	N.A.	N.A.
K_0	dpa/s	N.A.	$1.0 \pm 0.1\text{x}10^{-4}$	$1.0 \pm 0.1\text{x}10^{-4}$	N.A.	N.A.
D_{irr}	m^2/s	N.A.	$1.04\text{x}10^{-21}$	$1.04\text{x}10^{-21}$	N.A.	N.A.
$\frac{dr}{dt}$	m/s	N.A.	$-8.24\text{x}10^{-15}$	0	N.A.	N.A.
$\varphi\ (BDP)$	atoms/m^2·dpa	N.A.	$5.12 \pm 2.37\text{x}10^{21}$	$4.42 \pm 4.95\text{x}10^{21}$	N.A.	N.A.

Table A.7 NHM based BDP at 0 dpa for heavy ion irradiation of pre-existing α' precipitates at various damage rates with a polynomial fit for the precipitate evolution.

	Units	P18+H/1e-5	P18+H/1e-4	P18+H/3e-4	P19+H/1e-3
α' evolution fit	N.A.	Polynomial fit	Polynomial fit	Polynomial fit	Polynomial fit
C_e	at. fraction	0.105	0.105	0.105	0.105
C_m	at. fraction	0.122	0.122	0.122	0.13
C_p	at. fraction	0.862	0.862	0.862	0.853
r	m	$2.6\text{x}10^{-9}$	$2.6\text{x}10^{-9}$	$2.6\text{x}10^{-9}$	$2.8\text{x}10^{-9}$
n	m^{-3}	$7.39\text{x}10^{23}$	$7.39\text{x}10^{23}$	$7.39\text{x}10^{23}$	$4.7\text{x}10^{23}$
${k_s}^2(\alpha')$	m^{-2}	$2.6\text{x}10^{16}$	$2.6\text{x}10^{16}$	$2.6\text{x}10^{16}$	$1.6\text{x}10^{16}$
${k_s}^2(disl)$	m^{-2}	$3.0\text{x}10^{14}$	$3.0\text{x}10^{14}$	$3.0\text{x}10^{14}$	$3.0\text{x}10^{14}$
${k_s}^2(cavities)$	m^{-2}	0	0	0	0
${k_s}^2(total)$	m^{-2}	$2.6\text{x}10^{16}$	$2.6\text{x}10^{16}$	$2.6\text{x}10^{16}$	$1.6\text{x}10^{16}$
ξ	unitless	0.1	0.1	0.1	0.1
K_0	dpa/s	$1.38 \pm 0.2\text{x}10^{-5}$	$1.0 \pm 0.1\text{x}10^{-4}$	$2.9 \pm 0.7\text{x}10^{-4}$	$1.0 \pm 0.1\text{x}10^{-3}$
D_{irr}	m^2/s	$1.81\text{x}10^{-22}$	$9.00\text{x}10^{-22}$	$2.46\text{x}10^{-21}$	$1.27\text{x}10^{-20}$
$\frac{dr}{dt}$	m/s	$-3.86\text{x}10^{-15}$	$-2.00\text{x}10^{-14}$	$-1.56\text{x}10^{-13}$	0.0
$\varphi\ (BDP)$	atoms/m^2·dpa	$3.22 \pm 1.26\text{x}10^{20}$	$2.27 \pm 1.43\text{x}10^{20}$	$4.94 \pm 1.79\text{x}10^{20}$	$1.08 \pm 0.49\text{x}10^{20}$

Table A.8 NHM based BDP at 1 dpa for heavy ion irradiation of pre-existing α' precipitates at various damage rates with a polynomial fit for the precipitate evolution.

	Units	P18+H/1e-5	P18+H/1e-4	P18+H/3e-4	P19+H/1e-3
α' evolution fit	N.A.	Polynomial fit	Polynomial fit	Polynomial fit	Polynomial fit
C_e	at. fraction	0.105	0.105	0.105	0.105
C_m	at. fraction	0.130	0.131	0.141	0.138
C_p	at. fraction	0.692	0.687	0.671	0.84
r	m	$2.3\text{x}10^{-9}$	$2.3\text{x}10^{-9}$	$2.1\text{x}10^{-9}$	$2.8\text{x}10^{-9}$
n	m^{-3}	$8.7\text{x}10^{23}$	$8.04\text{x}10^{23}$	$8.58\text{x}10^{23}$	$4.13\text{x}10^{23}$
${k_s}^2(\alpha')$	m^{-2}	$2.5\text{x}10^{16}$	$2.4\text{x}10^{16}$	$2.2\text{x}10^{16}$	$1.5\text{x}10^{16}$
${k_s}^2(disl)$	m^{-2}	$3.0\text{x}10^{14}$	$3.0\text{x}10^{14}$	$3.0\text{x}10^{14}$	$3.0\text{x}10^{14}$
${k_s}^2(cavities)$	m^{-2}	0	0	0	0
${k_s}^2(total)$	m^{-2}	$2.5\text{x}10^{16}$	$2.4\text{x}10^{16}$	$2.3\text{x}10^{16}$	$1.5\text{x}10^{16}$
ξ	unitless	0.1	0.1	0.1	0.1
K_0	dpa/s	$1.38 \pm 0.2\text{x}10^{-5}$	$1.0 \pm 0.1\text{x}10^{-4}$	$2.9 \pm 0.7\text{x}10^{-4}$	$1 \pm 0.1\text{x}10^{-3}$
D_{irr}	m^2/s	$1.75\text{x}10^{-22}$	$9.01\text{x}10^{-22}$	$2.63\text{x}10^{-21}$	$1.42\text{x}10^{-20}$
$\frac{dr}{dt}$	m/s	$-3.48\text{x}10^{-15}$	$-1.80\text{x}10^{-14}$	$-1.35\text{x}10^{-13}$	$-5.77\text{x}10^{-14}$
$\varphi\ (BDP)$	atoms/m^2·dpa	$3.83 \pm 1.80\text{x}10^{20}$	$2.79 \pm 1.56\text{x}10^{20}$	$5.93 \pm 2.24\text{x}10^{20}$	$2.11 \pm 0.89\text{x}10^{20}$

Table A.9 NHM based BDP at 10 dpa for heavy ion irradiation of pre-existing α' precipitates at various damage rates with a polynomial fit for the precipitate evolution.

	Units	P18+H/1e-5	P18+H/1e-4	P18+H/3e-4	P19+H/1e-3
α' evolution fit	N.A.	Polynomial fit	Polynomial fit	Polynomial fit	Polynomial fit
C_e	at. fraction	N.A.	0.105	N.A.	N.A.
C_m	at. fraction	N.A.	0.155	N.A.	N.A.
C_p	at. fraction	N.A.	0.556	N.A.	N.A.
r	m	N.A.	1.6×10^{-9}	N.A.	N.A.
n	m^{-3}	N.A.	1.0×10^{24}	N.A.	N.A.
${k_s}^2(\alpha')$	m^{-2}	N.A.	2.0×10^{16}	N.A.	N.A.
${k_s}^2(disl)$	m^{-2}	N.A.	3.0×10^{14}	N.A.	N.A.
${k_s}^2(cavities)$	m^{-2}	N.A.	0	N.A.	N.A.
${k_s}^2(total)$	m^{-2}	N.A.	2.1×10^{16}	N.A.	N.A.
ξ	unitless	N.A.	0.1	N.A.	N.A.
K_0	dpa/s	N.A.	$1.0 \pm 0.1 \times 10^{-4}$	N.A.	N.A.
D_{irr}	m^2/s	N.A.	2.33×10^{-21}	N.A.	N.A.
$\frac{dr}{dt}$	m/s	N.A.	0.0	N.A.	N.A.
$\varphi\ (BDP)$	atoms/m^2·dpa	N.A.	$4.42 \pm 2.22 \times 10^{20}$	N.A.	N.A.

Table A.10 NHM based BDP at 0 dpa for heavy ion irradiation of pre-existing α' precipitates at various damage rates with an exponential fit for the precipitate evolution.

	Units	P18+H/1e-5	P18+H/1e-4	P18+H/3e-4	P19+H/1e-3
α' evolution fit	N.A.	Exponential fit	Exponential fit	Exponential fit	Exponential fit
C_e	at. fraction	0.105	0.105	0.105	0.105
C_m	at. fraction	0.122	0.122	0.122	0.13
C_p	at. fraction	0.862	0.862	0.862	0.853
r	m	$2.6\text{x}10^{-9}$	$2.6\text{x}10^{-9}$	$2.6\text{x}10^{-9}$	$2.8\text{x}10^{-9}$
n	m^{-3}	$7.39\text{x}10^{23}$	$7.39\text{x}10^{23}$	$7.39\text{x}10^{23}$	$4.7\text{x}10^{23}$
${k_s}^2(\alpha')$	m^{-2}	$2.6\text{x}10^{16}$	$2.6\text{x}10^{16}$	$2.6\text{x}10^{16}$	$1.6\text{x}10^{16}$
${k_s}^2(disl)$	m^{-2}	$3.0\text{x}10^{14}$	$3.0\text{x}10^{14}$	$3.0\text{x}10^{14}$	$3.0\text{x}10^{14}$
${k_s}^2(cavities)$	m^{-2}	0	0	0	0
${k_s}^2(total)$	m^{-2}	$2.6\text{x}10^{16}$	$2.6\text{x}10^{16}$	$2.6\text{x}10^{16}$	$1.6\text{x}10^{16}$
ξ	unitless	0.1	0.1	0.1	0.1
K_0	dpa/s	$1.38 \pm 0.2\text{x}10^{-5}$	$1.0 \pm 0.1\text{x}10^{-4}$	$2.9 \pm 0.7\text{x}10^{-4}$	$1.0 \pm 0.1\text{x}10^{-3}$
D_{irr}	m^2/s	$1.81\text{x}10^{-22}$	$9.00\text{x}10^{-22}$	$2.46\text{x}10^{-21}$	$1.27\text{x}10^{-20}$
$\frac{dr}{dt}$	m/s	$-4.83\text{x}10^{-15}$	$-3.85\text{x}10^{-14}$	$-1.50\text{x}10^{-13}$	$-5.12\text{x}10^{-13}$
$\varphi\ (BDP)$	atoms/m^2·dpa	$3.81 \pm 1.94\text{x}10^{20}$	$3.83 \pm 2.28\text{x}10^{20}$	$4.94 \pm 2.93\text{x}10^{20}$	$5.27 \pm 2.56\text{x}10^{20}$

Table A.11 NHM based BDP at 1 dpa for heavy ion irradiation of pre-existing α' precipitates at various damage rates with an exponential fit for the precipitate evolution.

	Units	P18+H/1e-5	P18+H/1e-4	P18+H/3e-4	P19+H/1e-3
α' evolution fit	N.A.	Exponential fit	Exponential fit	Exponential fit	Exponential fit
C_e	at. fraction	0.105	0.105	0.105	0.105
C_m	at. fraction	0.130	0.131	0.141	0.138
C_p	at. fraction	0.692	0.687	0.671	0.84
r	m	2.3×10^{-9}	2.3×10^{-9}	2.1×10^{-9}	2.8×10^{-9}
n	m^{-3}	8.7×10^{23}	8.04×10^{23}	8.58×10^{23}	4.13×10^{23}
${k_s}^2(\alpha')$	m^{-2}	2.5×10^{16}	2.4×10^{16}	2.2×10^{16}	1.5×10^{16}
${k_s}^2(disl)$	m^{-2}	3.0×10^{14}	3.0×10^{14}	3.0×10^{14}	3.0×10^{14}
${k_s}^2(cavities)$	m^{-2}	0	0	0	0
${k_s}^2(total)$	m^{-2}	2.5×10^{16}	2.4×10^{16}	2.3×10^{16}	1.5×10^{16}
ξ	unitless	0.1	0.1	0.1	0.1
K_0	dpa/s	$1.38 \pm 0.2\times10^{-5}$	$1.0 \pm 0.1\times10^{-4}$	$2.9 \pm 0.7\times10^{-4}$	$1 \pm 0.1\times10^{-3}$
D_{irr}	m^2/s	1.75×10^{-22}	9.01×10^{-22}	2.63×10^{-21}	1.42×10^{-20}
$\frac{dr}{dt}$	m/s	-3.74×10^{-15}	-2.71×10^{-14}	-1.23×10^{-13}	-4.27×10^{-13}
$\varphi\ (BDP)$	atoms/m^2·dpa	$3.99 \pm 1.99\times10^{20}$	$3.56 \pm 1.92\times10^{20}$	$5.57 \pm 2.70\times10^{20}$	$5.13 \pm 2.08\times10^{20}$

Table A.12 NHM based BDP at 10 dpa for heavy ion irradiation of pre-existing α' precipitates at various damage rates with an exponential fit for the precipitate evolution.

	Units	P18+H/1e-5	P18+H/1e-4	P18+H/3e-4	P19+H/1e-3
α' evolution fit	N.A.	Exponential fit	Exponential fit	Exponential fit	Exponential fit
C_e	at. fraction	N.A.	0.105	N.A.	N.A.
C_m	at. fraction	N.A.	0.155	N.A.	N.A.
C_p	at. fraction	N.A.	0.556	N.A.	N.A.
r	m	N.A.	$1.6\text{x}10^{-9}$	N.A.	N.A.
n	m^{-3}	N.A.	$1.0\text{x}10^{24}$	N.A.	N.A.
${k_s}^2(\alpha')$	m^{-2}	N.A.	$2.0\text{x}10^{16}$	N.A.	N.A.
${k_s}^2(disl)$	m^{-2}	N.A.	$3.0\text{x}10^{14}$	N.A.	N.A.
${k_s}^2(cavities)$	m^{-2}	N.A.	0	N.A.	N.A.
${k_s}^2(total)$	m^{-2}	N.A.	$2.1\text{x}10^{16}$	N.A.	N.A.
ξ	unitless	N.A.	0.1	N.A.	N.A.
K_0	dpa/s	N.A.	$1.0 \pm 0.1\text{x}10^{-4}$	N.A.	N.A.
D_{irr}	m^2/s	N.A.	$2.33\text{x}10^{-21}$	N.A.	N.A.
$\frac{dr}{dt}$	m/s	N.A.	$-1.16\text{x}10^{-15}$	N.A.	N.A.
$\varphi\ (BDP)$	atoms/m^2·dpa	N.A.	$4.52 \pm 2.23\text{x}10^{20}$	N.A.	N.A.

Table A.13 Mixing based BDP calculation for pre-existing a' precipitate subjected to 4.4 MeV heavy ion irradiation at various damage rates to 1 and 10 dpa.

Term	Units	P18+H/1e-5/1	P18+H/1e-4/1	P18+H/1e-4/10	P18+H/3e-4/1	P18+H/1e-3/1
K_0	dpa/s	$1.38 \pm 0.2 \times 10^{-5}$	$1.0 \pm 0.1 \times 10^{-4}$	$1.0 \pm 0.1 \times 10^{-4}$	$2.9 \pm 0.7 \times 10^{-4}$	$1 \pm 0.1 \times 10^{-3}$
t	dpa	0.28	0.80	0.3	0.85	0.40
c_1	atomic fraction	0.778	0.814	0.586	0.819	0.84
c_2	atomic fraction	0.112	0.121	0.145	0.124	0.134
D	m^2/s	7.12×10^{-24}	7.14×10^{-23}	7.55×10^{-23}	2.14×10^{-22}	7.27×10^{-22}
$\frac{dc}{dx}(0,t)$	m^{-4}	3.51×10^{37}	2.15×10^{37}	2.45×10^{37}	2.10×10^{37}	3.08×10^{37}
J_{recoil}	$atoms/m^2s$	2.50×10^{14}	1.54×10^{15}	1.75×10^{15}	4.50×10^{15}	2.24×10^{16}
BDP	$atoms/m^2dpa$	$2.50 \pm 1.15 \times 10^{20}$	$1.54 \pm 0.71 \times 10^{20}$	$1.76 \pm 0.72 \times 10^{20}$	$1.50 \pm 0.69 \times 10^{20}$	$2.24 \pm 1.03 \times 10^{20}$

Table A.14 Mixing based BDP calculation for pre-existing a' precipitate subjected to 1.5 MeV Proton irradiation at various damage rates to 1 and 10 dpa.

Term	Units	P19+P/1e-4/1	P19+P/1e-4/10
K_0	dpa/s	$1.0 \pm 0.1 \times 10^{-4}$	$1.0 \pm 0.1 \times 10^{-4}$
t	dpa	0.5	0.17
c_1	atomic fraction	0.900	0.903
c_2	atomic fraction	0.139	0.141
D	m^2/s	5.13×10^{-23}	1.56×10^{-22}
$\frac{dc}{dx}(0,t)$	m^{-4}	3.53×10^{37}	3.48×10^{37}
J_{recoil}	$atoms/m^2s$	1.81×10^{15}	5.43×10^{15}
BDP	$atoms/m^2dpa$	$2.27 \pm 0.70 \times 10^{19}$	$6.78 \pm 2.31 \times 10^{19}$

Appendix B: IRRADIATION PARAMETERS

The iron current, temperature, and pressure for each irradiation performed as part of this thesis are presented in this appendix.

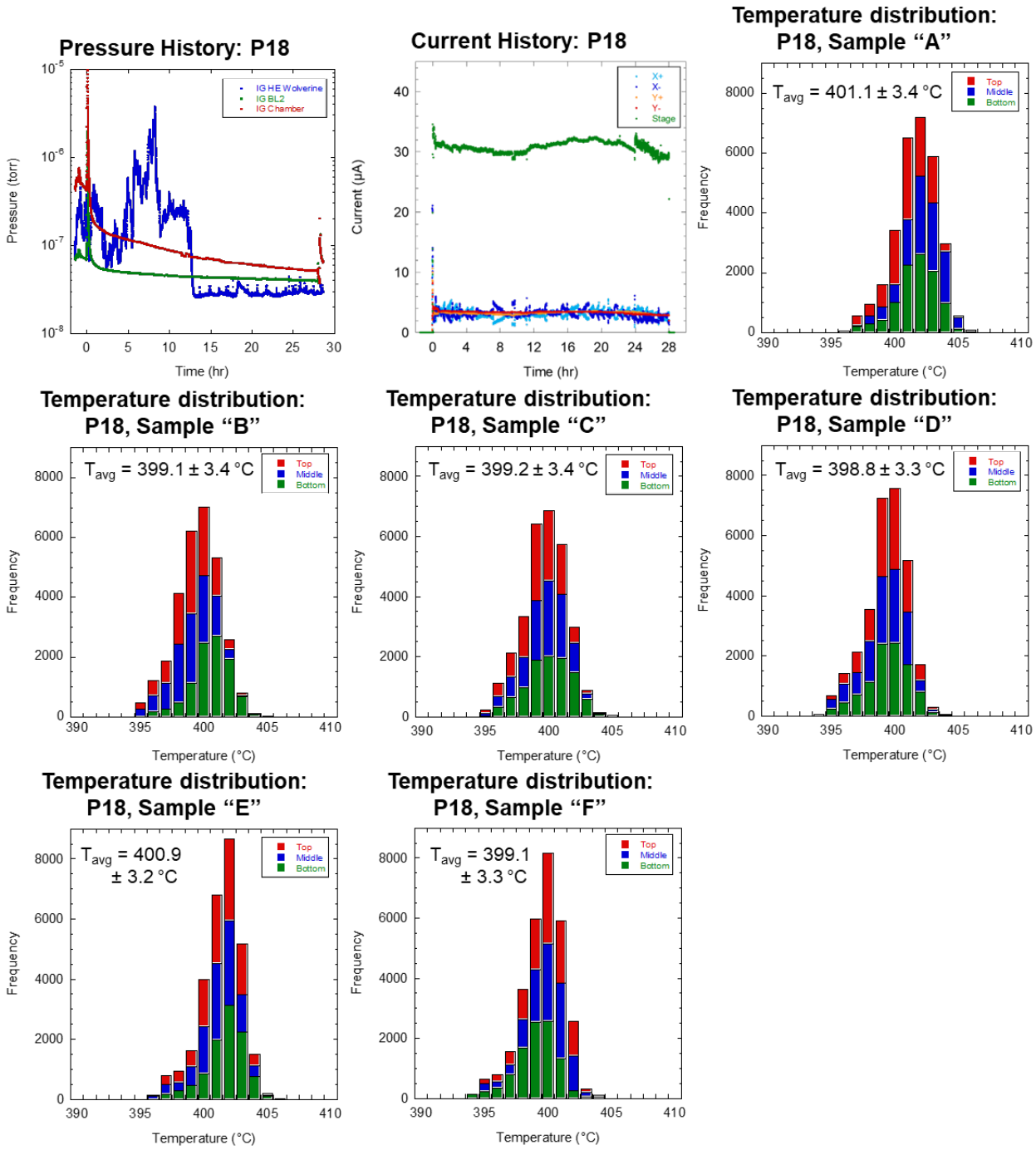

Figure B.1 Temperature, pressure, and current history for proton irradiation "P19" establishing the initial a' precipitate population with 2 MeV proton irradiation at a damage rate of $1x10^{-5}$ dpa/s to 1 dpa at 400C.

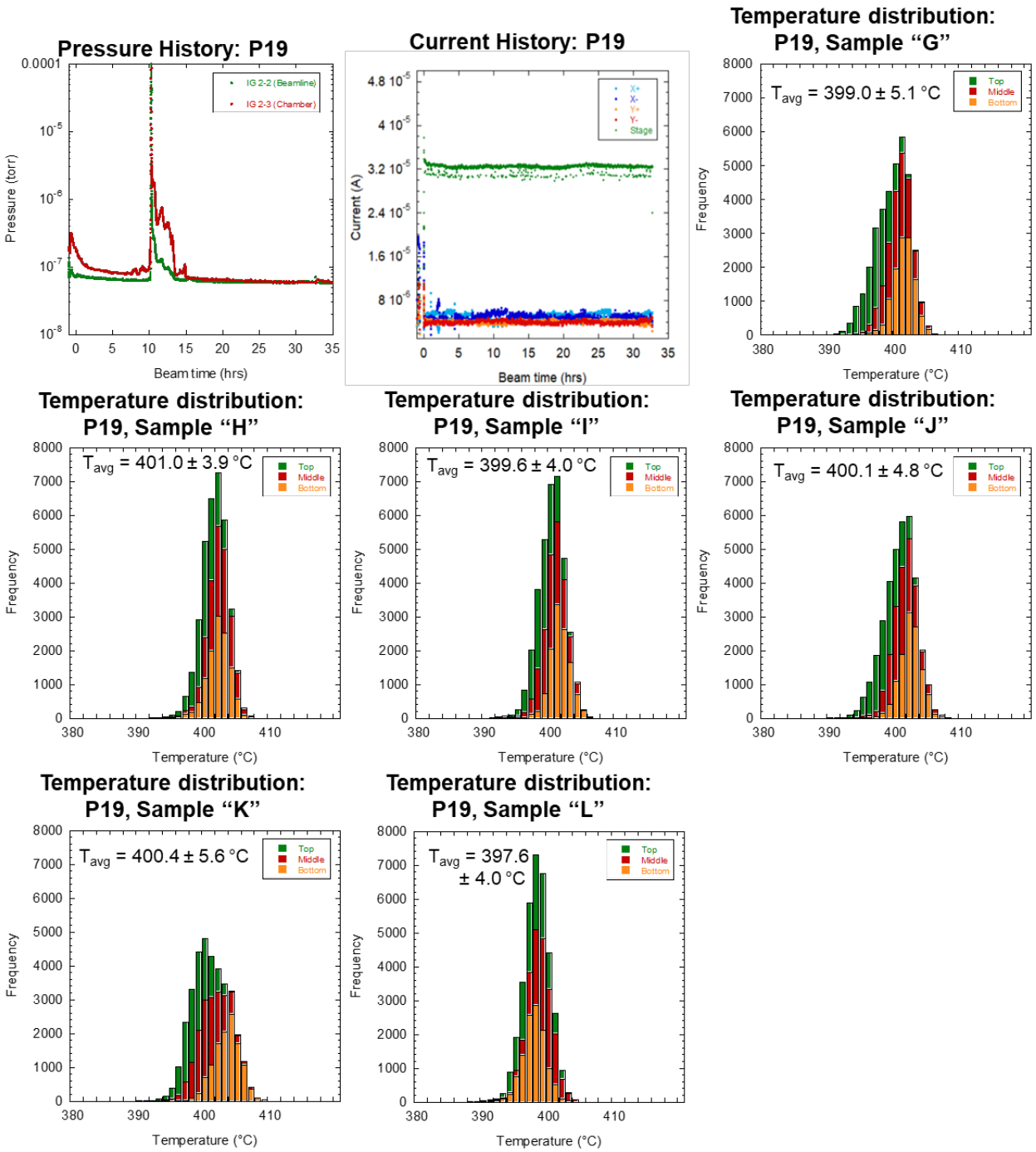

Figure B.2 Temperature, pressure, and current history for proton irradiation "P19" establishing the initial a' precipitate population with 2 MeV proton irradiation at a damage rate of 1x10^{-5} dpa/s to 1 dpa at 400C.

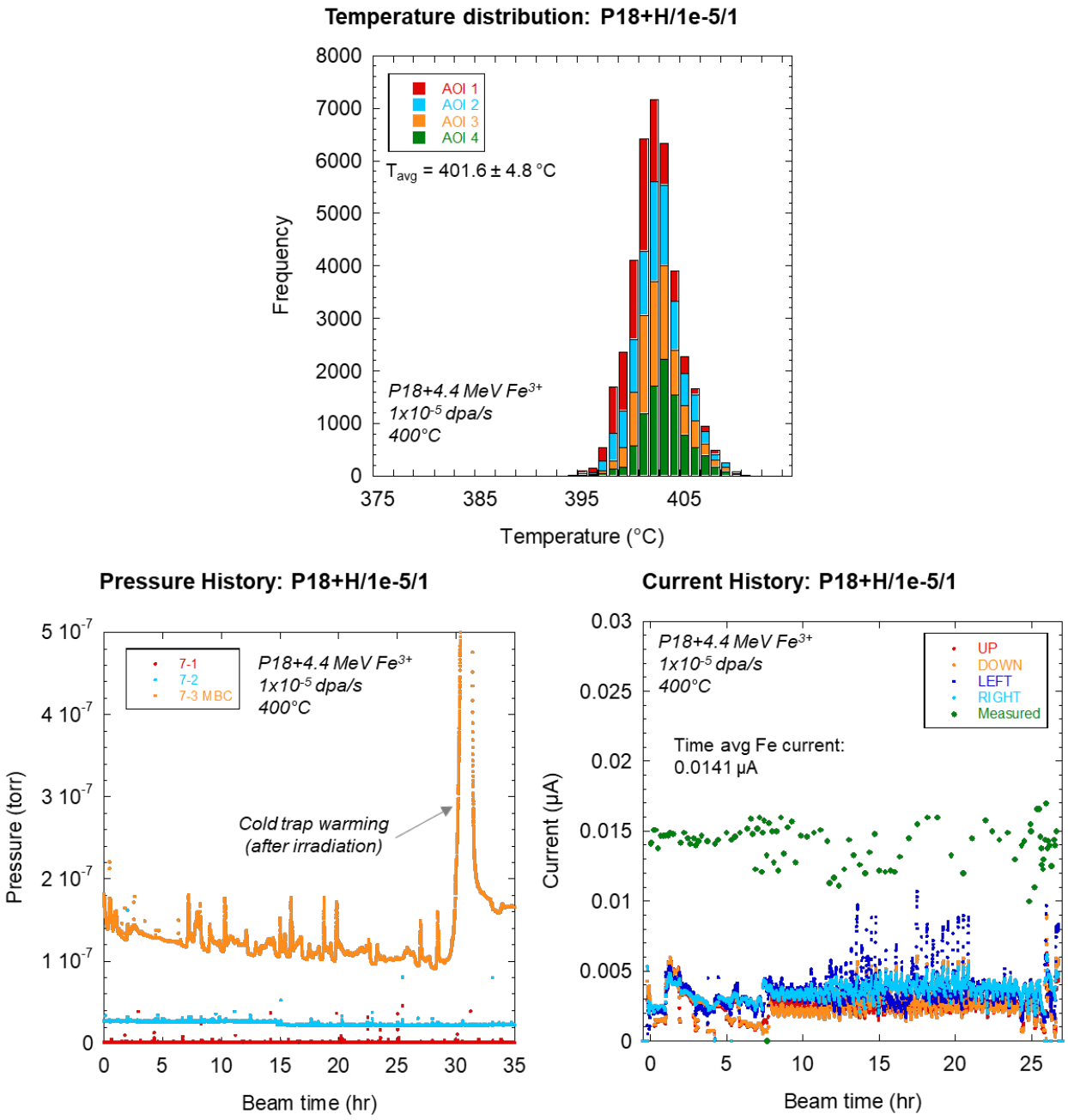

Figure B.3 Temperature, pressure, and current history for heavy ion irradiation of pre-existing a' precipitates at 1x10^{-5} dpa/s to 1 dpa at 400°C.

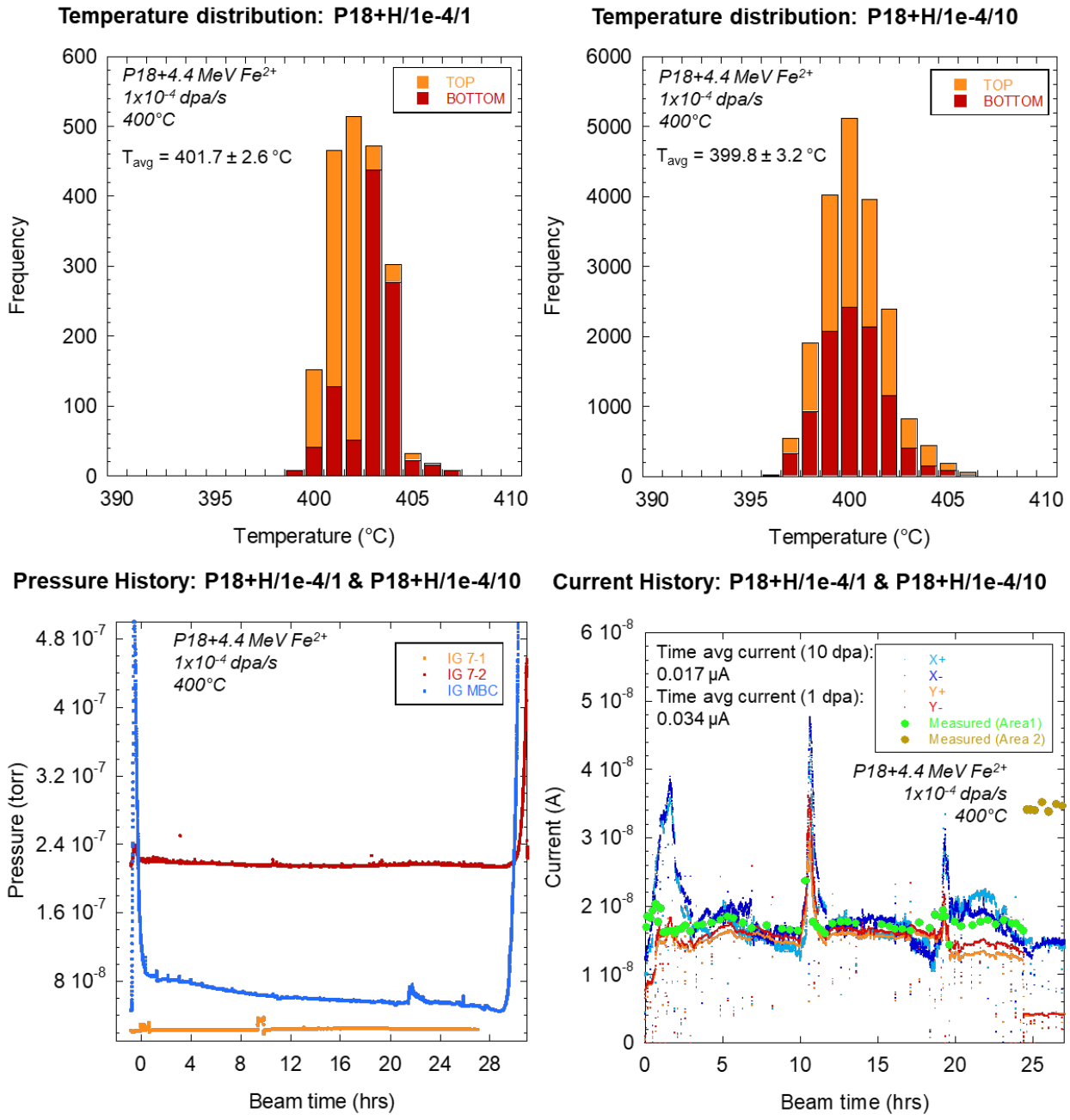

Figure B.4 Temperature, pressure, and current history for heavy ion irradiation of pre-existing a' precipitates at 1x10^{-4} dpa/s to 1 and 10 dpa at 400°C. Irradiation was completed in two phases: irradiation of "Area 1" to 9 dpa; then widening the irradiation area to "Area 2" to irradiate to 1 dpa creating two irradiated areas on the sample at 1 and 10 dpa.

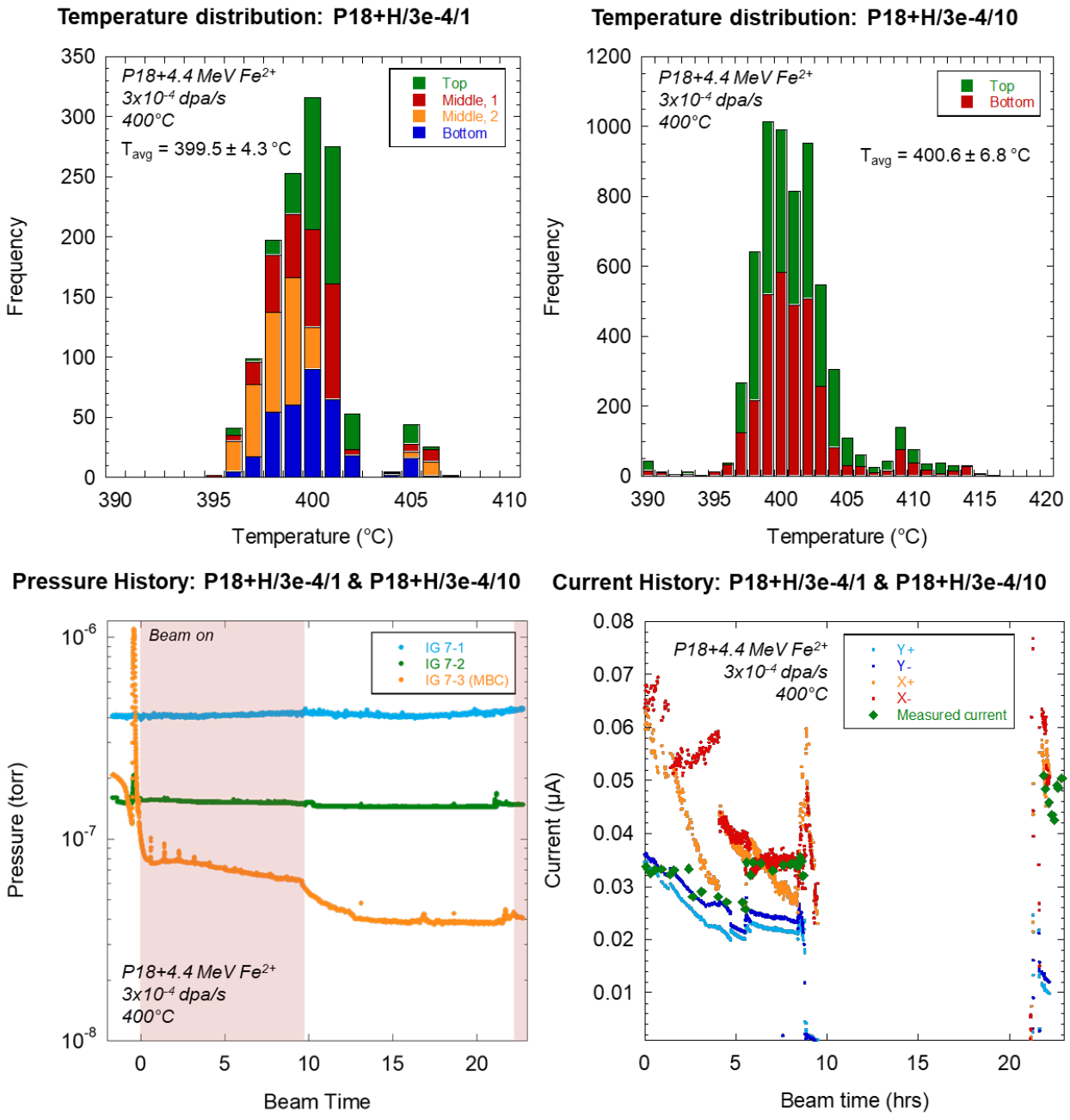

Figure B.5 Temperature, pressure, and current history for heavy ion irradiation of pre-existing a' precipitates at 3x10^{-4} dpa/s to 1 and 10 dpa at 400°C. Irradiation was completed in two phases: irradiation of "Area 1" to 9 dpa; then widening the irradiation area to "Area 2" to irradiate to 1 dpa creating two irradiated areas on the sample at 1 and 10 dpa.

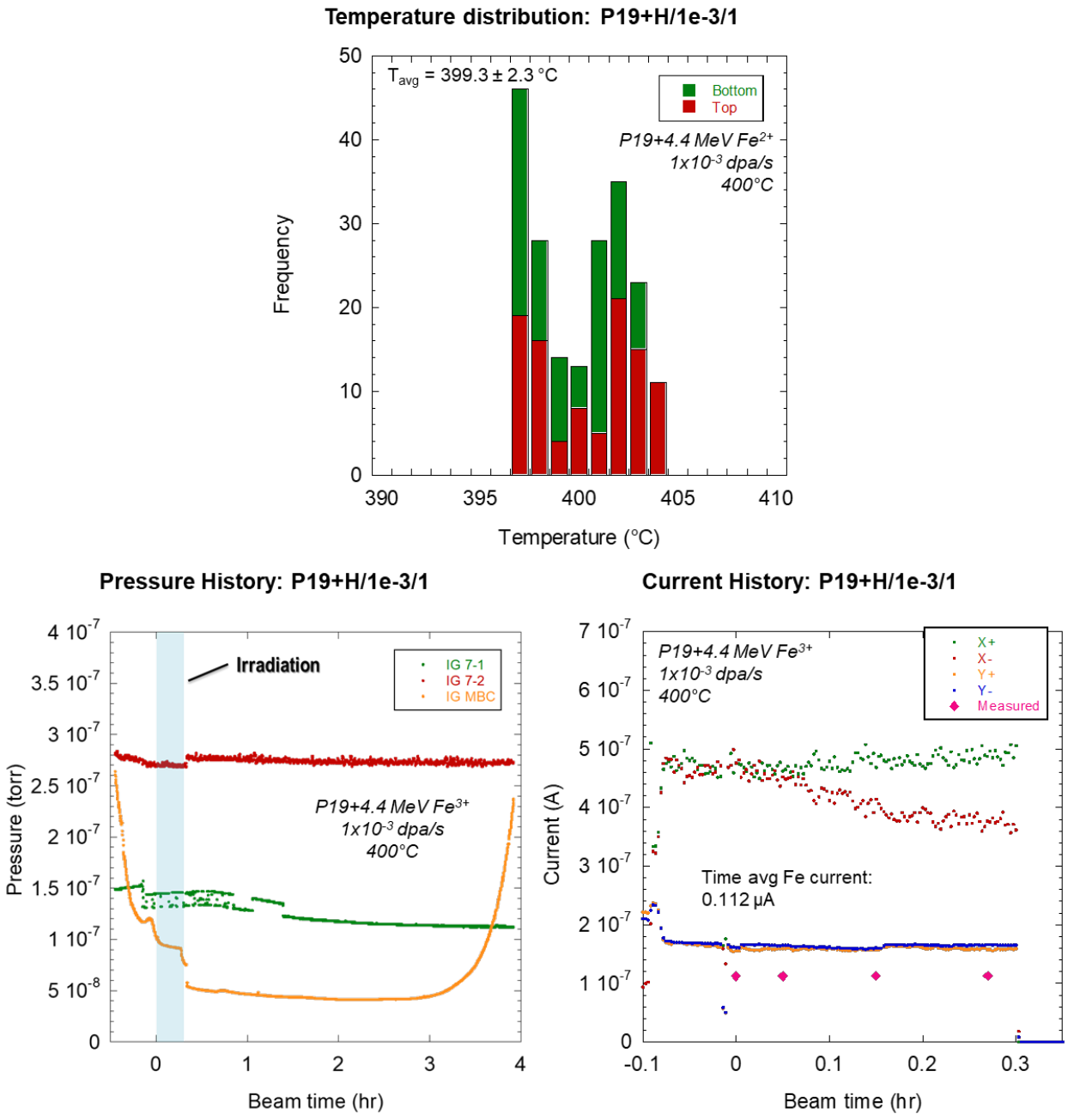

Figure B.6 Temperature, pressure, and current history for heavy ion irradiation of pre-existing a' precipitates at 1x10^{-3} dpa/s to 1 dpa at 400°C.

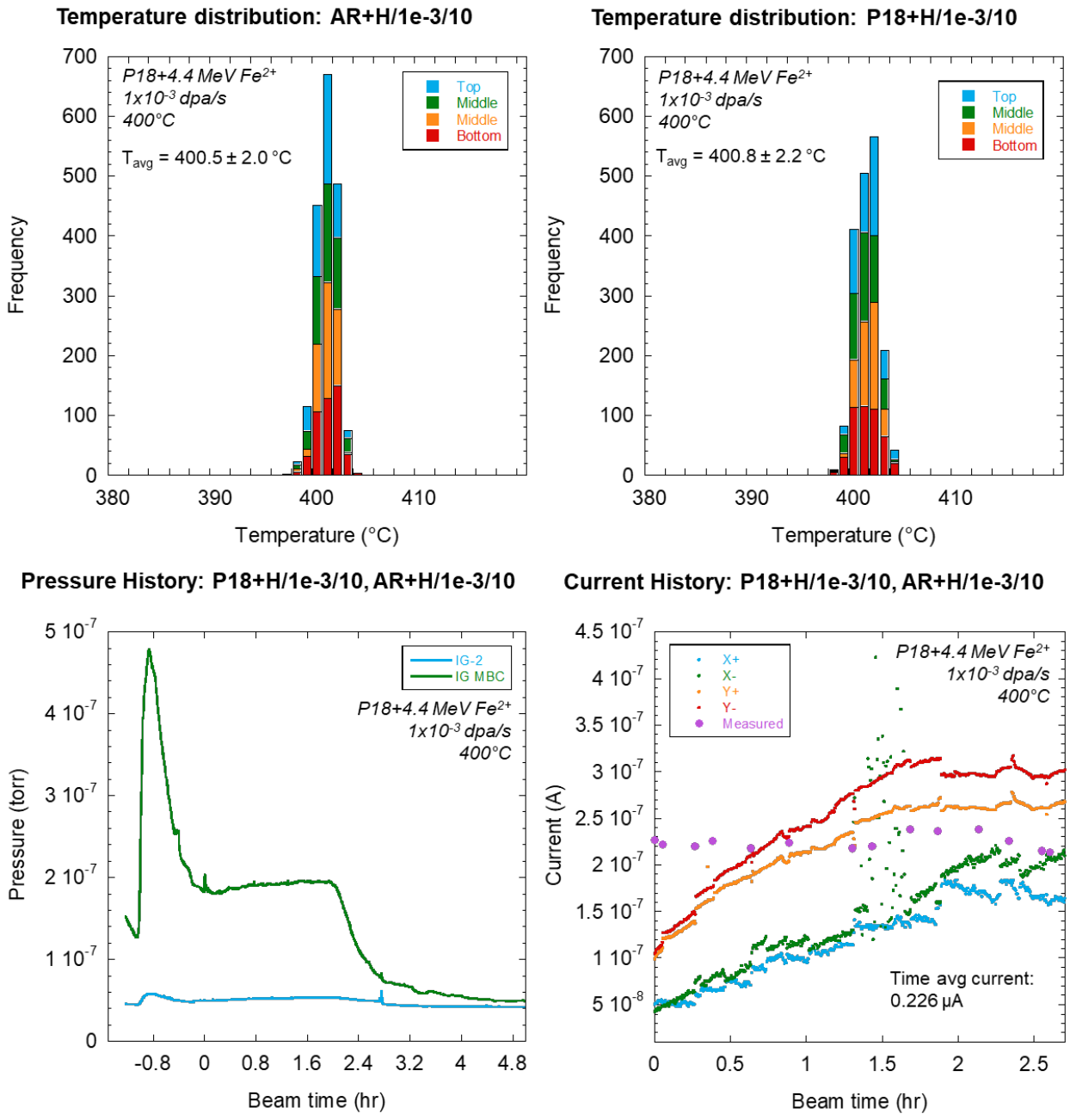

Figure B.7 Temperature, pressure, and current history for heavy ion irradiation of as received 15Cr at 1x10^{-3} dpa/s to 1 dpa at 400°C.

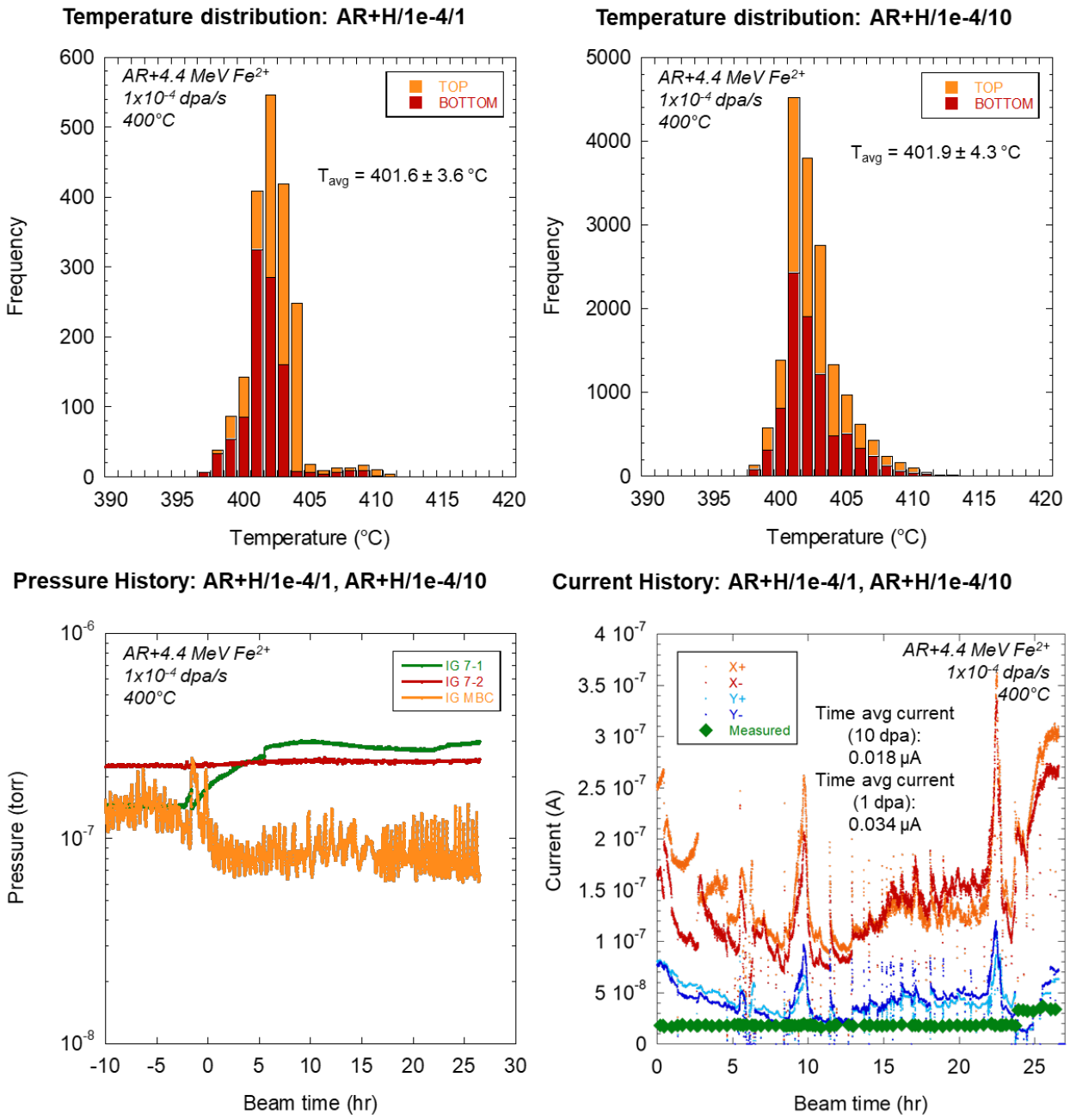

Figure B.8 Temperature, pressure, and current history for heavy ion irradiation of as received 15Cr at 1x10^{-4} dpa/s to 10 dpa at 400°C.

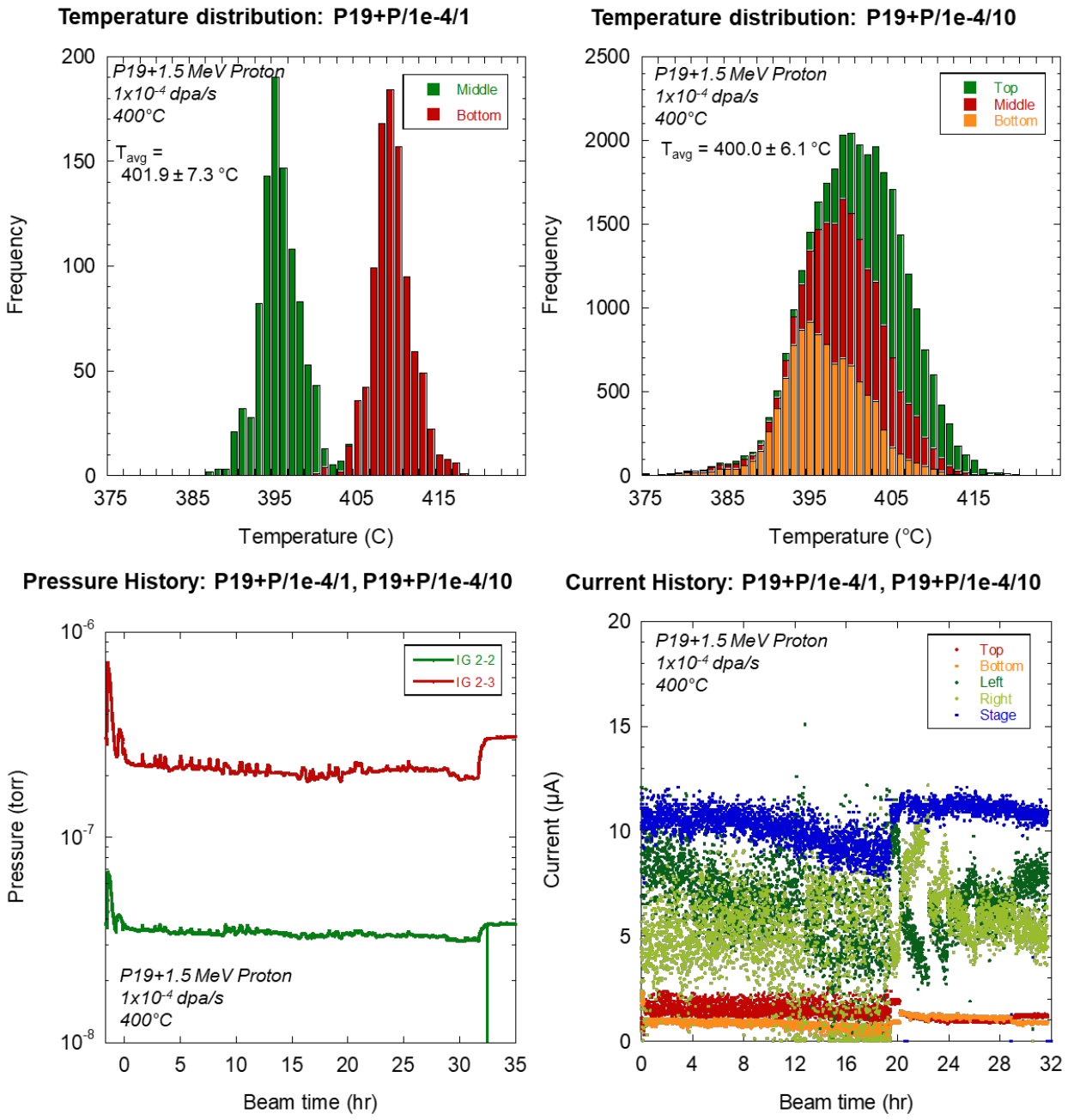

Figure B.9 Temperature, pressure, and current history for proton irradiation of pre-existing a' precipitates at 1x10^{-4} dpa/s to 1 and 10 dpa at 400°C. Irradiation was completed in two phases: irradiation of "Area 1" to 9 dpa; then changing the irradiation area to "Area 2" to irradiate to 1 dpa creating two irradiated areas on the sample at 1 and 10 dpa.

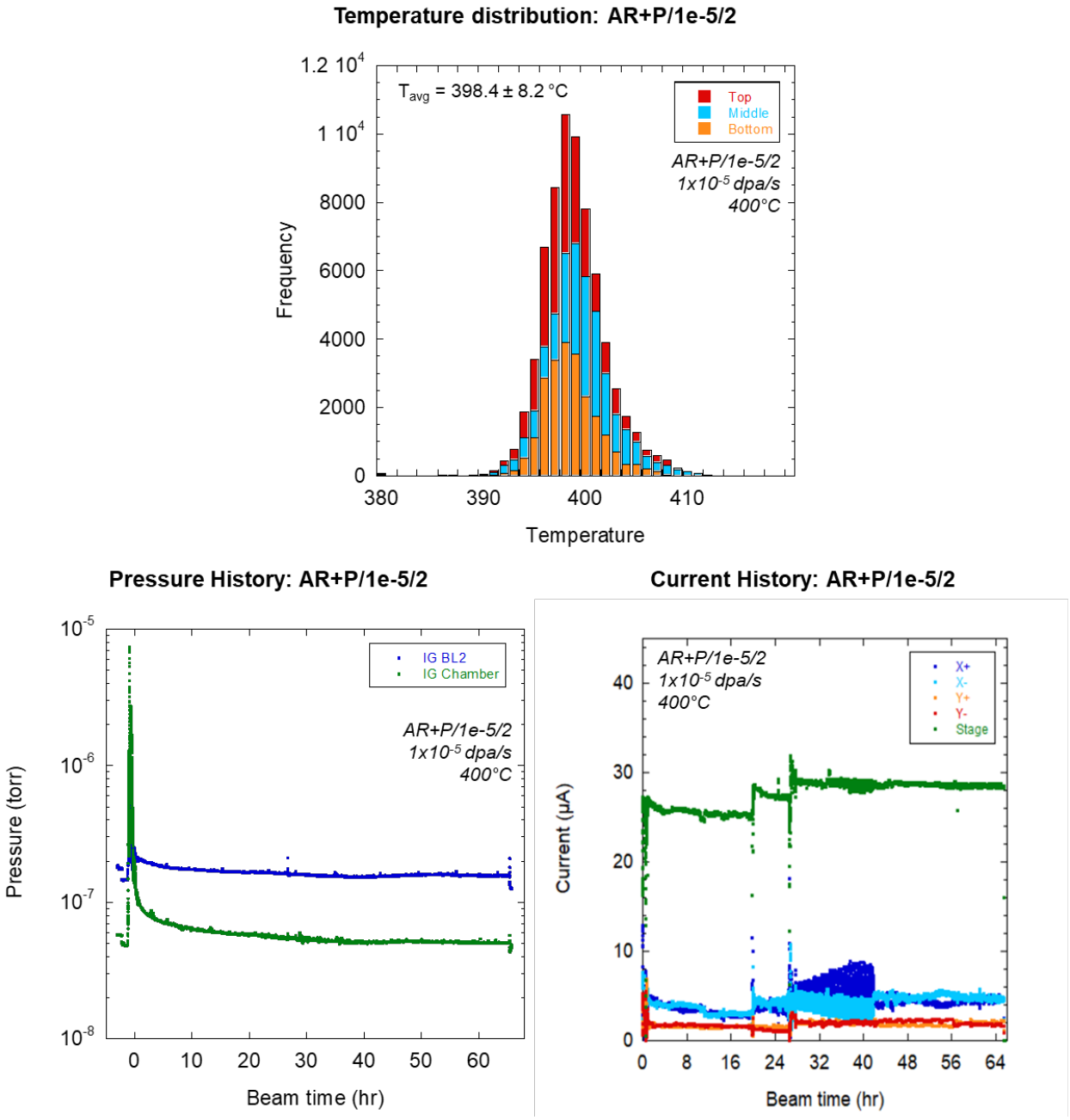

Figure B.10 Temperature, pressure, and current history for proton irradiation of as received 15Cr at 1x10^{-5} dpa/s to 2 dpa at 400°C.